Interferometric Spatio-Temporal Characterisation of Ultrashort Light Pulses

Matthias Maximilian Mang
Hertford College, Oxford

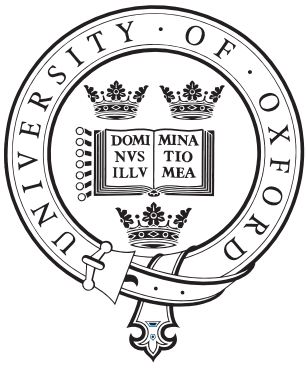

Submitted for the degree of Doctor of Philosophy
Trinity term 2014

Supervised by
Prof. Ian A. Walmsley

Clarendon Laboratory
University of Oxford
United Kingdom

Interferometric Spatio-Temporal Characterisation of Ultrashort Light Pulses

Matthias M. Mang
Hertford College, Oxford

Submitted for the degree of Doctor of Philosophy
Trinity term 2014

Abstract

The main topic of this thesis is the development of novel diagnostics for the characterisation of infrared femtosecond and extreme-ultraviolet (XUV) attosecond pulses. High-resolution interferometric methods are applied to high harmonic radiation, both to measure the properties of the XUV light and to relate this information to the physics of the fundamental generation process. To do so, a complete high harmonic beamline has been built and optimised to enable the observation of strong signatures of the macroscopic response of the medium. The distinct spatial characteristics of long and short trajectories are studied, as well as the interference between them. An interferometric measurement allows the extraction of the atomic dipole phase, which gives direct access to the sub-cycle electron dynamics.

A major focus of this thesis is on the development of a novel method which simultaneously characterises two independent electric fields as a function of any degree of freedom in which it is possible to shear one of the beams. Since each field alternately takes the role of the reference to retrieve the other field, this technique is referred to as mutual interferometric characterisation of electric-fields (MICE). One of the key features of MICE is that no sheared but otherwise identical replica of the test pulse needs to be generated, which is a typical requirement of self-referencing techniques. Furthermore, no a priori information is needed for the reconstruction. The strength and the wide applicability of MICE are demonstrated using two fundamentally different examples. First, the temporal pulse profiles of two infrared femtosecond pulses are simultaneously reconstructed in a single laser shot. In the second demonstration, the MICE approach is used to simultaneously reconstruct the wavefronts of two high harmonic beams. Having this new technique at hand, the phase properties of the different quantum trajectories are compared.

All pulse characterisation techniques implicitly assume full coherence of the beam. This, however, is often not the case in practice, in particular when dealing with complex XUV light sources. Here the standard characterisation techniques fail to provide an accurate description of the electric field. Instead, the electric field must be seen as a statistical mixture of different contributions to the overall field. Here an interferometric experiment is first proposed and then performed involving multiple lateral shears to measure the two-point correlation function of high harmonic radiation. This directly provides information about the existence and the magnitude of partial coherence of high harmonics.

Author's publications

Journal publications

1. M. M. Mang, C. Bourassin-Bouchet, and I. A. Walmsley, "Simultaneous spatial characterization of two independent sources of high harmonic radiation," *Opt. Lett.* **39,** 6142–6145 (2014).

2. C. Bourassin-Bouchet*, M. M. Mang*, I. Gianani, and I. A. Walmsley, "Mutual interferometric characterization of a pair of independent electric fields," *Opt. Lett.* **38,** 5299–5302 (2013) *equal contribution.

3. C. Bourassin-Bouchet, M. M. Mang, F. Delmotte, P. Chavel, and S. de Rossi, "How to focus an attosecond pulse," *Opt. Express* **21,** 2506–2520 (2013).

Peer-reviewed conferences

1. M. M. Mang, C. Bourassin-Bouchet, I. Gianani, and I. A. Walmsley, "Mutual interferometric characterization of electric fields," *Frontiers in Optics 2013/Laser Science XXIX*, October 2013.

Contents

List of Figures

List of Tables

Chapter 1

Introduction

"In considering the study of physical phenomena, not merely in its bearings on the material wants of life, but in its general influence on the intellectual advancement of mankind, we find its noblest and most important result to be a knowledge of the chain of connection, by which all natural forces are linked together, and made mutually dependent upon each other; and it is the perception of these relations that exalts our views and ennobles our enjoyments."

Alexander von Humboldt - *Cosmos*

The observation of the evolution of natural phenomena in time lies at the heart of a broad range of scientific disciplines. While the static world has already much to offer, and many areas in science and technology exploit the static world with large success and impact, it is ultimately the evolution of processes over time that provides us with the deepest insight into nature. Scientists across all disciplines are interested in tracking how the world evolves at all length- and timescales. This ranges from the astronomical scale,

the evolution of the universe since its birth about 14 billion years ago, to the microscopic world, such as the temporal evolution of chemical reactions. The better we can follow time-dependent natural phenomena, the more we can learn about their present state and their origin, and the better we can make accurate predictions about their future. In the context of this thesis, "following better in time" means answering the question: What are the fastest processes that can be recorded without appearing blurred? The human eye can distinguish about 60 events per second as separated in time. Processes evolving at a faster rate cannot be resolved by the eye and appear blurred. Modern technology has been able to push these limits to the nanosecond scale by the use of fast semiconductor detectors. However, electronics is not fast enough to resolve much shorter timescales. After the first experimental demonstration of the laser in 1960 by Maiman [1], it turned out that short flashes of light have the potential to access very short timescales. The development of mode-locking provided laser scientists with light pulses with durations in the femtosecond domain (1 fs = 10^{-15} s) [2, 3]. Since this corresponds to the timescale of the movement of nuclei in chemical reactions, femtosecond pulses provide access to the microscopic world. Indeed, the use of such lasers allowed chemists to track the formation and breaking of chemical bonds in "slow motion". For his contribution to the field of femtochemistry, Zewail was awarded the Nobel Prize in Chemistry in 1999 [4, 5]. Moreover, by shaping the waveform of the pulse appropriately, the force applied to the probed system can be used not only to monitor, but also to steer and control chemical reactions, a central theme in modern chemistry [6]. Femtosecond lasers are now used in a wide range of applications as diverse as precision processing of materials, plasma physics, precise frequency measurements and eye surgery.

The generation of femtosecond pulses is today well understood, and commercial laser systems are available for different parameter regimes. They are usually based on a Titanium:Sapphire laser medium at the centre wavelength of around 800 nm. There is, however, a fundamental limit to the minimum pulse duration achievable with such a system. A propagating physical field cannot be shorter than one period of the electric field. For a pulse centred at 800 nm, this corresponds to the single-cycle limit of 2.7 fs. With the development of pulse compression techniques based on nonlinear self-phase modulation in gas-filled hollow-core fibres it became possible to come very close to this limit [7, 8]. However, in order to reach even shorter pulse durations, the carrier wavelength of the pulse needs to be reduced. In comparison, a pulse with the duration of 100 as (1 as = 10^{-18} s) has a single-cycle limit of 30 nm. Since this lies in the extreme-ultraviolet (XUV) wavelength regime, a whole range of new challenges arises due to the exotic nature of this parameter space.

1.1 Breaking the femtosecond barrier

The availability of ultrashort pulses in the x-ray wavelength range has shown to have a dramatic impact in ultrafast science. Due to their short wavelength, x-rays offer Angstrom-sized spatial resolution. In addition, they possess a larger penetration depth through material compared to optical light. They can therefore be used to image thicker samples than is possible with other light sources or with electron microscopes. Of particular interest in this regard is the wavelength range between 2.3 nm and 4.4 nm. In this so-called “water window”, carbon is significantly absorbing, whereas water is transparent to

the radiation. Accessing this window therefore allows the in vivo imaging of proteins, cells and other biological samples with very high contrast [9–11]. The development of high-flux x-ray sources is, however, nontrivial. Synchrotrons, and in more recent years free-electron lasers (FELs), are large-scale facilities that generate collimated x-ray beams with very high intensities. The extreme brightness[1] of FELs, together with their ability to produce coherent x-ray pulses on the femtosecond timescale, makes them very attractive for a large variety of research areas. For instance, FEL laser sources have been used to determine the structure of proteins [12, 13] and viruses [14], with the ultimate goal of imaging single molecules [15, 16]. As a consequence of their enormous cost (1.15 billion Euros for the XFEL in Hamburg, Germany), only a handful of FELs exist around the world, and user access is strictly rationed. It is therefore a major scientific and technological goal to develop versatile table-top light sources that produce coherent and collimated x-ray beams. The most successful concept is based on high harmonic generation (HHG) [17, 18]. Here, a high-intensity laser beam is focused into a gas target, where a highly nonlinear process converts the infrared field into soft x-ray photons. Due to the oscillatory nature of the driving field, the emitted high harmonic field corresponds to a train of pulses. Most importantly, in the 1990's it was proposed that the emitted field has a temporal support on the attosecond timescale [19–21]. Indeed, in 2001 the first attosecond pulses from HHG were observed, both in the form of pulse trains [22] and, through different gating or filtering techniques, as an isolated pulse [23]. Further progress in the field has been able to reduce the duration of pulses from HHG down to 63 as for a pulse train [24] and 67 as for an isolated pulse [25]. The main impetus for the development of such short flashes of light

[1]The typical pulse energy is about 2-3 mJ at the SLAC Linac Coherent Light Source (LCLS), USA.

is that it allows the time-resolved analysis of electron dynamics in matter, since electronic motion typically occurs on an attosecond timescale. Typical attosecond experiments are designed in a pump-probe configuration: A first XUV attosecond pulse is interacting with a sample and initiates an ultrafast excited state evolution of the system. A subsequent pulse with femto- or attosecond duration probes the state of the system as a function of the time delay between the two pulses. Prominent examples of attoscience experiments that have been performed using such a scheme are the study of the Auger decay in atoms [26, 27], the photoemission of electrons from gases [28] and condensed matter [29], as well as electronic wave packet dynamics of simple [30, 31] and complex [32] molecules .

1.2 Metrology of ultrashort pulses

In the optical sciences the outcome of an experiment is usually encoded in the detected light field. Hence, with the development of novel light sources comes the need for characterising them in order to extract the information about the physical process that is to be studied. In ultrafast science, this naturally gives rise to the following question: How can an ultrashort pulse be characterised if there is no shorter event available to probe that pulse? The solution turns out to consist in making use of the pulse itself. The field of ultrashort pulse characterisation has matured in the femtosecond domain, where all currently used techniques use a variant of the pulse to probe itself by means of a nonlinear interaction taking place in a nonlinear crystal [33]. One of the most successful ways to characterise short pulses is interferometry. Since no electronic detector exists with a temporal resolution of femtoseconds or below, interferometry solves this dilemma by measuring the pulse

properties in the frequency domain since optical spectra can be measured by slow detectors. Any electric field can be described by its amplitude and its phase. The amplitude is readily measured using a spectrometer. The challenge lies in the determination of the phase. Interferometry is inherently phase-sensitive and thus represents a reliable and robust means to access the detailed characteristics of the pulse. All techniques developed in this thesis are based on interferometry. This is mainly due to the following two reasons: (1) The concepts of temporally characterising a pulse as well as the reconstruction algorithms can be readily transferred to the spatial characterisation of the electric field. Interferometry is therefore naturally well-suited for the full spatio-temporal characterisation of optical pulses. (2) The methodology developed for infrared femtosecond pulses can essentially be transferred to the characterisation of XUV attosecond pulses. Even though the experimental implementation will be fundamentally different, the main concept of the phase retrieval will stay the same. This is particularly important since in the XUV all conventional characterisation methods are not applicable anymore.

Characterisation of high harmonic radiation

The possibilities to manipulate XUV radiation are very limited. Because of the lack of non-linear crystals, along with the fact that the optics available in this wavelength regime are limited and only work for limited spectral ranges, the conventional pulse characterisation techniques developed in the infrared domain need to be abandoned. The spatio-temporal profile of high harmonic electric fields is highly structured, and new techniques need to be developed that are able to cope with this degree of complexity. In the temporal domain, the harmonic emission consists of well-separated spectral harmonics that are odd multiples

of the fundamental frequency, with zero intensity in between. While one single harmonic has a duration in the femtosecond range, the superposition of several harmonics evolves on the attosecond scale. Besides the temporal shape, the spatial degrees of freedom show a high complexity as well. The response of a single atom to the laser field, combined with the coherent superposition of the response from all emitters, leads to a complicated spatial field that carries distinct signatures from the generation process.

This thesis develops novel pulse characterisation methods for infrared femtosecond and extreme-ultraviolet attosecond pulses. The main incentive is to have versatile characterisation methods at hand that are applicable to a broad range of parameter spaces, as well as to utilise them for the study of the HHG process. The first part of this thesis develops a novel method that is able to simultaneously characterise a pair of independent fields in both space and time. The technique is demonstrated by the complete characterisation of infrared femtosecond pulses. In the second part of this thesis, this technique is transferred to the XUV attosecond domain and used to characterise the wavefronts of high harmonics. This method, as well as other interferometric experiments, are then utilised to study with attosecond precision the fundamental process of HHG. Furthermore, the concept of pulse characterisation is generalised to the case where the field that is to be measured is not fully coherent. For this case an alternative scheme is developed that retrieves statistical information about the harmonics.

1.3 Thesis outline

Chapter 2 introduces the basic concepts of ultrashort pulses and their properties. A mathematical framework is presented describing all relevant pulse properties in space and time. This is followed by an overview of the common methods for the spatio-temporal characterisation of femtosecond optical fields. Particular emphasis is placed on interferometric and spectrographic routines since those will be of importance in the remainder of this thesis.

Chapter 3 develops a novel pulse characterisation technique, called MICE, that is able to simultaneously characterise a pair of independent electric fields as a function of any degree of freedom in which it is possible to shear one of the beams. The chapter details the concept, outlines the algorithm and discusses possible ambiguities in the reconstruction. To demonstrate the broad applicability of MICE, it is first applied to a simulated wavefront reconstruction of complex optical beams. This is followed by an experimental reconstruction of the temporal profiles of two femtosecond laser pulses in a single laser shot.

Chapter 4 describes in detail the theory of high harmonic generation. Both the single-atom response as well as macroscopic effects are discussed in order to relate them to possible experimental outcomes. This is followed by the state of the art of the characterisation of attosecond pulses from HHG, both in the temporal and the spatial domains.

Chapter 5 presents in its first half the experimental setup for high harmonic generation that has been designed and built by the author in the Attolab at the University of Oxford. Detailed specifications of the optical setup, the XUV generation and the XUV spectro-

meter are given. In the second half of this chapter, experiments are presented that study the fundamental generation process. From the measured traces recorded in the far-field, the sub-cycle electron dynamics are characterised, and fundamental properties about the quantum paths of the electrons involved in the generation process are measured.

Chapter 6 transfers the method of MICE, developed in chapter 3, to the XUV attosecond domain. The wavefronts of two high harmonic beams are simultaneously reconstructed from a sequence of XUV interferograms. The obtained information is related to the sub-cycle characteristics of the generation process.

Chapter 7 generalises the concept of ultrashort pulse characterisation to the case where partial coherence of the radiated field prevents the commonly used techniques to provide accurate information about the field. An experimental routine is proposed that measures the two-point correlation function and fully characterises the field in terms of state mixtures. The corresponding experimental measurement is presented and preliminary results are shown.

Chapter 8 finally summarises the work presented in this thesis and discusses some perspectives and future prospects related to this work.

1.4 Author's contribution

The SEA-CAR-SPIDER data used in chapter 3 was taken by Tobias Witting and Dane Austin before the author's arrival in Oxford. The concept of MICE, as well as the idea and the procedure for measuring the two-point correlation function of high harmonics and applying the state mixture approach to such data was developed jointly by the author and

postdoc Charles Bourassin-Bouchet. All other work, in particular building a complete high harmonic beamline, its optimisation for the observation of harmonics originating from the different quantum trajectories, and the performance of all XUV experiments was carried out by the author.

Chapter 2

Metrology of ultrashort femtosecond pulses

"Optics is either very simple or else it is very complicated."

Richard Feynman

The aim of this thesis is the development of novel methods for the complete characterisation of infrared femtosecond and XUV attosecond pulses. This chapter introduces the key elements of ultrashort femtosecond pulse metrology and presents the state of the art technology. First, the mathematical foundation of electromagnetic pulses and their properties is explained. Then, some of the most important tools for their characterisation both in space and time are presented. Since a multitude of techniques have been developed to date, the main focus will be kept on the concepts relevant for this thesis. It will become clear that those methods are not directly transferable to the characterisation of XUV attosecond pulses. This is due to the limited availability of optics in the XUV, the very weak signal strength and the lack of a suitable nonlinear medium to act as a

time-nonstationary filter [33]. Also, the generation process itself for attosecond pulses is fundamentally different, which in laboratory settings is usually done via high harmonic generation. Therefore, the background about the generation and characterisation of XUV attosecond pulses will be discussed in a separate chapter 4.

2.1 Mathematical formalism

In general, the properties of all electromagnetic fields are described by Maxwell's equations for macroscopic media (in SI units):

$$\begin{aligned} \vec{\nabla} \cdot \vec{B} &= 0 & \vec{\nabla} \times \vec{H} &= \frac{\partial \vec{D}}{\partial t} + \vec{j} \\ \vec{\nabla} \cdot \vec{D} &= \rho & \vec{\nabla} \times \vec{\mathcal{E}} &= -\frac{\partial \vec{B}}{\partial t}, \end{aligned} \tag{2.1}$$

with the free charge density ρ, the free current density $\vec{j}$, the electric field $\vec{\mathcal{E}}$ and the electric displacement field $\vec{D} = \varepsilon_0 \vec{\mathcal{E}} + \vec{P}$ in a medium of polarisation $\vec{P}$ as well as the magnetic field strength $\vec{H}$ and the magnetic flux density $\vec{B} = \mu_0(\vec{H} + \vec{M})$ in a medium of magnetisation $\vec{M}$. ε_0 and μ_0 denote the vacuum electric permittivity and magnetic permeability, respectively, and are related to the vacuum speed of light by $c = 1/\sqrt{\varepsilon_0 \mu_0}$. A direct consequence of Maxwell's equations is the vacuum propagation equation for an electric field:

$$\left(\vec{\nabla}^2 - \frac{1}{c^2} \frac{\partial^2}{\partial t^2} \right) \vec{\mathcal{E}} = 0. \tag{2.2}$$

One solution of equation (2.2) are *plane waves*, with wave vector $\vec{k}$ and phase constant φ_0:

$$\vec{E}(\vec{r}, t) = \vec{E}_0 e^{i\left(\omega t - \vec{k} \cdot \vec{r}\right) + i\varphi_0}. \tag{2.3}$$

For mathematical convenience, in (2.3) the complex-valued *analytic representation* has been used. The real-valued electric field $\mathcal{E}$ is then simply twice the real part of the analytic field

$$\mathcal{E}(t) = E(t) + c.c. = 2\,\mathrm{Re}[E(t)]. \tag{2.4}$$

Inserting (2.3) into (2.2) and introducing the wavenumber $k = |\vec{k}|$ directly yields the *dispersion relation*

$$k = \frac{\omega}{c}. \tag{2.5}$$

Note that a monochromatic plane wave cannot represent a physically realistic field since its energy content is infinite in space and time. However, due to the linearity of (2.2), any superposition of planes waves is also a solution:

$$\vec{E}(\vec{r},t) = \int \mathrm{d}\omega \int \mathrm{d}^3k\, \vec{E}_0(\omega,\vec{k}) e^{i\left(\omega t - \vec{k}\cdot\vec{r}\right)} \tag{2.6}$$

This superposition is usually referred to as a *wave packet*. Wave packets are confined in time and space. In the temporal domain, this therefore represents a pulse of light. The temporal domain (given by $E(t)$) and the frequency domain (given by $\tilde{E}(\omega)$) are linked together by Fourier transforms:

$$\tilde{E}(\omega) = \int_{-\infty}^{\infty} E(t) e^{-i\omega t} \mathrm{d}t = FT\left[E(t)\right], \tag{2.7}$$

$$E(t) = \frac{1}{2\pi} \int_{-\infty}^{\infty} \tilde{E}(\omega) e^{i\omega t} \mathrm{d}\omega = FT^{-1}\left[\tilde{E}(\omega)\right]. \tag{2.8}$$

When considering only the pulse spectrum without any additional phase contribution, a larger bandwidth in the frequency domain results in a shorter pulse duration in the temporal domain, and vice versa.

The transition from a monochromatic wave to a short pulse can be well illustrated using the example of Gaussian frequency combs, see figure 2.1. Consider a monochromatic sine wave with frequency ω_0, as shown in the top left image of figure 2.1. The real time-dependent electric field is shown in the right column, which in this case is a uniform sine function. If then additional frequencies are added symmetrically around ω_0, beating occurs in the time domain. The mean frequency is not altered by this procedure. Adding more and more frequency components in the spectral domain has the effect of increasing the separation between the pulses, while leaving the pulse shape relatively unchanged. In the limit of a continuous Gaussian spectral distribution, a single pulse is left in the temporal domain, the envelope of which is also Gaussian. This example nicely illustrates the emergence of light pulses from continuous-wave light fields with regards to the corresponding spectral broadening. It also visualises how the desire to generate shorter and shorter pulses necessitates an increase in the bandwidth in the spectral domain.

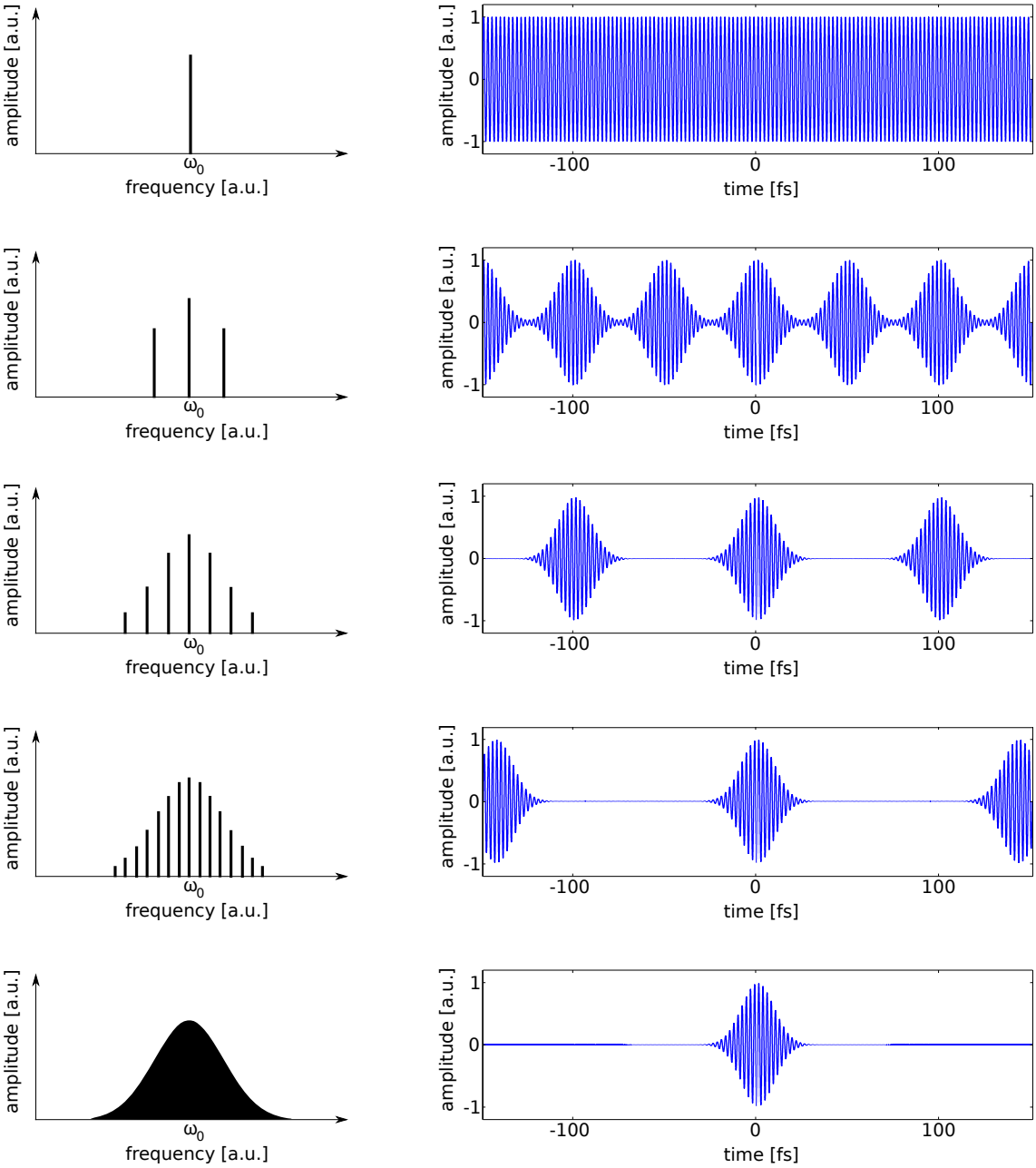

Figure 2.1: Concept of a gaussian frequency comb. Adding frequencies in the spectral domain while keeping the overall bandwidth the same transforms a uniform sine wave eventually into a single light pulse.

2.2 Properties of the spatio-temporal phase

The spatio-temporal electric field can be written as a product of an amplitude and a phase term:

$$E(x,t) = |E(x,t)| \exp\left[-i\phi(x,t)\right] \tag{2.9}$$

In the Fourier domain, the squared modulus of the electric field $|E(x,\omega)|^2$ represents the pulse spectrum and is usually conveniently measured with a spectrometer. Estimation of the phase is much more problematic. Indeed, if the phase takes highly complex shapes, it can significantly alter the pulse profile in space and time. Therefore, the key properties of the electric field phase are derived in the next section. For clarity, the spatial and temporal domains are treated separately.

2.2.1 Spectral and temporal phase

In order to highlight the different contributions to the spectral phase ϕ, it is helpful to expand it in a Taylor series[1]:

$$\phi(\omega) = \sum_n \frac{1}{n!}\phi^{(n)}(\omega_0)(\omega-\omega_0)^n. \tag{2.10}$$

Here, $\phi^{(n)}$ is the n-th frequency derivative of the phase, evaluated at the reference frequency ω_0. The different phase derivatives have the following physical interpretation: $\phi^{(0)}(\omega_0) = \phi_0$ quantifies the phase acquired at ω_0. It has a particular intuitive interpretation in the

[1]The Taylor expansion represents a polynomial approximation of the phase. In most cases, the first few terms are sufficient to describe the pulse properties. In the case of very complex pulses, higher orders need to be accounted for. In more "exotic" cases a Taylor expansion might be insufficient, for example close to a resonance where abrupt phase changes may occur.

time domain, as will be shown below. The group delay $T_g(\omega) = \partial\phi/\partial\omega$ quantifies the relative delay of a given spectral component. The group delay is closely related to the group velocity v_g,

$$\phi^{(1)}(\omega_0) = \left(\frac{\partial\phi}{\partial\omega}\right)\Big|_{\omega=\omega_0} = L\left(\frac{\partial k}{\partial\omega}\right)\Big|_{\omega=\omega_0} = \frac{L}{v_g}. \tag{2.11}$$

A purely linear phase represents a shift of the pulse envelope in the time domain with respect to a reference. In many applications, however, the arrival time of the pulse is of little interest and one is more interested in the pulse shape. The second order derivative $\phi^{(2)}(\omega_0)$ stands for the group delay dispersion (GDD) and quantifies the amount of quadratic phase on the pulse. It is related to the group velocity dispersion (GVD) by

$$GVD = \frac{d}{d\omega}\left[\frac{\partial k}{\partial\omega}\right]\Big|_{\omega=\omega_0} = \frac{1}{L}\left(\frac{\partial^2\phi}{\partial\omega^2}\right)\Big|_{\omega=\omega_0} = \left(-\frac{1}{v_g^2}\frac{dv_g}{d\omega}\right)\Big|_{\omega=\omega_0} \tag{2.12}$$

A non-vanishing GVD causes different frequencies to propagate within a medium with different velocities. For a positive GVD, the long-wavelength components propagate faster than the short-wavelength components, and vice versa. In the optical domain, most transparent media exhibit a positive GVD, a phenomenon known as *normal dispersion*. In contrast, in the case of *anomalous dispersion*, the GVD is negative. This effect usually occurs near a resonance frequency of the material. Finally, for more complex pulses, third-order dispersion and higher-order dispersion components may come into play. However, for very high orders, the polynomial approximation performed by the Taylor-expansion might not be the best approach anymore, and a numerical modelling of the medium or system might

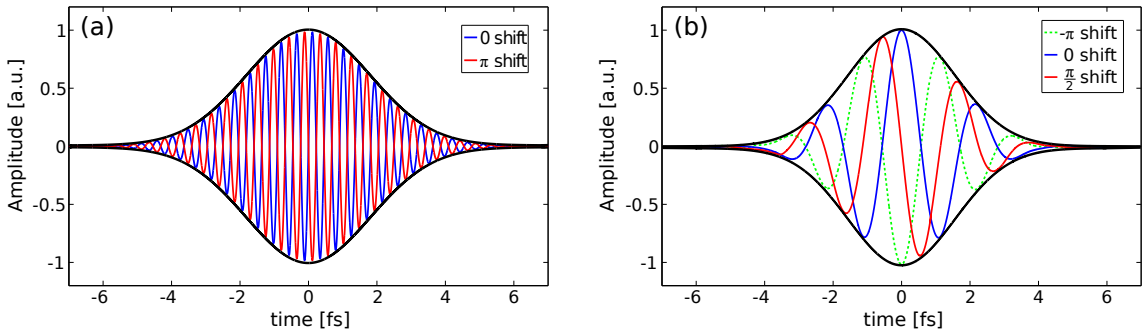

Figure 2.2: Influence of the CEP on the waveform contained in the pulse envelope for (a) a multi-cycle pulse, and (b) a few-cycle pulse. The first case is relatively insensitive to a change of CEP, whereas in the latter case this strongly influences the shape of the waveform and therefore also the peak of the electric field.

be more accurate.

By analogy, the temporal phase $\tilde{\phi}(t)$ can be expanded into a Taylor series at time t_0 as well:

$$\tilde{\phi}(t) = \sum_n \frac{1}{n!} \tilde{\phi}^{(n)}(t_0)(t - t_0)^n. \tag{2.13}$$

The zeroth-order term $\tilde{\phi}(t_0) = \phi_0$ is, due to the property of Fourier transforms, the same as in the frequency domain. However, in the time domain its physical meaning can be nicely illustrated where it quantifies the absolute phase offset (often referred to as *absolute phase*) between the peak of the carrier wave and the peak of the pulse intensity envelope. This is shown in figure 2.2 for (a) a multi-cycle pulse, and (b) a few-cycle pulse. A change of the absolute phase, also referred to as *carrier envelope phase (CEP)*, shifts the electric field within the pulse envelope, whereas the envelope itself stays unaltered. While in a multi-cycle pulse a change of CEP has only a small effect on the pulse properties, the change is much more dramatic for a few-cycle pulse. The interaction of such a pulse with a medium whose response is sensitive to the electric field will drastically change for different values of the CEP, since both the peak value of the electric field as well as the overall

waveform contained within the pulse envelope vary significantly with the CEP. This is shown in figure 2.2(b) for three different values of the CEP. The measurement and control of the CEP is therefore important for many experiments that use few-cycle pulses as a laser source. The next term in (2.13), $\tilde{\phi}^{(1)}(t_0)$, quantifies the linear temporal phase and leads to a shift of the carrier frequency ω_0, in analogy to the spectral domain. The phenomenon that a linear phase in one domain results in a shift in the Fourier domain is know as the *Fourier shift theorem*. The first order phase term also defines the instantaneous frequency $\omega(t)$

$$\omega(t_0) = \omega_0 - \frac{d\tilde{\phi}(t)}{dt}\bigg|_{t=t_0}. \tag{2.14}$$

The term with $\tilde{\phi}^{(2)}(t_0)$ describes the change of the instantaneous frequency with time. A pulse with a non-zero value of $\tilde{\phi}^{(2)}(t_0)$ is also called "linearly chirped", since here the instantaneous frequency $\omega(t)$ changes linearly with time. Higher-order terms can lead to nonlinear chirps and are simply referred to as third-order dispersion, fourth-order dispersion etc. In general, it is in most cases neither practical nor useful to consider phase terms beyond the sixth order. In a real laboratory scenario, usually the GDD is the dominant term, since this is the main contribution introduced, for example, by glass-based optics such as beamsplitters, lenses and prisms.

In the case where the GDD and all higher orders are zero, the pulse is said to be *bandwidth limited* or *Fourier transform limited* since it has the shortest duration possible for a given optical spectrum. The pulse duration is then determined by the full width at

half maximum (FWHM) spectral width $\Delta\nu$ and temporal width τ,

$$\Delta\nu \cdot \tau = \alpha. \tag{2.15}$$

The constant α depends on the pulse shape. For the common case of Gaussian pulses, $\alpha = 0.441$. (2.15) is known as the *time-bandwidth product* and indicates that for a given spectral width, there is a lower limit for the pulse duration. If second- or higher-order dispersion is present, the time-bandwidth product is always larger than in equation (2.15), which results in a longer pulse duration. A detailed discussion of a variety of aspects regarding the role of dispersion in ultrafast optics can be found in [34].

2.2.2 Spatial phase

Wavefront measurements of optical systems have historically been mainly developed to characterise optical aberrations. Aberrations may, for example, be introduced due to the geometry of the system, in particular when departing from the paraxial approximation, due to the variation of the refractive index with wavelength of optical materials, or simply because of fabrication defects of the optics. To quantify the magnitude of existing aberrations of a wavefront, rather than studying the wavefront as it arrives on a detector, it is more convenient to determine the difference between the measured wavefront and a reference spherical wave. To do so, the wave aberration function $W(\rho, \theta)$ is introduced, quantifying the optical path difference along one geometric ray between the reference sphere centred on the ideal image point and the actual wavefront at the exit pupil[2]. The

[2]Common examples for exit pupils of optical systems are lenses or apertures.

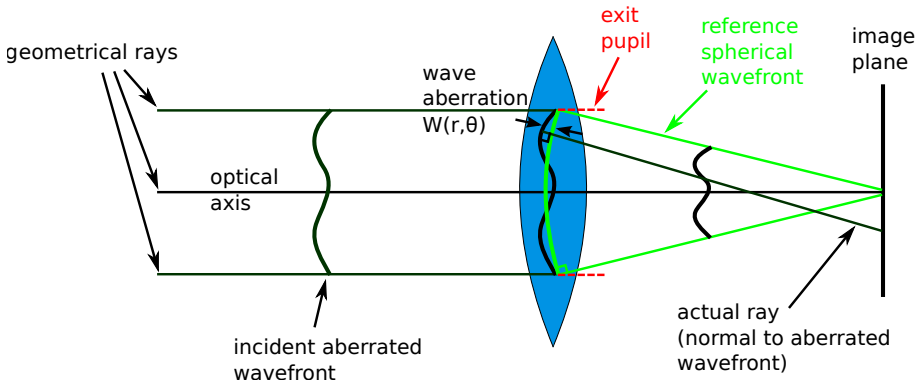

Figure 2.3: Wave aberration function for an optical imaging system. An undistorted wavefront centred on the exit pupil is focused (shown in green) onto the ideal focal spot along the optical axis. For the case of an aberrated wavefront, each section of the wavefront is focused to a spot where the ray perpendicular to this part of the wavefront crosses the image plane (shown in black).

principle is shown in figure 2.3. Due to the cylindrical symmetry of the exit pupil, it is convenient to use polar coordinates, which are related to Cartesian coordinates according to $(x, y) = (r\cos\theta, r\sin\theta)$. The previous section has analysed the properties of the spectral phase by performing a Taylor expansion and highlighting the effects of the individual phase terms. A similar approach can be performed for the spatial phase $\phi(x)$. In general, however, optical systems have circular pupils, so many analyses and calculations (e.g. diffraction calculations) will involve integration over a circular pupil. It is therefore more convenient to expand the phase into a set of polynomials that are orthogonal over a unit circle. A complete set of such polynomials are the Zernike circle polynomials $Z_n^m(\rho, \theta)$ [35, 36]. The expansion of the aberration function into Zernike polynomials takes the form

$$W(\rho, \theta) = \sum_{n=0}^{\infty} \sum_{m=0}^{n} c_{nm} Z_n^m(\rho, \theta), \tag{2.16}$$

where c_{nm} are the expansion coefficients that depend on the location of the object, and $\rho = r/a$ is the radial variable normalised to the radius a of the exit pupil. n and m are

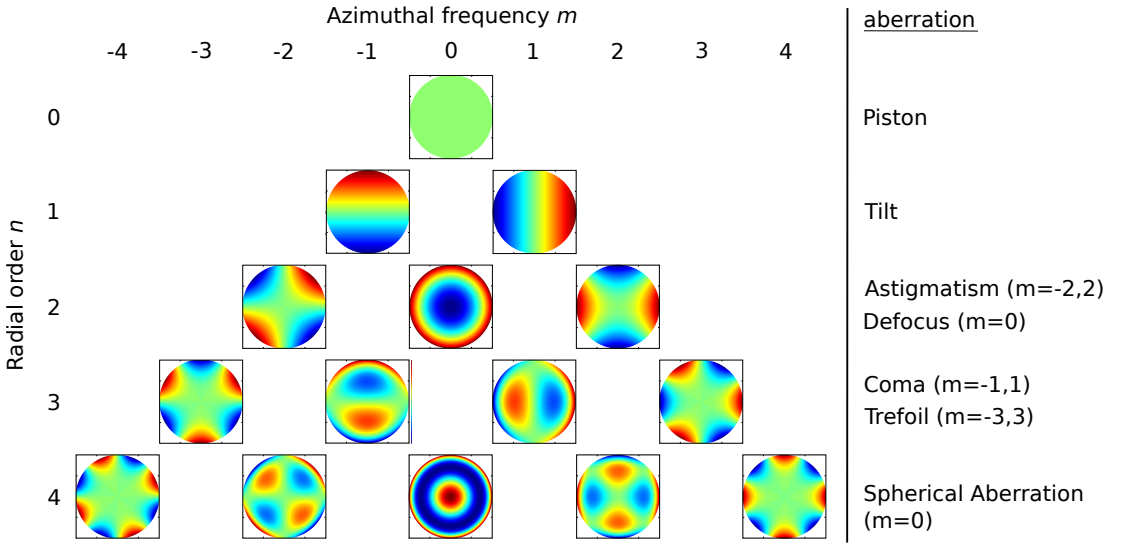

Figure 2.4: Zernike polynomials up to fourth order. Indicated are also the associated types of optical aberrations.

non-negative integer numbers, with $n - m \geq 0$. The orthonormal Zernike polynomials are useful to study wavefront aberrations since the different terms in (2.16) are associated with particular types of aberrations. Figure 2.4 displays the polynomials up to the fourth order, together with the corresponding aberrations. The mathematical expressions of the polynomials and a discussion of their main properties are given in appendix A.

2.2.3 Further remarks

Sections 2.2.1 and 2.2.2 have introduced the physical nature of the phase in the spectral and the spatial domain separately and explained the meaning of the different phase terms. It should be stressed, however, how closely related these two domains are. A flat phase in the spectral (spatial) domain leads to the shortest pulse (smallest beam spot) possible for a given spectrum (spatial intensity distribution). Further, as a consequence of the Fourier shift theorem, a linear phase in one domain shifts the pulse in the corresponding

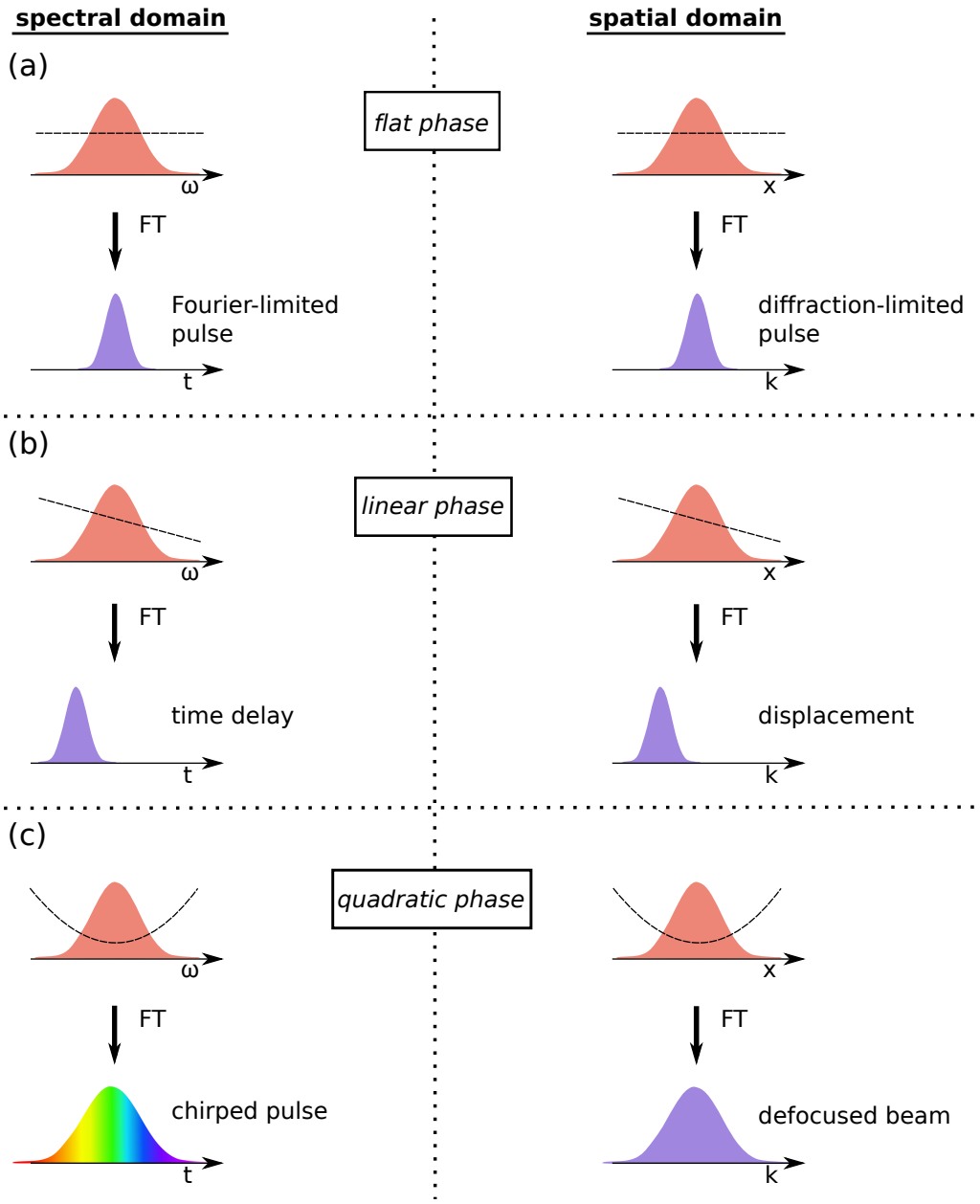

Figure 2.5: Effects of lower-order phase terms on the pulse in the Fourier domain for (a) flat, (b) linear, and (c) quadratic phase terms. Left column: Spectral and temporal domain. Right column: Spatial and spatial frequency domain.

Fourier domain. Finally, a quadratic phase in one domain results in a stretch in the Fourier domain. Those relationships are summarised in figure 2.5. It is important to keep these relations in mind when performing an experiment. On the one hand, this allows

the adaptation of the beam to a particular experiment in case certain pulse properties are desired. For example, in scenarios where a chirped pulse rather than a Fourier-limited pulse is needed, a specific amount of chirp can readily be introduced by propagating the beam through an appropriately chosen quadratic spectral phase modulator (such as a suitable piece of glass or an appropriately designed set of diffraction gratings). On the other hand, if the phase of a laser beam is measured with a pulse characterisation device, then, for lower-order phases, it becomes possible to determine the origin of a particular phase term and possibly even correct for it if needed. A residual quadratic spectral phase on the output of a chirped pulse amplifier (CPA) system, for example, might indicate that the separation of the two gratings that form the compressor at the CPA exit is not set to the correct value. Consequently, the quadratic phase stemming from the pulse stretcher and the additional material dispersion are not fully compensated for.

2.3 Propagation effects

After having introduced the nature of the spectral and the spatial phases, the question arises what phenomena actually cause variations of these phases. The answer turns out to be the propagation of an optical beam or ultrashort pulse, in particular when propagating through a dispersive medium. Depending on the particular underlying physical effect, the spatial and spectral phases may be affected separately, or in a correlated way. The latter case may lead to space-time coupling (STC), which means that the temporal field is spatially dependent. In the following, some general concepts on phase modulation in space and time are presented.

2.3.1 Phase modulation in dispersive media

In the majority of optics experiments, the laser beam will need to propagate through a medium. When interacting with the atoms or molecules of the medium, the light field induces electric dipole moments p. The sum over all N microscopic dipole moments inside the interaction volume then forms the overall polarisation P, $P = N \cdot p$. Therefore, for propagation inside a medium, the induced polarisation has to be inserted as a source term into the vacuum wave equation of (2.2),

$$\left(\nabla^2 - \frac{1}{c^2}\frac{\partial^2}{\partial t^2}\right)\vec{E} = \frac{1}{\varepsilon_0 c^2}\frac{\partial^2 \vec{P}}{\partial t^2}. \tag{2.17}$$

At low intensities, the polarisation is linear. As a consequence, the modified wave equation stays linear, which means that plane waves are a solution of (2.17). However, the dispersion relation now takes the form

$$k = \frac{n(\omega)\,\omega}{c}, \tag{2.18}$$

where $n(\omega)$ is the refractive index of the medium. The phase velocity v_{ph} in a medium is then $v_{ph} = c/n$. When a pulse propagates through a dispersive medium, the acquired phase is therefore $n(\omega)\frac{\omega}{c}\,L$, where L is the length of the medium[3]. Since the refractive index is wavelength-dependent, different wavelengths propagate at different phase and group velocities inside the medium, which is known as (chromatic) dispersion. In a good approximation, propagation through a medium adds mostly first- and second-order terms

[3]Besides exhibiting a phase modulation, the pulse amplitude is usually affected as well due to absorption. In a medium with absorption coefficient $\alpha(\omega)$, the spectrum is attenuated by a factor $\exp(-\alpha(\omega)L)$. Absorption of parts of the spectrum can lead to an elongation of the pulse. However, usually the phase modulations are more crucial to the shape of the resulting pulse.

to the spectral phase (see equation (2.10)). Since the first order merely corresponds to a time delay, the main effect of the medium is to add a positive chirp to the pulse. In many experimental scenarios this is an undesired effect. One way to remedy this is to introduce additional negative dispersion to the pulse by a suitable arrangement of prisms or gratings [37]. The combination of both can effectively cancel out the second-order phases, and result in a pulse close to the Fourier limit. For very broadband pulses, or when the intensity is high enough to cause nonlinear effects, the phase modulation can be much more complex, and higher-order terms come into play.

2.3.2 Gaussian beams

The previous section illustrated how propagation in a dispersive medium alters the spectral phase of a pulse. It will now be shown how the propagation of an optical beam affects its spatial properties. To do so, the solution for a plane wave is separated into its temporal and spatial components:

$$\vec{E}(\vec{r},t) = \vec{A}(\vec{r})\, e^{-i\vec{k}\vec{r}}\, e^{i\omega t} = \vec{E}(\vec{r})\, e^{i\omega t}. \tag{2.19}$$

Inserting (2.19) into (2.2) yields the *Helmholtz equation*:

$$\left(\nabla^2 + k^2\right) \vec{E}(\vec{r}) = 0. \tag{2.20}$$

In the *paraxial approximation*, the most interesting and useful solution of (2.20) is the Gaussian beam [38]. Gaussian beams are very common in laboratory settings. They form a stable solution of an electric field confined in a laser cavity, given by the fundamental

transverse mode TEM_{00}. Moreover, lasers usually emit beams that can be described reasonably well by a transverse Gaussian profile. In addition, the effect of lenses and other optics can be described by transforming a Gaussian beam into another Gaussian beam, but with different parameters. The characteristics of a Gaussian beam are therefore described here in more detail. The complex electric field amplitude is given by

$$E(r,z) = A_0 \frac{w_0}{w(z)} \exp\left[-\frac{r^2}{w^2(z)}\right] \exp\left[-ikz - ik\frac{r^2}{2R(z)} + i\zeta(z)\right]. \tag{2.21}$$

(2.21) describes a beam with a Gaussian radial intensity distribution and with the following parameters:

$$w(z) = w_0\sqrt{1+\left(\frac{z}{z_R}\right)^2} \qquad \text{Beam radius} \tag{2.22}$$

$$z_R = \frac{\pi w_0^2}{\lambda} \qquad \text{Rayleigh range} \tag{2.23}$$

$$b = 2z_R = \frac{2\pi w_0^2}{\lambda} \qquad \text{Confocal paramter} \tag{2.24}$$

$$R(z) = z\left[1+\left(\frac{z_R}{z}\right)^2\right] \qquad \text{Radius of curvature} \tag{2.25}$$

$$\zeta(z) = \arctan\left(\frac{z}{z_R}\right) \qquad \text{Gouy phase} \tag{2.26}$$

The schematic of a Gaussian beam is depicted in figure 2.6, along with the relevant parameters. The radial distance from the centre axis of the beam is $r = \sqrt{x^2+y^2}$, $w_0 = w(0)$ is the minimum value of $w(z)$ and is usually referred to as the *beam waist*, $A_0 = E(0,0)$, and z is the axial distance from the waist location.

In the framework of the interpretation of the experimental data presented in this thesis, it is instructive to analyse the behaviour of the wavefront of a Gaussian beam in greater

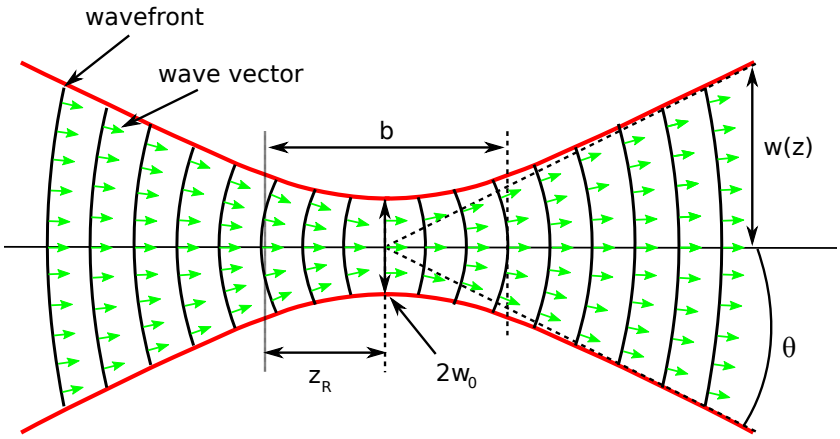

Figure 2.6: Evolution of a Gaussian beam around the waist. Highlighted are the main parameters to describe the beam. The black lines represent the wavefronts, and the green arrows are the wave vectors. They are perpendicular to the local wavefront and indicate the propagation direction of the local beam segment.

detail. The phase of the Gaussian beam (2.21) is

$$\varphi(r,z) = kz - \zeta(z) + \frac{kr^2}{2R(z)}. \tag{2.27}$$

The first term simply describes the phase of a plane wave. The second term, the Gouy phase [39, 40], is responsible for a total phase shift of π between $z = -\infty$ and $z = \infty$. Finally, the third term in (2.27) describes the deviation of the phase at off-axis points from the point on the axis in a given transverse plane, and therefore accounts for a curvature of the wavefront. The surfaces of constant phase are determined by $k[z+r^2/(2R(z))]-\zeta(z) = 2\pi q$. Since $\zeta(z)$ and $R(z)$ are slowly varying with z, this relationship takes the form of a paraboloidal surface with radius of curvature R, $z + r^2/(2R) = q\lambda + \zeta\lambda/(2\pi)$. The evolution of the wavefront of a Gaussian beam is therefore the following (see figure 2.7): At the waist position $z = 0$, the wavefronts are plane waves with infinite radius of curvature. The curvature increases up to a maximum at $z = z_R$ and subsequently decreases again.

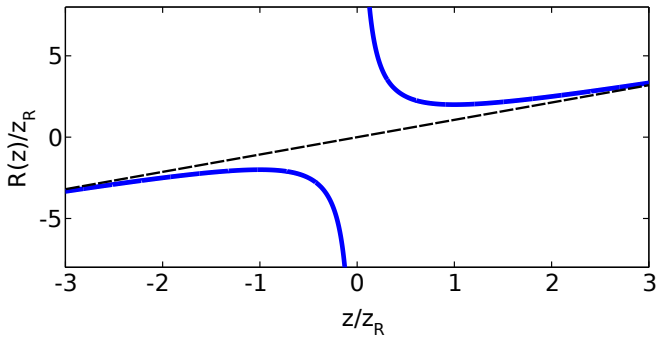

Figure 2.7: Radius of curvature of the wavefronts of a Gaussian beam. It is infinite at the waist position and takes its minimum value at $z = z_R$. For large z, it asymptotically approaches the radius of curvature of a spherical wave (dashed line).

Conversely, the radius of curvature takes its minimum value of $2z_R$ at $z = z_R$. For $z \gg z_R$, the wavefront is approximately equal to the one of a spherical wave with $R(z) \approx z$. The divergence angle is then given by $\theta = \lambda/(\pi w_0)$.

2.4 Measuring the spectral phase of ultrashort pulses

The previous part of this chapter has introduced the physical properties of the spectral and spatial phases and how they might manifest themselves in a measurement. In the following section the main methods are presented that allow the characterisation of the temporal electric field. Usually the spectrum can readily be measured with a spectrometer. Therefore, the challenge consists in obtaining the phase information. Ideally, this is done in time and in space. Over the years, a whole zoology of techniques and their different variants have been developed. Here, only the techniques and implementations relevant for this thesis are discussed. Those are associated with the areas of spectrography and interferometry. A more complete review on the domain of ultrashort pulse characterisation can be found in [33].

2.4.1 Correlations

How can the duration of an ultrashort pulse be measured when there is no shorter event available and when detectors are too slow? This question represents one of the key dilemmas of the ultrafast community since the emergence of pulsed laser sources in the 1960's [1, 41, 42]. In fact the only phenomenon available to probe the short pulse is the pulse itself. Correlation techniques were the first attempts to obtain information about the pulse duration.

Field autocorrelation

In a field autocorrelation, a replica of the pulse is utilised to probe the pulse itself. The concept is shown in figure 2.8(a). The input pulse is split into two arms by a Michelson interferometer, and the output is recorded on an integrating detector. Changing the

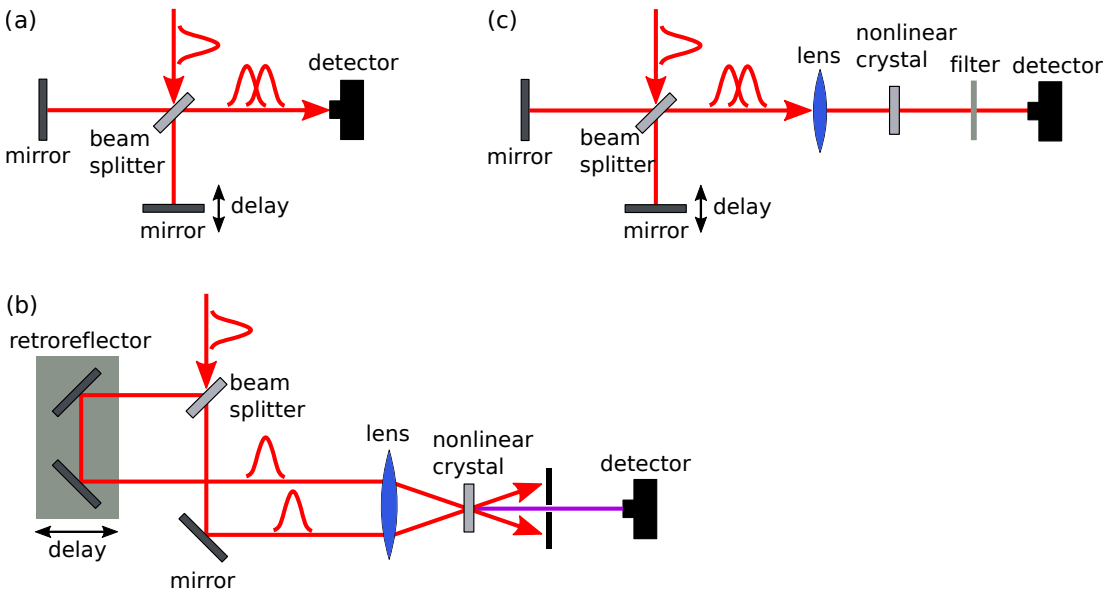

Figure 2.8: Experimental autocorrelation configurations. (a) Field autocorrelation, (b) Intensity autocorrelation, (c) Interferometric autocorrelation.

temporal overlap between both output pulses yields the measured intensity

$$I_{AC}(\tau) = \int_{-\infty}^{\infty} |E(t) + E(t-\tau)|^2 \mathrm{d}t = 2\int_{-\infty}^{\infty} I(t)\mathrm{d}t + 2\mathrm{Re}\left[\int_{-\infty}^{\infty} E(t)E^*(t-\tau)\mathrm{d}t\right], \quad (2.28)$$

where the last term represents the real part of the field autocorrelation

$$AC_{field}(\tau) = \int_{-\infty}^{\infty} E(t)E^*(t-\tau)\mathrm{d}t \quad (2.29)$$

According to the Wiener-Khinchin theorem, the Fourier transform of the autocorrelation function is the spectral intensity I_S,

$$\left|\tilde{E}(\omega)\right|^2 = \mathrm{FT}\left[\int_{-\infty}^{\infty} E(t)E^*(t-\tau)\mathrm{d}t\right] \quad (2.30)$$

The field autocorrelation therefore yields no information about the phase. In fact, this class of problems is known as the *one-dimensional phase-retrieval problem* which has been shown to be unsolvable, since infinitely many solutions exist [43, 44]. However, the autocorrelator forms the basis for more advanced methods.

Intensity autocorrelation

Far more common than the field autocorrelation, which only provides information on the spectrum, is the second order intensity autocorrelation.[4] Here, the pulse and its replica are mixed in a nonlinear crystal and recorded on the detector, as shown in figure 2.8(b).

[4] In principle this scheme can be extended to higher orders, $S_{n+1}(\tau) = \int I^n(t-\tau)I(t)\mathrm{d}t$. Since for large n the generated pulse I^n has a much shorter duration than I, a more accurate approximation of $I(t)$ can be obtained. However, due to the higher nonlinearities involved in the process, those techniques are not suitable for low-energy pulses.

The generated signal is measured as a function of the time delay between both pulses,

$$I_{int}(\tau) = \int_{-\infty}^{\infty} I(t)I(t-\tau)\mathrm{d}t. \tag{2.31}$$

The intensity autocorrelation does still not provide proper phase information about the pulse. However, due to the intensity dependence of the upconversion process, an estimate of the pulse duration can be obtained, since the upconverted signal is only non-zero when both input pulses overlap in time inside the crystal. If combined with a measurement of the spectrum, it can be estimated how much the pulse differs from its Fourier-limited duration. However, if the pulse is not Fourier-limited, I_{int} does not carry enough information to be able to determine exactly in what way the phase is distorted.

Interferometric autocorrelation

In a combination of the previous experimental configurations, the delay of the two output beams of a Michelson interferometer may be scanned in a collinear geometry, see figure 2.8(c). The coherent superposition of the second harmonic generation (SHG) signal from the two different beams and the SHG signal of the individual beams results in interference fringes with respect to delay. The interferometric autocorrelation trace then takes the form

$$I_{interf}(\tau) = \int_{-\infty}^{\infty} |E(t) + E(t-\tau)|^4 \,\mathrm{d}t. \tag{2.32}$$

I_{interf} is sensitive to the temporal phase of the pulse and can in theory be used to determine the pulse field. In practice, however, additional information such as the pulse spectrum or the interferogram of the fundamental light is usually required, and convergence of the

reconstruction has not yet been fully studied [45, 46].

Cross-correlation

In case a reference pulse I_{ref} is available, it can be cross-correlated with the test pulse I_{test},

$$I_{CC} = \int_{-\infty}^{\infty} I_{test}(t) I_{ref}(t-\tau)\,\mathrm{d}t. \tag{2.33}$$

In that way the profile of the test pulse may be obtained. This technique is particularly useful if the reference has a high intensity, or if its duration is much shorter than that of the test pulse. The latter variant has, for example, been shown to be useful in pulse shaping experiments [47], where the original, short pulse is used to probe the elongated shaped pulse.

2.4.2 Spectrography: FROG

The last section has shown that correlations are usually not capable of reconstructing the full electric field. However, based on those concepts, a solution has been found by resolving the autocorrelation signal in frequency. The trace recorded in this manner is called a *spectrogram* and is located in the time-frequency domain, with frequency and delay on the axes. Since spectrograms are two-dimensional objects, the reconstruction now represents a two-dimensional phase retrieval problem. In contrast to the one-dimensional case of the autocorrelation, two-dimensional phase retrieval problems essentially have unique solutions[5] [48–51]. They are not completely void of ambiguities, but, as will be explained

[5] As Barakat *et al.* pointed out regarding the problem of phase recovery in two or more dimensions, a "multiplicity [of solutions] is pathologically rare." [48]

below, those are only *trivial* ambiguities, which means their value does not fundamentally alter the pulse shape.

FROG

The implementation of a frequency-resolved autocorrelator is called frequency-resolved optical gating (FROG) [52]. FROG is a self-referencing technique where a replica of the test pulse is used as gate function that is scanned across the test pulse temporal profile. For each delay the spectrum is recorded. In the end, the data forms an array of $N \times N$ points, which is used to determine $2N$ points, i.e. N points each for intensity and phase. The algorithm performing this task is iterative and therefore not deterministic. Despite this fact, good and fast convergence properties have been shown. There are many different variants of FROG, each with certain advantages and disadvantages. Two of the most common ones shall be described here. An extensive discussion of FROG and its different implementations can be found in [53].

SHG FROG: In the SHG FROG configuration, as shown in figure 2.9(a), the test pulse and its delayed replica are mixed in a nonlinear crystal and the second harmonic signal is detected as a function of delay [54–56]. The FROG trace is the squared magnitude of the Fourier transform of the signal:

$$S_{SHG}(\omega,\tau) = \left| \int_{-\infty}^{\infty} E(t)E(t-\tau)\exp(-i\omega t)\mathrm{d}t \right|^2 . \tag{2.34}$$

The main advantage of SHG FROG is that it uses a low-order nonlinearity. It is therefore very sensitive and can be applied to the measurement of low-intensity pulses. One

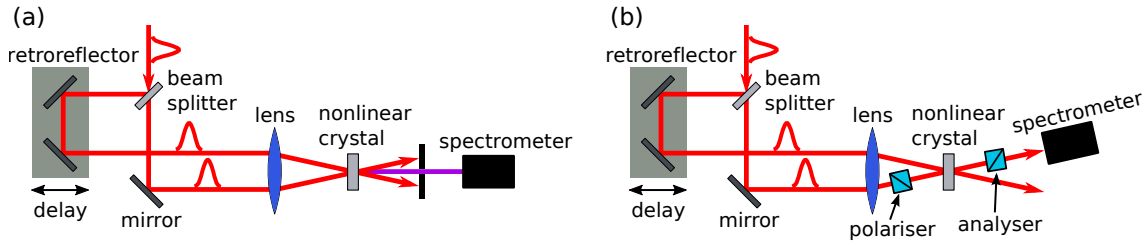

Figure 2.9: Experimental setup for (a) SHG FROG, (b) PG FROG.

disadvantage, however, is that it suffers from an ambiguity in the direction of time. Since the SHG FROG trace is symmetric, both $E(t)$ and its time-reversed version $E^*(-t)$ result in the same spectrogram. This ambiguity can be resolved, for example, if some a priori information is already known about the pulse. If this is not the case, a second FROG trace can be measured where a piece of glass is placed in the setup before the beam splitter. Since this introduces positive dispersion to the pulse, only one solution is consistent with both measurements. This, of course, is not ideal when single-shot operation is desired.

Polarization gate (PG) FROG: PG FROG uses a third-order nonlinear process to gate the test pulse [57]. An experimental setup for PG FROG is shown in figure 2.9(b). The probe pulse is sent through crossed polarisers, whereas the gate pulse is rotated by 45° by a half-wave plate. Both pulses overlap inside a third-order nonlinear medium, such as a piece of fused silica. Here the temporal variation of the gate pulse intensity induces a birefringence by means of the Kerr effect with the same temporal dependence. Thus the polarisation of the test pulse is rotated, with the amount of rotation being determined by the instantaneous gate pulse intensity. The analyser, oriented at 90° with respect to the polariser, only transmits the component of the test pulse that has been rotated enough to

match the polarisation axis of the analyser. The resulting PG FROG trace is given by:

$$S_{PG}(\omega,\tau) = \left| \int_{-\infty}^{\infty} E(t)|E(t-\tau)|^2 \exp(-i\omega t)\mathrm{d}t \right|^2 . \tag{2.35}$$

For PG FROG, no non-trivial ambiguities are known. Also, the nonlinear process is automatically phase-matched, so PG FROG supports pulses with large bandwidths. One disadvantage is that the polarisers need very high extinction ratios (extinction $< 10^{-5}$), which can be costly. In addition, since it uses a third-order nonlinearity, PG FROG is less sensitive than SHG FROG.

Phase retrieval in FROG

FROG uses an iterative algorithm to extract the spectral phase from a spectrogram. The first FROG reconstruction algorithm simply fitted the experimental trace to a model to extract the pulse parameters. However, the problem of phase retrieval has been long-standing in imaging science and other areas of physics, and more advanced algorithmic tools developed there have been applied to FROG [58]. Convergence and robustness of the algorithm were improved by using iterative Fourier transform based algorithms [57] and the method of generalised projections (GP) [59], which culminated in the principal component generalised projections algorithm (PCGPA) [60].

The PCGPA algorithm

The PCGPA is an algorithm that can be used to estimate the fields of the two pulses that give rise to the FROG trace. These may be two different pulses, i.e. the gate is not a

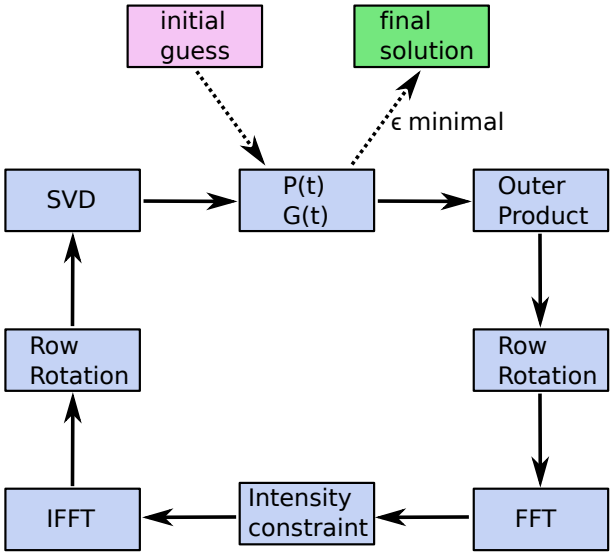

Figure 2.10: Concept of the PCGPA algorithm to reconstruct $P(t)$ and $G(t)$. It uses generalised projections to determine new guesses for both fields after each iteration. First, in the Fourier domain, the reconstructed signal (i.e. the measured FROG trace) is replaced by the measured intensity. Second, after an inverse Fourier transform, the next best guess for the fields is obtained by a singular value decomposition. The algorithm has converged when the FROG error is sufficiently small.

replica of the probe pulse. Its aim is to determine a pair of vectors, the outer product of which forms the experimentally measured FROG trace. Of course, the PCGPA works equally well on standard FROG traces, with the only difference that the test pulse and the gate are identical. The flow of the algorithm is schematically depicted in figure 2.10. The algorithm starts with two initial guesses for the fields, and the resulting FROG trace is calculated. After a Fourier transform the method of generalised projections (GP) is applied. Essentially, the new signal fields are found by projecting the current fields in the reconstruction onto a set of fields that satisfy a given constraint. In the PCGPA, the Fourier domain constraint consists in replacing the magnitude of the new trace by the experimentally measured trace. After an inverse Fourier transform the trace is brought back to outer product form. At this point, the “real space” constraint is applied: Determining

the best guess for the two fields that compose that trace. In the PCGPA, this is done by a singular value decomposition (SVD). The outer product pair with the largest weight[6] resulting from the SVD is taken as the new guess for the fields, and the procedure is repeated until the algorithm converges to the two fields. The goodness of the convergence is quantified by the difference between the measured and the reconstructed FROG trace, also known as the *FROG error*:

$$\epsilon = \left[\frac{1}{N^2} \sum_{i=1}^{N} \sum_{j=1}^{N} \left[I_{recon}(\omega_i, \tau_j) - I_{meas}(\omega_i, \tau_j) \right]^2 \right]^{1/2}, \tag{2.36}$$

where the summation is performed across the whole N^2 dataset with frequency index i and delay index j. Ideally, this error measure is minimised when the two reconstructed fields correspond to the actual real fields. However, as in any iterative reconstruction procedure, there is the problem of ambiguities, where two different sets of input fields yield the same FROG trace.

Ambiguities

There are a few properties of the pulse that FROG cannot measure. First, since only the magnitude squared of the signal is recorded by the detector, it is not possible to retrieve the absolute phase ϕ_0 (see section 2.2.1) . Second, since the input pulse is gating a replica of itself, there is no absolute time reference, and the arrival time of the pulse is not accessible. However, those quantities represent *trivial* ambiguities, which means that they do not change the shape of the pulse. In cases those quantities are required,

[6] The contributions with the largest weight are referred to as the *principal components*.

it is possible to perform specific experiments for this aim. Moreover, this problem is not unique to FROG, but is common to other complete pulse characterisation methods as well. Some implementations of FROG suffer from additional ambiguities (such as the direction-of-time ambiguity in SHG FROG), but usually those can be resolved with additional information or measurements. Therefore, when only one input field needs to be measured, FROG essentially yields unique solutions. However, if the PCGPA is used to characterise two different input fields, the issue of ambiguities becomes much more severe. The different approaches of characterising two independent fields, together with the corresponding ambiguities and possible solutions, are discussed in chapter 3.

Convergence

The PCGPA has been used in many FROG applications and has been proven to be a robust and reliable reconstruction algorithm. However, it has to be emphasised that theoretically, the convergence of FROG is not guaranteed. Indeed, as of yet there is no mathematical proof of the convergence of the reconstruction. One reason for this is that, while projections onto convex sets always converge, this is not the case for projections onto nonconvex sets[7] [55]. In FROG, neither of the constraint sets is convex. Convergence properties of any given FROG algorithm can therefore only be determined empirically[8].

[7] which is what the term *generalised* projections refers to.

[8] For FROG applications, the reconstruction of a double pulse represents a standard test of the reconstruction, even though more "pathological" tests may be performed as well.

2.4.3 Interferometry: SPIDER

A very different approach compared to spectrography for measuring the electric field of ultrashort pulses is interferometry. A milestone here was set by the development of Fourier Transform Spectral Interferometry (FTSI), which allowed the extraction of the spectral phase difference between the pulse and a known reference by means of a Fourier inversion [61, 62]. If, for example, a dispersive medium is placed in one arm of the interferometer, this allows the characterisation of the dispersive properties of the medium. Regarding the application of pulse measurement, an unknown test pulse can be fully characterised by measuring the phase difference if a known reference pulse is available. This might be the case, for example, where pulse shapers, pulse stretchers or compressors are used to manipulate the pulse. More generally, however, a reference pulse might not be available. In this case self-referencing characterisation techniques need to be used, such as Spectral Phase Interferometry for Direct Electric-field Reconstruction (SPIDER) [63, 64].

SPIDER

In SPIDER, the test pulse and a frequency-sheared replica are spectrally interfered on a spectrometer by introducing a time delay between the two pulses. A Fourier inversion algorithm allows the extraction of the phase difference between the pulses [65]. Generally, the phase difference between two identical pulses would simply cancel out, leaving only the linear phase $\omega\tau$ stemming from the time delay. To circumvent this, in SPIDER the replica of the test pulse is sheared in the spectral domain, which encodes the spectral phase in the interferogram, as will be shown below.

Consider the schematic experimental setup in figure 2.11. First, the test pulse is

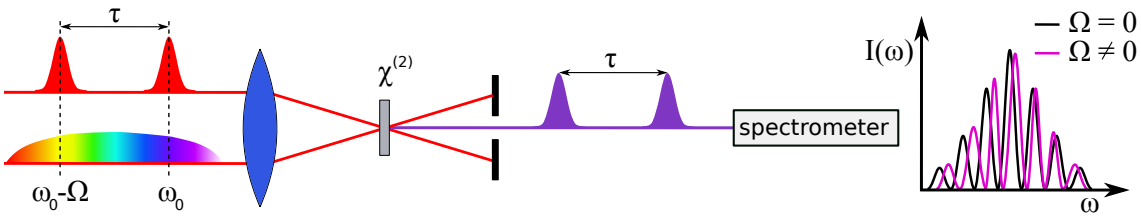

Figure 2.11: Schematic of a SPIDER setup. The test pulse and its time-delayed replica undergo sum-frequency generation in a nonlinear crystal and are upconverted with different monochromatic slices of the highly chirped ancillary pulse. The two sheared signal pulses, centred near twice the fundamental frequency, create a spectral interference pattern at the spectrometer. The time delay causes a fringe modulation with periodicity $2\pi/\tau$ (black fringes). For a nonzero spectral phase, the phase information is encoded in the deviation from the nominal uniform fringe spacing (pink fringes).

replicated and delayed in time. This can be achieved by using the reflections of the front and back surfaces of a glass etalon, or by an interferometer with adjustable delay in one arm. The latter option has the advantage that the shear can be changed continuously. Therefore several SPIDER measurements with different shears can be performed to, for example, check the consistency of the reconstruction. SPIDER itself requires two frequency sheared, but otherwise identical replicas of the test pulse. This is achieved by upconverting both pulses with a chirped and temporally stretched ancillary pulse. The chirp needs to be large enough such that each pulse is upconverted with a quasi-monochromatic slice of the ancillary pulse, centered at ω_0 and $\omega_0 + \Omega$. The spectral shear Ω introduced in this way between the pulses is then $\Omega = \tau/\phi^{(2)}$, where $\phi^{(2)}$ is the second-order dispersion coefficient. The two upconverted signal pulses are then centred near twice the carrier frequency of the

input pulse. Their interference pattern at the spectrometer takes the form:

$$\begin{aligned} I(\omega) &= |E(\omega-\omega_0-\Omega)+E(\omega-\omega_0)e^{i\omega\tau}|^2 \\ &= |E(\omega-\omega_0-\Omega)E_{anc}(\omega_0+\Omega)|^2+|E(\omega-\omega_0)E_{anc}(\omega_0)|^2 \\ &+ 2|E(\omega-\omega_0-\Omega)||E_{anc}(\omega_0+\Omega)||E(\omega-\omega_0)||E_{anc}(\omega_0)| \\ &\times \cos[\phi(\omega-\omega_0-\Omega)-\phi(\omega-\omega_0)-\phi_{anc}(\omega+\Omega)+\phi_{anc}(\omega_0)+\omega\tau]. \end{aligned} \tag{2.37}$$

The phase of the test pulse is thus encoded in the interferogram through the spectral phase difference $\theta(\omega)=\phi(\omega-\omega_0-\Omega)-\phi(\omega-\omega_0)$ between the two sheared signal pulse replicas. The amplitude of the ancillary pulse E_{anc} usually does not vary too much between the two upconversion frequencies separated by the shear Ω and therefore may only have a small effect on the interferogram fringe visibility. The contribution of the phase of the ancillary pulse ϕ_{anc} leads to a constant offset phase and may be set to zero in the reconstruction.

To extract the interferogram phase, a Fourier transform is applied, where the signal consists of the DC baseband and two AC sidebands. By applying a passband filter, one of the sidebands is isolated. The argument of the inverse Fourier transform of the sideband then represents the spectral phase difference θ plus the phase from the delay $\omega\tau$. To access θ, the delay phase has to be calibrated, which can be done by taking a measurement at zero shear, e.g. by using the fundamental wavelength. For small shears, θ is related to the gradient of the spectral phase,

$$\theta(\omega)=\Omega\frac{\phi(\omega-\omega_0-\Omega)-\phi(\omega-\omega_0)}{\Omega}\simeq\Omega\frac{\partial\phi(\omega-\omega_0)}{\partial\omega}. \tag{2.38}$$

The spectral phase ϕ is then obtained by concatenation[9] or integration [66].

Discussion

A key advantage of interferometric techniques such as SPIDER is that they benefit from an analytical reconstruction algorithm. This allows a rapid and deterministic reconstruction. Furthermore, the spectral phase is encoded in the separation of the fringes, not in their magnitude. As a consequence, SPIDER measurements are very robust regarding shot-to-shot fluctuations, a non-uniform detector response or the exact shape of the phase-matching function of the nonlinear process. Moreover, interferograms are 1D datasets, which is less data-intensive than 2D spectrograms.

However, interferometry is not void of ambiguities either. Similar to spectrographic techniques, the absolute phase as well as the pulse arrival time are not recovered. However, there is another notable ambiguity. The spectral phase can become undefined in cases where the pulse exhibits spectral gaps, i.e. areas where the intensity is smaller than the noise level. If such a gap is larger than the spectral shear, the phase difference, and therefore the spectral phase, will be random at one or more points between the components. Even though a multi-shear algorithm has been developed that uses a variety of large and small shears to "bridge the gap" and still maintain sufficient spectral resolution, the requirement for the pulse to contain a spectral region wider than the gap still holds [67, 68].

[9] Concatenation provides exact phase reconstruction for fields that satisfy the Shannon theorem, i.e. for fields whose temporal support lies within the interval $[-\pi/\Omega, \pi/\Omega]$. In other words, for a pulse with temporal support T, the shear Ω, which dictates the spectral sampling rate, must satisfy $\Omega \leq 2\pi/T$.

RMS field error

In FROG, the error in the reconstruction is usually estimated using the FROG error, given by equation (2.36). However, to allow comparison between different techniques it may be desirable to employ a more general error measure that can be applied independently of the exact functioning of the technique. A universal error is the root-mean-square (RMS) field error [66]. This error measure is useful, for example, for theoretically testing the accuracy of a novel characterisation method by comparing an initial simulated field E_{ini} and the field E_{retr} retrieved by a a characterisation device that is to be tested. For such a scenario, the field error ε is defined as the norm of the difference between the two fields,

$$\begin{aligned}\varepsilon = ||E_{ini} - E_{retr}|| &= \left[\int_{-\infty}^{\infty} \mathrm{d}t |E_{ini}(t) - E_{retr}(t)|^2\right]^{1/2} \\ &= \frac{1}{2\pi}\left[\int_{-\infty}^{\infty} \mathrm{d}\omega |\tilde{E}_{ini}(\omega) - \tilde{E}_{retr}(\omega)|^2\right]^{1/2}. \end{aligned} \tag{2.39}$$

Due to Parseval's theorem, the errors in the temporal and the spectral domains in (2.39) are equivalent. The error ranges between 0 (equal pulses) and 2 (pulses are inversions of each other) if the fields are normalised, which is done by calculating the norm $||E|| = \left[\int_{-\infty}^{\infty} \mathrm{d}t |E(t)|^2\right]^{1/2}$. Values of ε below 0.02 correspond to very good reconstructions, $0.02 \leq \varepsilon \leq 0.1$ are average reconstructions, and reconstructions with $\varepsilon > 0.1$ are considered as poor.

Some implementations of SPIDER

In analogy to FROG, many variants of SPIDER have been developed, each with particular strengths in specific parameter spaces. However, only two examples shall be described here

since these will be important for the experimental part of this thesis.

CAR-SPIDER: In the Chirped ARrangement for SPIDER (CAR-SPIDER), two spatially chirped upconverted replicas of the input pulse are spectrally interfered, with a spectral shear varying across the spatial coordinate (see figure 2.12(a)) [69]. A spatial chirp on the test pulse may be introduced by focusing into a long crystal with a suitably tailored phase-matching function, where each wave vector of the focused beam experiences a different upconversion frequency [70, 71]. The upconverted and spatially chirped test pulse replica $E(\omega - \omega_0 - \alpha x)$ is replicated using a Mach-Zehnder interferometer and spatially flipped with respect to the axis associated with the spatial chirp by using an odd number of reflections, resulting in $E(\omega - \omega_0 + \alpha x)$. Here α is the coefficient representing the slope of the spatial variation of the spectral shear. It needs to be calibrated only once by recording the individual spatially resolved spectra. As a consequence, the spectral shear is varying in space according to $\Omega = 2\alpha x$. At the entrance of an imaging spectrometer the spatially chirped test pulse replica forms an interferogram with its time-delayed mirror image. At each spatial position the generic 1D SPIDER reconstruction can be performed to retrieve the temporal pulse shape. However, due to the amount of shears available it is possible to perform the reconstruction at each spatial location x_0 with the corresponding shear $2\alpha x_0$. This may be beneficial, for example, for consistency checks since, within certain limits, the retrieved pulse shape should be independent of the spectral shear. A further advantage of CAR SPIDER is that its trace, although containing several shears, can be obtained in a single laser shot.

SEA-SPIDER: In the Spatially Encoded Arrangement (SEA) for SPIDER the spectral phase is encoded in spatial fringes instead of spectral fringes [72]. Its principle is

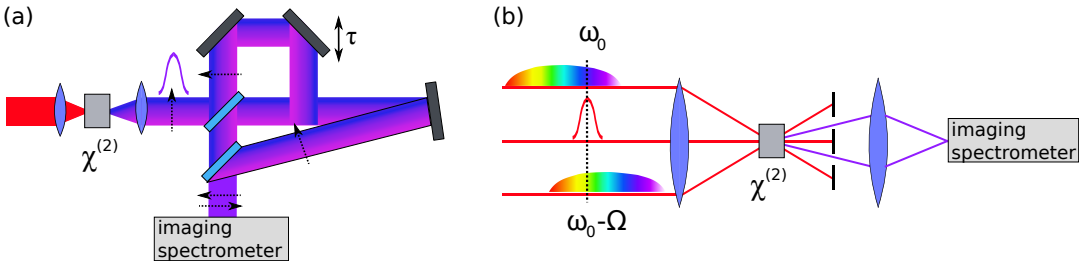

Figure 2.12: Different SPIDER implementations. (a) CAR-SPIDER setup. A spatially chirped test pulse replica is created by upconversion in a long nonlinear crystal. The chirped pulse and its flipped mirror image interfere on an imaging spectrometer, which results in a SPIDER trace with multiple shears. (b) SEA-SPIDER setup. The test pulse is mixed with two chirped and time-delayed ancillary pulses to produce a spatial interference pattern on the imaging spectrometer.

illustrated in figure 2.12(b). The test pulse is upconverted with two temporally chirped ancillary pulses, the relative time delay of which sets the spectral shear. The two generated frequency sheared replicas of the input pulse are then focused in a noncollinear geometry onto the entrance slit of an imaging spectrometer. A spatial interference pattern is created where the fringe spacing is determined by the angle between the two beams. The sideband of the interferogram is extracted using a 2D Fourier filtering routine. As in conventional SPIDER the spectral phase is then obtained by concatenation. However, since the SEA-SPIDER trace is spatially resolved, the phase difference $\phi(x_0, \omega-\omega_0-\Omega)-\phi(x_0, \omega-\omega_0)$ may be extracted for every spatial position x_0 along the slit dimension. The pulse can therefore be reconstructed at any spatial position across the beam. This allows the estimation of the amount of certain types of space-time coupling in the beam. A further advantage is that the constraints on the high spectrometer resolution in conventional SPIDER are relaxed by resolving the fringes in the spatial domain. Finally, it is possible to combine the two aforementioned techniques to record a spatial interferogram where the shear is varying in space. This so-called SEA-CAR-SPIDER technique is described in detail in section 3.4.1.

2.5 Measuring the spatial phase of optical beams

In contrast to the rather recent field of ultrashort pulse characterisation, devices for the measurement of the wavefronts of optical beams have a much longer history, mainly due to the early necessity to characterise optical aberrations and to optimise optical systems. Several techniques exist that reliably characterise wavefronts of monochromatic and polychromatic beams.

2.5.1 Shack-Hartmann Sensor

One of the most widespread devices for the measurement of the wavefronts of optical beams is the Shack-Hartmann wavefront sensor [73–75]. It uses an array of microlenses where each lenslet focuses the local wavefront onto a CCD, as illustrated in figure 2.13. If the beam is well collimated, the focal spots form a uniform grid on the detector. In contrast, an aberrated beam has a spatially varying local tilt of the wavefront. Since the wave vector is normal to the wavefront, the focal spots from an aberrated wavefront will deviate from the initial uniform grid. Even though the device works very well with monochromatic light, it is not spectrally resolving and therefore only of limited use when dealing with pulsed light[10].

2.5.2 Interferometric techniques

Interferometry has a longstanding history in optical shop testing to measure the aberrations induced by optical components [77]. Two of the most important implementations

[10] One way to overcome this problem is to apply several narrowband spectral filters for each wavefront measurement [76]. The sum of the individual wavefronts, weighted by the corresponding spectral intensity, has similar properties than the unfiltered pulse wavefront. Of course, the availability of high-quality spectral filters when dealing with ultrabroadband pulses represents a technical and practical limit.

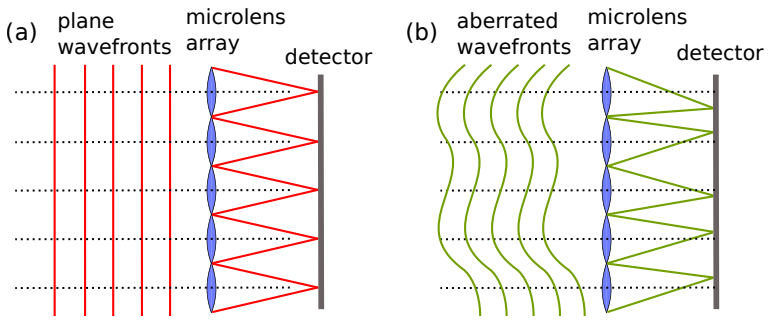

Figure 2.13: Principle of a Shack-Hartmann wavefront sensor. (a) A non-aberrated beam is focused by several microlenses onto the detector. The foci of the different segments define the reference grid. In (b) an aberrated beam is used as an input. The deviation of the foci positions from the reference grid quantifies the local wavefront.

regarding the characterisation of laser beams are described in this section.

Point diffraction interferometry

In point diffraction interferometry (PDI), the test beam interferes with a reference spherical wave [78], as shown in figure 2.14(a). The reference is derived from the test beam itself by placing a semi-transparent film with a very small hole in the centre into the test beam. The diffracted spherical wave from the hole forms the reference, whereas the semi-transparent film attenuates the transmitted field to roughly match the reference in intensity for higher fringe contrast. Since the reference phase is known, the test pulse phase can be recovered.

Lateral shearing interferometry

Lateral shearing interferometry (LSI) can be seen as the direct spatial analogue of spectral shearing interferometry. Figure 2.14(b) illustrates the concept. The test beam interferes with a replica of itself on a detector. A spatial carrier may be applied to the interferogram

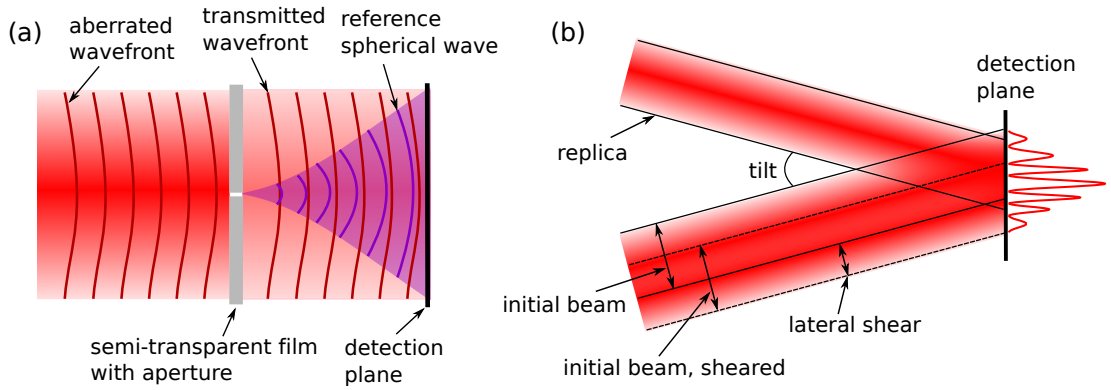

Figure 2.14: Implementations of interferometric wavefront measurements. (a) Point diffraction interferometry schematic setup. A test beam propagates through a semi-transparent film. A small aperture in the film generates a reference spherical wave which interferes with the test pulse on the detector. (b) Concept of lateral shearing interferometry. The test beam interferes with a replica of itself. A relative tilt acts as a spatial carrier of the interference pattern. A lateral shear on one arm encodes the phase into the interferogram.

by introducing a tilt between the two beams[11]. If an additional spatial shear is applied, the wavefront becomes encoded into the interferogram. For an aberrated wavefront, the fringe spacing will deviate from the nominal uniform spacing. An analogous algorithm to the one in spectral shearing interferometry can be applied to recover the wavefront of the test beam. Methods for applying the lateral shear include Mach-Zehnder [79], Michelson [80] or cyclic [81] interferometers, a plane parallel plate [82] or diffraction off a grating [83, 84].

Note that, while in the presented example of LSI a shear across one spatial dimension was considered, it is equally possible to apply a radial [85–88], rotational [89] or vectorial [90, 91] shear. This might be advantageous when the 2D wavefront needs to be characterised in a single shot. For a comprehensive discussion of applications of interferometry to optical testing the reader is referred to [77].

[11] Even though a spatial carrier allows for a robust encoding of the phase, this is not a necessity and many lateral shearing interferometers do without a carrier, with the drawback of a possibly lower sensitivity. For instance, beams with some amount of defocusing form a regular fringe pattern without the need for an additional carrier [77].

2.6 Spatio-temporal pulse characterisation

Arguably the ultimate goal of all pulse characterisation technology is to measure the full spatio-temporal pulse profile for arbitrary pulses shapes. Spectrographic techniques record 2D traces in the time-frequency domain, which provides per se no spatial information. Spectral shearing or lateral shearing interferometry are approaches that appear well-suited for tackling this problem since they record 1D traces, leaving the second dimension of an imaging spectrometer open to resolve the respective other domain. For example, SEA-SPIDER recovers the spatially resolved temporal pulse profile across one spatial dimension [72, 92]. By scanning the slit position along the orthogonal spatial dimension and assuming cylindrical symmetry one can, to some extent, draw conclusions about the 3D pulse profile. In analogy, spectrally resolved lateral shearing interferometry has been performed where the frequency-resolved gradient of the spatial phase $\partial\phi(x,\omega)/\partial x$ is recovered [93]. Integration yields the spectral phase up to an arbitrary function of frequency, $\phi(x,\omega)+\delta(\omega)$. It can be seen that the caveat of all those approaches is that the ubiquitous phase ambiguity of self-referencing techniques prevents the recovery of the full spatio-temporal phase. In the example of LSI, an additional spectral phase measurement needs to be performed to determine $\delta(\omega)$. However, the information such kinds of experiments provide can nevertheless be used to quantify the amount of space-time coupling in the beam. For example, spectrally resolved LSI has been performed to quantify the amount of spatial chirp and in this way to optimise the output of a CPA [93]. In a different experiment, the spatial dependence of the pulse duration of few-cycle pulses generated by filamentation has been characterised by scanning an aperture across the spatial beam profile [94].

2.6.1 Referencing techniques

There are several methods capable of performing spatio-temporal reconstructions if a known reference is available or if a reference can be generated from the test pulse. The FTSI approach can be extended to spatio-spectral Fourier transform interferometry. The test pulse and a reference are interfered in a 2D spectrometer, where the wavelength is resolved along one dimension, and the desired spatial beam axis is resolved in the perpendicular dimension. The carrier can be applied in either domain: A time delay can be used as spectral carrier [95–97], or a tilt between the two beams as spatial carrier [98]. In all cases the spectral phase difference is encoded in the sidebands of the Fourier transform of the interferogram and can be extracted at any point along the spatial dimension. Therefore the change of the temporal pulse shape across the spatial profile relative to the reference can be tracked by this method. Of course, as is common to all referencing techniques, the test beam and the reference must be mutually coherent in order for them to interfere. This is naturally fulfilled if they originate from the same source.

SEA-TADPOLE[12] is a variation of spatio-spectral interferometry (SI) [99–102]. The test beam and a well-characterised reference are coupled into two identical single-mode fibres. The output beams have a relative angle to each other, and the resulting spatial interferogram is spectrally resolved. Knowing the reference, the phase difference obtained directly yields the spectral phase of the test beam via FTSI. To obtain the spatial information, the test pulse fibre is scanned longitudinally and transversely across the beam. If the fibre is scanned through a focusing beam, the pulse evolution across the focal region can be reconstructed. The SEA-TADPOLE setup needs to be stable and isolated to avoid drifts of

[12]Spatially Encoded Arrangment of the Temporal Analysis by Dispersing a Pair of Light Electric-fields

the interferometer and the fibre during the scan, even though modifications of the original method have been developed to overcome this issue [103]. Recently, SEA-TADPOLE has been extended to measure collimated beams, with the significant advantage of being able to characterise ultra-high intensity femtosecond lasers [104].

In another approach, with ideas borrowed from digital holography, the test beam is interfered with a reference beam which can be generated from the original beam by spectral and spatial filtering[13] [105]. A tilt between both beams serves as spatial carrier, and the 2D wavefront $E(x, y; \omega_k)$ can be reconstructed for a given frequency ω_k. The selected wavelength is changed by angle-tuning interference filters, and the measurement is repeated each time. A discrete set of phase function is obtained. However, if the experiment is performed in a self-referencing way (the reference is generated from the test beam), the phase ambiguity prevents the correct linking of those phase functions. Therefore an additional FROG measurement is done to determine the spectral phase and to link the wavefronts of the different frequencies together. Note that such an approach will only be useful if the FROG trace is taken at a spatial location where all frequencies are present. This might not be fulfilled when strong STC is present in the beam, such as a large amount of spatial chirp, or when the pulse is exhibiting spectral gaps.

The previous method necessitates recording several images for each wavelength, requiring a stable train of identical pulses. Therefore the concept has been extended to STRIPED FISH[14] which records multiple digital holograms for different wavelengths at

[13]The spatial filtering is usually done by a small pinhole. The reference field will, at the location of the detection plane, therefore not be a tilted plane wave, but rather a curved quadratic wavefront. The pinhole is still the preferred method of choice, compared to e.g. a telescope with large magnification, since it creates a known spatial profile without the risk of aberrations.

[14]Spatially and Temporally Resolved Intensity and Phase Evaluation Device: Full Information from a Single Hologram

different spatial locations on the CCD in single laser shot [106, 107]. The different interferograms are generated by diffracting the test pulse off a coarse grating and passing through a tilted interference filter. Since each diffraction order has a different wave vector, and the filter passband frequency depends on the angle of incidence of the incoming light, each transmitted order consists of a quasi-monochromatic spatial interferogram. The combination of the phases of all interferograms yields $E(x, y, t)$. There is, however, a trade-off between spectral and spatial resolution, since a larger number of holograms leads to higher spectral, but lower spatial resolution.

2.6.2 Self-referencing techniques

The key challenge in the development of self-referencing spatio-temporal characterisation techniques is to overcome the phase ambiguity, common to all self-referencing techniques. This means that in general measurements have to be performed in both the spatial and the spectral domains.

One technique to perform this task is Shackled-FROG [108]. First, the 2D wavefront is measured by a Shack-Hartmann sensor. This is followed by an independent FROG measurement to measure the spectral phase and thus obtain the spatio-temporal evolution of the pulse. However, this approach does not work for large bandwidths or pulses with space-time coupling where the spatial phase is different for each frequency. One solution to this problem is to use a set of interference filters that are placed into the beam to select a quasi-monochromatic frequency and to repeat the wavefront measurement while scanning the passband frequency [76]. Disadvantages of this method include an increased number of measurements and a rather coarse frequency resolution, limited by the avail-

ability of suitable interference filters. To circumvent those issues, the wavefront sensor may be put into the detection plane of an imaging spectrometer. This yields the correct spatio-temporal profile, at the expense of one spatial dimension [109]. Another implementation uses an acousto-optic programmable dispersive filter (AOPDF) to act as a tunable bandpass filter instead of using interference filters, which adds more control and flexibility to the measurement [110].

Another technique for measuring the complete field as function of frequency and one spatial dimension is known as CROAK[15] [111]. In a SHG FROG-based setup, an imaging spectrometer records the spectra in the near-field, $I(x, \lambda)$, and in the far-field, $I(\theta, \lambda)$. An algorithm based on the Gerchberg-Saxton algorithm [112, 113], combined with a FROG measurement at one spatial location, reconstructs the field $E(x, \lambda)$.

An interferometric way to obtain $E(x, t)$ is to measure the spatially resolved spectral phase gradient by performing SPIDER on an imaging spectrometer, as well as to measure the spectrally resolved spatial phase gradient via LSI [114, 115]. From those gradients the complete spatio-temporal field is reconstructed. Both interferograms can be recorded in a single shot by using the first grating diffraction order for the LSI trace, and the second order for the SPIDER trace.

2.7 Outlook

The robust and accurate characterisation of ultrashort pulses represents one of the key challenges of the ultrafast community even today. Although SPIDER and FROG work reliably concerning the characterisation of IR femtosecond pulses, and variants of those

[15] Complete Retrieval of the Optical Amplitude and phase using the $(k_\perp, \omega)$spectrum

have been extended to a wide range of parameter spaces, several challenges remain. Those include extending the well-established, robust techniques to the measurement of the full four-dimensional electric field $E(x, y, z, t)$. Reconstruction algorithms should be fast to allow an online pulse-monitoring in the laboratory. In addition, competitive techniques should be capable of measuring complex pulses, such as those emerging from pulse shaping processes, or after certain nonlinear interactions. Prominent examples of complex pulses are those exhibiting spectral gaps. Moreover, there is the need to transfer the femtosecond technology to different wavelength ranges. In this regard, an active field of research is the characterisation of extreme-ultraviolet attosecond pulses. Finally, soon after the development of the first complete pulse characterisation device, FROG, in 1993, it quickly became clear that in many experiments full information would be obtained if one was able to characterise two pulses at the same time, such as the input and the output of an experiment.

This chapter has presented the state of the art of femtosecond metrology, together with the necessary theoretical background. In the next chapter, a novel pulse characterisation technique is developed that addresses each of the aforementioned challenges. The above summary of existing characterisation devices suggests that such a task can only be successful if different concepts are combined, to overcome the limitations and combine the strengths of each. In the work presented in this thesis, concepts used in SPIDER and FROG are combined to characterise infrared femtosecond and XUV attosecond pulses.

Chapter 3

Mutual interferometric characterisation of electric fields

"There is great pleasure in recognizing old things from a new point of view."

Richard Feynman

Since the development of femtosecond laser technology in the early 80's, measurement techniques that are capable of characterising pulses on such short time scales form the basis of modern ultrafast science. Their application is typically twofold: On the one hand, ultrashort pulse characterisation devices are used to measure short pulses produced by the laser system before they are used in experiments. This provides the experimenter with a known input field. Real-time monitoring of this pulse allows the optimisation of the pulse shape, for example by compensating for higher-order spectral phase terms in order to reach a pulse duration close to the Fourier limit. Moreover, pulse shaping can be performed and monitored in real-time in order to obtain a pulse with its properties adapted

to the particular needs of an experiment. On the other hand, characterisation devices are used to measure the output of an experiment. In ultrafast spectroscopy, an ideally well-characterised input pulse interacts with a sample medium and the output is recorded by a detector. Since all the information about the light-matter interaction is encoded in the output electric field, measuring this field allows one to extract information about the medium on ultrashort time scales. However, in an ideal scenario, the input and output fields are measured simultaneously, and possibly even in a single laser shot. This provides the most information that is available to deduce the spatio-temporal characteristics of the sample response. The reason for this is that both shot-to-shot fluctuations of the laser source as well as external decoherence (e.g. sample vibrations) and internal decoherence (temporal change of the medium properties) could lead to different results for different measurement instances.

In this chapter, a novel characterisation technique MICE (Mutual Interferometric Characterisation of two Electric-fields) is introduced. MICE is able to measure two beams simultaneously in any parameter space where it is possible to shear one of the beams. It can therefore readily be applied to the temporal reconstruction of ultrashort pulses, or the wavefront reconstruction of a light beam. In addition, MICE recovers the relative phase between both beams. After first reviewing the state of the art of two-pulse characterisation schemes, the concept of mutually referencing interferometry and the algorithm are discussed together with their limitations. Afterwards, the technique is demonstrated in two cases. The first example performs a wavefront reconstruction of two simulated electric fields. In the second example, experimental data obtained by a SEA-CAR SPIDER configuration is used to reconstruct the temporal profile of two infrared femtosecond pulses

in a single laser shot. The results of this chapter have been published in [116, 117].

3.1 The challenge of simultaneously measuring two independent fields

Shortly after the invention of FROG in 1993 [52, 57], which was the first self-referencing complete ultrashort pulse characterisation method, the importance of extending FROG to the measurement of two independent input fields was realised. Therefore, only two years later, a modification of FROG attempting to achieve this aim was introduced under the name TREEFROG (Twin Recovery of Electric-field Envelopes by the use of FROG) [118]. The TREEFROG reconstruction aims at extracting solutions for the probe $P(t)$ and the gate $G(t)$ from the FROG trace

$$I_{TREEFROG}(\omega,\tau) = \left| \int_{-\infty}^{\infty} P(t)G(t-\tau)\exp(i\omega\tau)\mathrm{d}t \right|^2 . \tag{3.1}$$

In a conventional FROG experiment, the gate $G(t)$ is derived from $P(t)$. TREEFROG instead can be regarded as the generalised case where the fields can be different. In this case, the standard FROG reconstruction is not sufficient to reconstruct both fields. However, mathematically similar scenarios are encountered in imaging science, where the challenge typically consists in reconstructing both an object and the illuminating electric field [119]. In mathematical terms, these types of problems are equivalent to a two-dimensional blind deconvolution, and iterative algorithms have been developed for its solution [120, 121]. Their adaptation to ultrashort pulse reconstruction using FROG is therefore also often

referred to as blind-FROG. The blind-FROG reconstruction starts with a guess for both $P(t)$ and $G(t)$. The key steps of the algorithm are equivalent to the standard FROG algorithm, i.e. replacing the reconstructed intensity by the measured intensity, and applying a generalised projection (GP) after an inverse Fourier transformation. The error function that needs to be minimised now takes the following form:

$$\epsilon = \sum \left| E'_{sig}(t,\tau) - P(t)G(t-\tau) \right|^2, \tag{3.2}$$

where $E'_{sig}(t,\tau)$ represents the signal field $E_{sig}(t,\tau) = P(t)G(t-\tau)$ after replacing the magnitude of $E_{sig}(t,\tau)$ with the square root of the measured trace in the Fourier domain. In the case of TREEFROG, the GP is applied such that updating the guess of each field and minimising equation (3.2) with respect to the field is only done for one field per iteration. This procedure is then alternated between the two fields for even and odd iterations. Even though it has been possible to reconstruct two different pulses using this procedure, in order to achieve reasonable convergence of the algorithm, it has been found that the independently measured spectra of both fields need to be inserted as an additional constraint. In a subsequent experiment, the two-field challenge was addressed in a polarization-gate TREEFROG and with an improved algorithm, the PCGPA (see section 2.4.2) [60]. However, the issue of blind-FROG suffering from many *nontrivial* ambiguities remained unsolved. For example, Seifert *et al.* have shown that blind-FROG leads only to a unique solution if the two pulse spectral intensities are known and the blind-FROG trace is non-centrosymmetric [122]. Ambiguities are reduced if the spectral intensities of both pulses are very different. For many common situations in the laboratory, as well as

for the experimental data analysed in this thesis, this is clearly not the case, which means that a blind-FROG reconstruction of such data might not have a unique solution.

Seifert *et al.* extended the XFROG method to two unknown pulses such that the FROG trace is always non-centrosymmetric, and therefore has no non-trivial ambiguities [123]. They named their technique VAMPIRE (a Very Advanced Method for Phase and Intensity Retrieval of E-fields). To achieve this, a spectral phase modulator is implemented, such as an unbalanced Mach-Zehnder interferometer with a dispersive element in one arm. An additional temporal phase modulator can be added in order to avoid relative phase ambiguities in case pulses with well-separated frequency components need to be characterised. The method has been demonstrated to be able to characterise two independent pulses. However, in order for it to guarantee unique solutions, both the pulse spectra as well as the characterisation of the filtering performed by the phase modulators have to be known *a priori*.

In 2012, blind-FROG was extended to a configuration where two polarisation-gate FROG traces are recorded at the same time, as shown schematically in figure 3.1 [124, 125]. In the first arm, the spectrogram $I_1(\omega, \tau)$ is recorded where field $E_1(t)$ is treated as the

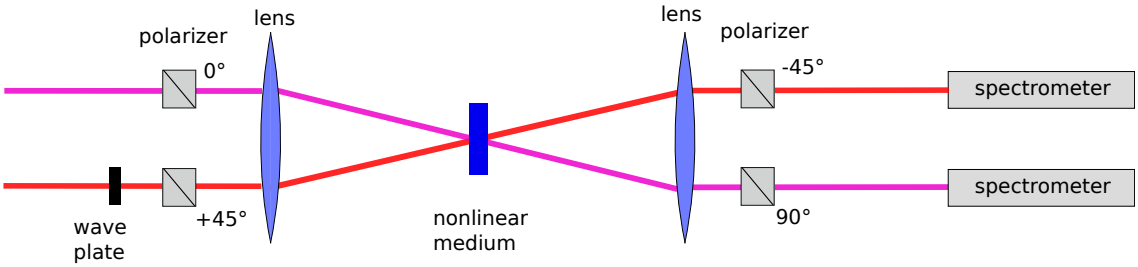

Figure 3.1: Double-blind polarisation-gating FROG. Inside the nonlinear medium, both pulses are mutually gating each other. Two separate spectrograms are recorded, from which both input pulses are retrieved.

unknown field, whereas in the second arm, $E_2(t)$ is the unknown field. The respective other field in each case, although unknown as well, is treated as if it was known, and each spectrogram is solved with respect to the assigned unknown field. Processing of $I_1(\omega, \tau)$ yields an improved guess for $E_1(t)$, which is then inserted into the processing of $I_2(\omega, \tau)$, resulting in an improved guess for $E_2(t)$. This procedure is iterated until both FROG traces match the respective experimental traces, quantified by the usual FROG error. Since for this technique two traces are recorded, it is referred to as double-blind FROG. Even though no nontrivial ambiguities are known in this variant of FROG, it comes at the cost of increased experimental complexity, since a major part of the setup needs to be replicated in order to record two spectrograms at the same time.

Finally, Measuring the Electric Field by Interferometric Spectral Trace Observation (MEFISTO) allows one to reconstruct from a collinear interferometric autocorrelation trace the complete field of an ultrashort pulse in an analytic way [126]. Even though traces are recorded in the time-frequency domain, as it is done in FROG, an analytic Fourier analysis can be performed to yield the electric field, due to the interferometric nature of data. An extension of the technique, blind-MEFISTO, has been proposed to simultaneously measure two independent pulses in an non-iterative way [127]. However, in this case, the different pulse spectra are required as an input as well, and an experimental demonstration of blind-MEFISTO is still lacking to date.

3.2 Mutual interferometric characterisation of two electric-fields

In the following, a novel two-pulse characterisation technique is introduced: Mutual Interferometric Characterisation of two Electric-fields (MICE). Through combination of elements of interferometry and spectrography it overcomes many problems of previous techniques and provides a rapid and robust reconstruction algorithm. The concept of MICE and its algorithm are discussed below, along with a discussion of its strengths and possible ambiguities.

3.2.1 Concept of mutually referencing interferometry

Conceptually, MICE consists of two different elements. First, procedures borrowed from interferometry allow the extraction of the interferometric product and therefore the phase difference between the two fields. The second step uses the the concept of *generalised projections* (GP) to separate the product into the two different fields. As described in chapter section 2.4.2, generalised projections are used in the FROG reconstruction, where they converge quite reliably to the initial input field [59]. However, their use is much more widespread. Particularly in imaging science, generalised projections have been used for many years to recover the image of an object illuminated by an incident light field [128]. In one of its most advanced versions, ptychography, a sample, typically a nano-object, is scanned through the focus of a beam, and each time the diffraction pattern is recorded. Iterative reconstruction algorithms based on generalised projections are now able to reconstruct both the object as well as the probe field [129, 130]. The accuracy

of the reconstruction is increased by using smaller step sizes of the object displacement, since this increases the redundancy in the data. In MICE, the very different concepts of interferometry and generalised projections are combined and, as will be shown below, inherit the advantages of both sides.

3.2.2 Algorithm

Consider the two input fields $E_1(\gamma)$ and $E_2(\gamma - \Gamma)$. Here, $E_2(\gamma - \Gamma)$ has been sheared by the amount Γ, and γ denotes the field variables x, y, z and t or their corresponding Fourier transform variables k_x, k_y, k_z and ω. In the following, each of those variables are treated independently in the interest of clarity, which is a valid assumption if there is no spatio-temporal coupling present in the beams[1]. If those two fields are brought to interference, the resulting interferogram $I_{j,k}$, sampled over J points and K shears, takes the following form, where j and k represent the sample indices:

$$I_{j,k} = |E_1(\gamma_j)|^2 + |E_2(\gamma_j - \Gamma_k)|^2 + 2\mathrm{Re}\left[E_1(\gamma_j)\, E_2^*(\gamma_j - \Gamma_k)\right] \tag{3.3}$$

The last term of equation (3.3) contains the interferometric product $E_1(\gamma_j)\, E_2^*(\gamma_j - \Gamma_k)$ which contains all the phase information about the fields. In the same way as it is done in SPIDER, a filter in the Fourier-domain is applied to isolate the AC sideband, denoted as $AC_{j,j-k}^{meas}$ [65]. At this stage, in SPIDER, $E_2(\omega - \Omega)$ is just a sheared replica of $E_1(\omega)$,

[1]Note that in principle MICE can be used to obtain information about space-time coupling in the beam as long as the pulse profile stays the same for the different shears at a given spatial or temporal location where the pulse is to be characterised. While the configuration of the single-shot SEA-CAR-SPIDER presented in section 3.4 may not be suitable for this application since the spectral shear is encoded in the spatial position, a multi-shot configuration can be employed for the different spectral shears. Reconstructions at different spatial positions then reveal information about the change of the temporal profile in space.

which means that the phase of E_1 can be obtained by integrating the phase difference extracted from the interferometric product, as detailed in section 2.4.3. However, in the more general case of MICE, both fields may be different. Therefore a different procedure needs to be found that is able to extract the phases of both fields individually. In other words, this means that the interferometric product needs to be unambiguously split into the individual fields E_1 and E_2 when $E_1 \neq E_2$.

To achieve this task, an approach similar to generalised projections is used. The least-squares error ϵ between the measured traces and the retrieved fields can be written as

$$\epsilon = \sum_{j,k}^{J,K} |AC_{j,j-k}^{meas} - E_1(\gamma_j) E_2^*(\gamma_j - \Gamma_k)|^2. \tag{3.4}$$

This error is minimised for the two fields $E_1(\gamma)$ and $E_2(\gamma - \Gamma)$ that best reproduce the measured interferograms for each shear. Minimisation of equation (3.4) must be performed numerically as closed form solutions for E_1 and E_2 cannot be obtained. To this end, setting to zero the derivative of (3.4) with respect to E_1 and E_2 yields the solution as a system of equations (see appendix B):

$$E_1(\gamma_j) = \frac{\sum_k AC_{j,j-k}^{meas} \cdot E_2(\gamma_j - \Gamma_k)}{\sum_k |E_2(\gamma_j - \Gamma_k)|^2} \tag{3.5}$$

$$E_2^*(\gamma_j) = \frac{\sum_k AC_{j+k,j}^{meas} \cdot E_1^*(\gamma_j + \Gamma_k)}{\sum_k |E_1(\gamma_j + \Gamma_k)|^2}. \tag{3.6}$$

This set of equations is solved by first inserting a random guess for E_2, typically chosen as a uniform distribution, into (3.5). This yields a first solution for E_1, which is then used

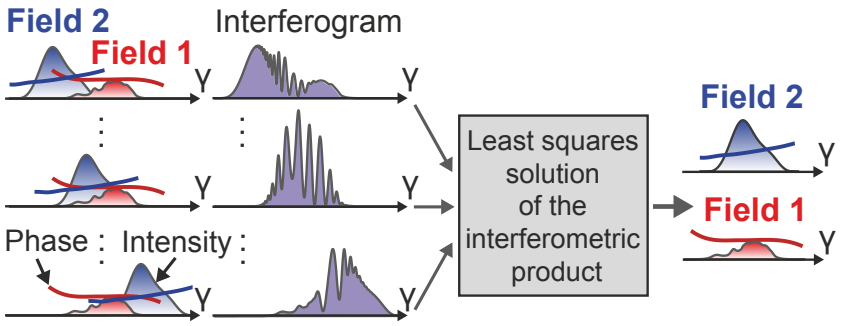

Figure 3.2: Schematic of the MICE reconstruction. Field 1 is sheared across Field 2 and the interferogram is recorded for each shear step. A least-squares minimisation identifies the two fields that best match the experimental data.

in (3.6) to provide an improved guess for E_2. This procedure is iterated until the error ϵ is minimised. The whole reconstruction algorithm is schematically summarised in figure 3.2. Since in each iteration step one field is used as a reference to retrieve the other field, the general MICE approach is referred to as *mutually referencing interferometry*.

3.2.3 Discussion

What is the main difference between the MICE algorithm and generalised projection-based algorithms such as the one used in blind-FROG or ptychography? All those algorithms have in common that a first guess of the fields is made and inserted into an iterative loop, which yields an improved guess. Minimising the error between the updated fields and the experimental traces eventually results in the two unknown fields, or, as in ptychography, in the probe field and the object image. The key advantage of MICE, however, is that the phase is already encoded in the fringe pattern, a significant advantage of all interferometric techniques. In contrast, in a FROG trace, this is not the case. Consequently, the convergence of the FROG algorithm is more involved and needs more iterations. Also, the inherent ambiguities of blind-FROG can be explained by this insufficient amount of

information in the data set. In contrast, as will be shown in the following two examples, the MICE algorithm is very stable, and a couple of iterations is usually sufficient to obtain a very good reconstruction.

The quality of the reconstruction depends on the amount of redundancy in the data. The higher the number of shears, and the larger the overlap between successive interferograms, the better the reconstruction. A minimum overlap between consecutive interferograms is, however, required for the algorithm to converge. If consecutive interferograms are located in completely distinct and mutually exclusive regions, the reconstruction would fail to converge.

Ambiguities

As explained in the previous section, MICE is not as prone to ambiguities in the reconstruction as, for example, blind-FROG, since more information is contained in the interferometric dataset than in a FROG trace. Nevertheless, MICE still suffers from one ambiguity: $E_1(\gamma)E_2^*(\gamma-\Gamma_k) = \alpha E_1(\gamma)\cdot(1/\alpha)E_2^*(\gamma-\Gamma_k)$, with α being a complex constant. As a consequence, each electric field is known up to an absolute phase and the absolute intensity. However, it is important to note that the relative phase between both fields is preserved.

The intensity ambiguity can easily be resolved by measuring the pulse spectra separately. If performing this additional measurement is undesired, the Fourier-domain DC baseband $|\alpha E_1|^2 + |(1/\alpha)E_2|^2$ from the MICE data may be used, since here the symmetry between the fields is broken. Regarding the phase ambiguity, this means that the carrier-envelope phase of the field cannot be retrieved, a problem that is common to all regular

pulse characterisation techniques such as SPIDER or FROG. If this quantity needs to be known as well, a significantly more complex experiment has to be performed. Examples include using the attosecond process of high harmonic generation as a fast gate [131–133], or measuring field-induced currents in a metal-dielectric-metal nanojunction [134].

3.3 Wavefront reconstruction simulation

In this section, the performance of MICE will be demonstrated on simulated data. The advantage here is that the MICE reconstruction can be tested under arbitrary and extreme conditions. The reconstruction of experimentally measured ultrashort pulses will be demonstrated thereafter.

In this example, MICE is used to reconstruct 2D wavefronts of optical beams. This experimental scenario becomes particularly interesting if we consider a beam (Field 1) having a highly complex spatial profile and wavefront that can neither be duplicated nor sheared. A second, smaller beam (Field 2) is spatially sheared across the full profile of Field 1 along both the x- and the y-axis. A schematic of this procedure for the shear along one axis is depicted in figure 3.3. If the two fields are aligned at an angle θ along the x-axis with respect to each other, a spatial interference pattern is formed due to

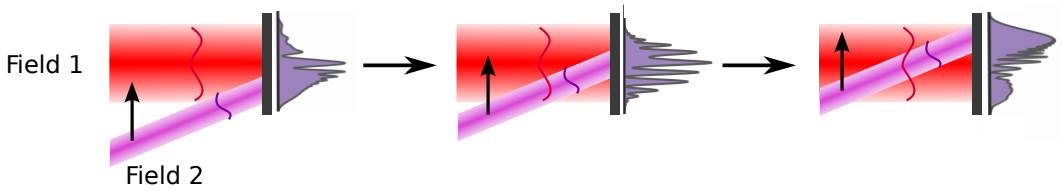

Figure 3.3: Schematic of the wavefront reconstruction along one axis. Both fields are aligned with a relative angle to each other, and Field 2 is sheared across the profile of Field 1.

the difference in k_x-vectors $\Delta k_x = k_{x,2} - k_{x,1}$ of the two beams, with a fringe spacing $2\pi/(k\sin(\theta)) = \lambda/\sin(\theta)$. In total, 16 x 16 spatial positions of Field 2 are considered on a 256 x 256 pixel detector. Interferograms for two different shears in the x- and y-direction are shown in figures 3.4(a) and (b). The original and reconstructed spatial intensity profiles and wavefronts are depicted in figure 3.5. It can be seen that, in spite of the highly complex structure of the fields, the reconstruction performs extremely well. Even the fine spatial features are accurately reconstructed. The small deviations from the original fields can be diminished by decreasing the shear step since this increases the redundancy in the data. Conversely, the upper limit on the shear step is given by the spatial extent of the smallest beam, Field 1, since consecutive interferograms need to have sufficient overlap.

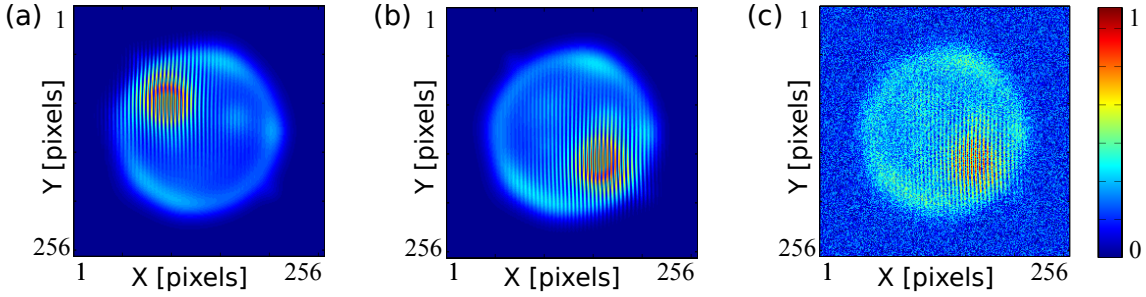

Figure 3.4: Interferograms between Field 1 and Field 2. (a) and (b) show interferograms for two different shears. (c) uses the same shear as in (b), but with 30% noise.

However, any electric field reconstruction method that is to be used in a real experimental setting needs to be tested under the presence of noise. In order to do so, uniformly distributed additive noise is added to each pixel of each interferogram. The noise level is given by a random number from the interval (0,1) times 30% of the maximum intensity of the most intense interferogram. An example is shown in figure 3.4(c). The reconstructed field for this case is shown in the right column of figure 3.5. Even in the case of such an extreme high-noise scenario the reconstruction for both the intensity profiles and the

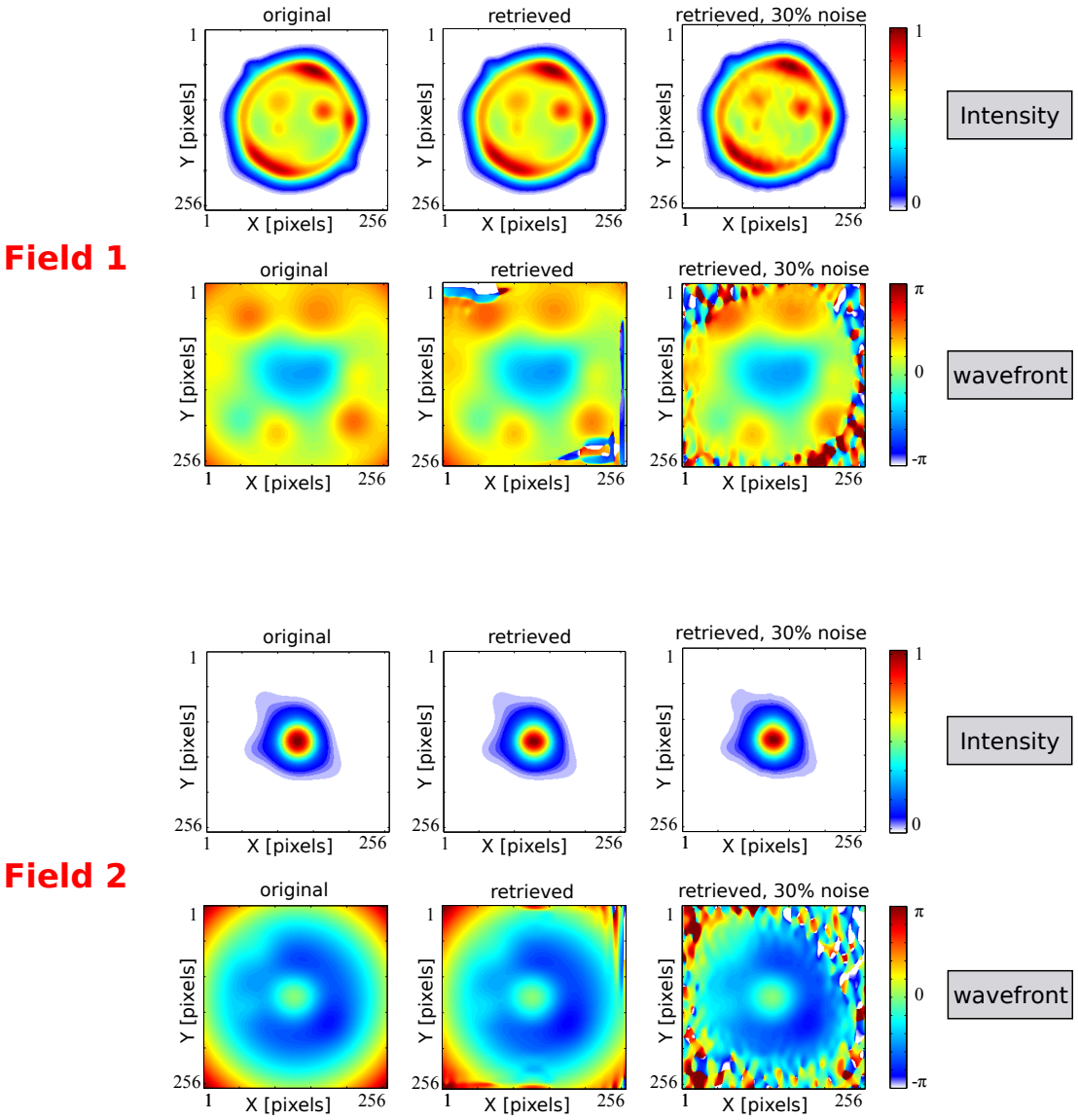

Figure 3.5: MICE two-dimensional spatial reconstruction of two independent and highly complex beams. Shown are the spatial intensity profiles (upper panels) and wavefronts (lower panels) for both beams, respectively. The left column represents the original fields and the middle column the reconstructed fields. In the right column, 30% noise has been added to each interferogram. The linear phase term has been removed for clarity.

wavefronts performs very well. The reason for this is that MICE combines advantages of both the interferometric method as well as of the generalised projections approach. In the first case, the Fourier-filtering suppresses noise. In the latter case, the least-squares minimisation acts as an additional noise filter. Overall, the MICE reconstruction is therefore able to cope with very noisy data.

3.4 Ultrashort pulse reconstruction using MICE

In this section, MICE will be demonstrated in an entirely different application. Experimental data will be used to reconstruct the temporal profiles of two infrared femtosecond pulses. To transpose MICE into the spectral domain, the ultrashort pulse must be sheared multiple times in the frequency domain. This is conveniently done in a single-shot way using techniques such as CAR-SPIDER [69] or spatially encoded arrangement (SEA-) CAR-SPIDER [135]. The MICE reconstruction in this section uses SEA-CAR-SPIDER data which was recorded by Tobias Witting and Dane Austin in this group at the University of Oxford before the author's arrival in Oxford. In the following, first the concept of SEA-CAR-SPIDER is explained in order to understand the nature of the experimental data used for the MICE reconstruction. Subsequently, a full MICE reconstruction is performed on this data. This is possible since any dataset in which one or both of the beams have been sheared in a given parameter space is suitable for MICE, as long as the beams overlap in this dimension. For more details about SEA-CAR-SPIDER, the reader is referred to the two SEA-CAR-SPIDER publications of the group [68, 135].

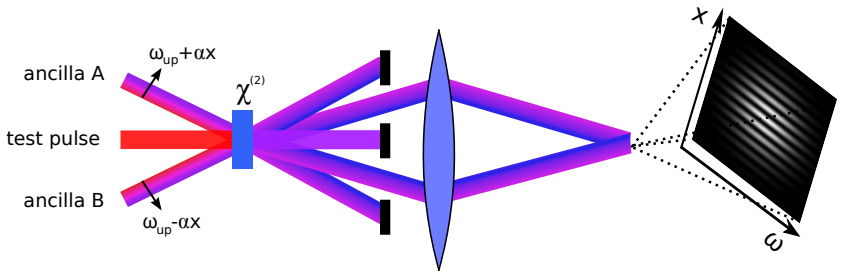

Figure 3.6: SEA-CAR-SPIDER concept. The test pulse is upconverted with two ancillas that are spatially chirped along the x-axis in a nonlinear crystal. The second harmonic upconverted beams are blocked, whereas the sum-frequency beams are re-imaged onto a 2D imaging spectrometer. The spectrometer slit is parallel to the x-axis, and the beams are spectrally dispersed along the orthogonal axis on the detector.

3.4.1 SEA-CAR-SPIDER and its data

SEA-CAR-SPIDER combines elements of SEA-SPIDER and CAR-SPIDER, both of which are described in section 2.4.3. The concept is depicted in figure 3.6. The test pulse is upconverted with two ancillary pulses in a nonlinear crystal. The ancillas have an opposite spatial chirp. Each spatial slice of the test pulse mixes with a monochromatic portion of the ancillary pulse. The ancillas can be generated in the following way: First, a copy of the test pulse is dispersed by a grating, which introduces a spatial chirp to the field with spatial chirp coefficient α. The spatially chirped field $E(\omega - \alpha x)$ is then duplicated by a beamsplitter. One of the two ancillary beams is laterally inverted along the x-axis by an odd number of reflections to form the field $E(\omega + \alpha x)$. After upconversion in the crystal, the sum-frequency fields between the test pulse and the two ancilla pulses are selected by a spatial mask and re-imaged onto the entrance slit of a 2D imaging spectrometer, which records the spectrally resolved interferogram:

$$S(\omega+\omega_{up},x) = |E(\omega+\alpha x)|^2 + |E(\omega-\alpha x)|^2 + 2\mathrm{Re}\left(|E(\omega+\alpha x)|\,|E(\omega-\alpha x)|\exp(i\Phi(\omega,x))\right) \tag{3.7}$$

$$\Phi(\omega,x) = \phi(\omega+\alpha x) - \phi(\omega-\alpha x) + k_x x + C(\omega), \tag{3.8}$$

where ω_{up} is the upconversion frequency common to both beams at $x = 0$ and $C(\omega)$ the zero-shear calibration phase. As in SEA-SPIDER, the two ancillas cross at an angle θ inside the crystal and therefore produce a spatial carrier in the recorded trace. The phase difference between the upconverted pulse (the *signal* pulse) and the spectrally sheared copy of itself is therefore encoded in the spatial interferogram. The advantage of spatially chirping the two ancilla pulses is, as in CAR-SPIDER, that several spectral shears can be recorded at the same time in a single interferogram. At a given point in the interferogram $x = x_0$, the effective spectral shear is $\Omega(x_0) = 2\alpha x_0$. In usual SEA-CAR-SPIDER, the different available shears across the beam can be used as a consistency check, since the temporal reconstruction should be unaffected by the shear. Moreover, if there is space-time coupling present in the beam, this technique can be used to measure the temporal field at different points in the beam to obtain quantitative information about it. Lastly, specific multishear-algorithms have been developed that use the redundant information contained in a measurement with several shears to increase the precision of the reconstruction [136].

The SEA-CAR-SPIDER reconstruction follows the following recipe: First, a 2D Fourier transform is performed and the positive AC sideband is isolated. After an inverse Fourier transform, the phase difference between the two signal pulses is given by the argument of the interferometric product. Before the integration step, the calibration phase needs

to be subtracted. This can be done at $x = 0$ where the shear is zero. The carrier term $k_x x$ represents a linear phase and plays no role in the reconstruction. As in the case of any SPIDER technique, the two signal pulses are assumed to be sheared replicas of each other. Thus the pulse spectral phase can be obtained by concatenation. An experimental demonstration of such a reconstruction, including a detailed error analysis, can be found in [135].

In the generalised case of MICE, this last assumption is dropped. Even if the pulses are different, both of them can be reconstructed. In the following MICE analysis, the two signal pulses of a SEA-CAR-SPIDER trace will be reconstructed. Due to the nature of any self-referencing technique, the temporal profiles of the two pulses are not expected to vary much from each other. However, imperfections in the setup or a possible change of the pulse spectrum or spectral phase with the shear can lead to different signal pulses for each shear and in this way compromise the accuracy of the reconstruction. To avoid such issues, in the next section the two-field MICE concept introduced in section 3.2.2 will be extended to three fields, where the third field quantifies the change of the pulse properties with the shear.

3.4.2 MICE reconstruction of three fields

In several experimental situations the pulse properties may change with the shear. For example, in the case of SEA-CAR-SPIDER, the upconversion process transfers the amplitude and phase properties of the monochromatic ancilla beam to the signal pulses $\mathcal{E}_{1,2}$. Since those properties can change significantly if many shears are utilised, this needs to be taken into account in the reconstruction. Mathematically, such a situation can be described by

multiplying the upconverted fields with a complex factor $a_{1,2}$ which depends only on the shear Ω, $\mathcal{E}_{1,2}(\omega - \Omega_{1,2}) \cdot a_{1,2}(\Omega_{1,2})$. Using the transformed variable $\omega - \Omega_1$, the product of the two fields appearing in equation (3.3) now takes the form $\mathcal{E}_1(\omega_j)\,\mathcal{E}_2^*(\omega_j - \Omega_k)\,\mathcal{A}(\Omega_k)$, where $\mathcal{A}(\Omega_k) = a_1 a_2^*(\Omega_1 - \Omega_2)$. Those modified fields are now used in equation (3.4), which is then differentiated with respect to the three fields. This results in a new set of equations:

$$\mathcal{E}_1(\omega_j) = \frac{\sum_k AC^{meas}_{j,j-k} \cdot \mathcal{E}_2(\omega_j - \Omega_k) \cdot \mathcal{A}^*(\Omega_k)}{\sum_k |\mathcal{E}_2(\omega_j - \Omega_k) \cdot \mathcal{A}(\Omega_k)|^2} \tag{3.9}$$

$$\mathcal{E}_2^*(\omega_j) = \frac{\sum_k AC^{meas}_{j+k,j} \cdot \mathcal{E}_1^*(\omega_j + \Omega_k) \cdot \mathcal{A}^*(\Omega_k)}{\Sigma_k |\mathcal{E}_1(\omega_j + \Omega_k) \cdot \mathcal{A}(\Omega_k)|^2} \tag{3.10}$$

$$\mathcal{A}(\Omega_k) = \frac{\sum_j AC^{meas}_{j,j-k} \cdot \mathcal{E}_1^*(\omega_j)\,\mathcal{E}_2(\omega_j - \Omega_k)}{\sum_j |\mathcal{E}_1(\omega_j)\,\mathcal{E}_2(\omega_j - \Omega_k)|^2} \tag{3.11}$$

As in the case of two fields, this system of equations can be solved iteratively. First, two randomly chosen fields for $\mathcal{E}_2$ and $\mathcal{A}$ are inserted into (3.9), which results in an estimate for field $\mathcal{E}_1$. The three fields are then successively updated by applying (3.10), (3.11) and (3.9).

Ambiguities

The adaptation of MICE to three fields leads to an additional ambiguity compared to the case of two fields: $\mathcal{E}_1(\omega)\,\mathcal{E}_2^*(\omega - \Omega)\,\mathcal{A}(\Omega) = \mathcal{E}_1 e^{\beta\omega} \cdot \mathcal{E}_2^* e^{-\beta(\omega-\Omega)} \cdot \mathcal{A} e^{-\beta\Omega}$, with β being a

complex constant. The real part of β defines the retrieved spectral densities up to an exponential factor. As in the case of the α-ambiguity, this can be resolved by separately measuring the spectra of each arm. The imaginary part of β has as a consequence that the spectral phases are known up to a linear term, i.e. an arbitrary delay. This is common to all pulse characterisation methods and does not affect the temporal pulse profile since an absolute time delay does not represent a meaningful quantity in terms of the pulse parameters. However, the relative delay between the fields is preserved.

3.4.3 Data processing

As a first step, the shear axis needs to be determined, a requirement common to all shearing interferometry techniques. To do so, each signal pulse was recorded separately, and a centre of mass fit results in the two shear axes. The individual chirped pulse spectra, together with their shear axes, are shown in figure 3.7.

Once this information has been determined, the interferogram can be processed. The raw interferogram is shown in figure 3.8(a). The fringe modulation appears along the x-axis. A 2D Fourier filter extracts the interferometric product, the modulus of which is

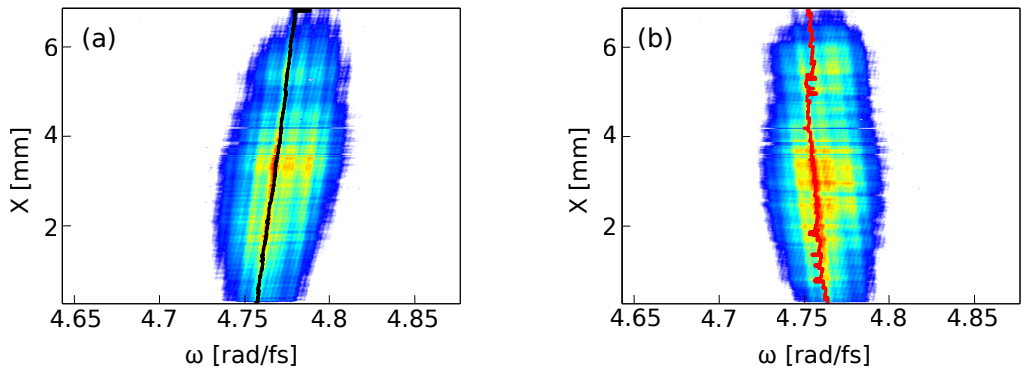

Figure 3.7: Shear calibration of the spatially resolved spectrum of the upconverted signal pulses. The shear axes are highlighted in (a) black and (b) red.

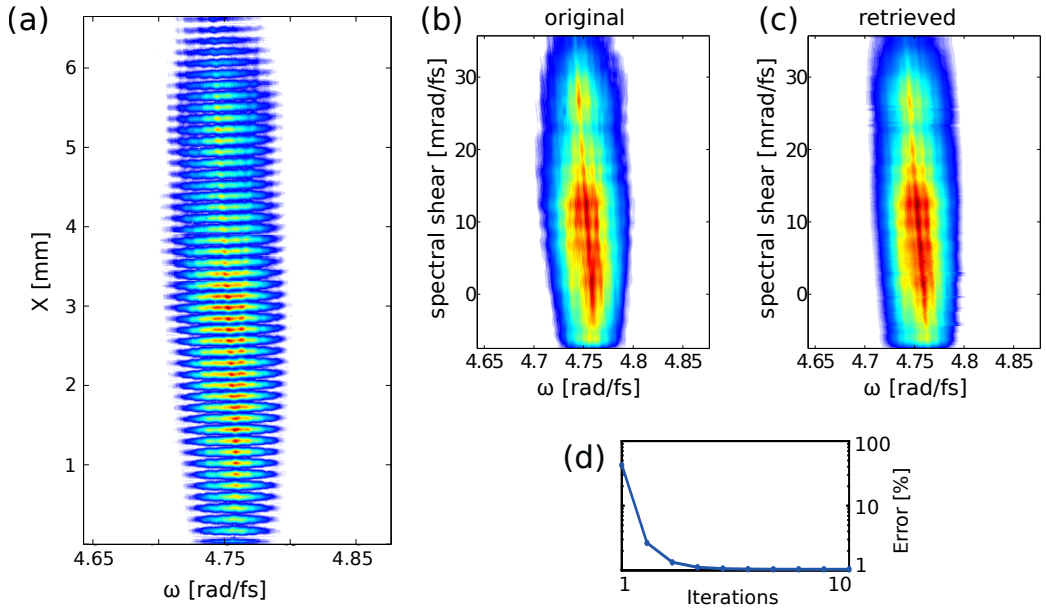

Figure 3.8: MICE data processing. (a) MICE interferogram between two spatially chirped signal pulses. Shown are also the moduli of the (b) original and (c) retrieved interferometric products. (d) Error between the original and retrieved interferometric products as a function of the number of iterations.

shown in figure 3.8(b). For comparison, figure 3.8(c) shows the retrieved interferometric product after 10 iterations of equations (3.9)-(3.11), which agrees well with the measured data. To quantify the difference between the measured and the retrieved quantities, the least-squares error ϵ has been introduced in equation (3.4). Figure 3.8(d) shows the normalised error $\epsilon/\Sigma_{j,k}|AC^{meas}|^2$ between the measured and retrieved interferometric products as a function of the number of iterations. As can be seen, the error decreases rapidly with increasing number of iterations. Indeed, after only three iterations, the error is below 2%.

The pulse spectra, averaged over 50 shots taken from each arm alone, and the reconstructed spectral phases of both pulses for 10 single-shot acquisitions are shown in figure 3.9(a). The shot-to-shot fluctuations are relatively low. The phases are nearly flat, indicating that the associated pulses have a duration close to the Fourier limit. The cor-

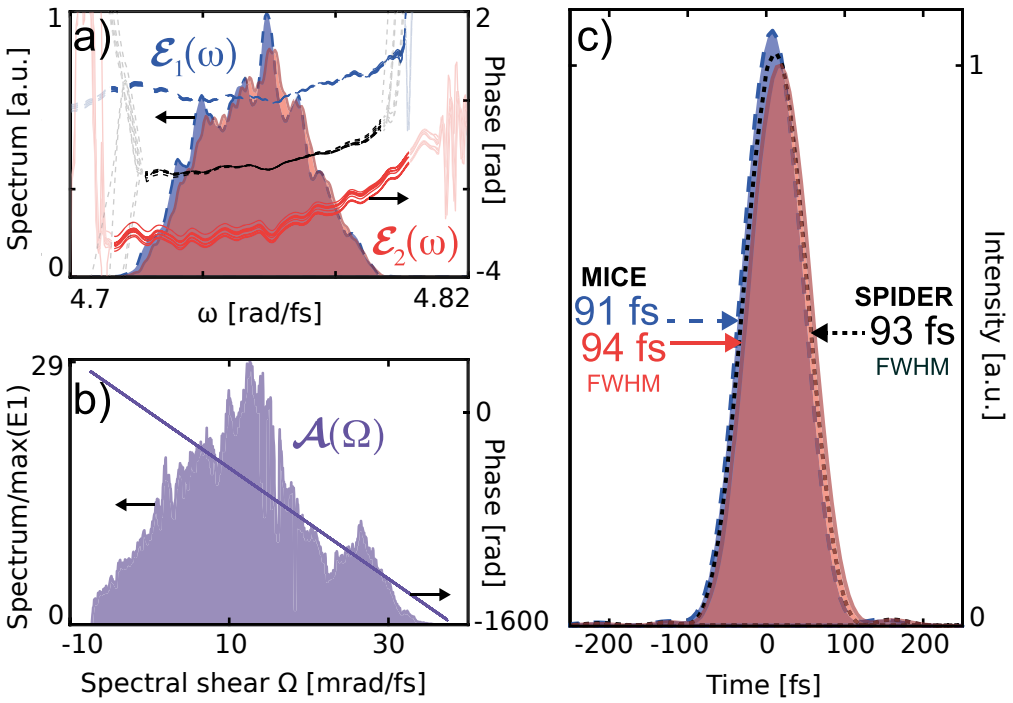

Figure 3.9: MICE reconstruction of two ultrashort pulses. (a) Spectra and spectral phases of fields $\mathcal{E}_1$ (dashed blue line) and $\mathcal{E}_2$ (red line) for 10 single-shot measurements. (b) Amplitude and phase of field $\mathcal{A}$. (c) Reconstructed single-shot temporal pulse profiles for $\mathcal{E}_1$ (dashed blue line) and $\mathcal{E}_2$ (red line). The black dotted lines stand for (a) the spectral phase, and (c) the pulse profile obtained with a standard SPIDER reconstruction.

responding reconstructed temporal profiles are shown in figure 3.9(c). It is obvious that the two pulses used to generate the SEA-CAR-SPIDER trace are almost identical. This is unsurprising since this represents a basic requirement for SPIDER to work. However, small differences in the pulse amplitudes, a delay of about 10 fs between the pulses as well as a difference in the pulse durations of 3 fs become apparent. This information has formerly been unaccessible via SPIDER. The third field $\mathcal{A}(\Omega)$ that only depends on the shear is depicted in figure 3.9(b). Its phase appears to be purely linear. This can be explained by the experimental arrangement in which the fringes are spatially encoded, and the shear varies linearly along the spatial axis.

For comparison, a SPIDER reconstruction on that same data has been performed using a small shear. The reconstructed spectral phase and pulse profile, indicated by black dotted lines in figures 3.9(a) and 3.9(c), are very close to the results obtained with MICE. This highlights the consistency of the MICE reconstruction.

Possible reasons for the difference in intensity of the two pulses could be slightly clamping the mirrors in the different arms of the interferometers with different strengths. Regarding the small residual time delay, the SEA-CAR configuration in principle guarantees the synchronisation in time of the two pulses. However, a slight asymmetry in the alignment of the different paths after the upconversion could account for the time delay of 10 fs, considering this corresponds to a path difference of 3 μm only. Finally, small errors in the calibration of the shear axes cannot be excluded as well.

3.5 Discussion and outlook

This chapter has introduced MICE, a novel technique that is able to simultaneously characterise two independent beams in any parameter space in which it is possible to shear one of the beams. It should be emphasised that, although this thesis mainly deals with ultrashort pulse measurements, in parts of this chapter the terminology "beam" has been used, to emphasise that MICE is not restricted to this domain alone.

Several assets make MICE preferential over conventional characterisation techniques. First, compared to SPIDER, no replica of the test pulse is needed. In addition, there is no need for a calibration of the linear carrier term, since no concatenation or integration of the phase is performed. Furthermore, in the domain of ultrafast science, MICE can be

used in a single-shot way if the fringes are resolved in additional dimensions, as shown in section 3.4 for SEA-CAR-SPIDER. Finally, the algorithm is rapid enough to allow it to be used as an online diagnostic in the laboratory. Those features make MICE well suited to a number of applications that are challenging for conventional FROG and SPIDER. For example, a matter of current research in our group is to use MICE in order to characterise pulses exhibiting large spectral gaps. Also, MICE can be transferred to completely different parameter regimes. In chapter 6, MICE is used to simultaneously characterise the wavefronts of two extreme-ultraviolet high harmonic sources.

Chapter 4

Generation and characterisation of high harmonic radiation

Most nonlinear phenomena can be described by perturbation theoretical calculations. Mathematically, this corresponds to expressing the polarisation of the medium by a power series

$$P(t) = \epsilon_0[\chi^{(1)}E(t) + \chi^{(2)}E^2(t) + \chi^{(3)}E^3(t) + ...] \tag{4.1}$$

Processes such as second harmonic generation or sum-frequency generation [137, 138] as well as phenomena that occur due to the intensity-dependent refractive index of some materials, such filamentation [139–142], self-phase modulation [143–145] or self-focusing [146], are all consequences of different terms in the polarisation (4.1). However, if the electric field becomes comparable to the atomic field strength,

$$E_{at} = \frac{1}{4\pi\epsilon_0}\frac{e}{a_0^2} = \frac{1}{4\pi\epsilon_0}\frac{e}{(4\pi\epsilon_0\hbar^2/m_e e^2)^2} \approx 5.1 \times 10^{11}\,\mathrm{V/m}, \tag{4.2}$$

the power series in (4.1) breaks down. Here, a_0 is the Bohr radius of hydrogen, e is the electron charge and m_e is the electron mass. The above field strength corresponds to a laser intensity of $I_{at} = 1/2\epsilon_0 c E_{at}^2 = 3.5 \times 10^{16}\,\mathrm{W/cm^2}$. Since the development of chirped-pulse amplifier (CPA) laser systems, this so-called *strong-field regime* became accessible at the laboratory scale [147–150]. Depending on the strength of the laser intensity, different scenarios may occur. Consider an electron bound in the ground state of a Coulomb potential. In argon, for example, this ionisation potential is $I_p = 15.8$ eV. If a strong light field irradiates the atom, this potential becomes distorted and the potential barrier is decreased. For very strong laser fields, this barrier is completely suppressed, and the electron is ionised (over-the-barrier ionisation) [151]. For fields that are weaker than the Coulomb barrier, two regimes can be distinguished, quantified by the Keldysh-parameter γ [152]:

$$\gamma = \sqrt{\frac{I_p}{2U_p}}. \tag{4.3}$$

U_p denotes the ponderomotive potential of the laser, which represents the average kinetic energy a free electron gains in a laser field of frequency ω and peak electric field E_{peak}, $U_p = e^2 E_{peak}^2/(4m_e\omega^2)$. For $\gamma > 1$, the ionisation can be described as a multiphoton process, where an atom or ion simultaneously absorbs N photons, with $N\hbar\omega > I_p$ and multiply charged ions can be created [153–156]. For $\gamma < 1$, the external laser field is strong enough to suppress the Coulomb barrier sufficiently so that the electron can be be released by tunnelling ionisation [157, 158]. For the types of experiments presented in this thesis, the laser peak intensity is on the order of 10^{14} W/cm^2, corresponding to $\gamma \lesssim 1$. One of the most prominent phenomena in this case is *high harmonic generation (HHG)*. HHG

is by far the most common scheme for the generation of attosecond pulses in table-top laboratory configurations. However, a few other schemes have been proposed. One method suggests using Raman scattering in a medium that acts as a molecular modulator [159]. An excitation pulse induces high-frequency oscillations of the refractive index of the medium due to the vibrational or rotational excitations. Those oscillations will imprint high-order Raman sidebands on a second field propagating through the medium. The overall bandwidth of this process may support few-femtosecond to sub-femtosecond durations [160]. In theory, this method offers the potential to produce isolated sub-femtosecond pulses in the visible or ultraviolet wavelength regime [161–164]. However, research in this area is still in its infancy.

Another strand of research is the coherent synthesis of pulses with spectra in different wavelength regimes [165, 166]. The prospect of coherently combining several pulses and the capabilities of shaping the waveforms of those individual components before the synthesis allows tailoring the resulting pulse with sub-cycle precision [167, 168]. The sub-cycle control of such waveforms has been used to trigger electron motion on sub-femtosecond timescales [165, 169].

Nevertheless, the most successful path in penetrating the attosecond domain has been via high harmonic generation. The first radiation of this type was observed from solid targets [170–172]. Only in the late 1980's, high harmonics from noble gases have been generated, which is the method still used in most laboratories today [173, 174]. The experiments for this thesis have been performed using argon gas cells. This chapter will therefore outline the underlying theory of HHG in rare gases. However, HHG has also been explored in a variety of other nonlinear media, such as HHG from molecules [175], bulk

crystals [176], clusters [177, 178], liquids [179, 180] and laser produced ablation plumes [181]. Finally it should be pointed out that with the recent progress in laser science and the continuous increase in laser power, high harmonics from solid targets have gained new interest again [182–185]. In these types of experiments a highly intense femtosecond laser (peak power typically 10^{18}-10^{20} W/cm^2) hits a polished surface and generates a plasma. The plasma effectively acts as a mirror and reflects the laser field. Its nonlinear response, however, leads to temporal distortions of the reflected wave, corresponding to a train of attosecond pulses [186]. Since the conversion efficiency is significantly higher than for HHG in gases, and since there is in principle no limitation to the applicable laser intensity[1], the generated harmonics can be much more intense than harmonics from gas media [187, 188].

4.1 Single-atom response

The HHG process is governed by two different mechanisms: The response of one single atom to the laser light, and the macroscopic response of all atoms within the interaction volume. In this section the theory of the single atom response is detailed. Section 4.1.1 describes the semi-classical model, which, despite its simplicity, provides a remarkably accurate description of many features of HHG. A quantum-mechanical treatment follows in section 4.1.2.

[1] The reason why there is a fundamental limit to the maximum driving laser intensity for HHG from gases is the onset of relativistic effects at intensities approaching 10^{18} W/cm^2. In this regime, the laser magnetic field can no longer be neglected. The associated force on the electron alters its trajectory and prevents it from recolliding with the parent ion.

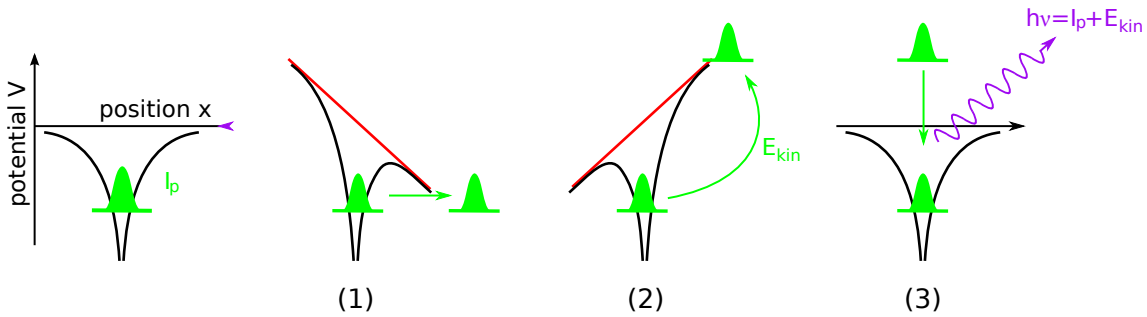

Figure 4.1: Three step model of high harmonic generation. Initially, the electron (green) is bound in the ground state of a Coulomb potential (black). (1) The linear laser potential (red) distorts the atomic potential such the electron may tunnel through the potential barrier. (2) The electron is accelerated in the continuum. When the electric field flips sign, the electron is driven back to the parent ion. (3) The electron recombines with the ion. As a result, a high-energy photon is emitted (purple) with an energy equal to the sum of the ionisation potential plus the electron kinetic energy.

4.1.1 Semi-classical treatment: Three-step model

Corkum has developed a powerful and intuitive semi-classical model of HHG which describes HHG in three steps [189]. Consider an electron in the ground state of a Coulomb potential $V_0 = -e/(4\pi\epsilon_0 r)$ at distance r from the nucleus, as schematically shown in figure 4.1. When an intense laser field of the form $E_0 \cos(\omega_0 t)$, assumed to be linearly polarised along the x-axis, interacts with the atom, the atomic potential becomes distorted, and the effective potential is the sum of the atomic potential and the laser potential,

$$V = \frac{-e}{4\pi\epsilon_0 r} + E_0 \cos(\omega_0 t) \cdot x. \tag{4.4}$$

As indicated in step (1) in figure 4.1, the atomic potential is lowered one side, which as a consequence increases the probability for the electron to leave the atom via tunnel ionisation. The electron subsequently enters the continuum, where the influence of the atomic potential is neglected. The electron is treated as a classical particle that is accelerated by

the oscillating laser field (step (2)). When the electric field changes sign, the slope of the potential is flipped and the electron is driven back to the parent ion, with which it may recombine (step (3)). In this case a photon is emitted, the energy of which is given by the sum of the ionisation potential and the kinetic energy the electron has gained in the continuum:

$$\hbar\omega = I_p + E_{kin}. \tag{4.5}$$

The energy of this emitted photon is typically in the extreme-ultraviolet to soft x-ray wavelength range. This process is repeated every half laser cycle. The spectrum of the emitted radiation thus consist of harmonics separated by $2\omega_0$. Due to the antisymmetry of the process, only odd harmonics occur.

The electron trajectory can be calculated by the classical equations of motion:

$$m_e\ddot{x}(t) = -eE_0\cos(\omega_0 t). \tag{4.6}$$

A solution to equation (4.6) can be found by assuming boundary conditions. First, the electron is taken to be located at the origin at the instant of ionisation t_i: $x(t_i) = 0$. Furthermore, it is assumed that the electron loses all its kinetic energy during the tunnelling processes, so that $\dot{x}(t_i) = 0$. Taking those conditions into account, the expression determining all possible classical trajectories is given by:

$$x(t) = \frac{eE_0}{m_e\omega_0^2}\cdot[\cos(\omega_0 t) - \cos(\omega_0 t_i)] + \frac{eE_0}{m_e\omega_0}\cdot\sin(\omega_0 t_i)(t - t_i). \tag{4.7}$$

The electron trajectories are plotted in figure 4.2 for different instants of ionisation. The

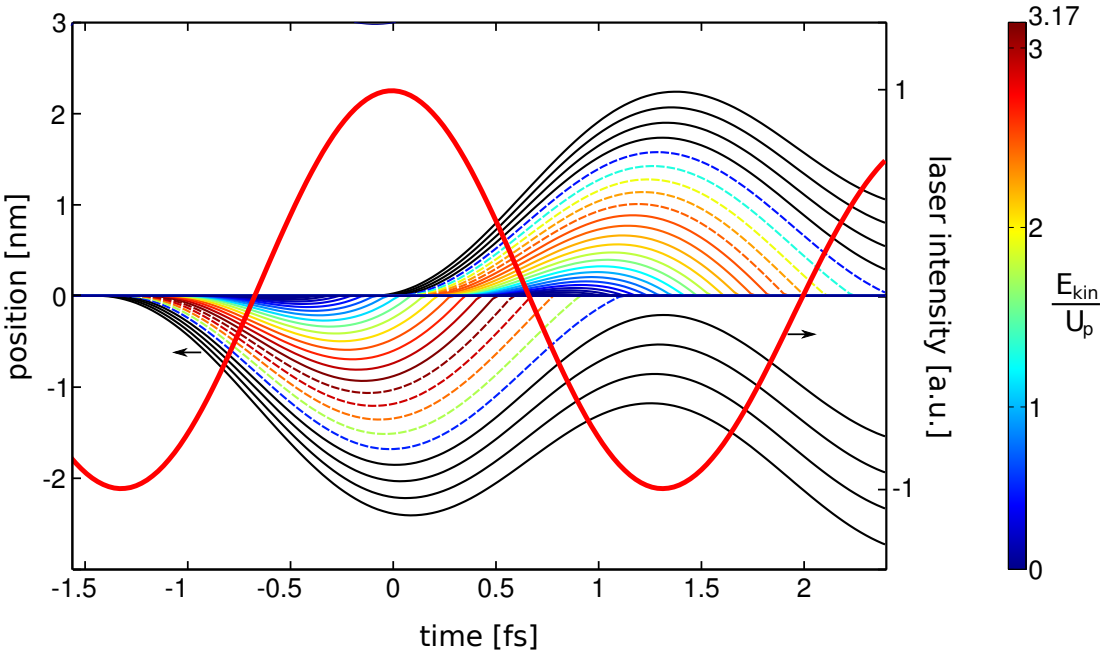

Figure 4.2: Classical electron trajectories for different ionisation times. Trajectories are shown for two half-cycle emissions driven by a laser with $I_{peak} = 1 \times 10^{14}\,\mathrm{W/cm^2}$ and $\lambda = 800\,\mathrm{nm}$. Solid coloured lines correspond to short trajectories, dashed lines to long trajectories. The colour of each trajectory represents the kinetic energy gain of the electron in the continuum. The black lines stand for trajectories where the electron does not recollide with the ionic core. Drawn in red is also the infrared driving field.

infrared driving laser ($\lambda = 800\,\mathrm{nm}$) has been simulated with a peak intensity of $I_{peak} = 1 \times 10^{14}\,\mathrm{W/cm^2}$. Depending on the ionisation time, the electron returns at different return times to the core with different energies. Two families of trajectories can be distinguished: Those that return very soon after the ionisation (short trajectories, solid lines), and those spending up to a full cycle in the continuum (long trajectories, dashed lines). The distance the electron is accelerated away from the core is decreasing with increasing ionisation time, and amounts up to 2 nm before the electron inverts its propagation direction. This amplitude can be significantly larger for higher intensities and longer wavelengths. The trajectory in between the two regimes (dark red) is the cutoff, where the electron gains the maximum kinetic energy $3.17\,U_p$. Finally, the black solid lines represent trajectories

where, after ionisation, the electron does not return to the nucleus. Hence they do not generate any harmonic signal.

4.1.2 Quantum treatment: The model of Lewenstein

The semi-classical model correctly predicts many features of HHG, such as the cutoff law and the ionisation and recombination times. However, there are important quantum mechanical effects that are not taken into account by this description. Examples include the quantum diffusion of wave packets, quantum interferences, the details of the tunnelling process or the emergence of frequencies beyond the cutoff. A full description must therefore be quantum-mechanical. Full quantum theories have been developed that aim at solving the time-dependent Schrödinger equation (TDSE), which in the length gauge and using the electric dipole approximation is given by [190–194]:

$$i\frac{\partial|\Psi(t)\rangle}{\partial t} = \left[-\frac{\nabla^2}{2} + V_0(x) + E(t)\cdot x\right]|\Psi(t)\rangle. \tag{4.8}$$

To ease the notation, atomic units are used ($e = m_e = c = \hbar = 1$). Even though this approach allows exact calculations, it is computationally very involved and needs long computation times even on modern computers. Lewenstein *et al.* have developed a quantum mechanical model, based on the strong field approximation (SFA), that is computationally less demanding and provides more physical insight [195]. It is based on three assumptions: (1) The contribution of all bound states other than the ground state can be neglected. (2) The depletion of the ground state can be neglected[2]. (3) When the

[2]This assumption is valid for intensities that are smaller than the saturation intensity.

electron is in the continuum, it can be described by the classical equations of motion and the influence of the atomic potential can be neglected. Assumptions (1) - (3) are generally valid for $\gamma < 1$. In that case, the expression for the time-dependent dipole moment, $x(t) = \langle \Psi(t)|x|\Psi(t)\rangle$, can be calculated according to[3]:

$$\vec{x}(t) = i \int_0^t \mathrm{d}t_i \int \mathrm{d}^3\vec{p}\ \cdot \vec{d}^*(\vec{p} + \vec{A}(t))\, \vec{E}(t_i) \cdot \vec{d}(\vec{p} + \vec{A}(t_i)) \exp[-iS(\vec{p}, t, t_i)] + c.c., \qquad (4.9)$$

where $\vec{p}$ it the canonical momentum with $\vec{p} = \vec{v} + \vec{A}(t)$, and $\vec{A}$ is the vector potential of the laser field. The exact form of the dipole matrix element depends on the atomic potential. A good approximation is the hydrogenic s-orbital,

$$\vec{d}(\vec{p}) = i \frac{8\sqrt{2}(2I_p)^{5/4}}{\pi} \frac{\vec{p}}{(p^2 + 2I_p)^3}. \qquad (4.10)$$

Expression (4.9) has an intuitive physical interpretation. The term $\vec{E}(t_i) \cdot \vec{d}(\vec{p} + \vec{A}(t_i))$ represents the probability amplitude that the electron is ionised at time t_i and enters the continuum state with the canonical momentum $\vec{p}$. Once in the continuum, the electron acts like a free particle and acquires the phase $e^{-iS(p,\vec{t,t_i})}$ between times t_i and t, where S denotes the quasi-classical action

$$S(\vec{p}, t, t_i) = \int_{t_i}^t \mathrm{d}t'' \left(\frac{[\vec{p} - \vec{A}(t'')]^2}{2} + I_p \right). \qquad (4.11)$$

[3]Note that, compared to the original paper by Lewenstein *et al.* [195] the signs in the arguments of the dipole matrix elements in equation (4.9) are flipped. Indeed, the Lewenstein paper erroneously considered an interaction term in the Hamiltonian written as $-E(t)x$, describing the behaviour of a positron rather than an electron.

Finally, the electron recombines with the parent ion at time t with the probability amplitude $\vec{d}^*(\vec{p}+\vec{A}(t))$.

In equation (4.9), an infinite number of electronic quantum paths between t_i and t contribute [196]. However, since over one laser field period the quasi-classical action varies much faster than the other factors in (4.9), only those paths will contribute where the phase is stationary:

$$\nabla_{\vec{p}} S(\vec{p}, t, t_i) = 0. \tag{4.12}$$

Since equation (4.12) is equal to the difference of the positions of the free electron for times t and t_i, $\nabla_{\vec{p}} S(\vec{p}, t, t_i) = \vec{x}(t) - \vec{x}(t_i)$, only those momenta $\vec{p}$ contribute where the electron is born at time t_i and returns to the same position at time t. Given that this position needs to be close to the origin such that the transitions to and from the ground state can occur, the Lewenstein model justifies one of the assumptions of the semi-classical model, $x(t_i) = 0$. Each pair of ionisation and recombination times (t_i, t) defines the corresponding canonical momentum, which is found by integration of equation (4.12),

$$\vec{p}_s = -\frac{1}{t - t_i} \int_{t_i}^{t} \vec{A}(t')\mathrm{d}t'. \tag{4.13}$$

The integral over $\vec{p}$ in equation (4.9) can then be simplified using a saddle-point method, which yields for the electric dipole moment:

$$\vec{x}(t) = i \int_0^\infty \mathrm{d}\tau \left(\frac{\pi}{\epsilon + i\tau/2}\right)^{3/2} \vec{d}^*(\vec{p}_{st}(t,\tau) + \vec{A}(t))\, \vec{d}(\vec{p_{st}}(t,\tau) + \vec{A}(t-\tau)) \tag{4.14}$$

$$\times \vec{E}(t-\tau) \exp[-iS(\vec{p}_{st}, t, t_i)] + c.c., \tag{4.15}$$

where the factor containing an infinitesimal ϵ is a regularisation constant related to quantum diffusion, and $\tau = t - t_i$ is the time spent in the continuum. Quantum diffusion is related to the spread of the electron wave packet in the continuum. A large spread reduces the recombination probability, which results in a negligible contribution from return times τ that are much larger the one laser cycle.

Further physical insight can be gained by applying the saddle-point technique to the action S. Differentiation of equation (4.11) with respect to $\vec{p}$, τ and t leads, besides to (4.12), to two further equations:

$$\frac{[\vec{p}_{st}(t,\tau) - \vec{A}(t-\tau)]^2}{2} + I_p = 0, \tag{4.16}$$

$$\frac{[\vec{p}_{st}(t,\tau) - \vec{A}(t)]^2}{2} + I_p = \omega_k. \tag{4.17}$$

Equation (4.16) is related to the semi-classical assumption that the electrons born with zero velocity have the largest contribution to the harmonic emission. However, this equation is only solvable if the electron is taken to have a negative kinetic energy at time $t - \tau$ to tunnel through the Coulomb barrier. The excursion time τ is then complex, where the imaginary part can be interpreted as the tunnelling time. Measuring the tunnelling time experimentally is an active field of current research [197–199]. Finally, (4.17) corresponds to the energy conservation law, where the energy w_k of a given harmonic is the sum of the electron kinetic energy plus the ionisation potential.

The quantum-mechanical Lewenstein model therefore confirms the assumptions and conclusions of the semi-classical model. In fact, both models predict for the location of

the cutoff of the harmonic spectrum[4,5]:

$$E_{cutoff} = I_p + 3.17\,U_p. \tag{4.18}$$

Furthermore, from the single-atom theory it follows that among all possible trajectories, there are two types of trajectories that contribute most to the harmonic emission: The long and the short trajectories. This distinction is made on the basis of the differences in trajectories of the electron in the continuum. For long trajectories, the electron can spend up to a full optical cycle $\tau_c \simeq 2\pi$ in the continuum, whereas the duration is much shorter for short trajectories. As highlighted above, the behaviour of the electron in the continuum can be described by the quasi-classical action (4.11), which gives rise to the atomic dipole phase.

4.1.3 Atomic dipole phase

Consider the expression for the atomic dipole given in equation (4.9). By calculating its representation in the Fourier domain and selecting a single quantum path with parameters (p, t_i, t_r) for harmonic order q, the dipole phase can be written as

$$\Phi_a = q\omega t_r - \frac{S(p, t_i, t_r)}{\hbar}. \tag{4.19}$$

The first term arises due to the delay between the times of ionisation t_i and recombina-

[4]The cutoff law has been modified to correct for certain effects such as tunnelling and quantum diffusion [195], propagation effects in a tight focusing geometry [200], or HHG from mid-IR wavelength laser sources [201].

[5]In contradiction to the semi-classical cutoff-law, harmonics with energies below the ionisation potential have been recently reported [202, 203]. This is due to an enhancement of the harmonics near atomic resonances.

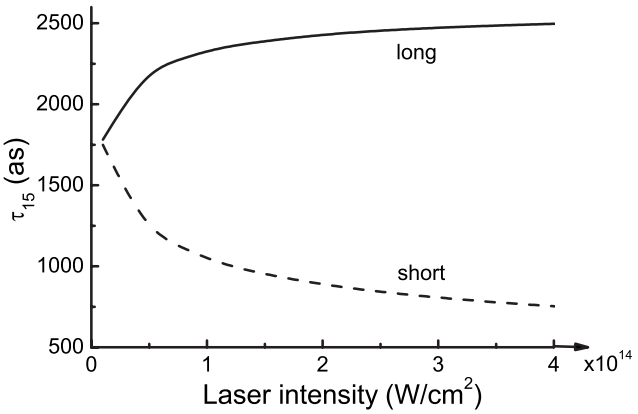

Figure 4.3: Dependence of the electron excursion time τ on the laser peak intensity for harmonic 15 for the short and the long trajectories. Figure taken from [204].

tion t_r. The second term is the phase accumulated in the continuum between the ionisation and recombination times. The action itself can be approximated by $\tau_c U_p$, where τ_c is the time spent in the continuum [195, 205]. Since $U_p \propto I$, the atomic dipole phase is linearly proportional to the laser intensity. Furthermore, τ_c is larger for long trajectories than for short trajectories. One can therefore write for the dipole phase for harmonic q:

$$\Phi_a = \Phi_q^{l,s}(x,t) = -\alpha_q^{l,s} I(x,t). \tag{4.20}$$

In (4.20), α is a proportionality constant that is related to the excursion time τ_c and is therefore different for long (l) and short (s) trajectories. The excursion times of both trajectories are very different for lower harmonic orders (plateau region). For increasing orders, they become more and more equal, until they finally merge in the cutoff. The same reasoning can be made with respect to the laser intensity, as illustrated in figure 4.3. For low intensities, a given harmonic will be in the cutoff, and the excursion times (or equivalently, the α-coefficients) for both trajectories have similar values. For increas-

ing intensities, the harmonic moves to the plateau region, and the properties of the two quantum paths become more and more different.

4.2 Macroscopic response

To simulate high harmonic generation more realistically, the single atom response may not be sufficient, since instead of considering only one atom, the coherent superposition of the emission of all atoms or molecules in the interaction volume needs to be taken into account. This then results in the overall macroscopic response of the medium. A full theoretical simulation involves first calculating the single-atom response for a suitable set of parameters, which is followed by propagating the laser field and the harmonic field through the medium using Maxwell's equations. A more direct and intuitive way to estimate the efficiency of the generation process is the model developed by Balcou *et al.* which is based on wave vector conservation [206]. Compared to perturbative nonlinear optics such as second harmonic generation, in HHG there is an additional momentum contribution originating from the electron's sojourn in the continuum, making the phase-matching of high harmonics a more complex matter. It is instructive to first only consider one-dimensional phase-matching along the propagation axis before proceeding to the more general case.

On-axis phase-matching

Perfect phase-matching occurs when the phase mismatch $\Delta\vec{k}$ between the induced polarisation and the generated field is zero. In this case all emitters contribute coherently to the harmonic field. Optimal phase-matching can usually only be achieved over a finite medium

length L, as will be shown below. It is therefore convenient to introduce the coherence length $L_{coh} = \pi/|\Delta\vec{k}|$, which quantifies the length over which the generated field and the induced polarisation are dephased by π. Only regions with large coherence lengths will significantly contribute to the harmonic signal. Phase-matching in the direction $\vec{k}_q$ is then achieved for

$$\vec{k}_q = \vec{\nabla}\Phi_{pol}, \tag{4.21}$$

where Φ_{pol} is the phase of the total polarisation of the medium. Different contributions need to be considered in this regard. For the sake of clarity, first only on-axis phase matching contributions along the z-axis are taken into account. In the simplified case of phase-matching of a plane wave in the perturbative regime (such as SHG), the q-th harmonic with wave vector k_q and $|\vec{k}_q| = q\omega/c$ would be perfectly phase-matched for $k_q = qk_0$, with $k_0 = \omega/c$ [207]. In the case of HHG, however, the situation becomes more complicated for several reasons. First, the focusing of the beam results in an additional Gouy phase:

$$\Phi_G = -\arctan\frac{z}{z_R}. \tag{4.22}$$

The wave vector of the fundamental beam $\vec{k}_1$ then reads:

$$\vec{k}_1(r,z) = k_0\vec{e}_z + \vec{\nabla}\Phi_G. \tag{4.23}$$

A second phase contribution comes from the atomic dipole phase. Since the intensity $I(z)$ is varying with z, the dipole phase follows the same dependence. For a Gaussian beam

this takes the form:

$$I(z) = \frac{I_0}{1 + 4z^2/b^2}. \tag{4.24}$$

The effective wave vector for the dipole phase then follows as

$$\vec{k}_a(r, z) = \vec{\nabla}\Phi_a(r, z). \tag{4.25}$$

Depending on the experimental configuration and the parameters chosen, further contributions may occur. One example is dispersion caused by neutral atoms or by ionisation of the medium. The latter typically becomes important if the laser intensity is larger than the saturation intensity, $I > I_{sat}$. In some experiments, high harmonics are generated in gas-filled hollow-core fibres [208–212]. Despite the fact that an additional source of dispersion, waveguide dispersion, comes into play in those systems, very high conversion rates have been demonstrated, in particular when using quasi-phase-matched capillary sources [213–217]. For clarity, in the following only the geometric phase and the dipole phase are considered.

The polarisation phase resulting from the propagation through a medium along the z-axis, as well as the individual components, are drawn in figure 4.4 for harmonic 29 for typical experimental parameters ($I_{peak} = 2 \times 10^{14}$ W/cm^2, $\omega_0 = 30\,\mu$m, $\lambda = 800\,$nm, $\alpha = 10 \times 10^{-14}$ cm^2/W). It can be seen that the phase variation across a medium of the length of a few mm is very large. More precisely, for negative z, which refers to a position of the medium before the laser focus, the phase varies very rapidly since the atomic dipole phase and the geometric phase add up to large phase values. In contrast, when the medium

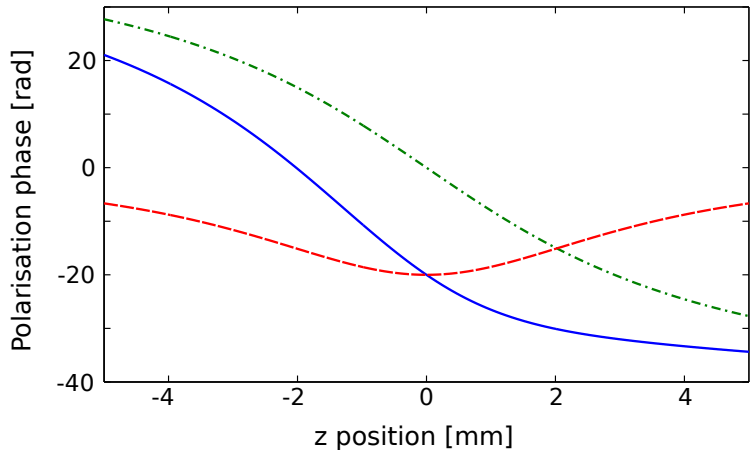

Figure 4.4: HHG on-axis phase matching. The total polarisation phase (solid blue) is the sum of the Gouy phase (dash-dotted green) and the atomic dipole phase (dashed red).

is placed after the focus, the dipole phase and the Gouy phase almost cancel out, and the phase variation is much less dramatic. Therefore, efficient *on-axis* phase-matching can be achieved in the latter case. This result explains the origin of short trajectories, which are generated on-axis with the medium place after the focus. However, since the laser beam and the medium have a spatial extent, *off-axis* phase-matching becomes possible as well.

Off-axis phase-matching

A more realistic study needs to take into account the radial extension of the laser and the source. The condition for phase-matching of HHG thus becomes a vector sum of the different contributions:

$$\vec{k}_q = q\vec{k}_1 + \vec{\nabla}\Phi_a(r,z). \tag{4.26}$$

The different components to the polarisation phase are drawn figure 4.5, this time however including the radial dimension. Figure 4.5(a) shows the geometric phase due to focusing, and 4.5(b) illustrates the atomic dipole phase. Whereas the first always has a component

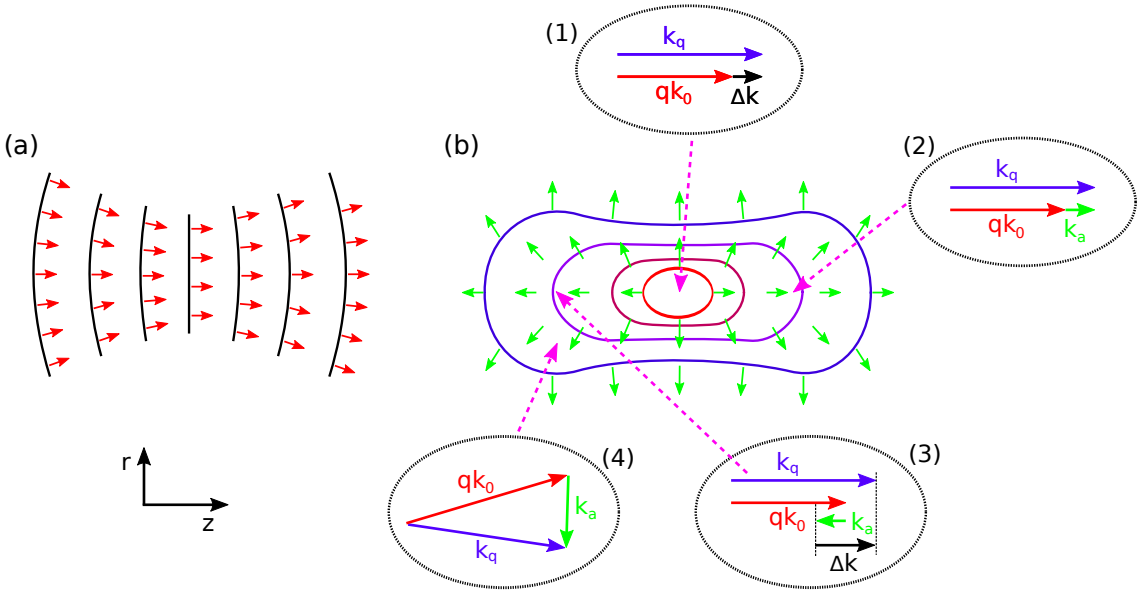

Figure 4.5: Phase-matching model of HHG. The laser beam is propagating along the z-axis to the right. (a) Wave vector (red arrows) $\vec{k}_1$ of the fundamental Gaussian beam due to focusing. (b) Map of the atomic dipole phase wave vector (green arrows) $\vec{k}_a$. Also shown are the contours of constant intensity. Different phase-matching scenarios are shown for situations where the medium is located (1) at the focus, (2) on-axis after the focus, (3) on-axis before the focus, and (4) off-axis before the focus. (2) gives rise to efficient generation of short trajectories, (4) of long trajectories.

in the propagation direction of the laser beam, the latter points away from the focal point. The effective phase mismatch can be evaluated using vector diagrams, as shown in figure 4.5(b). The properties from collinear phase-matching discussed above are reproduced by the corresponding diagrams, where the dipole phase acts favourably to the phase-matching if the medium is placed after the focus (position (2)), and increases the phase mismatch for a medium positioned before the focus (position (3)). Even though the peak intensity is the highest at the focal point, the phase mismatch reduces the harmonic conversion efficiency (position (1)). Counterintuitively, this position is therefore not the best to achieve the strongest harmonic signal. However, in addition to on-axis locations, now off-axis phase-matching is possible as well. This is indicated in position (4), where perfect phase-matching can be achieved by a non collinear arrangement of the wave vectors. The

harmonics generated in this way are the long trajectory harmonics.

The phase-matching model presented here is very intuitive and explains one of the most fundamental properties of the different quantum trajectories [206]: Short trajectories are generated on-axis and form a smooth, Gaussian-type spot. In contrast, long trajectories are generated off-axis in a ring around the laser axis and diverge much faster than the short trajectories. Consequently, the generated harmonic field takes an annular shape.

4.3 Characterisation of attosecond pulses

The characterisation of XUV attosecond pulses represents a formidable task. Due to the exotic wavelength and the brevity of the pulses, the number of optics available is very limited. Indeed, there is no nonlinear crystal for the XUV, and XUV optics are usually quite lossy, expensive and with limited spectral response. However, as it is detailed in this section, it is still possible to transfer a few concepts from IR femtosecond pulse characterisation to the attosecond regime.

4.3.1 Temporal metrology using photoelectrons

One of the earliest attempts to characterise XUV pulses was by intensity autocorrelation, where the non-resonant two-photon ionisation of Helium served as the nonlinear signal generating the autocorrelation trace [218]. Besides the disadvantage of the low signal strength, this method only provided an estimate of the pulse duration. The most widespread and reliable complete characterisation techniques of XUV attosecond pulses rely on photoelectron spectroscopy [219]. Here, an XUV field ionises an atomic gas in the

presence of a perturbative infrared field. Once the ionised electrons are in the continuum, the effect of the IR field is to act as a phase modulator[6] and alter the electron trajectory. In the single active electron approximation, the probability amplitude $a_{\vec{p}}(\tau)$ for the transition of the electron from the ground state to the continuum state $|\vec{v}\rangle$ with velocity $\vec{v}$ and kinetic energy W is obtained by solving the Schrödinger equation in the strong field approximation and is given by:

$$a_{\vec{v}}(\tau) = -i \int_{-\infty}^{+\infty} e^{i\phi_{IR}(t)} \vec{d}_{\vec{p}}(t) \vec{E}_{XUV}(t-\tau) e^{i(W+I_p)t} \, \mathrm{d}t, \tag{4.27}$$

where $\vec{p}(t) = \vec{v} + \vec{A}$ is the instantaneous momentum of the free electron in the continuum under the influence of the vector potential $\vec{A}$, τ is the time delay between the IR and XUV fields and $\vec{d}_{\vec{p}}(t)$ is the dipole matrix element of the transition. I_p is the phase accumulated by the ground state electron until ionisation at time t. Most importantly, the temporal phase imposed onto the free electron by the IR field is

$$\phi_{IR}(t) = -\int_{t}^{+\infty} \vec{v} \cdot \vec{A}(t') + \vec{A}^{\,2}(t')/2 \, \mathrm{d}t'. \tag{4.28}$$

When the infrared field is not present, the amplitude and phase properties of the XUV field are directly related to the ones of the photoelectrons. There is, however, an additional contribution to the photoelectron spectrum and phase that arises from the atoms. These properties are tabulated for many cases and can therefore be taken into account in the analysis. The XUV spectrum can thus be deduced from the photoelectron spectrum. The

[6] In the language of ultrashort pulse characterisation, the IR field takes the role of the time nonstationary filter [220].

main challenge consists in recovering the phase information from the photoelectrons. For this aim, the phase modulation of the photoelectron spectrum by the IR field needs to be exploited. Consider the case when the XUV pulse is much shorter than the period of the IR field. Figure 4.6(a) shows the scenario where the XUV pulse is coinciding with the far tails of the IR pulse. Here the IR field strength is essentially zero and no phase modulation occurs. In figure 4.6(b) and (d), the XUV pulse is temporally overlapping with a zero crossing of the electric field. In this region, the cosine-field is approximately linear. As described in section 2.2.1, a linear temporal phase leads to an overall shift in the frequency domain. Depending on whether the XUV pulse coincides with the rising or the falling slope of the IR field, the photoelectron spectrum is shifted in opposite directions. In contrast, if the delay between the two fields is chosen such that the XUV pulse is synchronised with the peak of the IR field (figure 4.6(c) and (e)), the temporal phase is approximately quadratic. As a consequence, the spectrum is temporally chirped. An example of a full streaking trace is shown in figure 4.6(f).

In summary, the photoelectron spectrum directly maps the XUV spectrum, where the process of using an IR field as a probe field is sensitive to the phase of the XUV pulse. Different experimental implementations have been developed that exploit these phenomena.

Attosecond streak camera

The attosecond streak camera makes use of the temporal phase modulation by the IR field (figure 4.6(c) and (e)) [23, 221–223]. Its effect on the photoelectron spectrum can be understood as follows: If the XUV pulse is Fourier transform limited, the temporal

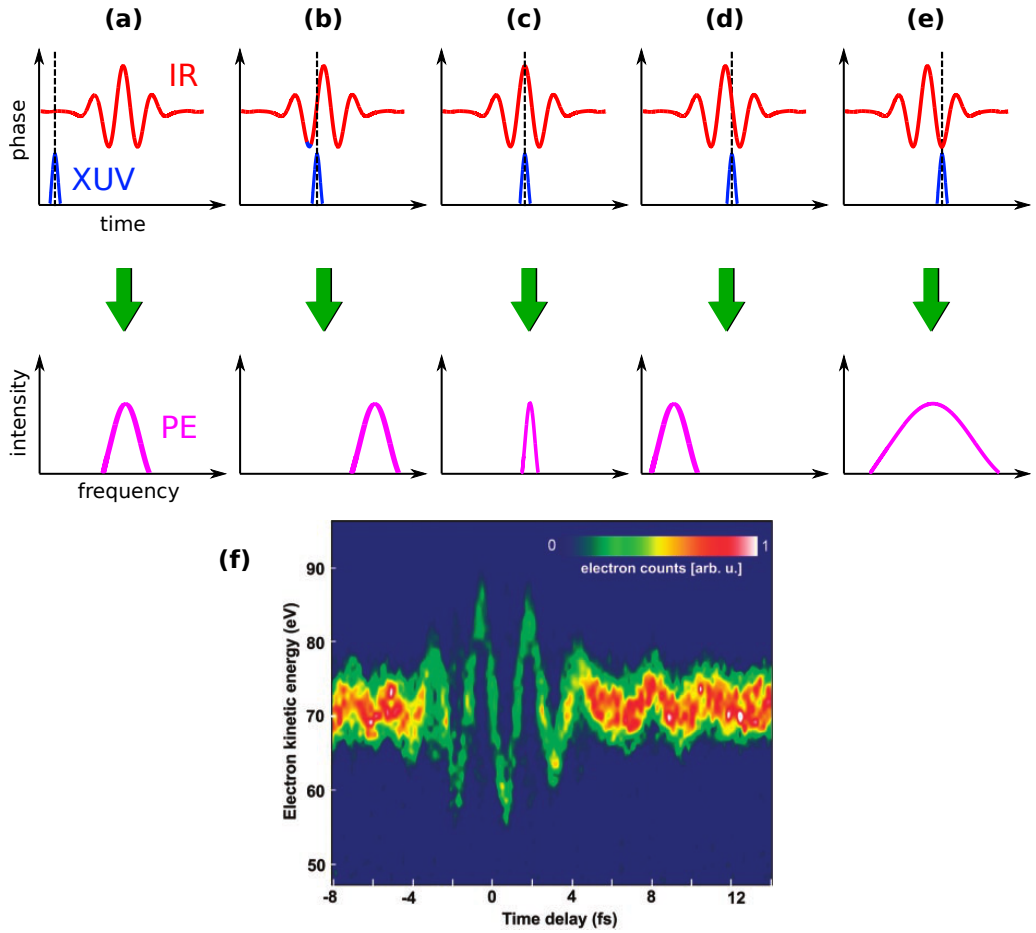

Figure 4.6: Streaking of an attosecond pulse (blue) with an infrared femtosecond field (red). Top row: Synchronisation in time between the two fields. Second row: Corresponding Fourier width of the photoelectron spectrum. (f) Example of a photoelectron spectrogram. A 250 as pulse is being streaked by a 750 nm IR field with duration <5 fs. The spectrogram maps the vector potential of the IR field. Spectrogram taken from [131].

stretch introduced by two subsequent peaks of the phase modulator (relative phase shift of π) will be identical. If, however, the XUV pulse is initially already positively chirped, then one peak will add more positive chirp and therefore broaden the photoelectron spectrum, whereas the subsequent peak will, due to the opposite sign of the quadratic phase, compensate for the initial chirp and therefore reduce the spectral bandwidth. By scanning the relative delay and evaluating the different spectral widths, the GDD can be recovered.

The attosecond streak camera only works with isolated attosecond pulses that are much shorter than the infrared pulse. To increase the temporal resolution, high laser intensities and large carrier frequencies of the phase modulator are beneficial.

RABBITT

A different parameter regime to the attosecond streak camera corresponds to the case when the XUV pulse is longer than the electric field period, and the dressing field intensity is around one to two orders of magnitude lower than in the streaking regime ($10^{10} - 10^{11}\,\mathrm{W/cm^2}$). In this case the oscillatory dressing field creates sidebands in the photoelectron spectrum, which originate from two-photon transitions from two consecutive odd harmonics [224]. If the dressing field has the same frequency as the beam generating the harmonics, these sidebands will be located equidistantly between neighbouring harmonics at the location of even harmonics. In one case, an electron absorbs an harmonic photon of order $(2q-1)$ and an additional IR photon from the weak dressing field. Hence its final energy is $(2q-1)\hbar\omega_{IR} + \hbar\omega_{IR} - I_p$. In the other case, an electron absorbs a harmonic photon of order $(2q+1)$ and emits an IR photon, leading to the same final energy $(2q+1)\hbar\omega_{IR} - \hbar\omega_{IR} - I_p$. Both paths therefore lead to the same energy state and interfere. By scanning the delay between the XUV and the dressing field, this interference results in a modulation of the sidebands, the phase of which depends on the relative phase between the two harmonics. This measurement thus yields the group delay of different harmonics forming a pulse train. This technique is called RABBITT[7] [225–227] and was the first to characterise the amplitude and phase of a group of 5 harmonics, with each pulse of the

[7] Resolution of Attosecond Beating By Interference of Two-photon Transitions

train having a duration of 250 as [22]. Note that since RABBITT relies on the two-photon interference of neighbouring harmonics, it is not applicable to isolated attosecond pulses.

FROG-CRAB

FROG-CRAB[8] transfers the tools from infrared femtosecond FROG to the attosecond regime [228]. In fact, by recalling equation (4.27), the photoelectron spectrum as a function of W and τ can be seen as a spectrogram,

$$S(W,\tau) = |a_{\vec{v}}(\tau)|^2 = \left| \int_{-\infty}^{+\infty} e^{i\phi_{IR}(t)} \vec{d}_{\vec{p}}(t) \vec{E}_{XUV}(t-\tau) e^{i(W+I_p)t} \mathrm{d}t \right|^2 . \tag{4.29}$$

By identifying $P(t)$ with the electronic wave packet $\vec{d}_{\vec{p}}(t)\vec{E}_{XUV}(t)$ and the gate function $G(t)$ with $e^{i\phi(t)}e^{iI_p t/\hbar}$, equation (4.29) takes the form of a general FROG trace:

$$S(W,\tau) = \left| \int_{-\infty}^{+\infty} P(t-\tau) G(t) e^{iWt/\hbar} \mathrm{d}t \right|^2 . \tag{4.30}$$

The PCPGA procedure from conventional FROG can therefore be applied to such a trace for the reconstruction (see section 2.4.2 for details). In fact, using the general blind-FROG approach allows the reconstruction of both the attosecond pulse as well the gate function, from which the infrared field can be recovered. FROG-CRAB represents the most generally applicable complete attosecond pulse characterisation technique today and does not require any prior knowledge of the relative durations or relative intensities of the two pulses. For these reasons it has become the most widespread characterisation method for attosecond pulses.

[8] Frequency-Resolved Optical Gating for the Complete Reconstruction of Attosecond Bursts

Photoelectron interferometry

In addition to the above time-frequency domain techniques, it has been proposed to transfer spectral interferometry into the XUV, in particular by using the concept of SPIDER that is well-established in the femtosecond domain. A direct application of SPIDER to photoelectron spectroscopy has been proposed for the case where the XUV pulse duration is long compared to the laser field period [229]. Two time-delayed XUV pulses are focused with a chirped optical pulse into a gas target. In analogy to the generic SPIDER, each XUV pulse interacts with a quasi-monochromatic frequency slice of the chirped pulse. In this manner two frequency-shifted but otherwise identical photoelectron wave packets can be created and then spectrally interfered. At this stage the standard SPIDER reconstruction procedure can be used to recover the phase of the XUV pulse.

A related approach has been proposed by Quéré *et al.* for the case where the XUV pulse is much shorter than the laser field period [230]. Two XUV pulses are focused into a gas target together with the laser field. Depending on the temporal synchronisation of the XUV pulses with the optical field, an energy shift will be applied to each pulse. As it was demonstrated in figure 4.6, by synchronising the XUV pulse with a zero crossing of the laser field, the XUV spectrum can be shifted independently of the photoelectron energy.

Both of these techniques benefit from the general advantages of interferometry, such as a fast and direct reconstruction of 1D datasets. However, drawbacks are that a photoelectron spectrometer with a high spectral resolution is required. Furthermore, the task of generating two identical XUV fields and as a consequence two frequency sheared but

otherwise identical photoelectron wave packets is very challenging. In fact neither method has been demonstrated experimentally to date.

4.3.2 All-optical characterisation

Even though characterisation methods using photoelectron spectroscopy are the most common techniques for attosecond pulse metrology, they come with significant drawbacks. First, the experimental apparatuses are very complex. In addition, for the recording of a spectrogram, many measurements are needed due to the low signal-to-noise ratio, requiring long measurement times. As a consequence, an excellent stability of the setup is very important. However, since the measurement is multi-shot, it is prone to the inevitable shot-to-shot fluctuations of the input field. Moreover, the extension to spatio-temporal characterisation is not possible since photoelectron spectra are spatially averaged over the interaction volume. Several efforts have therefore been undertaken for the development of all-optical characterisation methods.

XUV SPIDER

In XUV SPIDER, the idea is to measure the phase directly from the interferogram of the harmonic fields [231]. In this regard two different geometries have been proposed. In the spectrally encoded version, two collinearly aligned and time-delayed IR pulses are focused into the gas target where they generate two time-delayed XUV pulses. The need to introduce a spectral shear to one of the pulses is transferred from the harmonic field to the driving laser: An acousto-optic programmable dispersive filter (AOPDF) may be used to create spectrally sheared but otherwise identical femtosecond pulses. If the IR

pulses are generated with a spectral shear $\delta\omega$, the shift of the two generated harmonic spectra of order q will be $q\delta\omega$. The pulse phase is encoded in the spectral interferogram, where the time delay acts as a carrier. The standard SPIDER algorithm is then used to recover the phase. Even though this scheme has not been demonstrated to measure the phase of several harmonics or an isolated attosecond pulse, Mairesse *et al.* were able to characterise the phase of harmonic 11 using this technique [232]. One limitation of this scheme is that for high intensities the gas medium is ionised by the first pulse, which may result in different generation conditions for the second pulse. This problem can be avoided in the spatially encoded configuration, where the two driving beams are separated in space without any time delay. Due to a relative tilt between the two arms, two spatially separated high harmonic sources are formed in the medium, which in the far-field create a spatial interferogram. The SEA-SPIDER reconstruction algorithm can then be used to recover the electric field. The spatially encoded arrangement not only avoids the generation of the two harmonic fields in the same region of the gas medium, but also relaxes the constraints on the required spectral resolution, since the fringes are now resolved in the spatial domain.

Spatio-temporal in situ characterisation

Recently, Kim *et al.* have for the first time demonstrated an all-optical spatio-temporal characterisation of an isolated attosecond pulse [233]. The experiment is done *in situ*[9] by perturbing the HHG process using a weak secondary beam, chosen to be the second harmonic of the driving laser, that is aligned at an angle with the fundamental beam. The

[9] i.e. at the location where the pulse is generated

perturbing field alters the electron trajectories during the HHG process, which leads to a change in the propagation angle and the divergence of the high harmonic emission. By scanning the delay between the two laser fields, the resulting trace allows the reconstruction of the spatio-temporal XUV field. The same technique has also been used to measure the waveforms of few-cycle pulses for different CEP values [133].

4.3.3 Wavefront characterisation of HHG

A few techniques have been developed in recent years to spatially characterise high harmonic radiation. In direct analogy to the visible and near infrared wavelength regime, point diffraction interferometry (see section 2.5.2) has been used to characterise high harmonics by using a thin Al-foil with a small pinhole in the centre [234]. In a different application, a Hartmann sensor has been used, consisting of a hole array that is, in analogy to the Shack-Hartmann sensor in the visible range, probing the local tilt of the wavefront by measuring the deviation of the positions of the individual spot centroids from the reference positions [235, 236]. The main disadvantage of both techniques is that they average over all frequencies in the XUV beam, which masks some important features when dealing with ultra-broadband attosecond pulses. In contrast, SWORD[10] is a spectrally resolved characterisation method based on diffraction on a slit placed between the source and an XUV imaging spectrometer [237, 238]. The slit is scanned across the beam profile and 2D diffraction images are recorded each time. Since the centroids of the diffraction patterns depend on the slope of the wavefront at each slit position, the wavefront can be recovered by such a measurement.

[10]Spectral Wavefront Optical Reconstruction by Diffraction

A different slit diffraction based method is SCIMITAR[11], which uses diffraction by a pinhole pair formed by an arrangement of slits [239]. The pinhole separation can be varied continuously, and the resulting interferometric data allows the extraction of the wavefront as well as some information on the spatial coherence of the XUV beam. However, techniques involving the use of diffraction slits select only part of the wavefront and thus require long integration times and therefore high stability of the setup.

Methods based on the interference of two XUV sources avoid this issue and typically offer a higher resolution than slit diffraction experiments. One example is XUV lateral shearing interferometry [240]. The experimental setup is similar to the one shown in figure 6.1. Two spatially separated XUV sources are generated by the driving laser and a replica of it, both of which are aligned with a tilt relative to each other. The spectrally resolved XUV interferogram is measured on a spatially resolving spectrometer. If a lateral shear is applied to one of the arms, the gradient of the spatial phase becomes encoded in the fringe separation of the interferogram. Even though this technique benefits from the typical advantages of interferometry, the requirement of replicating and shearing the test beam can be experimentally very challenging.

4.4 Outlook

High harmonic generation has been extremely successful for over a decade in providing access to attosecond dynamical processes in a table-top laboratory environment. Its properties are well described by the semi-classical model, according to which an electron in the atomic ground state undergoes tunnel ionisation into the continuum where it is accel-

[11] SCanning Interference Measurement for Integrated Transverse Analysis of Radiation

erated by the laser field. Due to the oscillating field it may return to the ionic core and recombine. As a consequence a high energy photon is emitted. A full quantum treatment describes the atomic dipole moment as a sum over different quantum paths, in analogy to Feynman's path integral approach. The phase accumulated along one path is given by the quasi-classical action and can be approximated by the product of the ponderomotive energy U_p and the electron excursion time τ_q, $\phi_q^{l,s} \approx -U_p\tau_q^{l,s} \approx -\alpha_q^{l,s}I$. The phase is therefore linearly proportional to the laser intensity. When taking the emission of all atoms or molecules within the interaction volume into account, it turns out that only two categories of trajectories significantly contribute to the harmonic signal, the long and the short trajectories. The following chapter is dedicated to experiments characterising these macroscopic features. The detection of spatial signatures of the different quantum paths provides great information about the fundamental generation process. In addition, the measurement of the α-coefficients gives direct access to the sub-cycle electron dynamics.

Chapter 5

Experiments studying the macroscopic response of HHG

The single-atom theory describes HHG in three steps: (1) Tunnel ionisation of a ground-state electron, (2) Acceleration of the free electron in the continuum by the laser field, (3) Recombination with the parent ion, in the process of which a high-energy photon is emitted. Depending on the ionisation time with respect to the laser field, the electron can follow different trajectories in the continuum. In the single-atom picture, a multitude of trajectories with different phases and final kinetic energies contribute to the harmonic emission. The interference of all the different quantum paths results in very complex harmonic spectra. However, both theory and experiments have shown that by only taking the two main contributions into account, the harmonic spectra are reproduced with striking accuracy [196, 205]. Due to their different properties, the influence of the different trajectories can be both beneficial or detrimental to experiments [21, 227, 241]. Understanding the origin and properties of the two main families of trajectories therefore constitutes a

major cornerstone of attosecond science based on high harmonic generation.

The remainder of this thesis is dedicated to the development of tools and methods characterising high harmonic radiation with the aim of studying the fundamental generation process. Particular attention will be given to the properties of long and short trajectories. In order to do so, in the course of this thesis a complete high harmonic beamline has been designed and built from scratch. The first part of this chapter is dedicated to the description of the different elements of this setup, which can broadly be divided into the optical setup and the vacuum apparatus. The second half of this chapter describes how the apparatus has been tuned and optimised to efficiently generate and detect long and short trajectories. The setup offers control over all key parameters regarding the generation process, which is then utilised to study the characteristics of the two quantum trajectories as well as interferences between them. Finally, the developed expertise is used to directly measure the atomic dipole phase.

5.1 Experimental beamline for high harmonic generation

This section describes the experimental apparatus used for all XUV experiments in this thesis. An overview of the full optical setup is shown in figure 5.1. One centrepiece is the high power laser system. A commercial Ti:sapphire based CPA laser[1] produces pulses with a duration of ∼30 fs at a centre wavelength of $\lambda_0 = 800$ nm. Several diagnostics to measure the CPA output are in place. A point-lock system stabilises the beam pointing

[1] Oscillator: KMLabs Ti:sapphire Griffin (max. 3 nJ, 12 fs, 80 MHz), pumped by Verdi V6 Nd:YVO_2 pump laser (532 nm, cw, max. output 6 W).
Amplifier: KMLabs Dragon CPA (max. 3 mJ, 1 kHz), pumped by Photonics Industries DM30-527 Nd:YLF pump laser (527 nm, max. 30 mJ, 1 kHz).

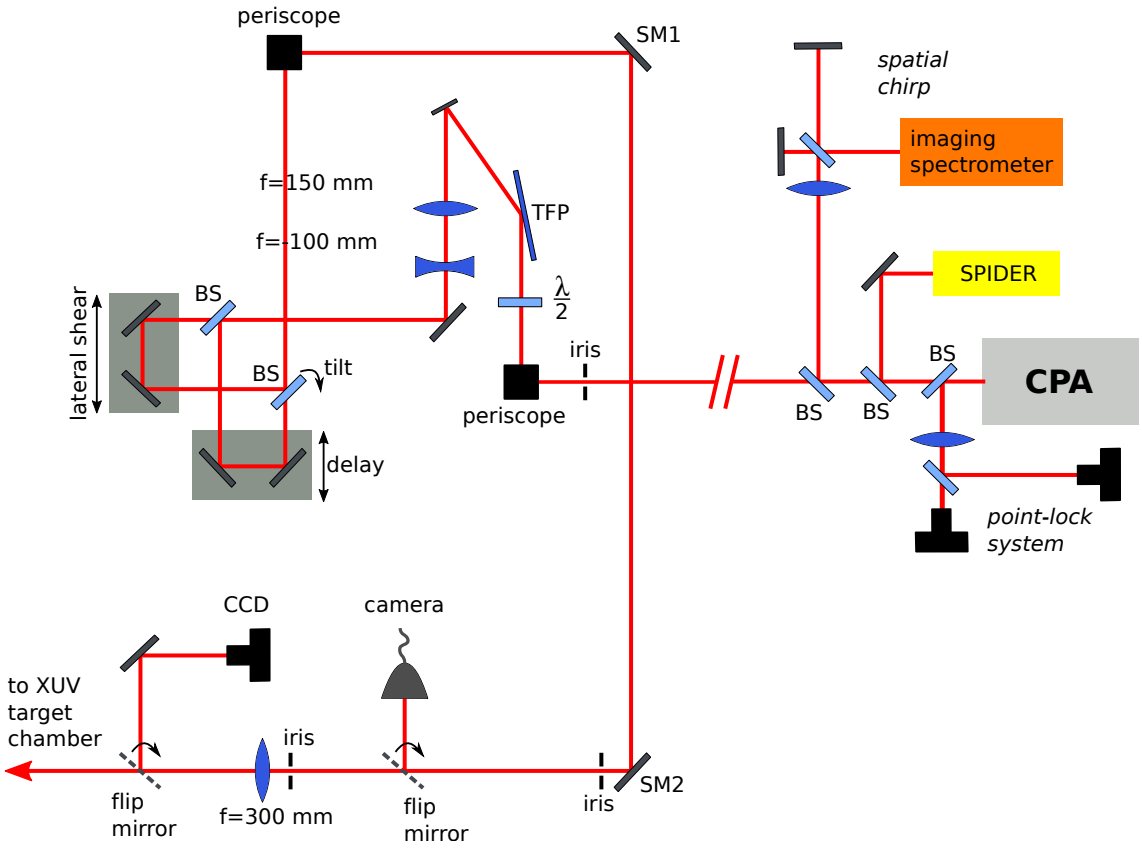

Figure 5.1: Layout of the full optical apparatus. The CPA output is diagnosed by SPIDER to monitor the temporal pulse duration. A point-lock system is used for beam pointing stabilisation and an interferometer and imaging spectrometer measure the spatial chirp along one axis. An iris is used as a main reference for the daily alignment of the laser beam to the XUV part of the setup. A half-waveplate, followed by a thin-film polariser (TFP), are used for continuous adjustment of the laser intensity. The subsequent telescope allows collimation of the beam. The beam then enters a Mach-Zehner interferometer where delay, tilt and lateral shear can be individually adjusted. Two steering mirrors (SM1 and SM2) are then used to align the laser into the vacuum apparatus with the help of two alignment irises. An imaging setup has been installed for the alignment of the two output beams of the interferometer, as well as for imaging of the laser foci.

using reference positions in the near- and far-field. The spatial chirp along one axis can be measured by using an unbalanced interferometer (to produce near- and far-field beam profiles on the spectrometer slit) which is followed by an imaging spectrometer. Finally, the pulse duration can be monitored by means of a generic SPIDER. However, since the beam passes through a few optics in transmission between the laser and the location of the XUV generation, the effective pulse duration at the HHG target will be longer

than the one measured directly at the output of the CPA. Fine-tuning of the CPA pulse compression is therefore done by observing the harmonics and optimising the harmonic yield in real-time. This is done by adjusting the distance between the two gratings of the CPA compressor, which changes the chirp of the pulse. The beam with pulse energy of 1 mJ then propagates to the XUV side of the laboratory. A $\lambda/2$ waveplate followed by a thin-film polariser in reflection act as a variable attenuator. Since the output of the CPA exhibits some divergence, a telescope ($f_1 = 150$ mm, $f_2 = -100$ mm) is used to collimate the beam. The beam then enters an interferometer allowing the adjustment of all degrees of freedom necessary for the XUV experiments.

5.1.1 Interferometer

A Mach-Zehnder-type interferometer, shown in figure 5.1, creates two identical replicas of the input pulse. A nano-positioning stage[2] allows the control of the relative delay between the two pulses to attosecond precision. The mirror pair in one arm can be moved perpendicularly to the incoming beam propagation axis by a motorised translation stage, which has the effect of applying a lateral shear to the beam. A relative tilt between the two beams can be applied by tilting the second beamsplitter in the interferometer. This creates spatial fringes in the far-field with an easily adjustable fringe separation. Due to the symmetry of the setup, the two beams exiting the interferometer should be identical. However, it was found that even small asymmetries in the two arms of the interferometer, e.g. due to small wavefront distortions introduced by the optics inside the interferometer, can create an asymmetry between the two arms. In fact, even when the two IR foci

[2]P-753.3CD, Physik Instrumente GmbH

inside the XUV chamber look identical when imaged onto a CCD, they may still produce harmonics with slightly different harmonic profiles and divergences. For the experiments in chapter 6 this does not represent a problem, since XUV MICE does not require the beams to be identical and can in fact be used to measure those differences. The measurement of the correlation function performed in chapter 7, however, does require identical beams. Great care needs to be taken on the mounting of the optics and the alignment of the interferometer to assure perfect symmetry in this case.

5.1.2 Focusing and foci imaging

All experiments performed in this thesis are based on interferometry between two spatially separated high harmonic sources. These sources are generated by focusing the two output arms of the interferometer into an argon gas target. If the two interferometer arms are aligned collinearly, both infrared beams are focused to the same focal spot. However, if the last beamsplitter is slightly tilted, the foci become spatially separated. Focusing is achieved using an f = 300 mm achromatic lens. Even though one can readily switch to lenses with longer focal lengths, the 300 mm lens has been chosen as the shortest focal length possible such that the lens is still outside the vacuum chamber. This is to ensure a tight focus in order to minimise the interaction between both sources. It is important to monitor and adjust the focal positions as well as to measure the focal spot sizes. For this reason the foci are imaged onto a CCD camera, as indicated in figure 5.1. By using a flip mirror before the vacuum chamber, the same focusing lens is used than for focusing into the vacuum chamber, ensuring reliable imaging of the focal spots as they appear inside the chamber.

In order to minimise external sources of decoherence, the full optical setup between the CPA and the input of the vacuum chamber has been enclosed. In addition, care was taken to minimise vibrations originating from the vacuum pumps. Those measures led to reasonably good stability of the XUV interferograms, which is important when averaging over multiple shots is needed due to low signal strength.

5.1.3 XUV apparatus - overview

The full vacuum apparatus for high harmonic generation is shown in figure 5.2. It consists of a XUV generation chamber and the XUV spectrometer. Both vacuum chambers are pumped by turbo molecular pumps[3]. Operation of the XUV detector which is based on microchannel plates (MCP) requires the pressure inside the spectrometer chamber to be below 10^{-6} mbar. With gas load, the pressure in the target chamber is between 10^{-3} mbar and 10^{-2} mbar. A small pinhole with diameter 1 mm is placed between the two chambers in order to enable differential pumping. The XUV generation in the target chamber and the XUV detection in the spectrometer are described in the following two sections.

5.1.4 XUV generation

The gas target for HHG is mounted on a manual x-y-z translation stage, allowing the full control of the target position relative to the laser focus. Different target designs are available. The first type of target falls into the category of continuous-flow targets. A Nickel tube is mounted on a Swagelok fitting that is attached to the gas feedthrough. The target hole is drilled by the focused laser itself. Advantages of this design are that the

[3]Oerlikon Leybold Vacuum TURBOVAC MAG W 300P, backing pump SCROLLVAC SC 5 D.

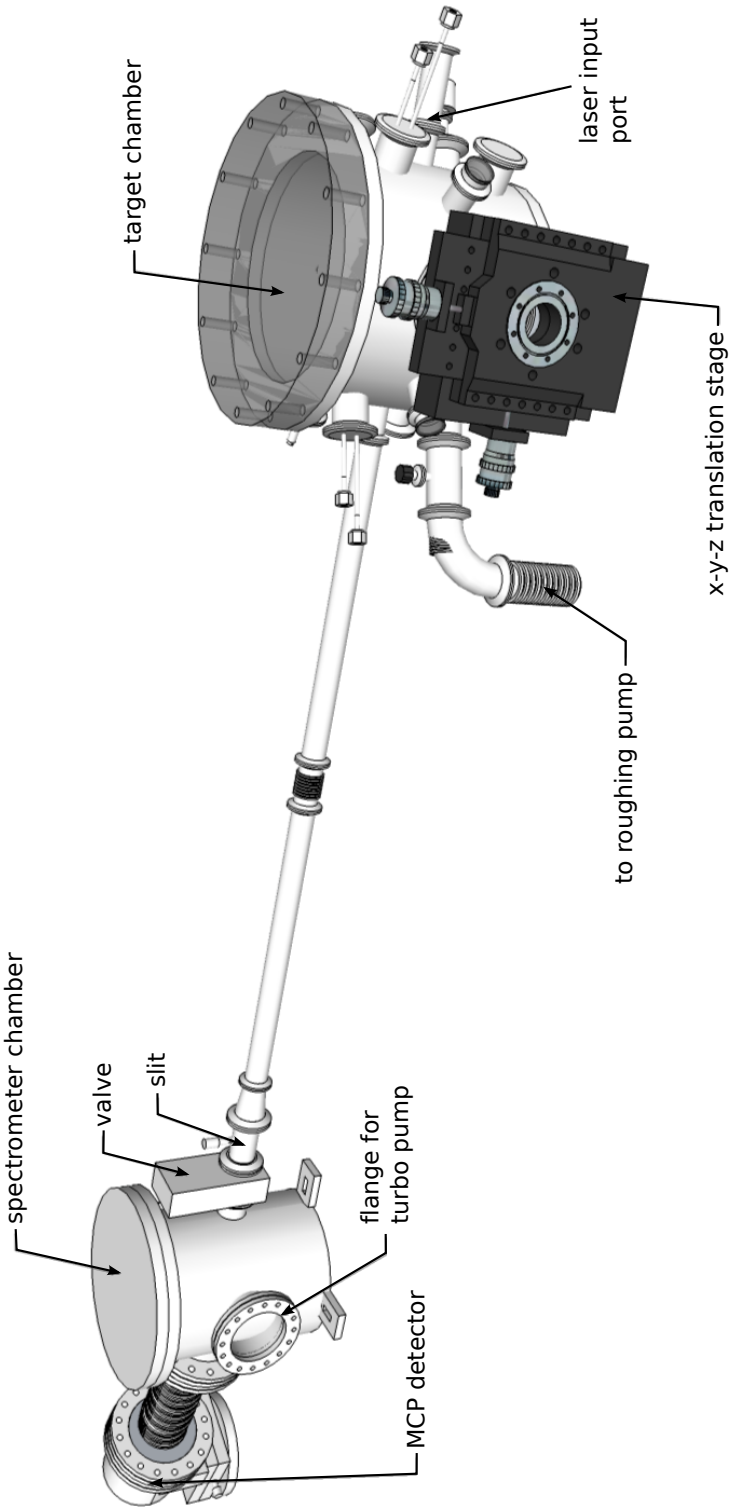

Figure 5.2: Full XUV apparatus. The laser beam propagates from the right to the left, entering the target chamber through an input window. It is then focused into a gas target, the position of which can be fully controlled via a manual x-y-z translation stage. The beam then propagates to the spectrometer. It is diffracted off a grating inside the spectrometer chamber, and the spatially resolved spectrum is measured by an MCP detector. A small slit can be placed at the entrance of the spectrometer to increase the spectral resolution.

targets are cheap, easily replaceable and, by squeezing the tube to the desired thickness, customised interaction lengths can be achieved.

The second target type is a piezo-driven pulsed gas valve[4] [242]. A piezo-driven poppet periodically opens and closes the gas inlet to release short bursts of gas. Due to the non-continuous gas flow, the pulsed gas valve can produce high gas densities by still keeping the overall gas load rather low. The piezo is triggered by the CPA laser. Exact synchronisation with the laser at the location of the gas target is achieved using a digital delay generator[5]. Backing pressures of 1-5 bars are usually applied to the valve. Different target designs are available for the pulsed valve. The gas jet can either be directed in propagation direction of the laser ("T"-shape) or perpendicularly to it ("I"-shape or conical design), each with different hole dimensions. For all main experiments performed in this thesis, the pulsed valve has been used as a gas target with a "T"-shaped target of length 3 mm and hole a diameter of 500 μm. As HHG gas species, argon was used throughout at a typical backing pressure of 3.5 bar.

5.1.5 XUV spectrometer

The high harmonics are detected by an XUV flat-field spectrometer. At the heart of the spectrometer lies an aberration-corrected concave grating from Hitachi[6]. Its technical specifications are summarised in appendix C. The grating has a nonuniform line-spacing and forms an aberration-corrected flat-field image at the detection plane [243–245]. It is curved in one dimension, along which the light "sees" the grooves of the grating and hence

[4] Attotech GR001
[5] Stanford Research Systems DG535
[6] Hitachi model 001-0640

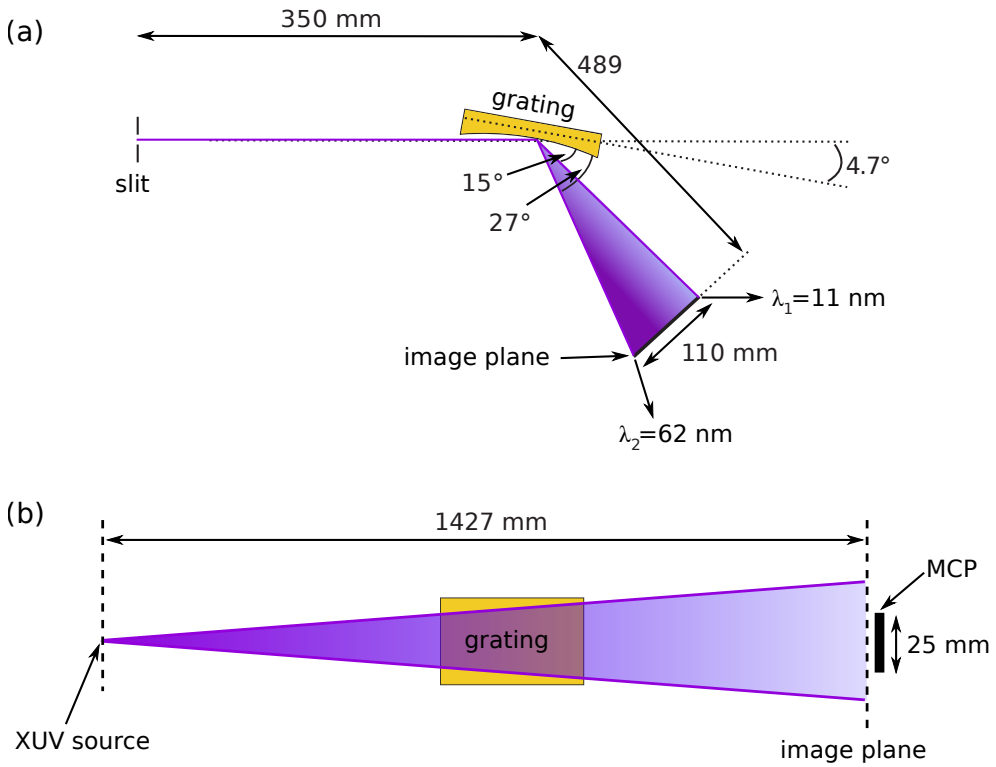

Figure 5.3: Geometry of the XUV spectrometer. (a) The concave aberration-corrected grating has a varied groove spacing and creates a flat-field image at the image plane for the indicated parameters. The desired range of harmonic orders is selected by adjusting the camera position along the image plane. (b) The grating is flat in the other direction, and therefore simply acts as a grazing-incidence reflector.

is spectrally dispersed. Along the perpendicular axis the grating just acts like a mirror and reflects the incoming light at grazing incidence. The light therefore just experiences natural diffraction between the source and the detector. Those two geometries are drawn in figure 5.3 (a) and (b), respectively, along with an indication of the relevant distances and angles. For experiments where high spectral resolution is required, a diffraction slit may be placed at the entrance of the spectrometer. Since this was not crucial for the experiments in this thesis, and since a slit would block the majority of the XUV flux, no spectrometer slit was used for the experiments presented here.

The full spectrometer setup is shown in figure 5.4. The XUV light is finally detected

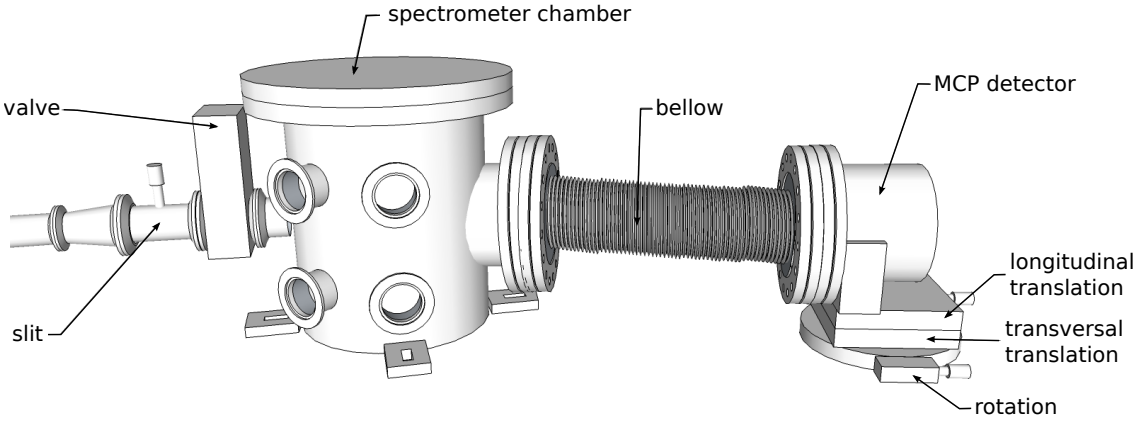

Figure 5.4: XUV spectrometer apparatus. The XUV grating is mounted inside the vacuum chamber. The MCP detector can be rotated and moved along the longitudinal direction to put the MCP in the image plane. The transversal position can also be adjusted to select the desired harmonic window. The spectrometer entrance position for a possible diffraction slit is also shown. The spectrometer is kept at a pressure below 10^{-6} mbar. A gate valve allows the isolation of the spectrometer from the remaining vacuum setup.

by an x-ray detector[7]. It consist of two microchannel plates[8] (MCP) with a diameter of 25 mm, where the x-ray photons release electrons. The electron current is amplified and finally hits a phosphor screen[9] which is then imaged via a lens onto a CCD camera[10]. The first MCP is coated with MgF_2 for enhanced sensitivity [246, 247]. The effective pixel size of the detector equals 32.47 μm. The whole detector is mounted on a motorised camera stage, which allows the longitudinal position (distance grating - detector), the transversal position and the tilt of the detector to be adjusted. The longitudinal alignment and the rotation are used to align the detector along the image plane. Since the grating has a relatively large dispersion, only a few harmonics can be simultaneously imaged on the detector. The transversal position can therefore be adjusted to select different harmonic orders for detection. A typical high harmonic spectrum where three different spectral

[7] Photek VID225
[8] Photonis
[9] Phosphor: P43
[10] Basler A312F

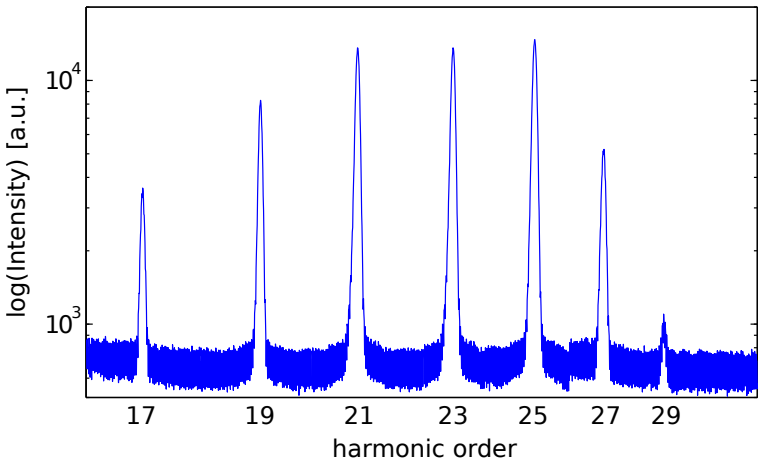

Figure 5.5: Typical high harmonic spectrum. The image was obtained by stitching together three different spectral windows recorded in the XUV spectrometer image plane.

windows are stitched together is shown in figure 5.5.

Spectral resolution

In all XUV experiments performed in this thesis, spatial interferograms were recorded. Spectral resolution was therefore not the main critical factor. Instead, it was important to achieve maximum XUV flux at the detector. For this reason no slit was put at the entrance of the spectrometer. However, the setup has been designed to be able to also perform spectral interferometry for the temporal characterisation of attosecond pulses. Importantly, the concept of the XUV MICE experiments performed in chapter 6 can also be applied to the spectral domain. It is therefore worth briefly reflecting on the spectrometer spectral resolution.

The effect of the spectrometer entrance slit is illustrated in figure 5.6. A ray tracing was performed to simulate the propagation of the geometrical rays from the source to the image plane, taking into account the diffraction off the grating. The final focal spot

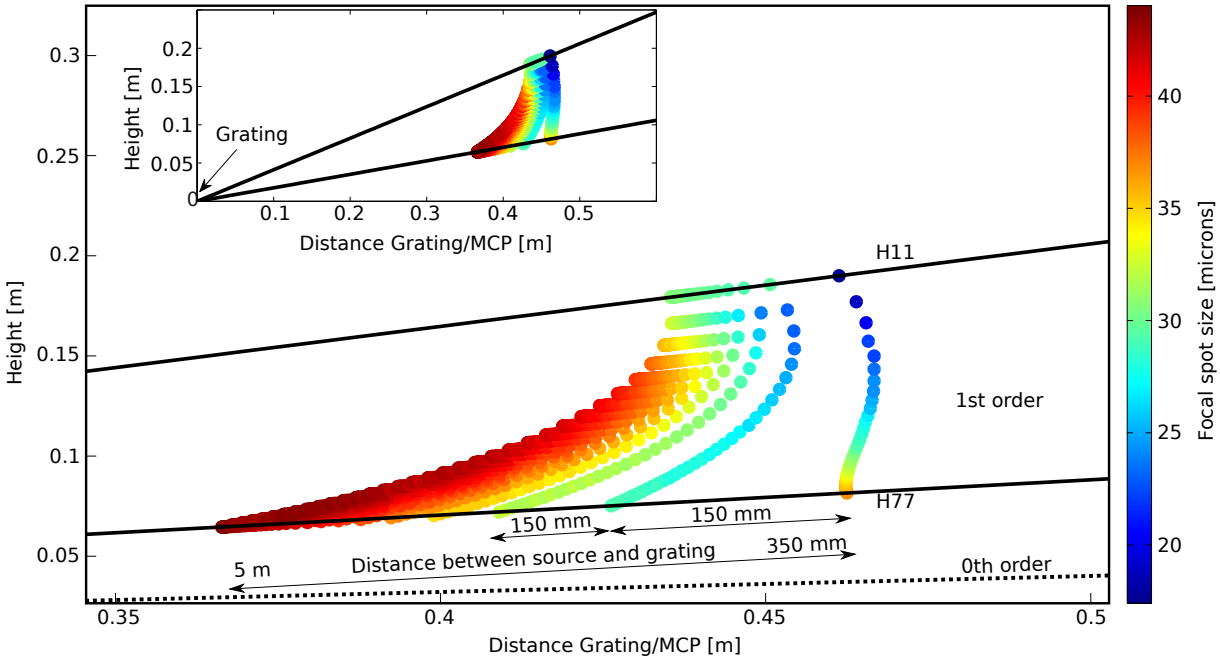

Figure 5.6: Ray tracing of the XUV spectrometer for the estimation of the spectrometer resolution. The geometrical rays originate at the source and are diffracted off the grating. If the slit is placed at 350 mm distance from the grating as an effective source, the foci of different harmonics lie roughly on a straight line and the resolution is optimised. For increasing source separation (in steps of 150 mm), the line of the foci becomes strongly curved, and the resolution decreases. Inset: Overview of the geometry as a function of the distance between the grating and the detector.

locations and spot sizes for different harmonic orders are shown for different distances between the source and the grating. Nominally, a spectrometer slit forms the effective source at a distance of 350 mm away from the grating. In comparison, when the source is moved away from this location the optimal image plane for each harmonic is determined by finding the location where the spot size of the corresponding bunch of rays associated with one harmonic is smallest. The distance between the grating and the optimal image plane is therefore flexible and decreases for an increasing distance between the source and the grating. The spot size that is obtained in the respective image planes for each harmonic is then used to quantify the detector resolution as a function of harmonic order. As can be seen in figure 5.6, the focal points of different harmonic orders for this case lie

approximately on a straight line, and the spot size reaches values of 20 μm for low harmonic orders. In the Oxford experimental beamline, no slit is used, and the real XUV source is approximately 940 mm away from the grating. Figure 5.6 indicates that for increasing distances between the source and the grating, the focal spots lie on a line that becomes more and more curved. The resolution decreases as a function of increasing distances, an effect which is more severe for higher harmonic orders. High spectral resolution therefore requires a narrow slit at the spectrometer entrance, possibly in combination with some other measures. For example, Mairesse *et al.* have tilted the MCP detector relative to the incoming beam propagation axis to decrease the effective MCP pore area [11] and hence increase the resolution [232].

5.1.6 Spectrometer calibration

In order to perform a wavelength calibration of the spectrometer, the wavelength dependence of spatial interferograms is utilised. The XUV fringe separation δx_q for different harmonic orders q of wavelength λ_q is measured as a function of the separation of the IR foci d. If L is the distance between source and detector, those quantities are connected with one another according to

$$d = \lambda_q L / \delta x_q. \tag{5.1}$$

The wavelength calibration for harmonics 19-25 is plotted in figure 5.7. As a sanity check, a different way to identify the harmonic orders is to compare the measured separation of

[11] MCP pores are 10 μm in diameter on a 12 μm pitch.

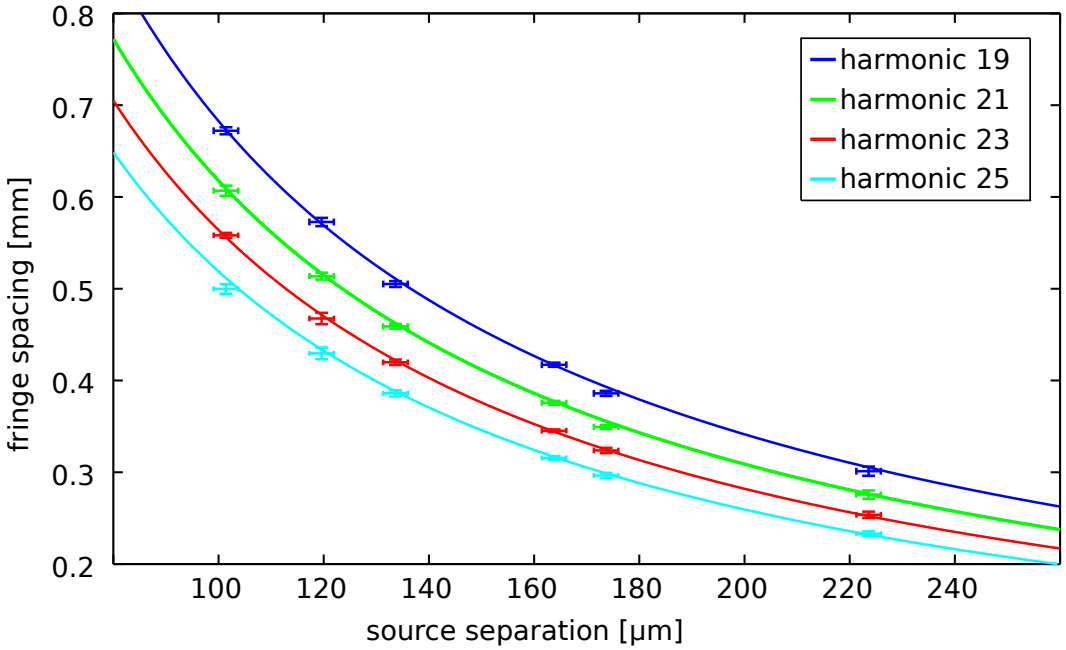

Figure 5.7: Spectrometer calibration for 4 different harmonic orders. The standard deviations in the XUV fringe spacing (vertical error bars) and the source separation (horizontal error bars) are calculated from a set of 10 different measurements.

the different harmonics with the grating equation:

$$m\lambda = \sigma_0(\sin\alpha + \sin\beta), \tag{5.2}$$

$$L = -469\text{mm} \times \cot\beta. \tag{5.3}$$

Here σ_0 is the nominal groove spacing, m is the diffraction order and α and β are the angles of incidence and diffraction, respectively. The factor of 469 mm results from the geometry of the particular grating used in the setup. For these methods to produce reliable results, it is important to keep the laser intensity at relatively low values to avoid any blue-shift due to ionisation of the medium.

5.2 Spatial signatures of quantum trajectories

The setup described in the first part of this chapter has been used in the remainder of this thesis to generate high harmonics. The aim of the experiments is twofold: To develop new characterisation methods for high harmonic radiation, and to use these and other techniques to study the fundamental generation process of higher-order harmonic radiation. Regarding the latter, among the most interesting features of HHG is the physics of the different quantum trajectories traversed by the electron after ionisation. Studying the properties of these trajectories provides one with the a fundamental understanding of the sub-cycle electron dynamics of HHG. This knowledge is crucial to be able to generate and control XUV attosecond pulses from HHG in experiments. For those reasons, the experimental setup described above has been optimised to be able to observe signatures of the different quantum trajectories on the far-field detector with high resolution and high signal-to-noise ratio. Experiments studying the physics of the different trajectories are described in the following sections.

5.2.1 Observation of harmonics from long and short trajectories

The performance of the experimental setup regarding the generation of the different quantum trajectories confirmed the general phase-matching model presented in section 4.2. To show this, figure 5.8 depicts the spatio-temporal profile of harmonics 19-27 when the gas target is placed before the laser focus. At this position, short trajectory harmonics are generated by on-axis phase matching. In addition, off-axis phase-matching enables the generation of harmonics from long trajectories. Those have larger divergences than short

trajectory harmonics and form an annular ring around those [248, 249]. These features can clearly be seen in figure 5.8. The target position was tweaked to optimise the intensity of the long compared to the short trajectories. However, the latter are always more intense than the former. Figure 5.8 also reveals that for increasing harmonic order, the annular structure originating from the long trajectories becomes less and less wide until both trajectories merge in the cutoff to form one single harmonic. This can be explained by the fact that in the plateau region, the α-coefficients, as defined in equation (4.20), and therefore the phase properties of both trajectories are very different, with α_q^l being larger than α_q^s [250]. For higher harmonic orders, the difference between the coefficients becomes smaller and smaller, which causes the spatial properties of harmonics from both trajectories to become more and more equal (see section 4.1.3).

To fully verify the validity of the Balcou model (section 4.2) at the experimental

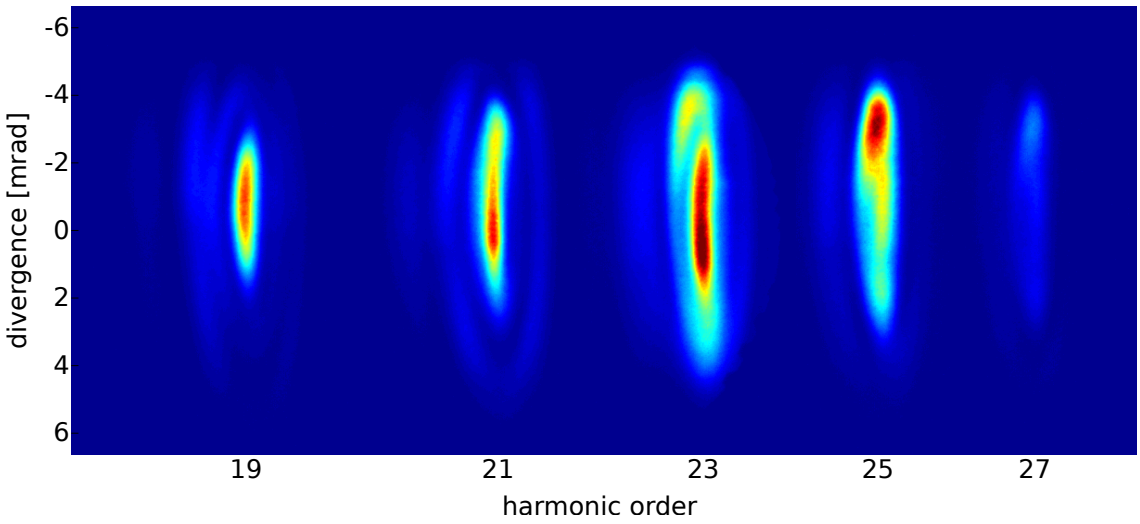

Figure 5.8: Spatio-spectral properties of long and short trajectories. The spatio-spectral profiles of harmonics 19-27 are shown for a scenario where the gas target is positioned before the laser focus. Short trajectory harmonics, forming intense collimated beams, can clearly be distinguished from the more divergent and less intense long trajectories. Both become more and more equal for increasing harmonic order, before they finally coalesce in the cutoff (not shown). For this image two spectral windows have been stitched together.

HHG beamline at Oxford, the gas target position was scanned across the focus along the propagation direction of the laser (z-axis). The resulting data is shown in figure 5.9 for harmonics 15-27. For this data, a spectral lineout taken at the harmonic central position is plotted as a function of the target position. The $z = 0$ position has been estimated geometrically. Positive values of z denote scenarios where the gas target is positioned after the laser focus, and vice versa. The full scan shows all properties of the phase-matching model: For positive values of z, only the spectrally narrow short trajectories appear. When the target is moved through the focus to negative z, long trajectory contributions appear. In analogy to the spatial domain, the spectral bandwidth is larger for long trajectories than for short trajectories. This is due to the fact that the temporal variation of the dipole phase induces a chirp[12] to the harmonic emission that depends on the quantum trajectory. This can be seen using the instantaneous frequency ω_i,

$$\omega_i(t) = -\frac{\partial \Phi_q^{l,s}(t)}{\partial t} = \alpha_q^{l,s} \frac{\partial I}{\partial t}. \tag{5.4}$$

Since $\alpha_q^l > \alpha_q^s$, the chirp of long trajectory harmonics significantly exceeds the one of short trajectory harmonics in the plateau region [251]. This can directly be seen in figure 5.9. For increasing harmonic orders, the difference in spectral bandwidth of both contributions becomes more and more equal. In order to show the long trajectory contributions with sufficient signal-to-noise, the short trajectory harmonics are saturating the detector, since their phase-matching is still more effective than the one of long trajectories. The harmonic chirp also causes space-time coupling of the harmonics. Indeed, contributions from the

[12] This chirp is often referred to as the *harmonic chirp*, in contrast to the *atto-chirp*, which is inherent to the generation process and results from the dependence of the recombination time on harmonic order.

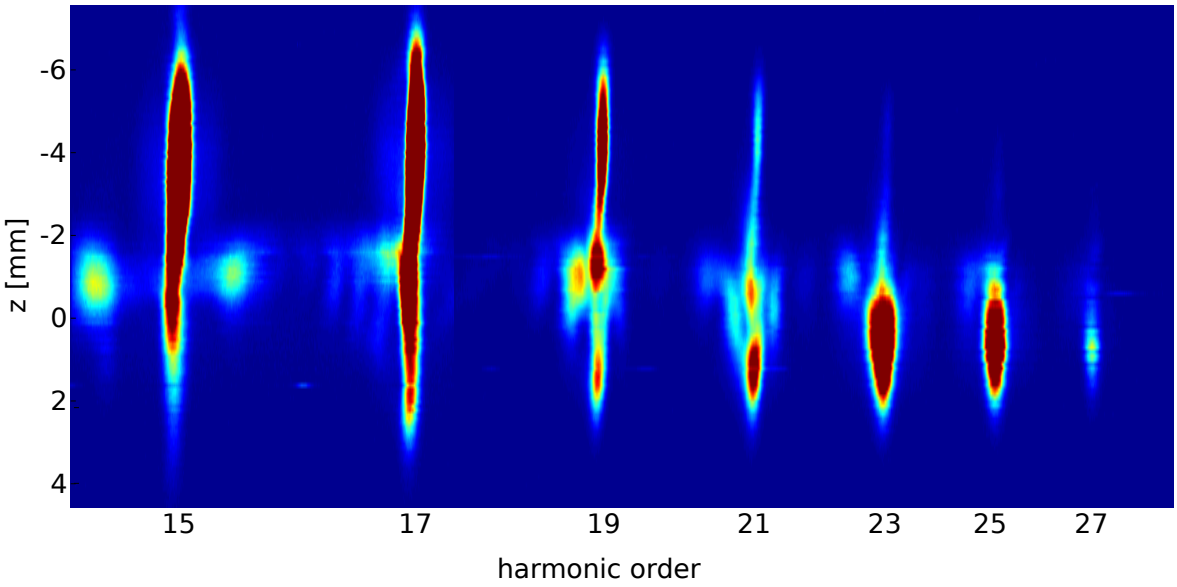

Figure 5.9: Spectral properties of long and short trajectories. The gas target position is varied across the laser focus (z=0) along the propagation axis (z-axis). The intense, narrowband harmonics from short trajectories are surrounded by the highly chirped and less intense long trajectory components. The bandwidth of both contributions becomes more and more equal for higher orders.

temporal wings of the pulse are generated with lower peak intensity than at the maximum of the envelope. Since the spectrometer effectively maps time to frequency, emission on the red or blue side of the harmonic becomes less divergent, as can also be seen in figure 5.8.

Examining figure 5.8 and figure 5.9 more closely, a further very sensitive physical phenomenon may be discovered. Here the long trajectory harmonics appear highly non-uniform and form a set of rings with increasing radius and very low intensity in between the rings. The appearance of several rings cannot be explained by the description of the long trajectory contribution alone. In fact, these rings represent interference fringes that result from the interference between the different quantum trajectories. These quantum path interferences are discussed in the next section.

5.2.2 Quantum-path interferences in high harmonic generation

Interference between the different quantum paths is a consequence of the difference in phase of the short trajectories, $\phi_q^s = \alpha_q^s I(r,t)$, and long trajectories, $\phi_q^l = \alpha_q^l I(r,t)$. Theoretically, higher order trajectories may also come into play, however, the two shortest quantum paths strongly dominate the interference pattern in practice. Since the phase difference $\Delta\phi_q^{ls} = -\Delta\alpha_q^{ls} I(r,t)$, with $\Delta\alpha_q^{ls} = \alpha_q^l - \alpha_q^s$, depends both on space and time, interference occurs in both of these domains. By varying the peak intensity I_{peak}, these oscillations with periodicity $2\pi/\Delta\alpha$ can directly be measured. As the intensity is increased, the rings move outwards. Since in the Oxford high harmonic beamline a spatially resolved XUV spectrometer is used, the interplay between the different trajectories manifests itself in spatio-temporal interference rings.

Figure 5.10(a) shows quantum path interferences (QPI) for harmonics 15-29. For this measurement, the gas target was placed before the laser focus at a position where both trajectories are phase-matched. I_{peak} was varied between 1.8×10^{13} W/cm^2 and 9.7×10^{13} W/cm^2, which changes the relative phase between the quantum paths. The peak intensity I_{peak} was estimated by calculating the ratio $P_{meas}/(R_{rep}\tau \cdot r^2\pi)$, where P_{meas} is the measured power, R_{rep} the laser repetition rate, τ the pulse duration and r the focal spot radius[13]. The relative error in estimating I_{peak} is always between 15% - 20%. To obtain a spectral range covering 8 harmonics as in figure 5.10, the MCP detector was moved along the image plane across three adjacent spectral windows and the measurement was repeated each time. The obtained images were stitched together to form figure 5.10.

[13]Note that the experimentally measured focal spot radius is related to the amplitude waist as defined in equations (2.21) and (2.22) by $w_0 = \sqrt{2} \cdot r$.

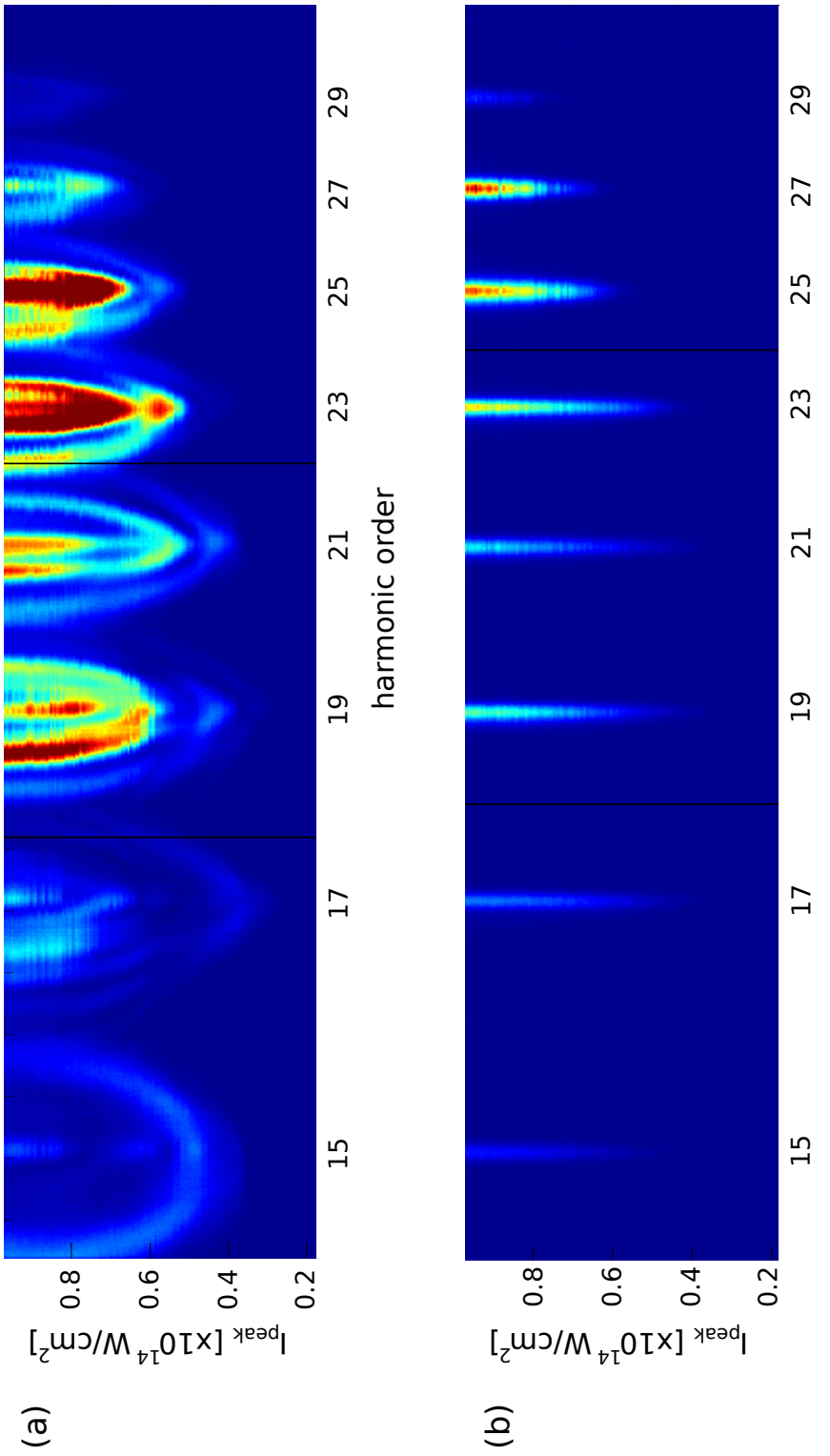

Figure 5.10: Quantum path interferences in high harmonic generation. (a) Intensity-dependence of long quantum trajectories. With increasing peak intensity the spectral broadening increases dramatically, and decreases with harmonic order. (b) Intensity-dependence of short quantum trajectories. The spectral width depends very little on the laser intensity. Three different spectral windows, corresponding to three different XUV detector positions and indicated by the black lines, have been stitched together to form the full image.

Furthermore, as can be noticed from figure 5.8, at the centre of the spatial profiles the short trajectory harmonics are much more intense than the long trajectory harmonics. To have maximal fringe contrast, a spectral lineout was taken at an off-axis position where the signal strengths of both contributions are balanced. In the presented experiment, the best contrast was measured at an off-axis location of 3.8 mrad. The integration times were 230 ms for figure 5.10(a) and 30 ms for 5.10(b), with the average taken over 10 measurements for each intensity value.

Figure 5.10(a) demonstrates that the long trajectory contributions exhibit significant spectral broadening. At high intensities, the broadening is large enough for neighbouring harmonics to overlap. Since the CPA laser is not CEP-stabilised, the spectral interference between neighbouring odd harmonics is smeared out [252]. For comparison, figure 5.10(b) shows the same scan where the target has been put after the laser focus, enabling only the generation of the spectrally narrow short trajectory harmonics. Indeed, the difference in the spectral widths of the harmonics shown in figures 5.10(a) and (b) is striking. In addition, the fringe contrast in figure 5.10(a) is comparatively high. The main difficulty regarding the detection of QPI lies in the fact that these oscillations are usually smeared out due to temporal and spatial averaging. Temporal averaging is caused by the laser pulse envelope. However, since the harmonics are chirped according to equation (5.4), an XUV spectrometer can be used to map time to frequency. The harmonic central frequency corresponds in time to the maximum of the pulse envelope. Harmonic emission generated on the leading edge of the pulse is shifted to higher frequencies, whereas emission of the trailing edge is shifted to lower frequencies. The use of a spectrometer with sufficient spectral resolution thus gets rid of temporal averaging. Considering the problem of the

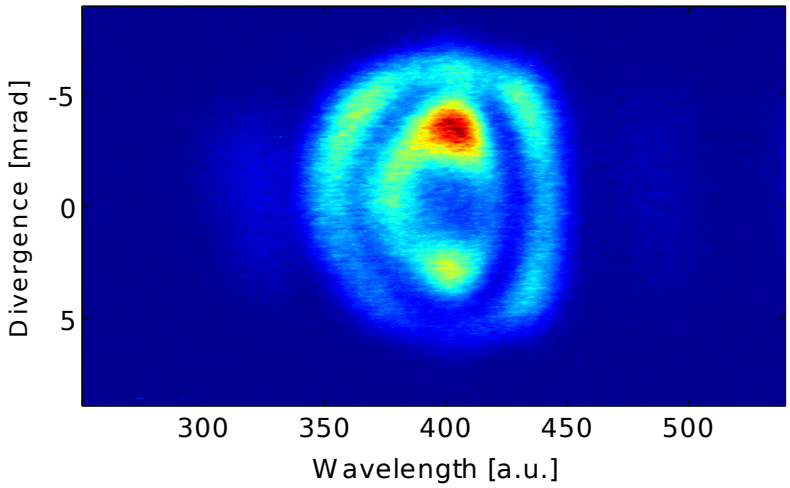

Figure 5.11: QPI of harmonic 21 where destructive interference annihilates the short trajectory component.

spatial averaging, this can occur in all three dimensions x, y, z. Averaging along the propagation direction can be avoided by choosing a gas target which is shorter than the laser confocal parameter. Regarding the other two axes, a spatial filter can be put after the generation medium to prevent averaging in the spatial dimension that is not resolved by the spectrometer. However, in the experiments presented here, this was not necessary because of the use of a spatially-resolving detector, resulting in a higher signal-to-noise ratio compared to previous experiments [253].

By tuning the laser intensity, gas target position, gas pressure and the driving laser beam size using an iris it is possible to control the relative strengths of the individual quantum path contributions. This control could be one possible explanation for the scenario obtained in figure 5.11 where the central short trajectory component vanishes. This phenomenon may be due to destructive interference between the different quantum paths. Since the laser intensity is far below the saturation intensity, ionisation can be excluded

as a cause for the depletion of the centre of the harmonic profile. Despite the usually larger relative weight of short trajectory components, this example shows how accurately the harmonic generation process can be manipulated.

To date QPI has only been reported by very few groups. The experiment presented here reproduces current results with an increased signal-to-noise ratio [204, 253–255]. By changing the intensity, the individual quantum paths can be controlled to attosecond precision. Since QPI occurs on a sub-cycle attosecond timescale, it does not require CEP-stabilisation. Even though theoretical simulations predict the occurrence of higher-order QPI, it has not yet been possible to observe these experimentally. This is presumably because of the strong intensity-dependence of the phases, making phase-matching very difficult.

5.3 Interferometric measurement of the atomic dipole phase

The discussion of the atomic dipole phase in previous parts of this thesis emphasised that it represents one of the most fundamental quantities of HHG. After experiments studied its influence on the harmonic emission such as on the temporal coherence of high harmonics [256, 257], it became clear that fully understanding and possibly even controlling the dipole phase properties is crucial [250, 258, 259]. Indeed, the dipole phase induces a negative chirp on the harmonics, in contrast to the usual optical Kerr effect occurring during the propagation of a laser pulse in a dielectric and which causes a positive chirp on the pulse. Compensation of this chirp is necessary, for instance, for temporally compressing harmonic

pulses [260]. Due to their different properties, many experiments require isolation of the different quantum paths, which can be achieved by changing the geometry [261, 262], spatial filtering [227] or manipulating the driving laser properties [263, 264].

Early measurements of the atomic dipole phase were based on studying the frequency chirp of harmonic pulses [265, 266]. However, a more direct way is to use interferometry of high harmonics. This has been done by Corsi *et al.*, where the relative shift between the interference fringes of short trajectories and the ones from long trajectories is used to extract the dipole phase [267, 268]. In this way, contributions of the different paths can clearly be discriminated.

5.3.1 Experiment

The experimental procedure employed here is similar to the one from Corsi *et al.* [267]. The experimental setup is described in section 5.1 and illustrated in figure 5.1. A Mach-Zehnder interferometer creates two identical copies of the input pulse which are overlapped in time using the precision delay stage. When a tilt is applied to the last beamsplitter, both IR beams are focused to two different focal spots in the focal plane inside the target chamber. These foci generate two spatially separated XUV sources, which then diffract into the far-field where they spatially interfere. Not shown in figure 5.1 is a variable attenuator, consisting of a $\lambda/2$-waveplate and polariser that have been placed in one arm of the interferometer. This allows to adjust the relative intensity between both arms. Regarding the XUV generation, both IR laser beams are focused slightly after the gas target to generate both short and long trajectory harmonics. The position of one XUV beam is spatially overlapped with the other beam by using the lateral shear stage, as indicated

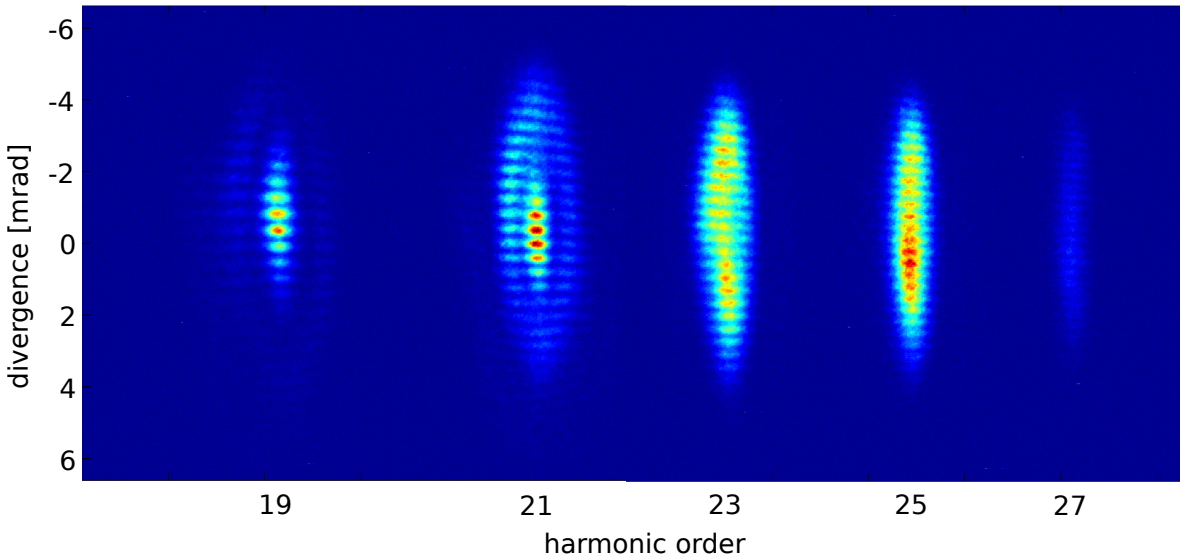

Figure 5.12: Interferogram resulting from the spatial interference of two XUV sources. The interference of short trajectory harmonics, occurring in the intense central region of the harmonic, can clearly be distinguished from the long trajectory interference which occurs in the less intense halo surrounding the short trajectories.

in figure 5.1, in order to compensate for the displacement due to the tilt. The target position is optimised for maximum fringe visibility. Once the optical setup is aligned and the target position set, these parameters are not changed anymore for the remainder of the experiment. An interferogram that has been prepared according to this procedure is shown in figure 5.12 for harmonics 19-27. Indeed, figure 5.8 represents the same measurement as figure 5.12 with the difference that one arm has been blocked. In figure 5.12, the central part of each harmonic exhibits interference between the short trajectory components of both beams. In contrast, the outer rings carry spatial interference fringes between the long trajectory components. The fringe spacing is given by equation (5.1) and therefore decreases with harmonic order.

To measure the dipole phase, the intensity of one arm is changed by δI using the variable attenuator in that arm. A change by δI results in a phase shift $\delta\phi_q^{l,s} = -\alpha_q^{l,s}\delta I$,

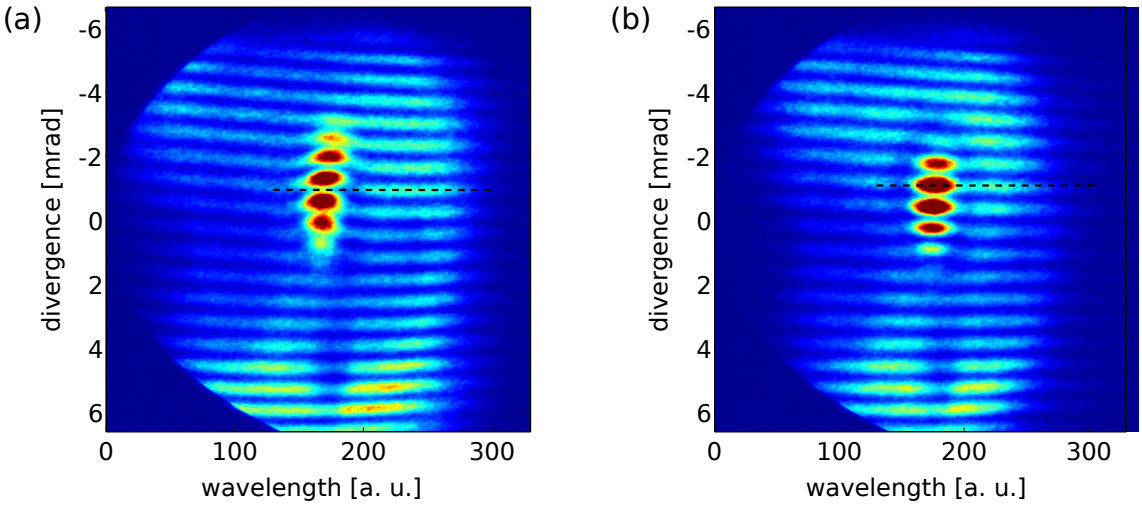

Figure 5.13: Interference of the respective quantum paths for harmonic 15 when the relative intensity between the two driving beams is changed. (a) Initial interferogram. (b) A change in intensity of $\delta I = 1.4 \times 10^{13}$ W/cm^2 causes a π shift of the long trajectory fringes relative to the ones from short trajectories, as indicated by the black dashed lines.

which is different for the different quantum paths since $\alpha_q^l > \alpha_q^s$. Indeed, due to the larger intensity-dependence of the long path, by changing the intensity the fringes in the outer part of the harmonic move faster than the fringes in the central part. Hence the α-coefficients can be extracted by measuring the shift of the fringes of the two emission zones as a function of the intensity unbalance. In practice, it is however not reliably possible to measure absolute fringe shifts due to the remaining instability of the setup, which causes an overall shift of the interferogram. It is therefore more suitable to measure relative fringe shifts between the two emission regions. This type of measurement does not recover the absolute phase anymore, however, the difference between the dipole phase coefficients is encoded in the data according to

$$\Delta\phi_q^{ls} = \delta\phi_q^l - \delta\phi_q^s = -\Delta\alpha_q^{ls}\delta I, \tag{5.5}$$

where $\Delta\alpha_q^{ls} = \alpha_q^l - \alpha_q^s$. Figure 5.13 shows two interferograms of harmonic 15 taken with peak intensity $I_{peak} = 6.6 \times 10^{13}$ W/cm^2. In 5.13(b), the intensity imbalance has been changed by $\delta I \approx 1.4 \times 10^{13}$ W/cm^2 compared to 5.13(a), which results in a relative phase shift of π, as highlighted by the black dashed lines. Note also the large spatio-spectral extent of the long trajectory signal for harmonic 15, which highlights the phase shift between both regions in a particularly clear manner.

5.3.2 Results

The results are plotted in figure 5.14 for different peak intensities. The chosen intensities are well below the saturation intensity of argon, $I_{sat} = 2.3 \times 10^{14}$ W/cm^2, ensuring that no ionisation effects compromise the results[14]. Linear fits are plotted together with the measured data points. The value of $\Delta\alpha_q^{ls}$ is then simply given by the slope of each fit. The extracted dipole phase differences $\Delta\alpha_q^{ls}$ are plotted in figure 5.15 for different peak intensities as a function of harmonic order. The results follow the theoretical single-atom predictions: For harmonics in the plateau, α_q^l and α_q^s are very different, leading to a large values of $\Delta\alpha_q^{ls}$. For increasing harmonic order, the α-coefficients become more and more equal, and $\Delta\alpha_q^{ls}$ therefore decreases. For low peak intensities $\Delta\alpha_q^{ls}$ is larger than for higher intensities. To put these results into context, the values for $\Delta\alpha_q^{ls}$ reported by Corsi *et al.* in [267] are plotted as well. Since their experiment has been performed with experimental parameters that are essentially identical to the ones used for this thesis such a comparison may be justified, even though uncertainties in the laser mode and the target alignment,

[14] Theoretical calculations indicate that for intensities larger than the saturation intensity the harmonic chirp behaves in a much more complicated manner than is described by the equation $\phi_q^{l,s} = -\alpha_q^{l,s} I$. Indeed, in this regime the chirps of the two quantum paths appear to have opposite signs [269].

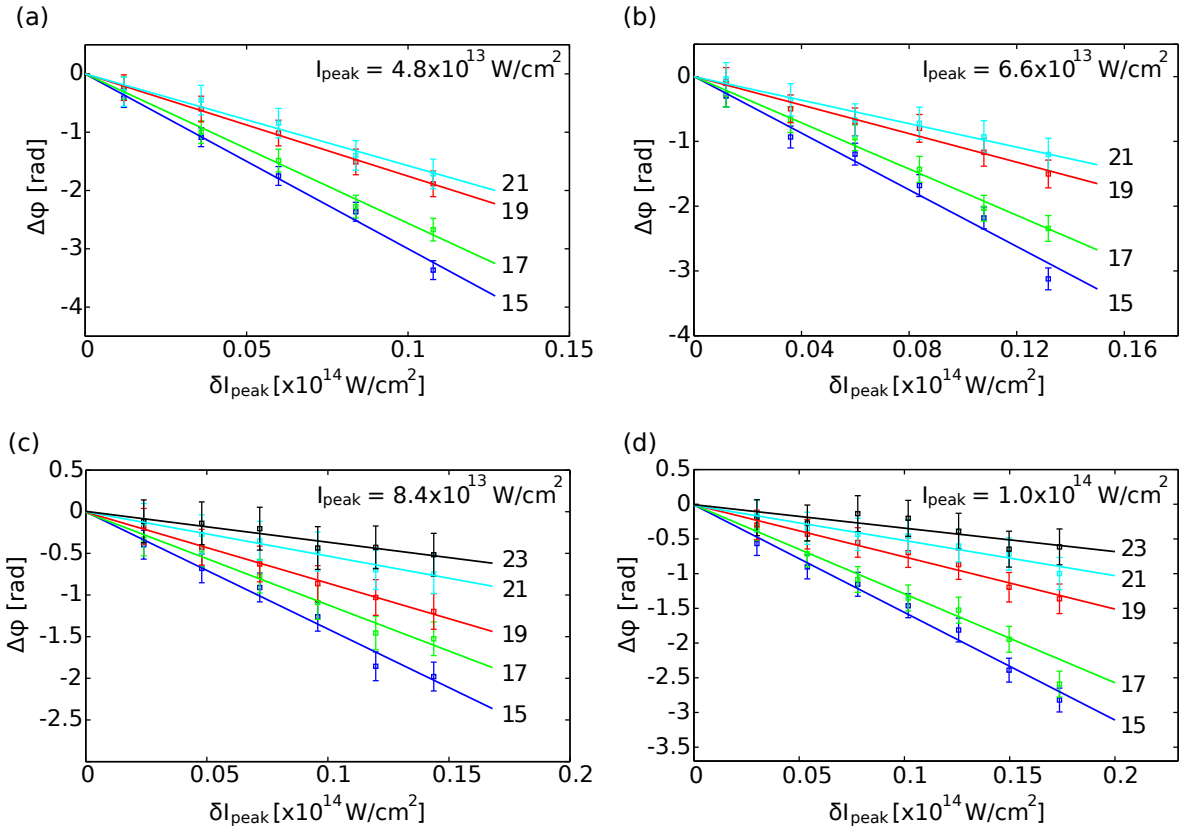

Figure 5.14: Experimental phase shifts between the inner and outer regions of the harmonics as a function of the intensity unbalance between the two driving beams for different harmonic orders. The measurement has been performed for four different values of the peak intensity.

different sources of noise in the setups as well as further possible errors in the measurement might not justify an exact direct comparison. Nonetheless, figure 5.15 shows that the measurement with peak intensity of 1.2×10^{14} W/cm^2 performed in [267] is in agreement with the results presented here, as well as with theoretical simulations [250, 270, 271]. However, it remains unclear why for a given harmonic $\Delta\alpha_q^{ls}$ is decreasing for increasing peak intensities, since the single-atom theory predicts the opposite behaviour (see figure 4.3). One possible explanation is that the α-coefficients were assumed to be constant, even though this only represents an approximation since they are in fact intensity-dependent, $\alpha = \alpha(I)$. Furthermore, due to the rather low peak intensity the measured spectral region

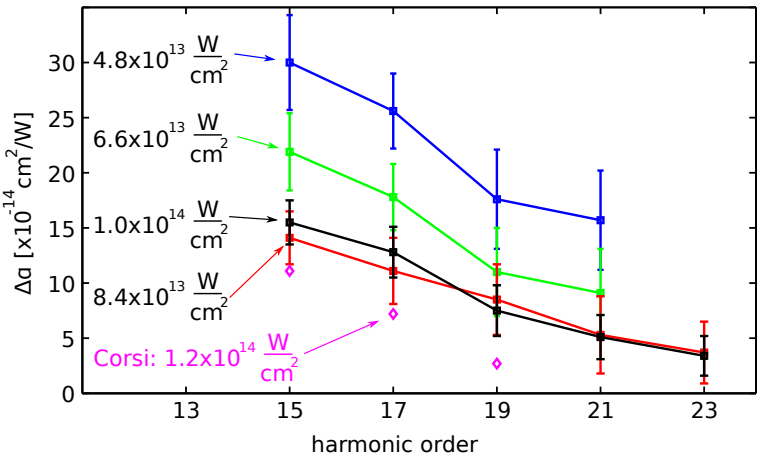

Figure 5.15: Difference in the α-coefficients of both trajectories as a function of harmonic order. The measurement is performed for four different intensity values. For comparison, the results reported by Corsi *et al.* [267] are drawn as well (purple).

was close to the harmonic cutoff, with the extent of the plateau region being very small. In such a regime the Lewenstein model may not be fully valid anymore.

Finally, we note that the above experiments have measured the difference between the α-coefficients of the long and short quantum paths. In order to obtain the absolute values of α, additional experiments need to be performed. One possibility is to the determine the ratio α_q^l/α_q^s from a measurement of the coherence times of the different quantum paths [267].

5.4 Outlook

The generation of high harmonics is determined by the sub-cycle electron dynamics described by the single-atom response, as well as by modifications occurring upon the propagation of the field through the generating medium. Single-atom theories predict the existence of several electronic quantum paths that contribute to the harmonic emission. Macroscopic phase-matching usually favours one or two of these quantum paths,

which will then determine the characteristics of the emitted harmonic field in the far-field. The properties of each quantum path are fundamentally described by the atomic dipole phase.

The first part of this chapter detailed the key parameters of the high harmonic beamline that was optimised in order to characterise the harmonic field and to conclude on the fundamental generation process regarding the different quantum paths. In the second part of this chapter, experiments were performed to measure the far-field signatures of these different types of emission. Since $\alpha_q^l > \alpha_q^s$, the phase associated to the long path varies much more rapidly than the one of the short path, leading to very different spatio-temporal properties of the atomic dipole moment. It was possible to observe quantum path interferences between the long and short trajectories in both the spatial and the spectral domains. Furthermore, by measuring the phase shift between the interference of the long paths relative to the one of the short paths as a function of the intensity unbalance between both arms it was possible to extract the differences between the atomic dipole phases of both cases.

The experiments described here demonstrate that it is possible to completely control the quantum path contributions involved in the generation process. Most importantly, this can be done with extremely high temporal resolution. Indeed, in both the QPI and the dipole phase measurements, the sub-cycle electron dynamics have been manipulated to a precision of a few 10 as. This is among the shortest timescales that are currently observed directly. The QPI approach and the measurement of the dipole phase of long and short trajectories represent important steps towards the full characterisation of the atomic dipole. The high sensitivity of these techniques makes them also suitable to investigate

HHG electron dynamics in more complex systems such as molecules or clusters [272, 273].

The above discussion has explained the spatial fingerprints of QPI via the dependence of the dipole phase on the spatial profile of the driving laser, with $\alpha_q^{l,s}$ as a scaling factor. It is instructive to consider a different viewpoint as well: Due to the different α-coefficients, the emitted fields originating from long and short quantum paths have different wavefront curvatures. The interference in the far-field of the two fields thus results in an annular fringe pattern. Measuring the wavefronts of both fields at the same time would represent a new and powerful tool to study the macroscopic response of the medium. The development and demonstration of such a technique is the subject of the next chapter.

Chapter 6

Simultaneous spatial characterisation of two independent sources of high harmonic radiation

Table-top sources of high harmonic radiation are today commonly used as a source of sub-femtosecond pulses, with pulse energies ranging from the extreme-ultraviolet (XUV) to the soft x-ray wavelength regime. The development of novel light sources goes hand in hand with the need for developing devices that are capable of accurately measuring those sources. Chapter 4.3 has introduced the main concepts and techniques for the characterisation of XUV attosecond pulses in the temporal and in the spatial domain. Due to the exotic wavelength range, the brevity of those pulses and the complexity of

the experimental apparatuses, only very few methods have been developed so far that are reliably used in laboratories around the world.

In this chapter, a novel technique is developed to, for the first time, simultaneously characterise the wavefronts of two high harmonic sources. For this aim, the concept of MICE is transferred to the XUV wavelength range. As has been emphasised in chapter 3, MICE is not restricted to any particular parameter space. The only requirement for MICE to work is that the two interfering sources are mutually coherent and that they overlap in the domain of interest. Even though the experimental setup and the properties of the test pulses here are fundamentally different to the situation in chapter 3, the strength of MICE lies in the fact that it is so broadly applicable to such different scenarios. In the following, the adaptation of MICE to the XUV is presented, which is applied to the reconstruction high harmonic wavefronts. This information is then used to characterise quantum path signatures of the generation process. The results of this chapter have been published in [274].

6.1 Theory of XUV MICE

6.1.1 Concept

The experimental setup for performing XUV MICE is explained in detail in chapter 5. Its concept is depicted in figure 6.1(a). The input pulse is split by a Mach-Zehnder-type interferometer. Delay and tilt between the two beams can readily be adjusted. Each arm is focused by an achromat f = 300 mm lens into an argon gas target produced by a pulsed gas valve with backing pressure 3.5 bar and target aperture of 500 μm. The generated

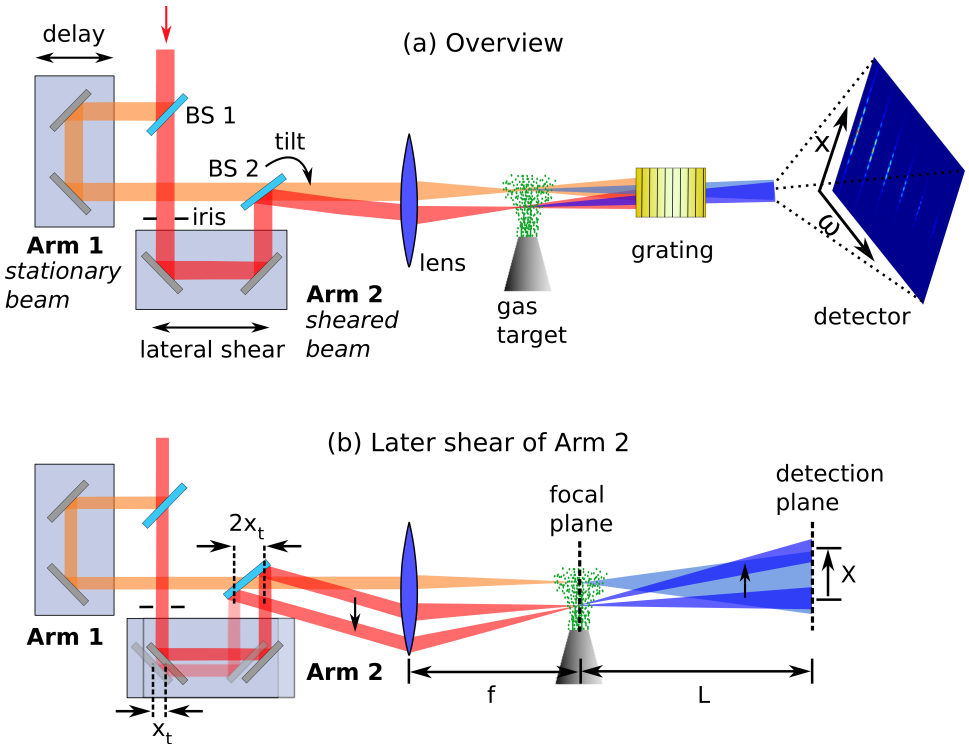

Figure 6.1: Experimental setup for the MICE reconstruction of high harmonic wavefronts. (a) Overview. Both interferometer arms are focused into the gas target where they undergo HHG. Delay, tilt and shear between the two arms can be adjusted such that the two harmonic beams create a spectrally resolved spatial interference pattern. (b) A lateral shear of Arm 2 before the focusing optic, a scenario shown here for two different shears, shifts this beam in the far-field across the profile of the stationary beam.

harmonics are then detected by the spatially resolving XUV spectrometer. The grating disperses the harmonics along the y-axis while they undergo free propagation along the x-axis. If a small tilt is applied to the last beamsplitter ("BS 2" in figure 6.1(a)), the foci of both arms become spatially separated along the x-axis. As a consequence, in the far-field, the two harmonic fields $E_1(x)$ and $E_2(x-X)$ create a spatial interference pattern. Here X indicates a lateral shear that has been applied to Arm 2. This can be done by translating the corresponding mirror pair perpendicularly to the incoming beam propagation axis. As indicated in figure 6.1(b), translation of the stage by the amount x_t shifts the generated XUV beam by $x_d = 2x_tL/f$ at the detector plane. In the paraxial approximation, the

interferogram phase then equals

$$\Phi(x,\omega) = \phi_2(x - X,\omega) - \phi_1(x,\omega) + Kx + \frac{X}{L}kx \tag{6.1}$$

Besides the phases $\phi_1(x,\omega)$ and $\phi_2(x,\omega)$ of the two harmonic beams, two additional terms appear in (6.1). The third term is due to the spatial carrier $K = dk/L$ of the two-source interference pattern with source separation d and wave number k. L is the distance from the source to the detector. The last term in (6.1) arises from an additional phase contribution for each shear due to the change in tilt of E_2 by which the shear is accomplished. Since the Rayleigh range z_R is much smaller than L, $z_R/L \approx 0.09 \ll 1$, the Fraunhofer approximation can be applied to understand the exact meaning of equation (6.1).

6.1.2 Interpretation of the far-field phase

When the detector is sufficiently far away from the source, the Fraunhofer approximation can be used to describe the diffraction of the source into the far-field. Here, the near-field phase $E(\frac{kx}{L}, \frac{ky}{L}, 0, \omega)$ at $z = 0$ and the far-field phase $E(x, y, L, \omega)$ at $z = L$ are directly linked by a Fourier transform. In the paraxial approximation, the expression for the electric field at the detection plane is

$$E(x,y,L,\omega) \approx \frac{-i}{\lambda L} \exp\left[\frac{ik(x^2+y^2)}{2L}\right] \tilde{E}\left(\frac{kx}{L}, \frac{ky}{L}, 0, \omega\right), \tag{6.2}$$

where $\tilde{E}$ is the spatial Fourier transform of E. In the following, only the spatial dimension resolved by the XUV spectrometer is considered. Plugging equation (6.2) into (6.1), the

final expression for the detected phase is obtained:

$$\Phi(x,\omega) = \tilde{\phi}_2\left(k\frac{x-X}{L},\omega\right) - \tilde{\phi}_1\left(k\frac{x}{L},\omega\right) + \frac{kX^2}{2L}, \tag{6.3}$$

with $\tilde{\phi}$ being the phase of the Fourier transform of the field at the lens focal plane $\tilde{\phi}(kx/L,\omega)$. The interpretation of (6.3) is the following: The last term in (6.1) is cancelled by the spherical wave contribution arising from the propagation from the source to the detector, which is given by the quadratic term in (6.2). This explanation is similar to that for high harmonic lateral shearing interferometry [240]. The measured phase difference thus quantifies the deviation of the wavefront from a perfect spherical wave at the detector plane. Alternatively, (6.3) can be seen as XUV MICE between the spatial Fourier transforms of both arms with wave number shear $K_{shear} = kX/L$. The last term in (6.3) is a residual phase term arising from the quadratic phase in (6.2) that is not cancelled. However, since it depends only on the shear, it can be accounted for in the MICE reconstruction. To do so, the MICE formalism for three fields, introduced in section 3.4.2, is adapted to high harmonic wavefronts.

6.1.3 XUV MICE wavefront reconstruction algorithm

Similar to section 3.4.2, the interferogram is modelled such that the sheared field $E_2(x-X)$ is multiplied with a function $A(X)$ that depends only on the shear X and accounts for the extra phase term in equation (6.3). The resulting interferogram, sampled over J points

and K shears with indices j and k, takes the form

$$I_{j,k} = |E_1(x_j)|^2 + |E_2(x_j - X_k)A(X_k)|^2 + 2\mathrm{Re}\left[E_1(x_j)E_2^*(x_j - X_k)A^*(X_k)\right]. \tag{6.4}$$

The MICE reconstruction extracts the products of the unknown fields (the AC term of the interferogram) $AC_i^{meas} = E_1(x)E_2^*(x - X)A^*(X)$ by means of a Fourier transform and filtering. The product is split into the different fields by employing a least-squares minimisation of the error ε between the measured AC-term and the three reconstructed fields E_1, E_2 and A,

$$\epsilon = \sum_{j,k}^{J,K} |AC_{j,j-k}^{meas} - E_1\left(x_j\right) E_2^*\left(x_j - X_k\right) A^*(X_k)|^2. \tag{6.5}$$

In analogy to (3.9)-(3.11), this leads to the following set of equations:

$$E_1\left(x_j\right) = \frac{\sum_k AC_{j,j-k}^{meas} \cdot E_2\left(x_j - X_k\right) \cdot A\left(X_k\right)}{\sum_k \left|E_2\left(x_j - X_k\right) \cdot A\left(X_k\right)\right|^2} \tag{6.6}$$

$$E_2^*\left(x_j\right) = \frac{\sum_k AC_{j+k,j}^{meas} \cdot E_1^*\left(x_j + X_k\right) \cdot A\left(X_k\right)}{\sum_k \left|E_1\left(x_j + X_k\right) \cdot A\left(X_k\right)\right|^2} \tag{6.7}$$

$$A^*\left(X_k\right) = \frac{\sum_j AC_{j,j-k}^{meas} \cdot E_1^*\left(x_j\right) \cdot E_2\left(x_j - X_k\right)}{\sum_j \left|E_1\left(x_j\right) \cdot E_2\left(x_j - X_k\right)\right|^2} \tag{6.8}$$

This system of equations can be solved by inserting a random guess for E_2 and A into equation (6.6) which leads to a first approximation of E_1. This, in turn, is then inserted

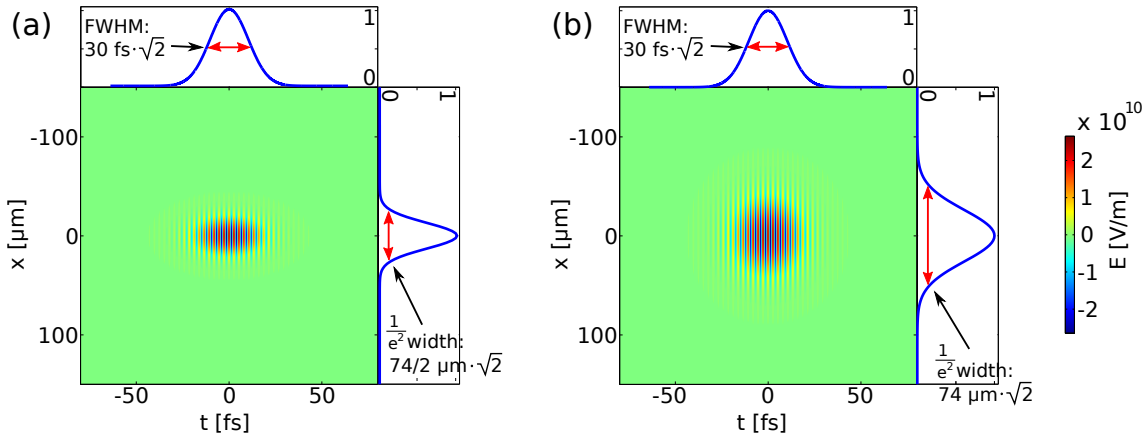

Figure 6.2: Infrared driving laser electric field for (a) Field 1 and (b) Field 2. Main panel: real electric field. Side panels: envelopes of the modulus of the electric field, together with the parameters used for the simulation.

into (6.7) which results in an updated value of E_2. These are inserted into (6.8), and the procedure is repeated until the algorithm converges to the three unknown fields.

6.2 Wavefront reconstruction of simulated data

XUV MICE is first demonstrated by reconstructing the spatial profile of simulated data. The single-atom response within the strong-field approximation is calculated for one trajectory at two independent source locations [195]. The laser parameters are chosen to be consistent with the experimental ones. The peak intensity of both fields at focus is $9 \cdot 10^{13}$ W/cm^2. The IR beams have Gaussian spatial and temporal profiles, with a pulse duration of 30 fs. To demonstrate the technique on distinctively different wavefronts, the spot size of Field 2 is set to 74 μm ($1/e^2$ width), whereas the one of Field 1 is only half of that size. The IR driving laser electric fields for both cases at the focus are shown in figure 6.2, together with their temporal and spatial envelopes. Each of the two beams then undergo high harmonic generation. The far-field spatio-spectral profiles are shown in figure 6.3(a)

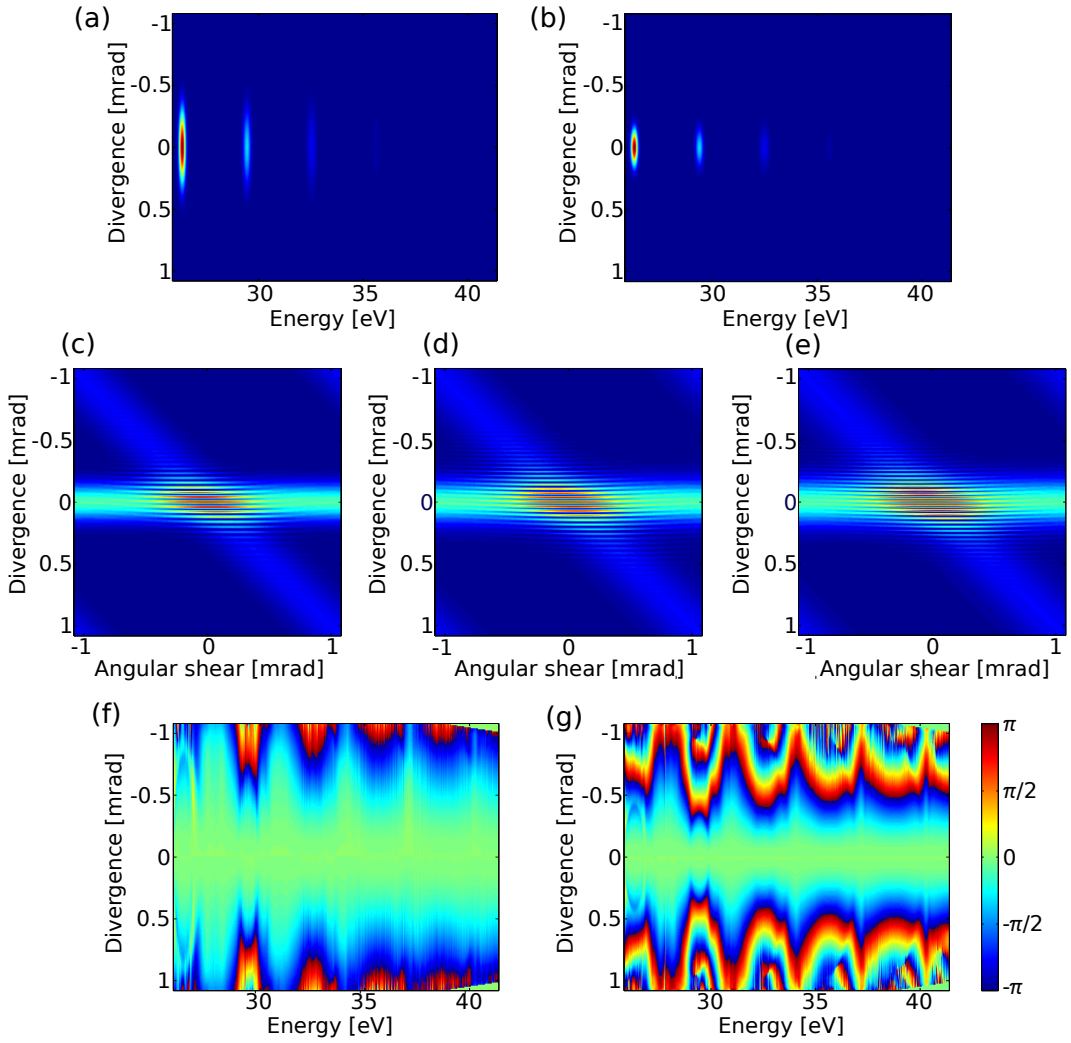

Figure 6.3: XUV MICE data using the simulated single-atom response. Shown are the far-field spatio-spectral profiles of (a) Field 1 and (b) Field 2. Full shear scans where Field 2 is sheared across the spatial profile of Field 1 is shown in (c)-(e) for harmonics 19 -23, respectively. Extracted phase profiles are shown for (f) Field 1 and (g) Field 2.

and (b) for the two XUV sources, respectively. The spatial extent of Field 1 is larger than that of Field 2 since the smaller source size results in a larger beam divergence. In a sequence of 255 shears, the far-field profile of Field 2 is spatially sheared across Field 1 along the x-axis at the detector plane. Field 1 is left untouched throughout.

The full shear scan is shown in figure 6.3 (c)-(e) for harmonics 19-23, respectively.

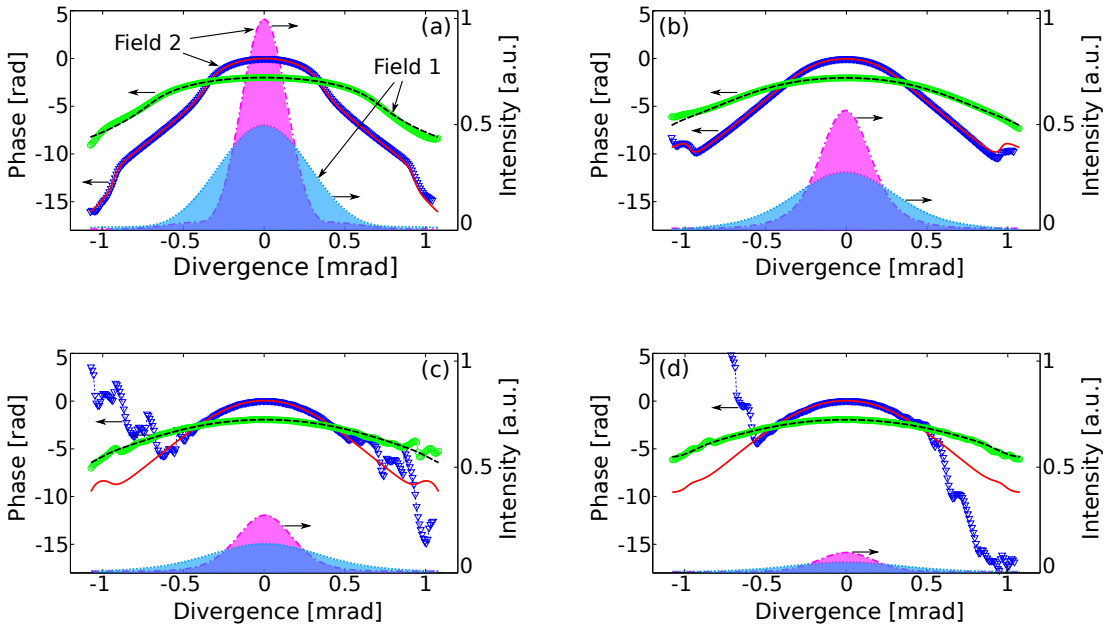

Figure 6.4: Simulation of the MICE spatial characterisation of two HHG fields. Shown are the reconstructed wavefronts (blue triangles and green circles) and the original wavefronts (solid red and dashed black lines) together with the spatial intensity profiles. (a) and (b) show the reconstruction for harmonic 19-21, respectively, after 3 iterations for the noiseless case. (c) and (d) represent the reconstruction for harmonics 23-25 for 20% noise on the interferogram, after 10 iterations. Spatial profiles are normalised to Field 1 of harmonic 19.

From this data set, the phase for each frequency can be extracted, as shown in figure 6.3(f) and (g) for both fields. Since the absolute phase of each wavefront is unknown, the phase at the centre of each wavefront is set to zero. The MICE reconstruction of the wavefronts of both fields from this set of interferograms is shown in figure 6.4(a)-(d) for harmonics 19-25, respectively, together with the original wavefronts. The divergence of Field 1 is larger than that of Field 2, resulting in a flatter far-field phase. This is consistent with the above choice of focal spot sizes, with the smaller source having a larger divergence and therefore a flatter wavefront in the far-field. Figures 6.4(a) and (b) have been simulated without any noise, whereas for 6.4(c) and (d), a noise level of 20% of the maximum of the most intense interferogram times a random value between (0,1)

has been added to each pixel of each each interferogram. This noise is significantly larger than is usual for experiments, yet the reconstruction in the region where the intensity is non-vanishing is very good. To quantify this, the reconstruction accuracy between the original and reconstructed fields is estimated by calculating the root-mean-square (RMS) field error for the different harmonics, as defined in equation (2.39). This error slightly varies with harmonic order and lies between $1\text{-}4 \times 10^{-2}$ in the noiseless case, and increases to $4\text{-}8 \times 10^{-2}$ in the case of high noise, which is still considered a reasonably good reconstruction. Despite the high noise level, the error increases only moderately due to the strong noise suppression of MICE.

6.3 Experimental results

XUV MICE experiments have been performed with mainly two aims: First, to demonstrate the technique on experimental XUV data. Second, to use its capabilities to study the fundamental generation process.

6.3.1 XUV MICE on equal sources

The experimental configuration shown in figure 6.1 is used to characterise a pair of XUV beams generated by high harmonic generation. In this first set of experiments, the gas target is positioned just after the laser focus to generate short trajectories only. Both infrared beams are prepared to be identical, which is ensured by the symmetry of the setup, to reconstruct two identical sources. At the focus, a source separation of 177 μm has been chosen. This relatively large separation guarantees that both sources do not interact with

each other and act as two independent sources [275]. A large source separation however leads to a small XUV fringe spacing at the detector, and therefore to a reduced fringe contrast. However, most of the interferograms presented in the following have been taken in single laser shots. The impact of sources of decoherence varying from shot to shot such as vibrations within the setup have thus been minimised. The interferogram visibility is then mainly limited by the finite detector resolution.

The measurement procedure involves recording a series of interferograms, leaving Arm 1 fixed and varying the shear of Arm 2. For each shear the XUV interference pattern as well as the signal of Arm 2 alone is recorded. The latter is used to calibrate the shear axis, which is shown in figure 6.5(a) for harmonic 25. The interferogram for harmonic 21 where both arms are well overlapped is shown in figure 6.5(b). Figure 6.5(c) shows the reconstructed wavefronts of harmonic 21 across the full spectral harmonic profile, setting to zero the offset phase at the centre of the harmonic. The wavefront curvature does not vary significantly across the harmonic spectral profile, in accordance to the contribution of a single quantum path. The wavefronts of both fields at the centre of each harmonic are shown in figures 6.5 3(d)-(f) for harmonic 21-25 after 5 iterations of equations (6.6)-(6.8) respectively. The wavefronts of both beams are nearly identical, which shows that XUV MICE is consistent by retrieving twice the same wavefront as expected. The small differences in the two beams are caused by residual asymmetries in the interferometer that are e.g. due to small wavefront distortions introduced by the optics. However, MICE does not require identical beams and can in fact be used to measure those differences. The wavefronts of all harmonics exhibit negative curvatures, with the modulus of the radius of curvature slightly increasing with harmonic order. This tendency may be attributed to the

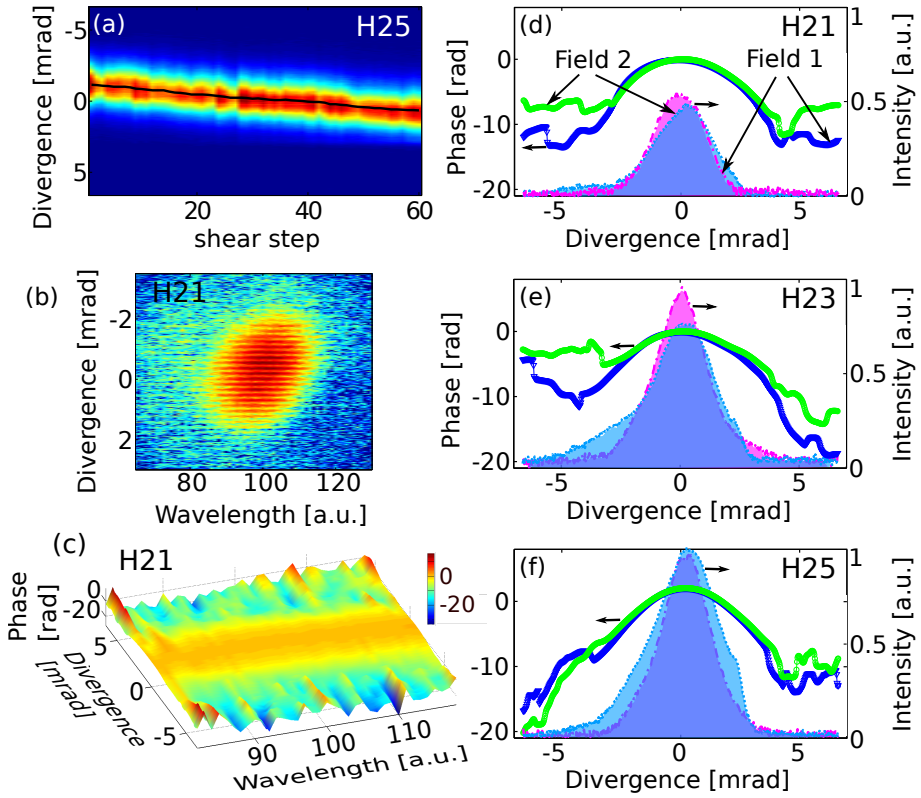

Figure 6.5: Experimental XUV MICE spatial characterisation of two XUV fields. (a) Shear calibration of harmonic 25. The black line indicates the shear axis. (b) Interferogram of harmonic 21. (c) Wavefront reconstruction across the full spectral profile of harmonic 21. The wavefronts and intensity profiles are shown for (d) harmonic 21, (e) harmonic 23, and (f) harmonic 25 for both fields at the centre of each harmonic. The intensity profiles are normalised to the profile of harmonic 25 of Field 1.

wavelength dependence of the atomic dipole phase, since for short trajectories this phase contribution increases with harmonic order. These features are consistent with previous work [240]. Furthermore, the error in retrieving the wavefronts for both beams is estimated by repeating the measurement several times, which gives an indication of the laser source instability. The standard deviation from 21 different reconstructions is up to 11%.

6.3.2 XUV MICE on distinct sources

In a second set of experiments we demonstrate the capability of XUV MICE to reconstruct the wavefronts of two non-identical XUV beams. The beam width of one of the two IR beams is reduced by putting an aperture in Arm 2 of the interferometer (see figure 6.1). This increases the Rayleigh range at the focus and therefore leads to a smaller divergence of the beam after the focus. Note that despite the simplicity of this procedure the phase-matching and therefore the generated harmonic field are fundamentally altered. In addition, using this approach, XUV MICE reveals quantum path signatures of high harmonic generation. For this aim the gas target is placed before the laser focus. Here, both the short and the long trajectories are phase-matched due to on-axis and off-axis phase-matching, respectively. The interferogram for harmonic 21 is depicted in figure 6.6(a). The characteristic annular structure from long trajectories is clearly visible. The wavefront reconstruction of both beams along the black dotted line is shown in figure 6.6(b). Since an aperture has been placed in Arm 2, the divergence of the driving beam in Arm 2 is smaller than that of Arm 1. This property is directly transferred to the harmonics. Hence, at a given detection plane situated in the far-field, the wavefront curvature of Field 2 is larger than that of Field 1. The curvature ratio between the two beams has been measured to be inversely proportional to the change in focal spot sizes, even though the strong intensity-dependence of HHG, the error in determining the actual source size as well as inhomogeneities of the laser beam result in some deviation from an exact numerical correspondence.

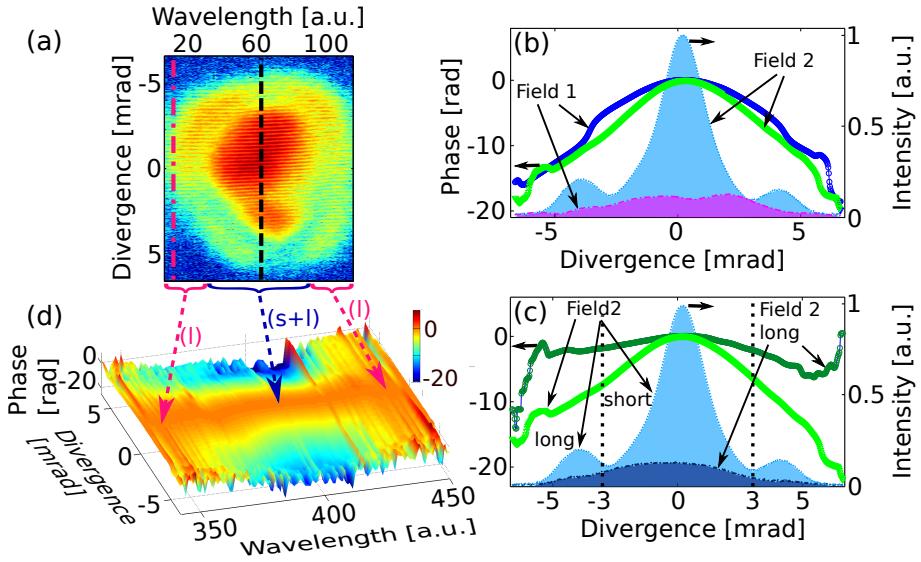

Figure 6.6: XUV MICE wavefront reconstruction of harmonic 21. (a) Interferogram exhibiting signatures of short (s) and long (l) trajectories. (b) Reconstruction of two fields with different wavefront curvatures along the black dotted line in (a), together with the spatial profiles. (c) Reconstruction of the wavefronts of Field 2 along the dotted black line (light green) and dash-dotted red lines (dark green) in (a). (d) Wavefront reconstruction of Field 2 across full harmonic spectral width.

6.3.3 Wavefront reconstruction of long and short trajectories

The same dataset can be used to study the macroscopic response of HHG. In the following, only Field 2 is considered. In figure 6.6(c), the wavefront at the position of the black dotted line of the interferogram is shown again. In addition, the wavefront is plotted at an off-axis location where only long trajectories are phase-matched, as highlighted by the red dash-dotted line. As indicated by the light blue profile in figure 6.6(c), the large central peak originates from short trajectories, whereas the two side lobes stem from long trajectories. We restrict our attention to the angular range from -3 mrad to +3 mrad, which allows us to compare the regions where only one respective quantum path contributes to the emitted signal. The reconstruction indicates that harmonics from short trajectories have a larger wavefront curvature than harmonics from long trajectories. This is in agreement

with the well-known model for phase-matching of HHG radiation, according to which long trajectory components are generated by off-axis phase-matching and have a much larger divergence than short trajectory components, which are generated on-axis [206]. Finally, in figure 6.6(d) the wavefronts of harmonic 21 are plotted across the full spectral harmonic profile. The wavefront curvature is the largest at the centre frequency of the harmonic spectrum, corresponding to short trajectories. Towards the wings of the harmonic profile, the contribution from long trajectories becomes important, leading to flatter wavefronts.

6.3.4 Towards the complete spatio-temporal attosecond pulse characterisation

The findings of this chapter indicate a way towards the complete spatio-temporal characterisation of attosecond pulses all-optically. In the results presented above, the wavefronts for each frequency across the harmonic have been locked together by setting to zero the offset phase at the centre of the harmonic. However, if the spectral phase is measured at one spatial position in one of the beams, all wavefronts are locked together with the correct relative spectral phase. In this case the full spatio-temporal structure of both XUV attosecond pulses can be obtained. Moreover, the XUV MICE approach can be used to measure the temporal profile of attosecond pulses all-optically. Here, the experimental configuration used in the above experiments would be adjusted such that spectral shears instead of spatial shears are applied to one of the beams. This can be done e.g. by using a pulse shaper on the IR driving laser [232, 276]. An analogous reconstruction procedure to the one demonstrated above results in the spatially resolved spectral phase, and, if the wavefront is known at one frequency, in the full spatio-temporal profile of both pulses.

6.4 Conclusion and outlook

This chapter has for the first time demonstrated the simultaneous reconstruction of the wavefronts of two independent XUV sources. XUV MICE is suitable to relate the far-field spatial signatures to the fundamental generation process. Furthermore, it offers very high resolution compared to other techniques. In slit-diffraction techniques, for example, the sampling rate of the wavefront is given by the number of different positions of the diffraction slit that is scanned across the beam profile. In contrast, methods based on interference of two XUV sources such as MICE or LSI typically offer an increased resolution of more than an order of magnitude at comparable measurement durations, since here the fundamental sampling limit is given by the detector pixel size. The main advantage of XUV MICE, however, is that it is not required to either replicate or shear the beam of interest, which in this spectral region can be very difficult. Instead, the shear is applied to an ancillary secondary beam which may be easier to manipulate. The only requirements are that both beams are mutually coherent and spatially and spectrally overlap at the detector. This technique therefore offers the potential to measure complex high harmonic sources that have been very challenging to characterise until now. Examples of such sources include quasi-phase-matched high harmonic sources [213–217], HHG from aligned molecules [277–279] or from transient gratings [280, 281], or HHG in the presence of a frequency-doubled laser field [282–288].

Chapter 7

Partial coherence in high harmonic generation

Decoherence is an ubiquitous phenomenon in experimental physics. Its consequences are, in the vast majority of cases, undesired and may compromise or even impede an experiment. Hence, a lot of effort is usually made to understand its origins and possibly minimise its influence. In the domain of attosecond science based on high harmonics, one can envisage three sources of decoherence a high harmonic experimental setup may suffer from: (1) Partial coherence of the laser field, (2) Fluctuations within the generation medium, (3) Limited detector resolution. Point (2) may, for instance, correspond to fluctuations in the gas density or an inhomogeneous gas distribution across the interaction region. In most of the used geometries and gas target designs for HHG, this has however not shown to be a problem. Regarding (3), x-ray detectors are usually based on MCPs or CCDs with enhanced spectral response in the x-ray regime. While resolution requirements are particularly stringent in imaging or interferometric applications, advanced detector designs

combined with suitable imaging geometries can be pushed to meet the needs of many experiments. Furthermore, it is possible to characterise the detector response and use this information via deconvolution to improve the effective detector performance. Partial coherence, however, is in most cases unavoidable. Partial coherence of high harmonic radiation can for instance directly be imposed by a partially coherent driving laser. In addition, the generation process itself may also degrade the coherence of the emitted harmonic field. Partial coherence is usually the component which is the least controlled and least understood or quantified in an experimental setup. This chapter therefore focuses its attention onto this latter phenomenon.

7.1 The notion of coherence in ultrafast optics

Ultrashort pulse characterisation usually assumes the electromagnetic field to be fully coherent. In this case the field amplitude and phase are well defined, and the challenge consists in retrieving the complete field. In many applications such an approach is justified. CPA laser systems for example produce trains of femtosecond pulses at high intensities. Even though such a pulse train is never perfectly stable, e.g. since it suffers from intensity fluctuations or timing jitter, the pulse duration retrieved by SPIDER or FROG is usually sufficiently accurate that one is able to use these pulses in experiments. However, it is often forgotten or at least not considered that any multi-shot device does not measure the field of a single pulse, but only the averaged field. Indeed, both FROG and SPIDER only retrieve the nonrandom component of a pulse train, which in ultrafast optics is known as the *coherent artifact* [289]. The randomly varying component cannot be measured by

conventional characterisation devices. The more the pulse properties vary from shot to shot, the less accurate and useful the retrieved pulse shape will be. In fact, the electric field of partially coherent fields is not well-defined anymore. It is for this reason that stochastic measures need to be employed which measure the statistics of the field in the pulse train. For any pulse train such a description represents the most complete and accurate description. Regarding the temporal averaging, it may of course be argued that both FROG and SPIDER are capable of single-shot measurements, and therefore reconstruct the non-averaged true electric field. However, in experiments that use a sequence of several shots, the knowledge of the pulse statistics is of high importance. In experiments where one input pulse is sufficient for its realisation it is still necessary to characterise that very same input pulse. The simultaneous characterisation of the pulse used for experiments on one hand, and that of a pick-off of a small fraction of the pulse for its characterisation on the other hand, could in principle be performed using MICE.

Partial coherence in the XUV

The above remarks were essentially directed towards infrared femtosecond pulses. However, the problem of partial coherence is expected to be much more severe in the case of XUV pulses. The reason for this is that due to the extreme nonlinearities typically involved in the generation process, initial fluctuations of the driving laser are strongly amplified. In high harmonic generation, if the driving laser were fully coherent, and no additional decoherence were imparted by the generation process, the XUV pulse should be fully coherent. In fact, the component of the harmonic phase inherited from the laser field is simply q times the laser phase. Therefore, if the laser phase is completely correlated

in space, the harmonic phase will also exhibit complete correlation. In a more realistic setting, however, the laser field will not be fully coherent, and the XUV pulse will inherit the preexisting partial coherence of the driving laser. In addition, during the generation process the coherence is usually further decreased. One reason is the time and space dependence of the atomic dipole phase, which causes the phase evolution at two points in the beam not to be exactly the same [290]. Another factor which becomes important for large intensities is the free-electron production due to ionisation of the medium. A time and space dependent electron density will build up in the medium. Small fluctuations in the density for example can alter the phase evolution for different points in the beam and in this way decrease the overall coherence [291, 292]. Even though high spatial coherence has been measured for harmonic beams [291], measuring their statistical properties is expected to greatly enhance experimental outcomes.

Experiments have also been performed regarding the temporal coherence of high harmonics, where it was found that short trajectories exhibit much larger coherence times than long trajectories because of the rapid phase variation of the latter [256, 257]. It should also be noted that probably the most extreme case where partial coherence in the XUV wavelength regime is significant is for free-electron lasers (FEL) since these are naturally incoherent. Here no two pulses are the same and indeed can fluctuate by large amounts. For this reason FEL pulses have not yet been fully characterised. Considering the concept of partial coherence in the XUV is therefore of paramount importance.

The present chapter addresses the issue of partial coherence in high harmonic generation. Spatial coherence measurements of high harmonics have almost uniquely been performed in the form of double-slit interference experiments [291–294]. Measurements

using a Fresnel-mirror interferometer [290] have also been reported. Even though such measurements provide useful information about the correlation between two specific points of the beam, they fail to provide the full statistics of the pulses. In the following chapter a method is proposed for the measurement of the two-point correlation function. Such a measurement retrieves the complete statistical properties of the beam and therefore represents the most complete characterisation. By decomposing the correlation function into coherent modes, the partial coherence is fully quantified. First, the theoretical concepts of optical coherence are introduced in section 7.2. Then a measurement procedure is developed to characterise a partially coherent beam. Finally, experimental results are shown in section 7.4.

7.2 Theory of optical coherence

The study of optical coherence attempts to determine the statistical properties of light and their influence on the observable characteristics of optical fields [295, 296]. Per definition, the concept of coherence compares the field oscillations at one given position for different instants of time (temporal coherence) or at different positions at the same time (spatial coherence). The overall field is built up by the emission coming from every point in space. If at two different positions the elementary field oscillations are in phase for all times, the field at these points is fully coherent. If, however, for example due to external decoherence, the phase evolution at one point is altered, the coherence is decreased.

7.2.1 Quantifying coherence

A commonly used quantity to describe the statistics of an electric field is the mutual coherence function Γ[1]:

$$\Gamma(\vec{r}_1, \vec{r}_2, \tau) = \langle E^*(\vec{r}_1, t_1) E(\vec{r}_2, t_2) \rangle, \tag{7.1}$$

where the angle brackets denote time averaging or, equivalently for ergodic fields, ensemble averaging of the field E at two points in space and two instants in time, with $\tau = t_2 - t_1$. For simplicity the field is usually taken as a scalar, although the formalism can readily be extended to the vectorial case [297]. A Fourier transform with respect to time results in the cross-spectral density W,

$$W(\vec{r}_1, \vec{r}_2, \omega) = \frac{1}{2\pi} \int_{-\infty}^{\infty} \Gamma(\vec{r}_1, \vec{r}_2, \tau) e^{-i\omega\tau} \mathrm{d}\tau. \tag{7.2}$$

The correlation between two points in space $\vec{r}_1$ and $\vec{r}_2$ at frequency ω is conveniently quantified by the spectral degree of coherence $\mu(\vec{r}_1, \vec{r}_2, \omega)$, which can be expressed as

$$\mu(\vec{r}_1, \vec{r}_2, \omega) = \frac{W(\vec{r}_1, \vec{r}_2, \omega)}{\sqrt{|E(\vec{r}_1, \omega)||E(\vec{r}_2, \omega)|}}. \tag{7.3}$$

The modulus of the spectral degree of coherence takes only values between 0 and 1, where 1 represents full coherence, and 0 complete incoherence. The importance of μ is that it can directly be accessed by double-slit diffraction experiments, as will be shown below.

[1] The mutual coherence function satisfies a wave equation, which means that the statistical properties of the field evolve in a well-defined manner upon propagation. A large proportion of the study of optical coherence involves studying the behaviour of the evolution of Γ.

7.2.2 Partial coherence in double-slit interferometry

Until today, Young's double slit experiment is the most prominent experiment to measure spatial coherence of a beam, and due to its simplicity, it is also the most widespread method [298, 299]. In those experiments a partially coherent wave field impinges onto a double slit, as shown in figure 7.1. The field at a point P in the plane of a spectrally resolving detector is given by the squared modulus of the sum of the two fields,

$$\begin{aligned} I(\vec{r},\omega) &= |K_1 E(\vec{\xi_1},\omega) + K_2 E(\vec{\xi_2},\omega)|^2 \\ &= |K_1|^2 |E(\vec{\xi_1},\omega)|^2 + |K_2|^2 |E(\vec{\xi_2},\omega)|^2 \\ &+ 2\sqrt{|E(\vec{\xi_1},\omega)||E(\vec{\xi_2},\omega)|}\mathrm{Re}\{K_1^* K_2 \mu(\omega)\}. \end{aligned} \tag{7.4}$$

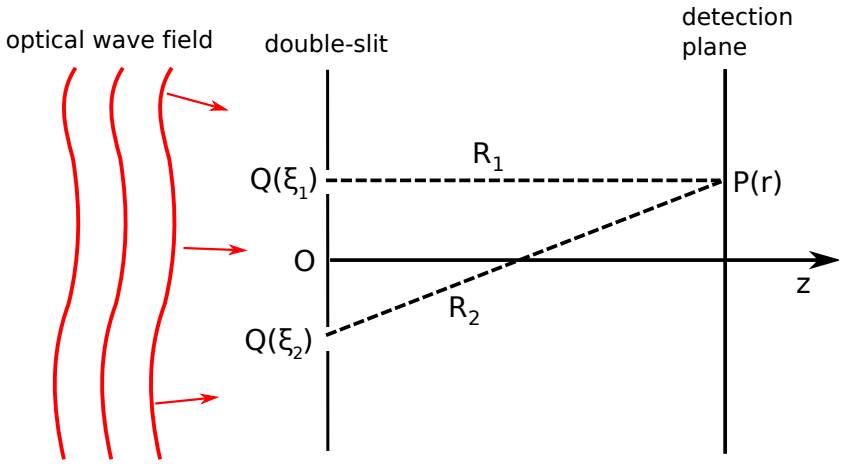

Figure 7.1: Young's double-slit experiment. A partially coherent light field impinges onto the double-slit. The fields from both slits diffract into the far-field where they add up coherently and form and interference pattern, the phase of which depends on the paths difference between the two source locations and P.

The propagation of the field between the slit location Q and the point P in the detection plane is given by the propagator K_i for field i:

$$K_i = -\frac{ikA}{2\pi}\frac{\exp(ikR_i)}{R_i}, \tag{7.5}$$

where R is the distance between Q and P. Often valid assumptions are $|K_1| \approx |K_2| = K$ and $|E(\vec{\xi_1}, \omega)|^2 \approx |E(\vec{\xi_2}\,\omega)|^2 = |E(\omega)|^2$. Writing $\mu(\omega) = |\mu(\omega)|\exp(i\phi)$ and $K_1^* K_2 = K^2 \exp(ik(R_2 - R_1)$, the interferogram in equation (7.4) reduces to

$$I(\vec{r}, \omega) = 2K^2|E(\omega)|^2(1 + |\mu(\omega)|\cos[\phi + k(R_2 - R_1)]. \tag{7.6}$$

A key parameter to characterise the interferogram in (7.6) is the fringe visibility V, defined by

$$V(\omega) = \frac{I_{max}(\omega) - I_{min}(\omega)}{I_{max}(\omega) + I_{min}(\omega)}. \tag{7.7}$$

By inserting the corresponding values for I_{max} and I_{min} from equation (7.6) into (7.7), it follows that the fringe visibility in a double-slit experiment is a direct measure of the modulus of the spectral degree of coherence at the two pinholes,

$$V(\omega) = |\mu(\omega)|. \tag{7.8}$$

This result forms the basis of almost all coherence measurements of high harmonic radiation until today [201, 239]. However, although such kinds of experiments provide a good estimation of the spatial coherence across the beam, they do not represent a field charac-

terisation as such since they only determine the correlation of one point with one other point. To fully characterise the beam, the correlation of each point x with each x', here taken for one spatial dimension x, needs to be measured. The quantity representing such a measurement is the two-point correlation function $C(x, x')$, which is essentially derived from $\Gamma(\vec{r}_1, \vec{r}_2, \tau = 0)$ for equal times,

$$C(x, x') = \langle E(x)E^*(x')\rangle. \tag{7.9}$$

The degree of coherence then takes the form

$$\mu = \frac{\iint \mathrm{d}x\mathrm{d}x' |C(x, x')|^2}{\left(\int\limits_{x=x'} \mathrm{d}x C(x, x)\right)^2} \tag{7.10}$$

$C(x, x')$ contains all possible second-order correlations between points in space and thus represents a full statistical representation of the field.

7.2.3 Reconstruction of state mixtures

A very powerful way to characterise a partially coherent light field is to think about it in terms of pure and mixed states. The two-point correlation function may then be described in terms of its eigenvalues λ_n and eigenfunctions ψ_n:

$$C(x, x') = \sum_n \lambda_n \psi_n^*(x)\psi_n(x'), \tag{7.11}$$

where the eigenfunctions and eigenvalues satisfy

$$\int C(x,x')\psi_n(x)dx = \lambda_n\psi_n(x'). \tag{7.12}$$

The eigenfunctions can be made orthonormal according to

$$\int \psi_n^*(x)\psi_{n'}(x)\mathrm{d}x = \delta_{n,n'}, \tag{7.13}$$

and form a complete set

$$\sum_n \psi_n^*(x)\psi_n(x') = \delta(x-x'). \tag{7.14}$$

Equation (7.11) represents the *coherent mode decomposition*, where the positive-valued eigenvalues λ_n indicate the weight of each mode [296, 300, 301]. The overall level of coherence or purity is given by

$$\nu = \frac{\left(\int_n \lambda_n^2\right)^{1/2}}{\int_n \lambda_n}. \tag{7.15}$$

For $\nu = 1$ the field is in a pure state, whereas $\nu < 1$ represents a mixed state. $1/\nu^2$ quantifies the effective number of significant coherent modes.

Interestingly, the presented formalism is very similar to quantum state tomography in quantum optics, the aim of which is to reconstruct the full density matrix of a photon [302, 303]. The concept of decoherence and mixed states is of course fundamental in this context and turns out to be most fruitful in its application to others domains, including classical optics. One prominent example is the field of coherent diffractive imaging, where the knowledge of the underlying modes of a partially coherent x-ray beam has led to

dramatic improvements of the resolution of the reconstructed images [304].

Finally, we note that the retrieval of mixed states in HHG experiments includes all three sources of decoherence that were mentioned at the beginning of this chapter: Partial coherence of the light field, decoherence within the medium, and detector point spread. Different experimental configurations may suffer from each of those with different weight. While in HHG interferometry partial coherence is expected to be much more problematic than medium fluctuations, the latter are usually a major concern in coherent diffractive imaging applications, most notably in the form of vibrations of the sample [305].

7.3 Measurement of the two-point correlation function - theory

We propose to measure the two-point correlation function by carrier-encoded lateral shearing interferometry using multiple shears [306]. In fact, the experimental procedure is identical to the one used for the MICE reconstruction in chapter 6. A series of lateral shears X is applied to one of the driving beams exiting the Mach-Zehnder interferometer, which moves one of the generated harmonic beams across the profile of the other beam at the detector. The recorded interferogram for $x' = x - X$ and tilt K then becomes

$$I(x) = |E(x)|^2 + |E(x')|^2 + E(x)E^*(x') \exp(i(Kx + Xkx/L)) + c.c. \tag{7.16}$$

In analogy to equation (6.1) the term Xkx/L represents an additional phase introduced for each shear which results in a tilt of the fringes. However, in an experiment this phase can

be calibrated and compensated for. By applying a suitable filter in the Fourier domain, one of the two sidebands at $k = \pm K$ is extracted. An inverse Fourier transform directly yields the interferometric component $\langle E(x)E^*(x')\exp(iKx)\rangle = C(x,x')\exp(iKx)$. The angle brackets denote ensemble averaging. Importantly, this includes temporal averaging, which needs to be longer than the temporal fluctuations of the source. For each shear the corresponding two-source interferogram is recorded. One single interferogram corresponds to one slice of the correlation function. In terms of Young's experiment, this corresponds to the scenario where one slit position is fixed while the other slit is scanned across the full extent of the beam. By combining the measurements of many lateral shears, the complete correlation function is retrieved.

The idea for the measurement of the correlation function is first demonstrated by simulating the reconstruction procedure. The initial electric field is defined on a grid of 400 spatial points and 40 shots. One shot represents one physical realisation of the field, and the correlation function then averages over all shots. The electric field varies in amplitude and phase from shot to shot. The electric field amplitude and the unwrapped phase are shown in figures 7.2(a) and (b), respectively [307]. The two-point correlation function associated with this ensemble of fields is shown in amplitude in 7.2(c) and phase in 7.2(d). The ensemble-averaged field is then replicated and sheared across the spatial profile of the stationary beam. Figure 7.3(a) illustrates the full shear scan. A noise level of 1% of the maximum of the most intense interferogram, weighted by a random value taken from the interval (0,1) for each pixel, has been added to the trace. After a 2D Fourier transform, Fourier filtering allows the extraction of one of the sidebands, as highlighted by the black rectangle in figure 7.3(c). An inverse 2D Fourier transform brings the trace

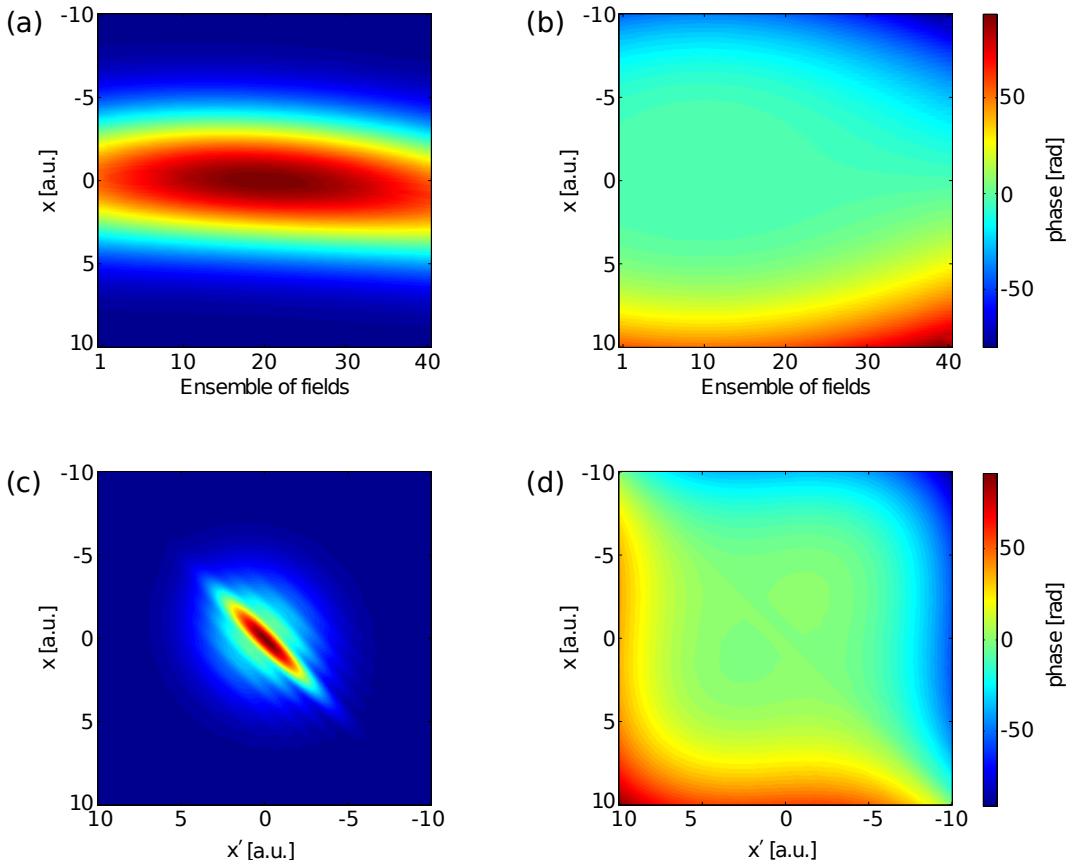

Figure 7.2: Illustration of the original ensemble of fields. (a) Amplitude and (b) phase. The associated two-point correlation function for this ensemble is shown in (c) in amplitude and (d) phase.

back to the original domain. After a row rotation of the trace for compensation of the shear, and subtraction of the carrier phase, the correlation function is retrieved, as shown in figures 7.3(c)-(d). The reconstruction shows a remarkable accuracy with respect to the original trace and thus illustrates the validity of this procedure.

7.3.1 Spectral mode decomposition

In order to characterise the purity of the field, $C(x, x')$ is decomposed into its underlying coherent modes. This is done by means of an eigenvalue decomposition, where the different modes correspond to the associated eigenvectors, weighted by the eigenvalues.

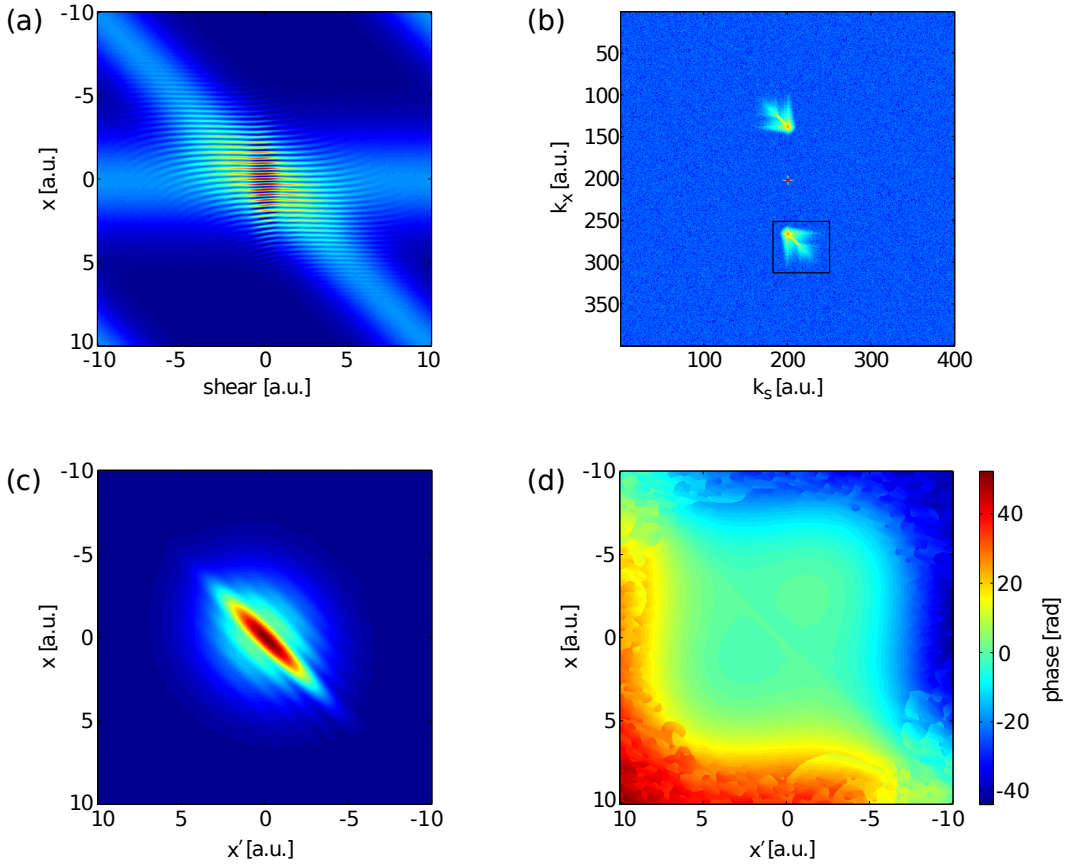

Figure 7.3: Reconstruction of the correlation function. (a) Full shear scan, where a replica of the field is sheared along the x-axis across the original field. A noise level of 1% of the maximum of the most intense interferogram has been added to the trace. (b) Fourier domain filtering routine. The black rectangle highlights the filter. (c)-(d) Amplitude and phase of the reconstructed correlation function, respectively.

The reconstruction of the first 15 modes is drawn in figure 7.4 for the original field in (a) and the reconstructed field in (b). The original (retrieved) purity equals 0.55 (0.56), with an effective mode number of 3.3 (3.2). Furthermore, figures 7.4(c)-(d) show the first 4 modes for both cases. Even though the first mode is dominating the field, there are several other modes that contribute to the overall field. The shape of the higher-order modes becomes more and more complex. For this simulation the original field has been chosen with complex amplitude and phase fluctuations from shot to shot to demonstrate

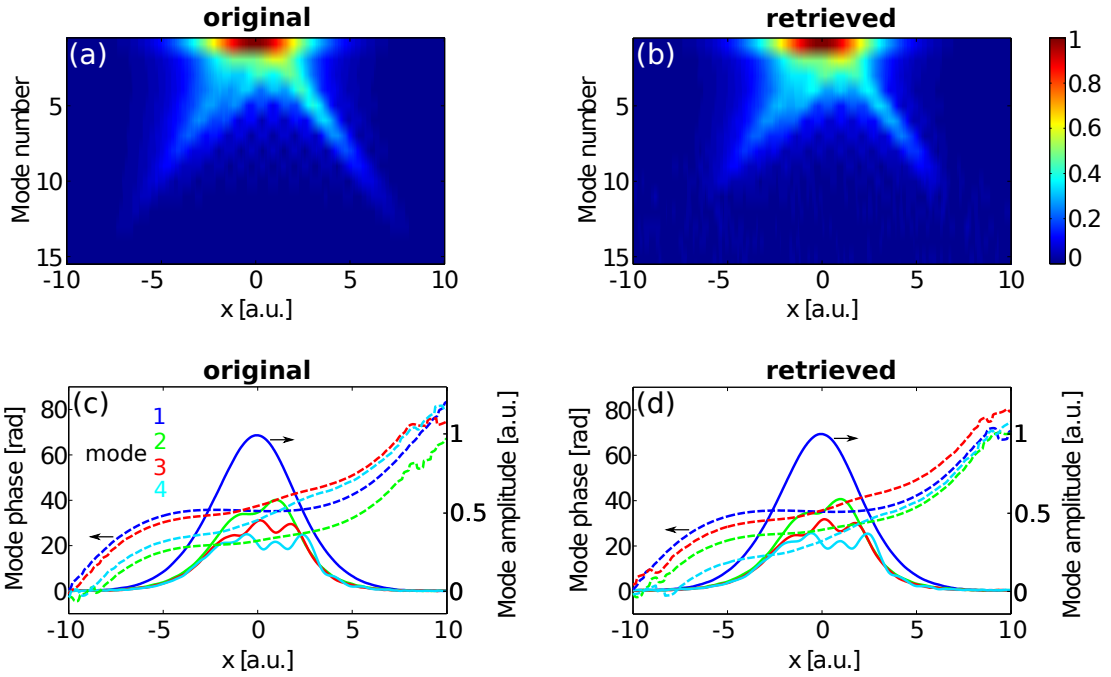

Figure 7.4: Estimation of the modal composition. The modulus of the original and retrieved modes are shown in (a) and (b), respectively. (c) and (d) plot the amplitudes (solid lines) and phases (dashed lines) of the first 4 modes in both cases. The amplitudes and phases of the modes are drawn with the same colour for each mode.

this feature. In reality, however, for the case of a typical laser field used in laboratories it may be sufficient to describe the field by very few modes only, with the first mode being the dominant mode. As a cross-check, the same reconstruction was applied to a field which stays identical from shot to shot. In this case the correlation function is a matrix of rank one and the mode decomposition yields only one mode with the purity being 1.0.

7.4 Measurement of the two-point correlation function - experiment

The measurement concept detailed above has been implemented in the laboratory. The recipe for the experimental procedure is very similar to the one for the MICE reconstruc-

tion of high harmonic wavefronts in chapter 6. The main difference is that now the profile of one beam needs to be sheared across the full profile of the second beam in order to measure the correlations between all pairs (x, x'). In contrast, in MICE it is sufficient to consider an angular shear range where both beams are always reasonably well overlapped in the far-field. A larger number of shears increases the redundancy in the data, however, a reasonably small number of shears is often sufficient for a good reconstruction when the datasets that are not too noisy. In the following experiments, the necessity to cover the whole spatial extent added a significant amount of complexity for several reasons:

1. The shear range is much larger than the size of the MCP. In fact, the measurement is started where only a small fraction of the sheared arm is hitting the MCP. This does not impede the experiment, since the crucial regions of the signal are where interferences occur. If the dimension of one harmonic beam is not larger than the size of the MCP, these regions will always be located on the detector. However, this configuration is not ideal, and in particular where the sheared arm is strongly clipped by the edges of the MCP distortions of the signal may occur.

2. Due to the increased angular shear range, and since the gas target is not placed exactly at the focus, the requirement of having two independent sources becomes more stringent. To prevent the two fields from interacting with each other even for large angular shears, the source separation has to be set as large as possible. Since this entails a decreasing XUV fringe spacing, this needs to be compromised with the decrease in fringe visibility, which has to remain adequate for the reconstruction.

3. The two sources need to be identical, and must not change for varying shears. In

practice, this represents a significant experimental challenge. In addition, although generating two identical harmonic beams has already been found to be vey challenging in previous experiments [232, 240], this task is dramatically more difficult for QPI sources. The large intensity-dependence of long trajectories and the extreme sensitivity of the interferences between the different quantum paths makes it difficult to replicate such a source. Tiny differences in the clamping strengths of the mirrors inside the interferometer, slight bending of the thin beamsplitters, or any other small asymmetry in the setup can change the wavefronts of the IR beams. Since these distortions are amplified in HHG by a factor equal to the harmonic order, even small differences of the driving beams may result in significant differences in amplitude and divergence of the harmonics. Therefore, very careful beam alignment, mounting of the optics, and the selection of optics from the same batch are some of the required steps to obtain identical sources.

7.4.1 Initialisation

Before the shear scan can be performed, it needs to be ensured that the two harmonic beams are very close to identical. As explained above, great care needs to be taken regarding the setup and the alignment to achieve this. Figure 7.5 shows the individual spectra from both arms for harmonics 17-25. The correspondence is remarkable, both in the central part of the harmonic and in particular also in the surrounding annular part originating from the highly intensity-sensitive long trajectories.

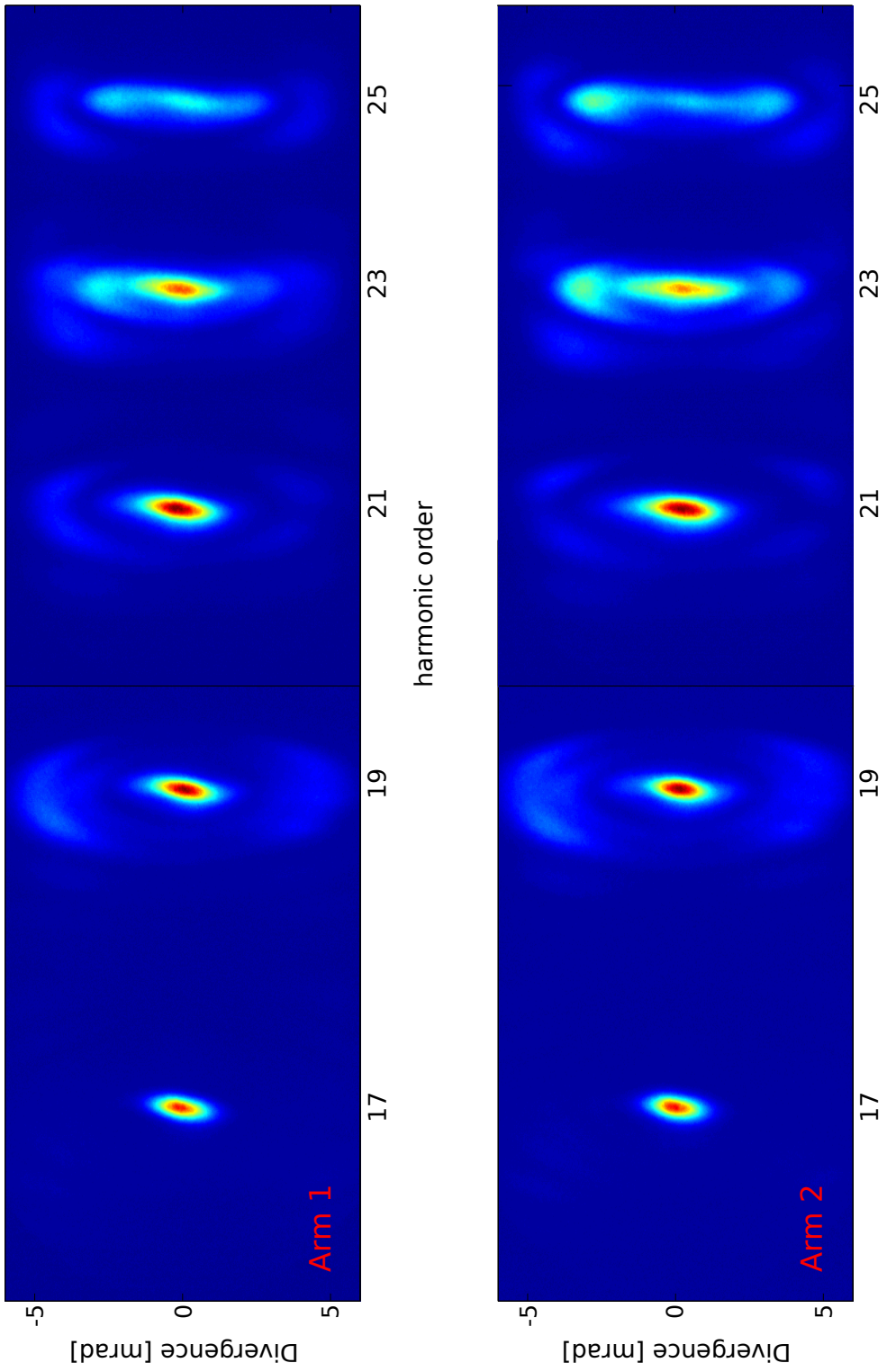

Figure 7.5: Initialisation step: The spatio-spectral profiles of both beams are nearly identical. This is particularly difficult for the long-trajectory halo due to its strong intensity dependence.

7.4.2 Reconstruction

This section details the analysis of harmonic 21, since its profile exhibits QPI interferences where the first fringe is well separated from the central part of the harmonic (see figure 7.5). A spatial lineout at the centre frequency of the harmonic is taken for the full dataset. The experimental setup is identical to the one shown in figure 6.1, which was used for the MICE experiments of chapter 6. In analogy to MICE, interferometer Arm 2 is laterally sheared with respect to Arm 1 which shifts the generated XUV beam from Arm 2 across the profile of the other beam at the detector, as illustrated in figure 6.1. Figure 7.6 shows the interferograms for three different values of the angular shear for harmonics 17-25. For increasing shears, the beam of the nonstationary beam moves "downwards" at the detector. In figure 7.6(a), only a small fraction of the beam, corresponding the long trajectories, is contained within the detector area. Here the annular long trajectory contributions from both beams interfere on opposite sides of the two beams. In figure 7.6(b), both beams are well overlapped, and very pronounced interference fringes between the long trajectories of both beams, and separately between the short trajectories, are visible. Finally, figure 7.6(c) illustrates the opposite scenario of (a) for a very large shear, where part of the sheared beam has already moved beyond the lower edge of the detector.

The experiment is performed at a peak intensity of 1.2×10^{14} W/cm^2. The spectra of the individual arms are integrated over 6 ms and averaged over 20 measurements. In contrast, the integration time of the interferograms is varied between 5 ms and 37 ms for optimal signal-to-noise ratio at each shear position, with an average taken over 20 measurements each time.

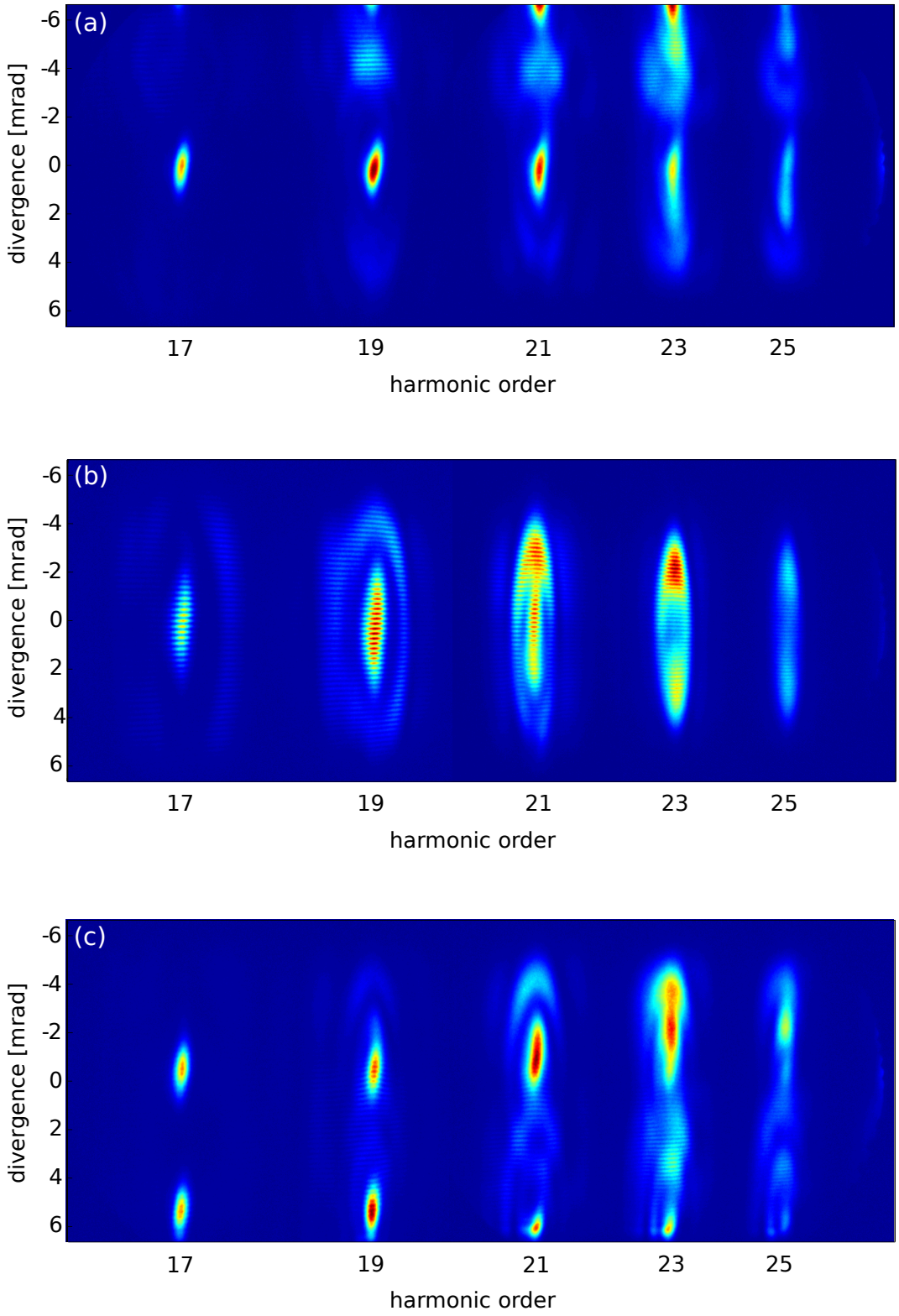

Figure 7.6: Interferometric traces for three different angular shears of the nonstationary beam. The sheared beam is moving downwards for increasing shears. (a) Only a small fraction of the sheared arm is within the detector area. Only long trajectory components of opposite ends of the halo from both beams exhibit interference. (b) Interferogram where both beams are well overlapped. (c) Interferogram where the largest part of the sheared arm has moved beyond the lower detector edge.

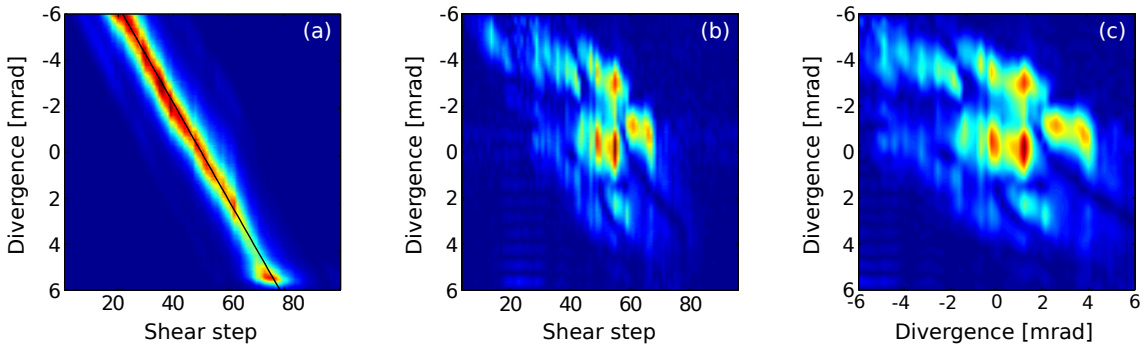

Figure 7.7: Data processing for the retrieval of the two-point correlation function of harmonic 21. (a) Shear axis calibration. (b) Extracted AC term. (c) AC term after interpolation along the shear axis.

The reconstruction involves first a calibration of the shear axis, which is shown in figure 7.7(a). The depicted image shows reduced signal for large shears. This appeared to be independent of alignment. A possible explanation is a non-uniform detector sensitivity. In this case the real signal before arriving at the detector would stay the same, and the overall reconstruction should not be affected by this. However, future improvements of the experiment may benefit from a calibration of the detector response. An alternative explanation might be based on slow drifts in the setup due to temperature fluctuations, which typically occur on the timescale of tens of seconds or longer.

As a next step, a Fourier filtering routine retrieves the AC term, the modulus of which is shown in figure 7.7(b). The vertical axis represents the divergence θ, whereas the horizontal axis corresponds to the shear index. In order to represent the correlation function $C(\theta, \theta')$ on equal axes, the shear axis is interpolated, by making use of the shear calibration, to match the θ-axis. This step is illustrated in figure 7.7(c). Finally, a row rotation is performed, which results in the final two-point correlation function $C(\theta, \theta')$. Its absolute value is depicted in figure 7.8(a). To obtain the phase of $C(\theta, \theta')$, the linear

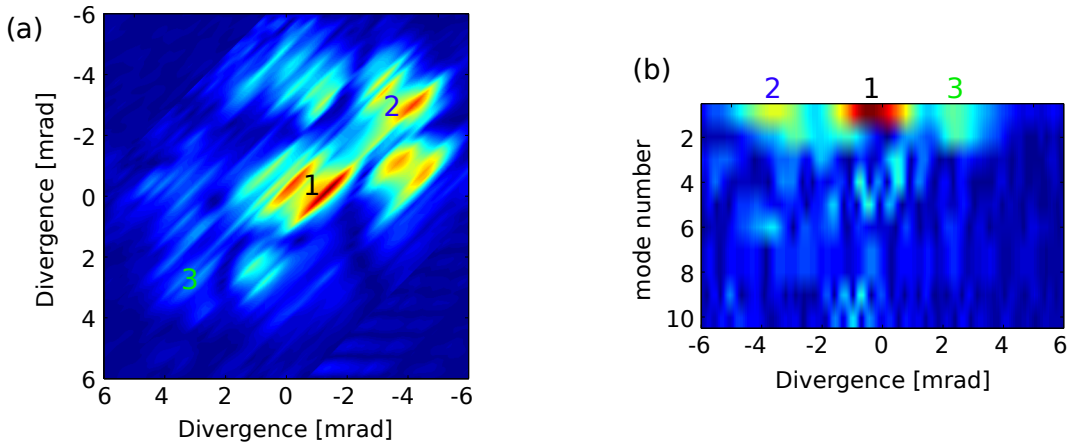

Figure 7.8: Reconstruction of the two-point correlation function of harmonic 21 and decomposition into coherent states. (a) Reconstructed correlation function. (b) Coherent mode decomposition, showing the first 10 modes. Region (1) indicates signal from short trajectories, regions (2) and (3) from long trajectories.

carrier term Kx needs to be subtracted. For this aim the tilt $K = 2\pi s/(\lambda L)$ has been determined by measuring the IR foci separation $s = 174.2$ μm. However, it turned out that the resulting phase was very noisy, hiding any underlying phase structure. In order to proceed with the analysis, the phase has therefore been set to zero. Lastly, the correlation function is decomposed into coherent modes. Figure 7.8(b) shows the mode profiles of the first 10 modes. The results of the reconstruction are discussed in the next section.

7.4.3 Discussion

Regarding the correlation function in figure 7.8(a), different regions can be distinguished. As indicated in the figure, region (1) corresponds to the central short trajectory harmonics which show high coherence. Regions (2) and (3) may be attributed to the long quantum paths. Indeed, a lineout along the diagonal $\theta = \theta'$ should correspond to the intensity profile of the harmonic. This is in qualitative agreement with the profile shown in figure 7.5, with the upper section of the annular ring of harmonic 21 (corresponding to region (2)

in figure 7.8(a)) being more intense than the lower section (corresponding to region (3)). The origin of the off-centre non-diagonal components has not yet been fully identified. It is possible that they are consequences of the long trajectories since they vanish for harmonic 17 where almost no long trajectories are detected, as will be shown below. However, understanding the full underlying physics would require further investigation, possibly supported by simulations and theoretical modelling.

An undesired effect that results from the shot-to-shot fluctuations is that the shape of the different regions in $C(\theta, \theta')$ appears highly structured. After the row rotation, this sub-structure appears to be tilted in figure 7.8(a). However, in a scenario with very low fluctuations, the different lobes are expected to exhibit smooth shapes, and the internal structure should mostly disappear.

Despite these effects, $C(\theta, \theta')$ is decomposed into coherent modes. Figure 7.8(b) indicates that mainly 2 modes are contributing to the overall partially coherent field. Even though the decomposition is only expected to provide at best qualitative results since the phase of $C(\theta, \theta')$ has been set to zero, the obtained modes explain the basic spatial features of the harmonics. Indeed, the first mode is supposed to simply represent the harmonic spatial profile. This is clearly observed in figure 7.8 where region (1) corresponds to short trajectories, and (2) and (3) can be associated with long trajectories.

To validate the above findings, the same analysis is performed for harmonic 17. As can be seen in figure 7.5, the halo surrounding the short trajectory component is very weak. This is reflected in the retrieved correlation function, shown in figure 7.9(a), where the off-centered diagonal lobes have almost disappeared. Regarding the associated mode decomposition in figure 7.9(b), modes with n>2 are even less important than in the case

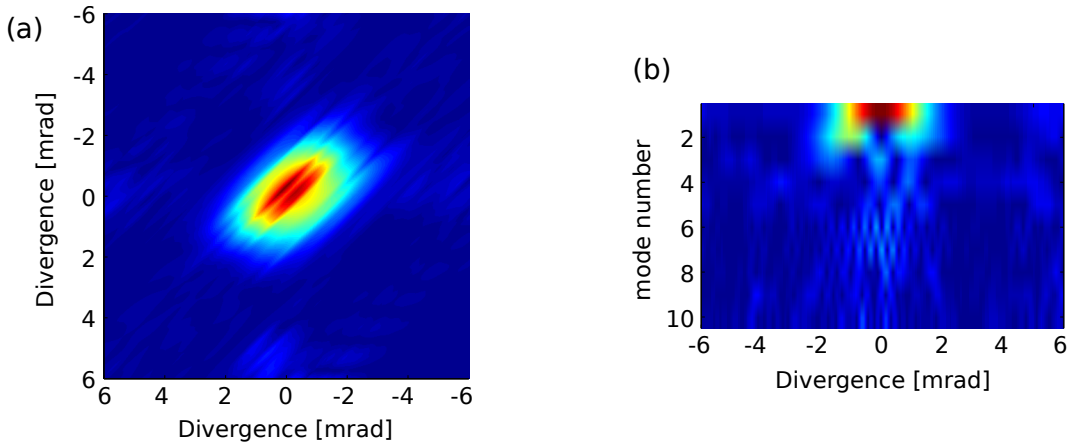

Figure 7.9: Reconstruction of the two-point correlation function of harmonic 17 and decomposition into coherent states. (a) Reconstructed correlation function. (b) Coherent mode decomposition, showing the first 10 modes.

of harmonic 21. In particular, the first mode now consists of only one central peak, which agrees with the interpretation of the contribution of only the short quantum path.

7.5 Conclusion and outlook

Partial coherence, fluctuations within the generating medium, and the detector point spread are all sources of decoherence that may significantly compromise the capability of high harmonic setups. It is only to a limited amount that these can be alleviated in the laboratory through experimental or technological progress. A method to quantify, and possible even correct for, these sources of decoherence is therefore of uttermost importance. The most general description of such a scenario is using statistical tools, in particular correlation functions, and the concept of state mixtures. In this chapter an experiment has been proposed that, from a series of sheared interferograms, retrieves the two-point correlation function of high harmonic beams. A coherent mode decomposition allows the quantification of the degree of coherence present in the experiment. Preliminary

experimental data has been taken, and the amount partial coherence within this dataset has been estimated. Although the fringe visibility was excellent for all angular shears and for both quantum paths, the strong shot-to-shot fluctuations imposed a limit to the reliability of the reconstruction. Some of the artifacts observed can clearly be traced back to this source of error.

In the current experimental setup, the complete beam path between the CPA and the vacuum apparatus was enclosed. However, due to other experimental activity in the laboratory, it was not possible to globally enclose the full table with large lids that cover the full width of the table. Instead, the setup was enclosed in a modular way using boxes and beam tubes that are attached together. Even though no major gap was left, this does not represent a perfect seal for protection against the strong air-conditioning.

A different source of noise comes from the vibrations of the vacuum pumps. However, there are a few ways to improve the vibration isolation in the laboratory [308, 309]. First, the breadboard inside the vacuum chamber can be directly mounted on the optical table, with the posts passing through edge-welded bellows between the chamber and the table. In this way the optics inside the chambers (in the Oxford lab this mainly concerns the XUV grating) are rigidly mounted on the high-mass optical table and are isolated from the vacuum chambers. Second, the chambers and vacuum pumps may be supported on steel frames that have no contact with the optical table. The bellows prevent vibrations originating from the vacuum pumps from reaching the optical table. Third, the pump vibrations can further be damped by immersing the hydroformed flexible bellows attaching the pumps to the vacuum chambers into large bins filled with silica sand. Since the pumps are the mains source of vibrations, these measures are expected to significantly improve

the stability of the setup.

Finally, partial coherence of the source can be minimised, for instance, by stabilising the intensity, possibly combined with a carrier-envelope phase (CEP) stabilisation. Although fluctuations of the CEP are not expected to play a major role for multi-cycle pulses, an intensity- and CEP-stabilised laser would provide a more stable pulse train also for shorter pulse durations. It is planned to implement the CEP stabilisation of the laser in the Oxford Attolab soon.

Chapter 8

Conclusion

The desire to study the fastest motions in nature has made attoscience one of the most dynamic fields of physics today. The prospect of freezing motion promises accessing new regimes and timescales that have been hidden until now. A popular concept is the aim to produce real-time "movies" of chemical processes and watch electrons in molecules form and break bonds during chemical reactions. The combination of tools from atomic and laser physics has created sources of XUV attosecond pulses, most notably through high harmonic generation. Today, HHG represents a versatile table-top source of ultrashort XUV pulses. Underlying theories, explaining HHG in terms of the single-atom response on the one hand, and the macroscopic response describing the coherent superposition of the emission of all atoms on the other hand, have successfully explained many properties of HHG observed in experiments.

Due to its extreme nature, the characterisation of high harmonic radiation is very difficult, and most methods developed in the field of femtosecond pulse characterisation are not directly applicable to this more exotic regime anymore. Instead, new concepts

need to be developed that take into account the extreme brevity of the pulses and the fact that their carrier wavelength lies in the XUV to soft x-ray wavelength range. Almost all techniques for the temporal characterisation of attosecond pulses rely on photoelectron spectroscopy. Since these measurements require very long integration times, and due to their cost and the experimental complexity in their setting up and operation, alternative routes towards the complete spatio-temporal characterisation are being sought with great interest and effort.

8.1 Summary

This thesis describes the development of all-optical pulse characterisation methods and their application to the study of the HHG process. Most importantly, the concept of Mutual Interferometric Characterisation of two Electric-fields (MICE) has been developed, which allows the retrieval of the electric field of two independent beams, including their relative phase. MICE generalises the concepts of referencing interferometry (one beam is known, one unknown) and self-referencing interferometry (both beams are unknown, but not independent of each other) to the case where both signal pulses are unknown and independent. Major advantages of MICE include: (1) No reference is required. (2) It is not necessary to either replicate or shear the beam that is to be characterised. This is particularly important when MICE is applied to extreme light sources where it is very difficult to achieve this task. In chapter 6, this feature has been exploited by transferring MICE to the XUV regime. (3) The concept of MICE is very general. It can be applied to both the temporal and the spatial characterisation, or a combination of those. (4) In its most

general form, MICE reconstructs three fields: the two test beams and a third field that quantifies the shear-dependent change of the amplitude and phase of the sheared beam. This feature is extremely useful, since it takes into account spurious effects that may occur in the measurement process and which would otherwise prevent the measurement from producing accurate results. For instance, this may correspond to the change of amplitude and phase of the test pulse in the upconversion with an ancillary beam (see chapter 3). (5) MICE is highly robust to noise. The reason for this is that it utilises methods for noise suppression from both interferometry, via Fourier filtering, and spectrography, via least-squares minimisation.

The general applicability of MICE has been experimentally demonstrated on two fundamentally different examples. First, the temporal profiles of two femtosecond pulses have been reconstructed in a single laser shot. Second, MICE has been used to reconstruct the wavefronts of two high harmonic sources.

Further, this thesis describes experiments which were aimed at studying the fundamental HHG process in terms of the different quantum trajectories. Not only was it possible to detect spatial signatures from the short and the long trajectories, but it was also possible to observe inferences between them. These quantum path interferences are very sensitive and a direct consequence of the sub-cycle electron dynamics. The experimental setup therefore represents an ideal testbed for probing the subtleties of the generation process. In this regard, it was not only possible to generate one QPI source, but in fact two QPI sources, and the interference pattern of both was studied and optimised. Such a configuration has been used to directly measure the difference in atomic dipole phases between the two main quantum paths.

Finally, the concept of ultrashort pulse characterisation has been reconsidered in the case where decoherence prevents conventional characterisation methods to provide accurate results. In particular in more exotic parameter spaces, this phenomenon can be significant due to (1) partial coherence of the driving laser, (2) fluctuations of the generation medium, and (3) limited detector resolution. Experiments that require high resolution such as interferometry or coherent diffractive imaging [310] may become significantly compromised by those effects. Only to some extent it may be possible to alleviate these effects by technical improvements of the setup.

A complementary and maybe more elegant way is to alter the processing of the data and to take into account the possibility of the occurrence of mixed states instead of a single pure state. In chapter 7 such a method has been developed. Based on an interferometric experiment with multiple lateral shears it is possible to directly extract the two-point correlation function. The correlation function represents a statistical description of the field, averaged over an ensemble of fields. The amount of decoherence can further be quantified by decomposing the correlation function into coherent modes. For partially coherent fields, more than one mode will appear in the decomposition, indicating the presence of a mixed state. This procedure has been experimentally implemented. As an important step it has been demonstrated that is is possible to generate two nearly identical QPI sources. Using a complete shear scan, the correlation function has been reconstructed and it was possible to draw some qualitative conclusions related to its structure. However, an full quantitative analysis was not possible at this stage. This was mainly attributed to the strong shot-to-shot fluctuations of the harmonics, which led to distortions of the trace in amplitude and phase. However, several possibilities have been proposed to significantly

improve the stability of the setup. Furthermore, due to the rich physics involved in the measurement of the states mixtures present in QPI sources, a proper interpretation of the data would require simulations of the emitted harmonic field. To take into account the complete physics involved in the process, those simulations need to include the single-atom response as well as propagation of the laser and harmonic fields in the medium. Such simulations are computationally involved and were not available in Oxford. However, recent possibilities for a collaboration will provide the group with such simulated data. These simulations, combined with further measurements on an improved setup, will help to unravel the physics behind QPI.

8.2 Outlook

The tools and concepts developed in this thesis promise to have applications in a wide range of experiments. MICE may be used in any application where a spatial or temporal beam characterisation is desired. In order to be able to perform MICE, either the beam of interest needs to be replicated and sheared in the dimension of interest, or a secondary source is available to which the shear can be applied. The latter option may often be preferred, especially in the cases of more exotic light sources such as XUV fields from HHG. The only requirements are that the fields are mutually coherent and that they overlap in the degree of freedom that is associated with the shear.

Even though MICE can readily be used instead of conventional characterisation techniques such as SPIDER or FROG, more interesting scenarios are those where conventional methods fail to reconstruct the field, and where one can benefit from the particular

strengths of MICE. One such example is the reconstruction of a pulse exhibiting large spectral gaps. With SPIDER it has been shown that the relative phase between the spectral regions on opposite sides of the gap can only be recovered if the pulse contains a spectral region the extent of which is larger than the spectral null. This constraint is relaxed in MICE, where an ancillary pulse that covers the spectrum of the test pulse and which has no spectral gaps is used to recover the relative phase between very large gaps. This application of MICE in fact represents a current research project pursued in Oxford, and simulations applying MICE to such a scenario have already succeeded in recovering the phase over large spectral gaps. This feature is particularly interesting regarding the emerging field of pulse synthesis, where different spectral components are coherently combined to one output pulse. MICE may also prove useful in the characterisation of highly structured pulses, such as the output of hollow-core fibres or photonic crystal fibres.

The application of MICE to the XUV opens the possibility to characterise the full spatio-temporal profile of XUV attosecond pulses all-optically. In this regard the spatial characterisation of different harmonics has been demonstrated in this thesis. Regarding the temporal characterisation, spectral shears instead of spatial shears need to be applied to one of the XUV beams, which may be achieved using a pulse shaper. Indeed, one of the main difficulties in applying self-referencing techniques to the XUV is the difficulty in producing a frequency-sheared but otherwise identical replica of the harmonic beam that is to be characterised. This constraint is alleviated in MICE, making it an attractive alternative to all-optical characterisation methods. Moreover, MICE will be of particular interest in the characterisation of complex HHG sources that cannot be replicated or sheared. Examples of such sources are those where more than one laser beam is involved

in the generation process such as quasi-phase-matched high harmonic sources, HHG from aligned molecules or transient gratings, and HHG in the presence of a frequency-doubled laser field.

Finally, the quantification of partially coherent XUV light and other sources of decoherence is of paramount importance, in particular for experiments that require high resolution such as interferometry or coherent diffractive imaging. Knowledge about the nature of the state mixtures present in the system promises great advancement in all HHG experiments, similar to the developments the mixed states approach has experienced in ptychography. In combination with MICE, these interferometric characterisation tools provide maximum information about the electric field. It is expected that their application to a wide of range of experiments and parameter spaces will be most fruitful.

Appendix A

Zernike polynomial expansion in aberrated optical systems

The Zernike polynomials form a complete set of orthogonal basis functions over a unit circle and are as such ideally suited as a tool to quantify the shape of wavefronts and their aberrations. The wave aberration function can be decomposed in terms of the Zernike polynomials

$$W(\rho,\theta) = \sum_{n=0}^{\infty} \sum_{m=0}^{n} c_{nm} Z_n^m(\rho,\theta), \tag{A.1}$$

where n and m are non-negative integers with $n - m \geq 0$. The even polynomials are

$$Z_n^m(\rho,\theta) = [2(n+1)/(1+\delta_{m0})]^{1/2} R_n^m(\rho)\cos(m\theta), \tag{A.2}$$

and the odd ones are

$$Z_n^{-m}(\rho,\theta) = [2(n+1)/(1+\delta_{m0})]^{1/2} R_n^m(\rho)\sin(m\theta), \tag{A.3}$$

with the Kronecker delta δ_{ij}. In (A.2) and (A.3), the polynomials have been normalised, and therefore form an orthonormal basis. The radial circle polynomials are given by

$$R_n^m(\rho) = \sum_{s=0}^{(n-m)/2} \frac{(-1)^s (n-s)!}{s!(\frac{n+m}{2}-s)!(\frac{n-m}{2}-s)!} \rho^{n-2s}. \tag{A.4}$$

Since the Zernike polynomials are orthogonal, they satisfy the orthogonality condition

$$\frac{1}{\pi} \int_0^1 \int_0^{2\pi} Z_n^m(\rho,\theta) Z_{n'}^{m'}(\rho,\theta) \rho \mathrm{d}\rho \mathrm{d}\theta = \delta_{mm'} \delta_{nn'}. \tag{A.5}$$

Any aberration function can be decomposed into Zernike polynomials according to (A.1), whereby the expansion coefficients are determined by

$$c_{nm} = \frac{1}{\pi} \int_0^1 \int_0^{2\pi} W(\rho,\theta) Z_n^m(\rho,\theta) \rho \mathrm{d}\rho \mathrm{d}\theta. \tag{A.6}$$

One main advantage of using the Zernike polynomials is that the standard deviation of the an aberration term $c_{nm} Z_n^m(\rho,\theta)$ is simply equal to the corresponding expansion coefficient c_{nm}. The magnitude of the different aberrations can therefore easily be determined. The Zernike polynomials up to fourth order are shown in table A.1 [77, 311]. Here, ρ and θ represent the polar coordinates at the circular exit pupil of an optical system. Indicated are also the aberrations associated with each polynomial.

Table A.1: Mathematical expressions of the Zernike Polynomials up to fourth order, together with the corresponding aberrations.

n	m	$Z_n^m(\rho,\theta)$	Aberration
0	0	1	Piston (constant term)
1	-1	$2\rho\sin(\theta)$	Tilt in y-direction
1	1	$2\rho\cos(\theta)$	Tilt in x-direction
2	-2	$\sqrt{6}\rho^2\sin(2\theta)$	Primary astigmatismus at $\pm 45°$
2	0	$\sqrt{3}(2\rho^2-1)$	Defocus
2	2	$\sqrt{6}\rho^2\cos(2\theta)$	Primary astigmatismus at $0°$
3	-3	$\sqrt{8}\rho^3\sin(3\theta)$	Trefoil
3	-1	$\sqrt{8}(3\rho^2-2\rho)\sin(\theta)$	Coma along y-axis
3	1	$\sqrt{8}(3\rho^2-2\rho)\cos(\theta)$	Coma along x-axis
3	3	$\sqrt{8}\rho^3\cos(3\theta)$	Trefoil
4	-4	$\sqrt{10}\rho^4\sin(4\theta)$	Quadrafoil
4	-2	$\sqrt{10}(4\rho^4-3\rho^2)\sin(2\theta)$	Secondary astigmatism at $\pm 45°$
4	0	$\sqrt{5}(6\rho^4-6\rho^2+1)$	Spherical Aberration, Defocus
4	2	$\sqrt{10}(4\rho^4-3\rho^2)\cos(2\theta)$	Secondary astigmatism at $\pm 0°$
4	4	$\sqrt{10}\rho^4\cos(4\theta)$	Quadrafoil

Appendix B

Least-squares minimisation in MICE

The least-squares minimisation in the MICE algorithm leading to the coupled set equations (3.5) and (3.6) can be derived in the following way: We start with the expression for the least-squares error

$$\epsilon = \sum_{\Gamma} |AC(\gamma, \gamma - \Gamma) - E_1(\gamma) E_2^*(\gamma - \Gamma)|^2. \tag{B.1}$$

The least-squares minimisation is performed by setting to zero the differentiation with respect to the two fields. We use the Wirtinger derivatives to simplify the differentiation of complex functions [312]. According to these, the partial differential operator associated with the complex quantity E^* becomes

$$\frac{\partial}{\partial E^*} = \frac{1}{2}\left(\frac{\partial}{\partial \mathrm{Re}(E)} + i\frac{\partial}{\partial \mathrm{Im(E)}}\right), \tag{B.2}$$

where the differentiation is split into the differentiation with respect to the real and imaginary parts. In order to solve $\partial\varepsilon/\partial E^* = 0$, the two components are therefore calculated separately first. To simplify the notation the arguments of the fields are omitted. Differentiation with respect to the real part of E^* is written as

$$\frac{\partial\varepsilon}{\partial\,\mathrm{Re}(E_1)} = \sum \frac{\partial}{\partial\,\mathrm{Re}(E_1)}[(AC - (\mathrm{Re}(E_1) + i\mathrm{Im}(E_1))E_2^*) \times (AC^* - (\mathrm{Re}(E_1) - i\mathrm{Im}(E_1))E_2)]. \tag{B.3}$$

Performing the differentiation directly leads to

$$\frac{\partial\varepsilon}{\partial\,\mathrm{Re}(E_1)} = \sum[-E_2^*AC^* + |E_2|^2(\mathrm{Re}(E_1) - i\mathrm{Im}(E_1)) - E_2AC + |E_2|^2(\mathrm{Re}(E_1) + i\mathrm{Im}(E_1))]. \tag{B.4}$$

Since $-E_2^*AC^* - E_2AC = -2\mathrm{Re}(-E_2^*AC^*) = -2\mathrm{Re}(E_2AC)$, equation (B.4) can be rewritten as

$$\frac{\partial\varepsilon}{\partial\,\mathrm{Re}(E_1)} = 2\sum[-\mathrm{Re}(E_2AC) + |E_2|^2\mathrm{Re}(E_1)]. \tag{B.5}$$

The differentiation with respect to $\mathrm{Im}(E_1)$ is calculated accordingly. The result is

$$\frac{\partial\varepsilon}{\partial\,\mathrm{Im}(E_1)} = 2\sum[-\mathrm{Im}(E_2AC) + |E_2|^2\mathrm{Im}(E_1)] \tag{B.6}$$

Using equations (B.5) and (B.6), the least-squares minimisation becomes

$$\frac{\partial \varepsilon}{\partial (E_1^*)} = \frac{1}{2}\left(\frac{\partial \varepsilon}{\partial \,\mathrm{Re}(E_1)} + i\frac{\partial \varepsilon}{\partial \,\mathrm{Im}(E_1)}\right) \tag{B.7}$$

$$= \sum [-(\mathrm{Re}(E_2 AC) + i\mathrm{Im}(E_2 AC)) + |E_2|^2(\mathrm{Re}(E_1) + i\mathrm{Im}(E_1))]$$

$$= \sum \left[-E_2 AC + |E_2|^2 E_1\right]$$

$$= 0 \tag{B.8}$$

Since $E_1(\gamma)$ does not depend on the shear Γ, equation (B.8) leads to the final equation for field $E_1(\gamma)$:

$$E_1(\gamma) = \frac{\sum_\Gamma AC(\gamma, \gamma - \Gamma)E_2(\gamma - \Gamma)}{\sum_\Gamma |E_2(\gamma - \Gamma)|^2} \tag{B.9}$$

To obtain equation (3.6), the variable γ is transformed according to $\gamma \to \gamma + \Gamma$ which transfers the shear from E_2 to E_1. In matrix notation this action corresponds to a row rotation. By differentiating equation (B.1) with respect to E_2 and performing an analogous calculation as above, equation (3.6) is recovered.

Appendix C

XUV spectrometer grating

The XUV grating is a mechanically ruled aberration-corrected concave grating, creating a flat-field image over a certain wavelength range at the image plane. The geometry for installation of the grating is shown in chapter 5 in figure 5.3. Table C.1 indicates the technical specifications of the grating:

Table C.1: Technical specifications of Hitachi grating model 001-0640.

Category	Value
Grooves/mm	1200
Radius of curvature [mm]	5649
Blank Size H x W x T [mm]	30 x 50 x 10
Wavelength range [nm]	11-62
Extension of flat-field image plane [mm]	110.16
Angle of Incidence	85.3°
Blaze angle	3.7°
Material	Pyrex

The grating has varied groove spacing σ at position ω in accordance with the following:

$$\sigma = \sigma_0 / \left(1 + \frac{2b_2}{R}\omega + \frac{3b_3}{R^2}\omega^2 + \frac{4b_4}{R^3}\omega^3\right). \tag{C.1}$$

Here σ_0 is the nominal groove spacing, R is the radius of curvature and b_2, b_3, b_4 are the ruling parameters. For the grating used in Oxford (Hitachi model 001-0640), $b_2 = -8.9$, $b_3 = 86.3$, $b_4 = -1349$. The wavelength along the focal plane can then be calculated according to the grating law:

$$m\lambda = \sigma_0(\sin\alpha + \sin\beta), \tag{C.2}$$

where m is the diffraction order and α and β are the angles of incidence and diffraction, respectively.

Bibliography

[1] T. H. Maiman. Stimulated optical radiation in ruby. *Nature*, 187:493–494, 1960.

[2] L. E. Hargrove, R. L. Fork, and M. A. Pollack. Locking of he-ne laser modes induced by synchronous intracavity modulation. *Appl. Phys. Lett.*, 5(1):4–5, 1964.

[3] D. E. Spence, P. N. Kean, and W. Sibbett. 60-fsec pulse generation from a self-mode-locked ti:sapphire laser. *Opt. Lett.*, 16(1):42–44, Jan 1991.

[4] A. H. Zewail. Laser femtochemistry. *Science*, 242:1645–1653, 1988.

[5] H. Ihee, V. A. Lobastov, U. M. Gomez, B. M. Goodson, R. Srinivasan, C.-Y. Ruan, and A. H. Zewail. Direct imaging of transient molecular structures with ultrafast diffraction. *Science*, 291(5503):458–462, 2001.

[6] T. Brixner, N. H. Damrauer, and G. Gerber. Femtosecond quantum control. *Adv. At., Mol., Opt. Phys.*, 46:1–54, 2001.

[7] M. Nisoli, S. De Silvestri, and O. Svelto. Generation of high energy 10 fs pulses by a new pulse compression technique. *Appl. Phys. Lett.*, 68(20):2793–2795, 1996.

[8] T. Brabec and F. Krausz. Intense few-cycle laser fields: Frontiers of nonlinear optics. *Rev. Mod. Phys.*, 72:545–591, Apr 2000.

[9] Z. Chang, A. Rundquist, H. Wang, M. M. Murnane, and H. C. Kapteyn. Generation of coherent soft x rays at 2.7 nm using high harmonics. *Phys. Rev. Lett.*, 79:2967–2970, Oct 1997.

[10] Ch. Spielmann, N. H. Burnett, S. Sartania, R. Koppitsch, M. Schnürer, C. Kan, M. Lenzner, P. Wobrauschek, and F. Krausz. Generation of coherent x-rays in the water window using 5-femtosecond laser pulses. *Science*, 278(5338):661–664, 1997.

[11] N. Ishii, S. Adachi, Y. Nomura, A. Kosuge, Y. Kobayashi, T. Kanai, J. Itatani, and S. Watanabe. Generation of soft x-ray and water window harmonics using a few-cycle, phase-locked, optical parametric chirped-pulse amplifier. *Opt. Lett.*, 37(1):97–99, Jan 2012.

[12] L. Redecke, K. Nass, D. P. DePonte, T. A. White, D. Rehders, A. Barty, F. Stellato, M. Liang, T. R.M. Barends, S. Boutet, G. J. Williams, M. Messerschmidt, M. M. Seibert, A. Aquila, D. Arnlund, S. Bajt, T. Barth, M. J. Bogan, C. Caleman, T.-C. Chao, R. B. Doak, H. Fleckenstein, M. Frank, R. Fromme, L. Galli, I. Grotjohann, M. S. Hunter, L. C. Johansson, S. Kassemeyer, G. Katona, R. A. Kirian, R. Koopmann, C. Kupitz, L. Lomb, A. V. Martin, S. Mogk, R. Neutze, R. L. Shoeman, J. Steinbrener, N. Timneanu, D. Wang, U. Weierstall, N. A. Zatsepin, J. C. H. Spence, P. Fromme, I. Schlichting, M. Duszenko, C. Betzel, and H. N. Chapman. Natively inhibited trypanosoma brucei cathepsin b structure determined by using an x-ray laser. *Science*, 339(6116):227–230, 2013.

[13] H. N. Chapman, P. Fromme, A. Barty, T. A. White, R. A. Kirian, A. Aquila, M. S. Hunter, J. Schulz, D. P. DePonte, U. Weierstall, R. B. Doak, F. R. N. C. Maia, A. V. Martin, I. Schlichting, L. Lomb, N. Coppola, R. L. Shoeman, S. W. Epp, R. Hartmann, D. Rolles, A. Rudenko, L. Foucar, N. Kimmel, G. Weidenspointner, P. Holl, M. Liang, M. Barthelmess, C. Caleman, S. Boutet, M. J. Bogan, J. Krzywinski, C. Bostedt, S. Bajt, L. Gumprecht, B. Rudek, B. Erk, C. Schmidt, A. Homke, C. Reich, D. Pietschner, L. Struder, G. Hauser, H. Gorke, J. Ullrich, S. Herrmann, G. Schaller, F. Schopper, H. Soltau, K. U. Kühnel, M. Messerschmidt, J. D. Bozek, S. P. Hau-Riege, M. Frank, C. Y. Hampton, R. G. Sierra, D. Starodub, G. J. Williams, J. Hajdu, N. Timneanu, M. M. Seibert, J. Andreasson, A. Rocker, O. Jonsson, M. Svenda, S. Stern, K. Nass, R. Andritschke, C.-D. Schroter, F. Krasniqi, M. Bott, K. E. Schmidt, X. Wang, In. Grotjohann, J. M. Holton, T. R. M. Barends, R. Neutze, S. Marchesini, R. Fromme, S. Schorb, D. Rupp, M. Adolph, T. Gorkhover, I. Andersson, H. Hirsemann, G. Potdevin, H. Graafsma, B. Nilsson, and J. C. H. Spence. Femtosecond x-ray protein nanocrystallography. *Nature*, 470(7332):73–77, 02 2011.

[14] M. M. Seibert, T. Ekeberg, F. R. N. C. Maia, M. Svenda, J. Andreasson, O. Jonsson, D. Odic, B. Iwan, A. Rocker, D. Westphal, M. Hantke, D. P. DePonte, A. Barty, J. Schulz, L. Gumprecht, N. Coppola, A. Aquila, M. Liang, T. A. White, A. Martin, C. Caleman, S. Stern, C. Abergel, V. Seltzer, J.-M. Claverie, C. Bostedt, J. D. Bozek, S. Boutet, A. A. Miahnahri, M. Messerschmidt, J. Krzywinski, G. Williams, K. O. Hodgson, M. J. Bogan, C. Y. Hampton, R. G. Sierra, D. Starodub, I. Andersson, S. Bajt, M. Barthelmess, J. C. H. Spence, P. Fromme, U. Weierstall, R. Kirian, M. Hunter, R. B. Doak, S. Marchesini, S. P. Hau-Riege, M. Frank, R. L. Shoeman, L. Lomb, S. W. Epp, R. Hartmann, D. Rolles, A. Rudenko, C. Schmidt, L. Foucar, N. Kimmel, P. Holl, B. Rudek, B. Erk, A. Homke, C. Reich, D. Pietschner, G. Weidenspointner, L. Struder, G. Hauser, H. Gorke, J. Ullrich, I. Schlichting, S. Herrmann, G. Schaller, F. Schopper, H. Soltau, K.-U. Kuhnel, R. Andritschke, C.-D. Schroter, F. Krasniqi, M. Bott, S. Schorb, D. Rupp, M. Adolph, T. Gorkhover, H. Hirsemann, G. Potdevin, H. Graafsma, B. Nilsson, H. N. Chapman, and J. Hajdu. Single mimivirus particles intercepted and imaged with an x-ray laser. *Nature*, 470(7332):78–81, 02 2011.

[15] A. Fratalocchi and G. Ruocco. Single-molecule imaging with x-ray free-electron lasers: Dream or reality? *Phys. Rev. Lett.*, 106:105504, Mar 2011.

[16] K. J. Gaffney and H. N. Chapman. Imaging atomic structure and dynamics with ultrafast x-ray scattering. *Science*, 316(5830):1444–1448, 2007.

[17] P. B. Corkum and Ferenc Krausz. Attosecond science. *Nat. Phys.*, 3:381–387, 2007.

[18] F. Krausz and M. Ivanov. Attosecond physics. *Rev. Mod. Phys.*, 81(1):163–234, Feb 2009.

[19] G. Farkas and C. Tóth. Proposal for attosecond light pulse generation using laser induced multiple-harmonic conversion processes in rare gases. *Phys. Rev. A*, 168:447–450, 1992.

[20] S. E. Harris, J. J. Macklin, and T. W. Hänsch. Atomic scale temporal structure inherent to high-order harmonic generation. *Opt. Commun.*, 100:487–490, 1993.

[21] P. Antoine, A. L'Huillier, and M. Lewenstein. Attosecond pulse trains using high-order harmonics. *Phys. Rev. Lett.*, 77:1234–1237, 1996.

[22] P. M. Paul, E. S. Toma, P. Breger, G. Mullot, F. Augé, Ph. Balcou, H. G. Muller, and P. Agostini. Observation of a train of attosecond pulses from high harmonic generation. *Science*, 292(5522):1689–1692, 2001.

[23] M. Hentschel, R. Kienberger, Ch. Spielmann, G. A. Reider, N. Milosevic, T. Brabec, P. Corkum, U. Heinzmann, M. Drescher, and F. Krausz. Attosecond metrology. *Nature*, 414:509–513, 2001.

[24] D. H. Ko, K. T. Kim, J. Park, J. h. Lee, and C. H. Nam. Attosecond chirp compensation over broadband high-order harmonics to generate near transform-limited 63 as pulses. *New J. Phys.*, 12(6):063008, 2010.

[25] K. Zhao, Q. Zhang, M. Chini, Y. Wu, X. Wang, and Z. Chang. Tailoring a 67 attosecond pulse through advantageous phase-mismatch. *Opt. Lett.*, 37(18):3891–3893, Sep 2012.

[26] M. Drescher, M. Hentschel, R. Kienberger, M. Uiberacker, V. Yakovlev, A. Scrinzi, Th. Westerwalbesloh, U. Kleineberg, U. Heinzmann, and F. Krausz. Time-resolved atomic inner-shell spectroscopy. *Nature*, 419:803–807, 2002.

[27] M. Uiberacker, Th. Uphues, M. Schultze, A. J. Verhoef, V. Yakovlev, M. F. Kling, J. Rauschenberger, N. M. Kabachnik, H. Schröder, M. Lezius, K. L. Kompa, H.-G. Muller, M. J. J. Vrakking, S. Hendel, U. Kleineberg, U. Heinzmann, M. Drescher, and F. Krausz. Attosecond real-time observation of electron tunnelling in atoms. *Nature*, 446:627–632, 2007.

[28] M. Schultze, M. Fieß, N. Karpowicz, J. Gagnon, M. Korbman, M. Hofstetter, S. Neppl, A. L. Cavalieri, Y. Komninos, Th. Mercouris, C. A. Nicolaides, R. Pazourek, S. Nagele, J. Feist, J. Burgdörfer, A. M. Azzeer, R. Ernstorfer, R. Kienberger, U. Kleineberg, E. Goulielmakis, F. Krausz, and V. S. Yakovlev. Delay in photoemission. *Science*, 328(5986):1658–1662, 2010.

[29] A. L. Cavalieri, N. Müller, Th. Uphues, V. S. Yakovlev, A. Baltuska, B. Horvath, B. Schmidt, L. Blümel, R. Holzwarth, S. Hendel, M. Drescher, U. Kleineberg, P. M. Echenique, R. Kienberger, F. Krausz, and U. Heinzmann. Attosecond spectroscopy in condensed matter. *Nature*, 449:1029–1032, 2007.

[30] F. Kelkensberg, C. Lefebvre, W. Siu, O. Ghafur, T. T. Nguyen-Dang, O. Atabek, A. Keller, V. Serov, P. Johnsson, M. Swoboda, T. Remetter, A. L'Huillier, S. Zherebtsov, G. Sansone, E. Benedetti, F. Ferrari, M. Nisoli, F. Lépine, M. F. Kling, and M. J. J. Vrakking. Molecular dissociative ionization and wave-packet dynamics studied using two-color xuv and ir pump-probe spectroscopy. *Phys. Rev. Lett.*, 103:123005, Sep 2009.

[31] G Sansone, F. Kelkensberg, J. F. Perez-Torres, F. Morales, M. F. Kling, W. Siu, O. Ghafur, P. Johnsson, M. Swoboda, E. Benedetti, F. Ferrari, F. Lepine, J. L. Sanz-Vicario, S. Zherebtsov, I. Znakovskaya, A. L'Huillier, M. Yu. Ivanov, M. Nisoli, F. Martin, and M. J. J. Vrakking. Electron localization following attosecond molecular photoionization. *Nature*, 465:763–766, 2010.

[32] F. Calegari, D. Ayuso, A. Trabattoni, L. Belshaw, S. De Camillis, S. Anumula, F. Frassetto, L. Poletto, A. Palacios, P. Decleva, J. B. Greenwood, F. MartÃŋn, and M. Nisoli. Ultrafast electron dynamics in phenylalanine initiated by attosecond pulses. *Science*, 346(6207):336–339, 2014.

[33] I. A. Walmsley and C. Dorrer. Characterization of ultrashort electromagnetic pulses. *Adv. Opt. Phot.*, 1:308–437, 2009.

[34] I. Walmsley, L. Waxer, and C. Dorrer. The role of dispersion in ultrafast optics. *Rev. Sci. Instrum.*, 72(1):1–29, 2001.

[35] F. Zernike. Diffraction theory of knife-edge test and its improved form, the phase contrast method. *Mon. Not. R. Astron. Soc.*, 94:377–384, 1934.

[36] F. Zernike. Beugungstheorie des schneidenverfahrens und seiner verbesserten form, der phasenkonstrastmethode. *Physica*, 1:689–704, 1934.

[37] R. L. Fork, O. E. Martinez, and J. P. Gordon. Negative dispersion using pairs of prisms. *Opt. Lett.*, 9(5):150–152, May 1984.

[38] B. E. A. Saleh and M. C. Teich. *Fundamentals of photonics.* John Wiley & Sons, Inc., 1991.

[39] L. G. Gouy. Sur une propriété nouvelle des ondes lumineuses. *C. R. Acad. Sci. Paris*, 110:1251–1253, 1890.

[40] L. G. Gouy. Sur la propagation anomale des ondes. *Ann. Chim. Phys.*, 24:145–213, 1891.

[41] R. J. Collins, D. F. Nelson, A. L. Schawlow, W. Bond, C. G. B. Garrett, and W. Kaiser. Coherence, narrowing, directionality, and relaxation oscillations in the light emission from ruby. *Phys. Rev. Lett.*, 5:303–305, Oct 1960.

[42] F. J. McClung and R. W. Hellwarth. Giant optical pulsations from ruby. *J. Appl. Phys.*, 33(3):828–829, 1962.

[43] E. J. Akutowicz. On the determination of the phase of a fourier integral, i. *Trans. Amer. Math. Soc.*, 83:179–192, 1956.

[44] E. J. Akutowicz. On the determination of the phase of a fourier integral, ii. *Trans. Amer. Math. Soc.*, 8:234–238, 1957.

[45] K. Naganuma, K. Mogi, and H. Yamada. General method for ultrashort light pulse chirp measurement. *IEEE J. Quant. Electron.*, 25:1225–1233, 1989.

[46] K. Naganuma, K. Mogi, and H. Yamada. Time direction determination of asymmetric ultrashort optical pulses from second-harmonic generation autocorrelation signals. *Appl. Phys. Lett.*, 54(13):1201–1202, 1989.

[47] D. Meshulach, D. Yelin, and Y. Silberberg. Adaptive real-time femtosecond pulse shaping. *J. Opt. Soc. Am. B*, 15(5):1615–1619, May 1998.

[48] R. Barakat and G. Newsam. Necessary conditions for a unique solution to two-dimensional phase recovery. *J. Math. Phys.*, 25(11):3190–3193, 1984.

[49] R. H. T. Bates. Uniqueness of solutions to two-dimensional fourier phase problems for localized and positive images. *Comp. Vis., Graph., Im. Process.*, 25(2):205–217, 1984.

[50] R. G. Lane, W. R. Fright, and R. H. T. Bates. Direct phase retrieval. *IEEE Trans. Acoust. Speech. Signal Process.*, ASSP-35:520–526, 1987.

[51] J. R. Fienup. Reconstruction of a complex-valued object from the modulus of its fourier transform using a support constraint. *J. Opt. Soc. Am. A*, 4(1):118–123, Jan 1987.

[52] D. J. Kane and R. Trebino. Characterization of arbitrary femtosecond pulses using frequency-resolved optical gating. *IEEE J. Quant. Electron.*, 29(2):571–579, 1993.

[53] R. Trebino. *Frequency-Resolved Optical Gating: The Measurement of Ultrashort Laser Pulses*. Kluwer Academic Publishers, 2000.

[54] J. Paye, M. Ramaswamy, J. G. Fujimoto, and E. P. Ippen. Measurement of the amplitude and phase of ultrashort light pulsesfrom spectrally resolved autocorrelation. *Opt. Lett.*, 18(22):1946–1948, Nov 1993.

[55] K. W. DeLong, R. Trebino, J. Hunter, and W. E. White. Frequency-resolved optical gating with the use of second-harmonic generation. *J. Opt. Soc. Am. B*, 11(11):2206–2215, Nov 1994.

[56] J. Paye. How to measure the amplitude and phase of an ultrashort light pulse with an autocorrelator and a spectrometer. *IEEE J. Quant. Electron.*, 30:2693–2697, 1994.

[57] R. Trebino and D. J. Kane. Using phase retrieval to measure the intensity and phase of ultrashort pulses: frequency-resolved optical gating. *J. Opt. Soc. Am. A*, 10(5):1101–1111, May 1993.

[58] R. P. Millane. Phase retrieval in crystallography and optics. *J. Opt. Soc. Am. A*, 7(3):394–411, Mar 1990.

[59] K. W. DeLong, D. N. Fittinghoff, R. Trebino, B. Kohler, and K. Wilson. Pulse retrieval in frequency-resolved optical gating based on the method of generalized projections. *Opt. Lett.*, 19(24):2152–2154, 1994.

[60] D. J. Kane, G. Rodriguez, A. J. Taylor, and T. S. Clement. Simultaneous measurement of two ultrashort laser pulses from a single spectrogram in a single shot. *J. Opt. Soc. Am. B*, 14(4):935–943, Apr 1997.

[61] C. Froehly, A. Lacourt, and J. C. Viénot. Notions de réponse impulsionnelle et de fonction de transfert temporelles des pupilles optiques, justifications expérimentales et applications. *Nouv. Rev. Opt.*, 4(4):183–196, 1973.

[62] L. Lepetit, G. Chériaux, and M. Joffre. Linear techniques of phase measurement by femtosecond spectral interferometry for applications in spectroscopy. *J. Opt. Soc. Am. B*, 12(12):2467–2474, 1995.

[63] C. Iaconis and I. A. Walmsley. Spectral phase interferometry for direct electric-field reconstruction of ultrashort optical pulses. *Opt. Lett.*, 23:792, 1998.

[64] C. Iaconis and I. A. Walmsley. Self-referencing spectral interferometry for measuring ultrashort optical pulses. *IEEE J. Quant. Electron.*, 35:501, 1999.

[65] M. Takeda, H. Ina, and S. Kobayashi. Fourier-transform method of fringe-pattern analysis for computer-based topography and interferometry. *J. Opt. Soc. Am.*, 72(1):156–160, Jan 1982.

[66] C. Dorrer and I. A. Walmsley. Accuracy criterion for ultrashort pulse characterization techniques: application to spectral phase interferometry for direct electric field reconstruction. *J. Opt. Soc. Am. B*, 19(5):1019–1029, May 2002.

[67] D. Keusters, H.-S. Tan, P. O'Shea, E. Zeek, R. Trebino, and W. S. Warren. Relative-phase ambiguities in measurements of ultrashort pulses with well-separated multiple frequency components. *J. Opt. Soc. Am. B*, 20(10):2226–2237, Oct 2003.

[68] D. R. Austin, T. Witting, and I. A. Walmsley. Resolution of the relative phase ambiguity in spectral shearing interferometry of ultrashort pulses. *Opt. Lett.*, 35(12):1971–1973, Jun 2010.

[69] S. P. Gorza, P. Wasylczyk, and I. A. Walmsley. Spectral shearing interferometry with spatially chirped replicas for measuring ultrashort pulses. *Opt. Express*, 15(23):15168–15174, Nov 2007.

[70] A. S. Radunsky, E. M. Kosik Williams, I. A. Walmsley, P. Wasylczyk, W. Wasilewski, A. B. U'Ren, and M. E. Anderson. Simplified spectral phase interferometry for direct electric-field reconstruction by using a thick nonlinear crystal. *Opt. Lett.*, 31(7):1008–1010, Apr 2006.

[71] S.-P. Gorza, A. S. Radunsky, P. Wasylczyk, and I. A. Walmsley. Tailoring the phase-matching function for ultrashort pulse characterization by spectral shearing interferometry. *J. Opt. Soc. Am. B*, 24(9):2064–2074, Sep 2007.

[72] E. M. Kosik, A. S. Radunsky, I. A. Walmsley, and C. Dorrer. Interferometric technique for measuring broadband ultrashort pulses at the sampling limit. *Opt. Lett.*, 30(3):326–328, Feb 2005.

[73] J. Hartmann. Bemerkungen über den Bau und die Justirung von Spektrographen. *Zeitschrift für Instrumentenkunde*, 20:17, 1900.

[74] R. V. Shack and B. C. Platt. Production and use of a lenticular hartmann screen. *J. Opt. Soc. Am.*, 61(5):656, May 1971.

[75] B. C. Platt and R. Shack. History and principles of shack-hartmann wavefront sensing. *J. Refract. Surg.*, 17:573–577, 2001.

[76] C. P. Hauri, J. Biegert, U. Keller, B. Schaefer, K. Mann, and G. Marowski. Validity of wave-front reconstruction and propagation of ultrabroadband pulses measured with a hartmann-shack sensor. *Opt. Lett.*, 30(12):1563–1565, Jun 2005.

[77] D. Malacara, editor. *Optical Shop Testing*. John Wiley & Sons, Inc., 2007.

[78] R. N. Smartt and W. H. Steel. Theory and application of point-diffraction interferometers. *Jpn. J. Appl. Phys.*, 14:352–356, 1975.

[79] W. J. Bates. A wavefront shearing interferometer. *Proc. Phys. Soc.*, 59(6):940, 1947.

[80] D. Kelsall. Optical frequency response characteristics in the presence of spherical aberration measured by an automatically recording interferometric instrument. *Pro. Phys. Soc.*, 73(3):465, 1959.

[81] P. Hariharan and D. Sen. Cyclic shearing interferometer. *J. Sci. Instrum.*, 37(10):374, 1960.

[82] M. V. R. K. Murty. The use of a single plane parallel plate as a lateral shearing interferometer with a visible gas laser source. *Appl. Opt.*, 3(4):531–534, Apr 1964.

[83] V. Ronchi. *Ann. Sc. Norm. Super. Pisa*, 15, 1923.

[84] V. Ronchi. Forty years of history of a grating interferometer. *Appl. Opt.*, 3(4):437–451, Apr 1964.

[85] D. S. Brown. *Radial Shear Interferograms*. Interferometry N.P.L Symposium No. 11. Her Majesty's Stationary Office, London, London, 1959.

[86] D. S. Brown. Radial shear interferometry. *J. Sci. Instrum.*, 39(2):71, 1962.

[87] P. Hariharan and D. Sen. Radial shearing interferometer. *J. Sci. Instrum.*, 38(11):428, 1961.

[88] S. C. Som. Theory of a compact radial shearing laser interferometer. *Opt. Acta*, 17(2):107–113, 1970.

[89] M. V. R. K. Murty and E. C. Hagerott. Rotational-shearing interferometry. *Appl. Opt.*, 5(4):615–619, Apr 1966.

[90] G. Páez and M. Strojnik. Phase-shifted interferometry without phase unwrapping: reconstruction of a decentered wave front. *J. Opt. Soc. Am. A*, 16(3):475–480, Mar 1999.

[91] G. Paez, M. Strojnik, and G. Garcia Torales. Vectorial shearing interferometer. *Appl. Opt.*, 39(28):5172–5178, Oct 2000.

[92] T. Witting, F. Frank, C. A. Arrell, W. A. Okell, J. P. Marangos, and J. W. G. Tisch. Characterization of high-intensity sub-4-fs laser pulses using spatially encoded spectral shearing interferometry. *Opt. Lett.*, 36(9):1680–1682, May 2011.

[93] C. Dorrer and I. A. Walmsley. Simple linear technique for the measurement of spaceâĂŞtime coupling in ultrashort optical pulses. *Opt. Lett.*, 27:1947, 2002.

[94] A. Zaïr, A. Guandalini, F. Schapper, M. Holler, J. Biegert, L. Gallmann, A. Couairon, M. Franco, A. Mysyrowicz, and U. Keller. Spatio-temporal characterization of few-cycle pulses obtained by filamentation. *Opt. Express*, 15(9):5394–5404, Apr 2007.

[95] J. P. Geindre, A. Mysyrowicz, A. Dos Santos, P. Audebert, A. Rousse, G. Hamoniaux, A. Antonetti, F. Falliès, and J. C. Gauthier. Frequency-domain interferometer for measuring the phase and amplitude of a femtosecond pulse probing a laser-produced plasma. *Opt. Lett.*, 19(23):1997–1999, Dec 1994.

[96] J. Jasapara and W. Rudolph. Characterization of sub-10-fs pulse focusing with high-numerical-aperture microscope objectives. *Opt. Lett.*, 24(11):777–779, Jun 1999.

[97] W. Amir, T. A. Planchon, C. G. Durfee, J. A. Squier, P. Gabolde, R. Trebino, and M. Müller. Simultaneous visualization of spatial and chromatic aberrations by two-dimensional fourier transform spectral interferometry. *Opt. Lett.*, 31(19):2927–2929, Oct 2006.

[98] D. Meshulach, D. Yelin, and Y. Silberberg. Real-time spatial–spectral interference measurements of ultrashort optical pulses. *J. Opt. Soc. Am. B*, 14(8):2095–2098, Aug 1997.

[99] P. Bowlan, P. Gabolde, A. Shreenath, K. McGresham, R. Trebino, and S. Akturk. Crossed-beam spectral interferometry: a simple, high-spectral-resolution method for completely characterizing complex ultrashort pulses in real time. *Opt. Express*, 14(24):11892–11900, Nov 2006.

[100] P. Bowlan, P. Gabolde, M. A. Coughlan, R. Trebino, and R. J. Levis. Measuring the spatiotemporal electric field of ultrashort pulses with high spatial and spectral resolution. *J. Opt. Soc. Am. B*, 25(6):A81–A92, Jun 2008.

[101] P. Bowlan, P. Gabolde, and R. Trebino. Directly measuring the spatio-temporal electric field of focusing ultrashort pulses. *Opt. Express*, 15(16):10219–10230, Aug 2007.

[102] P. Bowlan, H. Valtna-Lukner, M. L ohmus, P. Piksarv, P. Saari, and R. Trebino. Measuring the spatiotemporal field of ultrashort bessel-x pulses. *Opt. Lett.*, 34(15):2276–2278, Aug 2009.

[103] P. Bowlan and R. Trebino. Using phase diversity for the measurement of the complete spatiotemporal electric field of ultrashort laser pulses. *J. Opt. Soc. Am. B*, 29(2):244–248, Feb 2012.

[104] V. Gallet, S. Kahaly, O. Gobert, and F. Quéré. Dual spectral-band interferometry for spatio-temporal characterization of high-power femtosecond lasers. *Opt. Lett.*, 39(16):4687–4690, Aug 2014.

[105] P. Gabolde and R. Trebino. Self-referenced measurement of the complete electric field of ultrashort pulses. *Opt. Express*, 12(19):4423–4429, Sep 2004.

[106] P. Gabolde and R. Trebino. Single-shot measurement of the full spatio-temporal field of ultrashort pulses with multi-spectral digital holography. *Opt. Express*, 14(23):11460–11467, Nov 2006.

[107] P. Gabolde and R. Trebino. Single-frame measurement of the complete spatiotemporal intensity and phase of ultrashort laser pulses using wavelength-multiplexed digital holography. *J. Opt. Soc. Am. B*, 25(6):A25–A33, Jun 2008.

[108] F. Bonaretti, D. Faccio, M. Clerici, J. Biegert, and P. Di Trapani. Spatiotemporal amplitude and phase retrieval of bessel-x pulses using a hartmann-shack sensor. *Opt. Express*, 17(12):9804–9809, Jun 2009.

[109] E. Rubino, D. Faccio, L. Tartara, P. K. Bates, O. Chalus, M. Clerici, F. Bonaretti, J. Biegert, and P. Di Trapani. Spatiotemporal amplitude and phase retrieval of space-time coupled ultrashort pulses using the shackled-frog technique. *Opt. Lett.*, 34(24):3854–3856, Dec 2009.

[110] S. L. Cousin, J. M. Bueno, N. Forget, D. R. Austin, and J. Biegert. Three-dimensional spatiotemporal pulse characterization with an acousto-optic pulse shaper and a hartmann-shack wavefront sensor. *Opt. Lett.*, 37(15):3291–3293, Aug 2012.

[111] F. Bragheri, D. Faccio, F. Bonaretti, A. Lotti, M. Clerici, O. Jedrkiewicz, C. Liberale, S. Henin, L. Tartara, V. Degiorgio, and P. Di Trapani. Complete retrieval of the field of ultrashort optical pulses using the angle-frequency spectrum. *Opt. Lett.*, 33(24):2952–2954, Dec 2008.

[112] R.W. Gerchberg and W.O. Saxton. A practical algorithm for the determination of phase from image and diffraction plane pictures. *Optik*, 35:237–246, 1972.

[113] W. O. Saxton. *Computer Techniques for Image Processing in Electron Microscopy.* Academic Press, 1978.

[114] C. Dorrer, E.M. Kosik, and I.A. Walmsley. Spatio-temporal characterization of the electric field of ultrashort optical pulses using two-dimensional shearing interferometry. *Appl. Phys. B*, 74(1):s209–s217, 2002.

[115] C. Dorrer, E. M. Kosik, and I. A. Walmsley. Direct space time-characterization of the electric fields of ultrashort optical pulses. *Opt. Lett.*, 27(7):548–550, Apr 2002.

[116] M. M. Mang, C. Bourassin-Bouchet, I. Gianani, and I. A. Walmsley. Mutual interferometric characterization of electric-fields. In *Frontiers in Optics 2013*. Opt. Soc. Amer., 2013. FTu4F.2.

[117] C. Bourassin-Bouchet, M. M. Mang, I. Gianani, and I. A. Walmsley. Mutual interferometric characterization of a pair of independent electric fields. *Opt. Lett.*, 38(24):5299–5302, Dec 2013.

[118] K. W. DeLong, R. Trebino, and W. E. White. Simultaneous recovery of two ultrashort laser pulses from a single spectrogram. *J. Opt. Soc. Am. B*, 12(12):2463–2466, Dec 1995.

[119] B. C. McCallum and J. M. Rodenburg. Simultaneous reconstruction of object and aperture functions from multiple far-field intensity measurements. *J. Opt. Soc. Am. A*, 10(2):231–239, Feb 1993.

[120] G. R. Ayers and J. C. Dainty. Iterative blind deconvolution method and its applications. *Opt. Lett.*, 13(7):547–549, Jul 1988.

[121] J. H. Seldin and J. R. Fienup. Iterative blind deconvolution algorithm applied to phase retrieval. *J. Opt. Soc. Am. A*, 7(3):428–433, Mar 1990.

[122] B. Seifert, H. Stolz, and M. Tasche. Nontrivial ambiguities for blind frequency-resolved optical gating and the problem of uniqueness. *J. Opt. Soc. Am. B*, 21(5):1089–1097, May 2004.

[123] B. Seifert and H. Stolz. A method for unique phase retrieval of ultrafast optical fields. *Meas. Sci. Tech.*, 20(1):015303, 2009.

[124] T. C. Wong, J. Ratner, V. Chauhan, J. Cohen, P. M. Vaughan, L. Xu, A. Consoli, and R. Trebino. Simultaneously measuring two ultrashort laser pulses on a single-shot using double-blind frequency-resolved optical gating. *J. Opt. Soc. Am. B*, 29(6):1237–1244, Jun 2012.

[125] T. C. Wong, J. Ratner, and R. Trebino. Simultaneous measurement of two different-color ultrashort pulses on a single shot. *J. Opt. Soc. Am. B*, 29(8):1889–1893, Aug 2012.

[126] I. Amat-Roldán, I. G. Cormack, P. Loza-Alvarez, and D. Artigas. Measurement of electric field by interferometric spectral trace observation. *Opt. Lett.*, 30(9):1063–1065, May 2005.

[127] I. Amat-Roldan, D. Artigas, I. G. Cormack, and P. Loza-Alvarez. Simultaneous analytical characterisation of two ultrashort laser pulses using spectrally resolved interferometric correlations. *Opt. Express*, 14(10):4538–4551, May 2006.

[128] E. Yudilevich, A. Levi, G. J. Habetler, and H. Stark. Restoration of signals from their signed fourier-transform magnitude by the method of generalized projections. *J. Opt. Soc. Am. A*, 4(1):236–246, Jan 1987.

[129] P. Thibault, M. Dierolf, O. Bunk, A. Menzel, and F. Pfeiffer. Probe retrieval in ptychographic coherent diffractive imaging. *Ultramicroscopy*, 109(4):338 – 343, 2009.

[130] P. Thibault, M. Dierolf, A. Menzel, O. Bunk, C. David, and F. Pfeiffer. High-resolution scanning x-ray diffraction microscopy. *Science*, 321(5887):379–382, 2008.

[131] E. Goulielmakis, M. Uiberacker, R. Kienberger, A. Baltuska, V. Yakovlev, A. Scrinzi, Th. Westerwalbesloh, U. Kleineberg, U. Heinzmann, M. Drescher, and F. Krausz. Direct measurement of light waves. *Science*, 305:1267–1269, 2004.

[132] G. G. Paulus, F. Lindner, H. Walther, A. Baltuška, E. Goulielmakis, M. Lezius, and F. Krausz. Measurement of the phase of few-cycle laser pulses. *Phys. Rev. Lett.*, 91:253004, Dec 2003.

[133] K. T. Kim, C. Zhang, A. D. Shiner, B. E. Schmidt, F. Légaré, D. M. Villeneuve, and P. B. Corkum. Petahertz optical oscilloscope. *Nat. Photon.*, 7:958–962, 11 2013.

[134] T. Paasch-Colberg, A. Schiffrin, N. Karpowicz, S. Kruchinin, S. Özge, S. Keiber, O. Razskazovskaya, S. Mühlbrandt, A. Alnaser, M. Kübel, V. Apalkov, D. Gerster, J. Reichert, T. Wittmann, J. V. Barth, M. I. Stockman, R. Ernstorfer, V. S. Yakovlev, R. Kienberger, and F. Krausz. Solid-state light-phase detector. *Nat. Photon.*, 8:214–218, 2014.

[135] T. Witting, D. R. Austin, and I. A. Walmsley. Ultrashort pulse characterization by spectral shearing interferometry with spatially chirped ancillae. *Opt. Express*, 17(21):18983–18994, Oct 2009.

[136] D. R. Austin, T. Witting, and I. A. Walmsley. High precision self-referenced phase retrieval of complex pulses with multiple-shearing spectral interferometry. *J. Opt. Soc. Am. B*, 26(9):1818–1830, Sep 2009.

[137] J. A. Armstrong, N. Bloembergen, J. Ducuing, and P. S. Pershan. Interactions between light waves in a nonlinear dielectric. *Phys. Rev.*, 127:1918–1939, Sep 1962.

[138] J. F. Ward. Calculation of nonlinear optical susceptibilities using diagrammatic perturbation theory. *Rev. Mod. Phys.*, 37:1–18, Jan 1965.

[139] E. T. J. Nibbering, P. F. Curley, G. Grillon, B. S. Prade, M. A. Franco, F. Salin, and A. Mysyrowicz. Conical emission from self-guided femtosecond pulses in air. *Opt. Lett.*, 21(1):62–64, Jan 1996.

[140] R. S. Bennink, V. Wong, A. M. Marino, D. L. Aronstein, R. W. Boyd, C. R. Stroud, S. Lukishova, and D. J. Gauthier. Honeycomb pattern formation by laser-beam filamentation in atomic sodium vapor. *Phys. Rev. Lett.*, 88:113901, Feb 2002.

[141] S. Tzortzakis, L. Bergé, A. Couairon, M. Franco, B. Prade, and A. Mysyrowicz. Breakup and fusion of self-guided femtosecond light pulses in air. *Phys. Rev. Lett.*, 86:5470–5473, Jun 2001.

[142] A. Braun, G. Korn, X. Liu, D. Du, J. Squier, and G. Mourou. Self-channeling of high-peak-power femtosecond laser pulses in air. *Opt. Lett.*, 20(1):73–75, Jan 1995.

[143] R. G. Brewer. Frequency shifts in self-focused light. *Phys. Rev. Lett.*, 19:8–10, Jul 1967.

[144] F. Shimizu. Frequency broadening in liquids by a short light pulse. *Phys. Rev. Lett.*, 19:1097–1100, Nov 1967.

[145] A. C. Cheung, D. M. Rank, R. Y. Chiao, and C. H. Townes. Phase modulation of q-switched laser beams in small-scale filaments. *Phys. Rev. Lett.*, 20:786–789, Apr 1968.

[146] P. L. Kelley. Self-focusing of optical beams. *Phys. Rev. Lett.*, 15:1005–1008, Dec 1965.

[147] D. Strickland and G. Mourou. Compression of amplified chirped optical pulses. *Opt. Commun.*, 56(3):219 – 221, 1985.

[148] P. Maine, D. Strickland, P. Bado, M. Pessot, and G. Mourou. Generation of ultrahigh peak power pulses by chirped pulse amplification. *IEEE J. Quant. Electron.*, 24(2):398–403, Feb 1988.

[149] M. D. Perry and G. Mourou. Terawatt to petawatt subpicosecond lasers. *Science*, 264(5161):917–924, 1994.

[150] G. A. Mourou, C. P. J. Barty, and M. D. Perry. Ultrahigh-intensity lasers: Physics of the extreme on a tabletop. *Phys. Today*, 51:22, 1998.

[151] S. Augst, D. Strickland, D. D. Meyerhofer, S. L. Chin, and J. H. Eberly. Tunneling ionization of noble gases in a high-intensity laser field. *Phys. Rev. Lett.*, 63:2212–2215, Nov 1989.

[152] L. V. Keldysh. Ionization in the field of a strong electromagnetic wave. *Zh. Eksp. Teor. Fiz.*, 47:1945, 1964. [Sov. Phys. JETP 20:1307 (1965)].

[153] A. L'Huillier, L. A. Lompre, G. Mainfray, and C. Manus. Multiply charged ions induced by multiphoton absorption processes in rare-gas atoms at 1.064μm. *J. Phys. B*, 16(8):1363, 1983.

[154] M. D. Perry, A. Szoke, O. L. Landen, and E. M. Campbell. Nonresonant multiphoton ionization of noble gases: Theory and experiment. *Phys. Rev. Lett.*, 60:1270–1273, Mar 1988.

[155] M. D. Perry, O. L. Landen, A. Szöke, and E. M. Campbell. Multiphoton ionization of the noble gases by an intense 10^{14}-w/cm^2 dye laser. *Phys. Rev. A*, 37:747–760, Feb 1988.

[156] T. S. Luk, U. Johann, H. Egger, H. Pummer, and C. K. Rhodes. Collision-free multiple photon ionization of atoms and molecules at 193 nm. *Phys. Rev. A*, 32:214–224, Jul 1985.

[157] F Yergeau, S L Chin, and P Lavigne. Multiple ionisation of rare-gas atoms by an intense co 2 laser (10 14 w cm -2). *J. Phys. B*, 20(4):723, 1987.

[158] S. L. Chin, W. Xiong, and P. Lavigne. Creation of multiple charges (up to xe6+)from xe atoms by an intense co2 laser. *J. Opt. Soc. Am. B*, 4(5):853–854, May 1987.

[159] S. Baker, I. A. Walmsley, J. W. G. Tisch, and J. P. Marangos. Femtosecond to attosecond light pulses from a molecular modulator. *Nat. Photon.*, 5:664–671, 2011.

[160] H.-S. Chan, Z.-M. Hsieh, W.-H. Liang, A. H. Kung, C.-K. Lee, C.-J. Lai, R.-P. Pan, and L.-H. Peng. Synthesis and measurement of ultrafast waveforms from five discrete optical harmonics. *Science*, 331(6021):1165–1168, 2011.

[161] N. Zhavoronkov and G. Korn. Generation of single intense short optical pulses by ultrafast molecular phase modulation. *Phys. Rev. Lett.*, 88:203901, May 2002.

[162] S. Gundry, M. P. Anscombe, A. M. Abdulla, E. Sali, J.W. G. Tisch, P. Kinsler, G. H. C. New, and J. P. Marangos. Ultrashort-pulse modulation in adiabatically preparedraman media. *Opt. Lett.*, 30(2):180–182, Jan 2005.

[163] Y. Kida, T. Nagahara, S. Zaitsu, M. Matuse, and T. Imasaka. Pulse compression based on coherent molecular motion induced by transient stimulated raman scattering. *Opt. Express*, 14(7):3083–3092, Apr 2006.

[164] Y. Kida, S. Zaitsu, and T. Imasaka. Generation of intense 11-fs ultraviolet pulses using phase modulation by two types of coherent molecular motions. *Opt. Express*, 16(18):13492–13498, Sep 2008.

[165] A. Wirth, M. Th. Hassan, I. Grguraš, J. Gagnon, A. Moulet, T. T. Luu, S. Pabst, R. Santra, Z. A. Alahmed, A. M. Azzeer, V. S. Yakovlev, V. Pervak, F. Krausz, and E. Goulielmakis. Synthesized light transients. *Science*, 334(6053):195–200, 2011.

[166] M. T. Hassan, A. Wirth, I. Grguraš, A. Moulet, T. T. Luu, J. Gagnon, V. Pervak, and E. Goulielmakis. Attosecond photonics: Synthesis and control of light transients. *Rev. Sci. Instrum.*, 83(11):111301, 2012.

[167] G. Sansone, E. Benedetti, F. Calegari, C. Vozzi, L. Avaldi, R. Flammini, L. Poletto, P. Villoresi, C. Altucci, R. Velotta, S. Stagira, S. De Silvestri, and M. Nisoli. Isolated single-cycle attosecond pulses. *Science*, 314:443–446, 2006.

[168] T. Brixner and G. Gerber. Quantum control of gas-phase and liquid-phase femtochemistry. *ChemPhysChem*, 4(5):418–438, 2003.

[169] M. F. Kling, P. von den Hoff, I. Znakovskaya, and R. de Vivie-Riedle. (sub-)femtosecond control of molecular reactions via tailoring the electric field of light. *Phys. Chem. Chem. Phys.*, 15:9448–9467, 2013.

[170] N. H. Burnett, H. A. Baldis, M. C. Richardson, and G. D. Enright. Harmonic generation in co2 laser target interaction. *Appl. Phys. Lett.*, 31(3):172–174, 1977.

[171] R. L. Carman, D. W. Forslund, and J. M. Kindel. Visible harmonic emission as a way of measuring profile steepening. *Phys. Rev. Lett.*, 46:29–32, Jan 1981.

[172] R. L. Carman, C. K. Rhodes, and R. F. Benjamin. Observation of harmonics in the visible and ultraviolet created in co_2-laser-produced plasmas. *Phys. Rev. A*, 24:2649–2663, Nov 1981.

[173] A. McPherson, G. Gibson, H. Jara, U. Johann, T. S. Luk, I. A. McIntyre, K. Boyer, and C. K. Rhodes. Studies of multiphoton production of vacuum-ultraviolet radiation in the rare gases. *J. Opt. Soc. Am. B*, 4(4):595–601, Apr 1987.

[174] M. Ferray, A. L'Huillier, X. F. Li, L. A. Lompre, G. Mainfray, and C. Manus. Multiple-harmonic conversion of 1064 nm radiation in rare gases. *J. Phys. B*, 21(3):L31, 1988.

[175] Y. Liang, S. Augst, S. L. Chin, Y. Beaudoin, and M. Chaker. High harmonic generation in atomic and diatomic molecular gases using intense picosecond laser pulses-a comparison. *J. Phys. B*, 27(20):5119, 1994.

[176] S. Ghimire, A. D. DiChiara, E. Sistrunk, P. Agostini, L. F. DiMauro, and D. A. Reis. Observation of high-order harmonic generation in a bulk crystal. *Nat. Phys.*, 7:138–141, 2011.

[177] T. Ditmire, T. Donnelly, R. W. Falcone, and M. D. Perry. Strong x-ray emission from high-temperature plasmas produced by intense irradiation of clusters. *Phys. Rev. Lett.*, 75:3122–3125, Oct 1995.

[178] J. W. G. Tisch, T. Ditmire, D. J. Fraser, N. Hay, M. B. Mason, E. Springate, J. P. Marangos, and M. H. R. Hutchinson. Investigation of high-harmonic generation from xenon atom clusters. *J. Phys. B*, 30(20):L709, 1997.

[179] A. D. DiChiara, E. Sistrunk, T. A. Miller, P. Agostini, and L. F. DiMauro. An investigation of harmonic generation in liquid media with a mid-infrared laser. *Opt. Express*, 17(23):20959–20965, Nov 2009.

[180] H. G. Kurz, D. S. Steingrube, D. Ristau, M. Lein, U. Morgner, and M. Kovačev. High-order-harmonic generation from dense water microdroplets. *Phys. Rev. A*, 87:063811, Jun 2013.

[181] R. A. Ganeev. High-order harmonic generation in a laser plasma: a review of recent achievements. *J. Phys. B*, 40(22):R213, 2007.

[182] U. Teubner and P. Gibbon. High-order harmonics from laser-irradiated plasma surfaces. *Rev. Mod. Phys.*, 81:445–479, Apr 2009.

[183] C. Thaury and F. Quéré. High-order harmonic and attosecond pulse generation on plasma mirrors: basic mechanisms. *J. Phys. B*, 43(21):213001, 2010.

[184] T. Baeva, S. Gordienko, and A. Pukhov. Theory of high-order harmonic generation in relativistic laser interaction with overdense plasma. *Phys. Rev. E*, 74:046404, Oct 2006.

[185] H. Vincenti, S. Monchocé, S. Kahaly, G. Bonnaud, Ph. Martin, and F. Quéré. Optical properties of relativistic plasma mirrors. *Nat. Commun.*, 5, 03 2014.

[186] Y. Nomura, R. Hörlein, P. Tzallas, B. Dromey, S. Rykovanov, Zs. Major, J. Osterhoff, S. Karsch, L. Veisz, M. Zepf, D. Charalambidis, F. Krausz, and G. D. Tsakiris. Attosecond phase locking of harmonics emitted from laser-produced plasmas. *Nat. Phys.*, 5:124–128, 2009.

[187] G. D. Tsakiris, K. Eidmann, J. Meyer ter Vehn, and F. Krausz. Route to intense single attosecond pulses. *New J. Phys.*, 8(1):19, 2006.

[188] G. Sansone, L. Poletto, and M. Nisoli. High-energy attosecond light sources. *Nat. Photon.*, 5:655–663, 2011.

[189] P. B. Corkum. Plasma perspective on strong field multiphoton ionization. *Phys. Rev. Lett.*, 71:1994–1997, 1993.

[190] J. L. Krause, K. J. Schafer, and K. C. Kulander. High-order harmonic generation from atoms and ions in the high intensity regime. *Phys. Rev. Lett.*, 68:3535–3538, Jun 1992.

[191] K. C. Kulander and B. W. Shore. Calculations of multiple-harmonic conversion of 1064-nm radiation in xe. *Phys. Rev. Lett.*, 62:524–526, Jan 1989.

[192] J. H. Eberly, Q. Su, and J. Javanainen. Nonlinear light scattering accompanying multiphoton ionization. *Phys. Rev. Lett.*, 62:881–884, Feb 1989.

[193] S. Chelkowski, T. Zuo, and A. D. Bandrauk. Ionization rates of h_2^+ in an intense laser field by numerical integration of the time-dependent schrödinger equation. *Phys. Rev. A*, 46:R5342–R5345, Nov 1992.

[194] V. C. Reed and K. Burnett. Loss of harmonic generation in intense laser fields. *Phys. Rev. A*, 46:424–429, Jul 1992.

[195] M. Lewenstein, Ph. Balcou, M. Yu. Ivanov, Anne L'Huillier, and P. B. Corkum. Theory of high-harmonic generation by low-frequency laser fields. *Phys. Rev. A*, 49:2117–2132, 1994.

[196] P. Saliéres, B. B. Carré, L. Le Déroff, F. Grasbon, G. G. Paulus, H. Walther, R. Kopold, W. Becker, D. B. Milošević, A. Sanpera, and M. Lewenstein. Feynman's path-integral approach for intense-laser-atom interactions. *Science*, 292(5518):902–905, 2001.

[197] P. Eckle, A. N. Pfeiffer, C. Cirelli, A. Staudte, R. Dörner, H. G. Muller, M. Büttiker, and U. Keller. Attosecond ionization and tunneling delay time measurements in helium. *Science*, 322(5907):1525–1529, 2008.

[198] A. N. Pfeiffer, C. Cirelli, M. Smolarski, and U. Keller. Recent attoclock measurements of strong field ionization. *Chem. Phys.*, 414(0):84 – 91, 2013. Attosecond spectroscopy.

[199] E. Yakaboylu, M. Klaiber, and K. Z. Hatsagortsyan. Wigner time delay for tunneling ionization via the electron propagator. *Phys. Rev. A*, 90:012116, Jul 2014.

[200] C.-G. Wahlström, J. Larsson, A. Persson, T. Starczewski, S. Svanberg, P. Salières, Ph. Balcou, and Anne L'Huillier. High-order harmonic generation in rare gases with an intense short-pulse laser. *Phys. Rev. A*, 48:4709–4720, Dec 1993.

[201] T. Popmintchev, M.-C. Chen, D. Popmintchev, P. Arpin, S. Brown, S. Ališauskas, G. Andriukaitis, T. Balčiunas, O. D. Mücke, A. Pugzlys, A. Baltuška, B. Shim, S. E. Schrauth, A. Gaeta, C. Hernández-García, L. Plaja, A. Becker, A. Jaron-Becker, M. M. Murnane, and H. C. Kapteyn. Bright coherent ultrahigh harmonics in the kev x-ray regime from mid-infrared femtosecond lasers. *Science*, 336(6086):1287–1291, 2012.

[202] M. Chini, X. Wang, Y. Cheng, H. Wang Y. Wu, E. Cunningham, P.-C. Li, J. Heslar D. A. Telnov S.-I Chu, and Z. Chang. Coherent phase-matched vuv generation by field-controlled bound states. *Nat. Photon.*, 8:437–441, 2014.

[203] D. C. Yost, T. R. Schibli, J. Ye, J. L. Tate, J. Hostetter, M. B. Gaarde, and K. J. Schafer. Vacuum-ultraviolet frequency combs from below-threshold harmonics. *Nat. Phys.*, 5:815–820, 2009.

[204] T. Auguste, P. Salières, A. S. Wyatt, A. Monmayrant, I. A. Walmsley, E. Cormier, A. Zaïr, M. Holler, A. Guandalini, F. Schapper, J. Biegert, L. Gallmann, and U. Keller. Theoretical and experimental analysis of quantum path interferences in high-order harmonic generation. *Phys. Rev. A*, 80:033817, Sep 2009.

[205] M. Lewenstein, P. Salières, and A. L'Huillier. Phase of the atomic polarization in high-order harmonic generation. *Phys. Rev. A*, 52:4747–4754, Dec 1995.

[206] P. Balcou, P. Salières, A. L'Huillier, and M. Lewenstein. Generalized phase-matching conditions for high harmonics: The role of field-gradient forces. *Phys. Rev. A*, 55:3204–3210, Apr 1997.

[207] R. W. Boyd. *Nonlinear Optics*. Elsevier: Academic Press, 3 edition, 2008.

[208] A. Rundquist, C. G. Durfee, Z. Chang, C. Herne, S. Backus, M. M. Murnane, and H. C. Kapteyn. Phase-matched generation of coherent soft x-rays. *Science*, 280:1412–1415, 1998.

[209] C. G. Durfee, A. R. Rundquist, S. Backus, C. Herne, M. M. Murnane, and H. C. Kapteyn. Phase matching of high-order harmonics in hollow waveguides. *Phys. Rev. Lett.*, 83:2187–2190, 1999.

[210] E. Constant, D. Garzella, P. Breger, E. Mével, Ch. Dorrer, C. Le Blanc, F. Salin, and P. Agostini. Optimizing high harmonic generation in absorbing gases: Model and experiment. *Phys. Rev. Lett.*, 82:1668–1671, Feb 1999.

[211] Y. Tamaki, Y. Nagata, M. Obara, and K. Midorikawa. Phase-matched high-order-harmonic generation in a gas-filled hollow fiber. *Phys. Rev. A*, 59:4041–4044, May 1999.

[212] E. Goulielmakis, M. Schultze, M. Hofstetter, V. S. Yakovlev, J. Gagnon, M. Uiberacker, A. L. Aquila, E. M. Gullikson, D. T. Attwood, R. Kienberger, F. Krausz, and U. Kleineberg. Single-cycle nonlinear optics. *Science*, 320(5883):1614–1617, 2008.

[213] A. Paul, R. A. Bartels, R. Tobey, H. Green, S. Weiman, I. P. Christov, M. M. Murnane, H. C. Kapteyn, and S. Backus. Quasi-phase-matched generation of coherent extreme-ultraviolet light. *Nature*, 421(6918):51–54, 01 2003.

[214] E. A. Gibson, A. Paul, N. Wagner, R. Tobey, D. Gaudiosi, S. Backus, I. P. Christov, A. Aquila, E. M. Gullikson, D. T. Attwood, M. M. Murnane, and H. C. Kapteyn. Coherent soft x-ray generation in the water window with quasi-phase matching. *Science*, 302(5642):95–98, 2003.

[215] M. Zepf, B. Dromey, M. Landreman, P. Foster, and S. M. Hooker. Bright quasi-phase-matched soft-x-ray harmonic radiation from argon ions. *Phys. Rev. Lett.*, 99:143901, Oct 2007.

[216] K. O'Keeffe, T. Robinson, and S. M. Hooker. Quasi-phase-matching high harmonic generation using trains of pulses produced using an array of birefringent plates. *Opt. Express*, 20(6):6236–6247, Mar 2012.

[217] K. O'Keeffe, D. T. Lloyd, and S. M. Hooker. Quasi-phase-matched high-order harmonic generation using tunable pulse trains. *Opt. Express*, 22(7):7722–7732, Apr 2014.

[218] P. Tzallas, D. Charalambidis, N. A. Papadogiannis, K. Witte, and G. D. Tsakiris. Direct observation of attosecond light bunching. *Nature*, 426:267–271, 2003.

[219] F. Quéré, Y. Mairesse, and J. Itatani. Temporal characterization of attosecond xuv fields. *J. Mod. Opt.*, 52(2-3):339–360, 2005.

[220] I. A. Walmsley and V. Wong. Characterization of the electric field of ultrashort optical pulses. *J. Opt. Soc. Am. B*, 13(11):2453–2463, Nov 1996.

[221] M. Drescher, M. Hentschel, R. Kienberger, G. Tempea, C. Spielmann, G. A. Reider, P. B. Corkum, and F. Krausz. X-ray pulses approaching the attosecond frontier. *Science*, 291(5510):1923–1927, 2001.

[222] J. Itatani, F. Quéré, G. L. Yudin, M. Yu. Ivanov, F. Krausz, and P. B. Corkum. Attosecond streak camera. *Phys. Rev. Lett.*, 88:173903, Apr 2002.

[223] R. Kienberger, E. Goulielmakis, M. Uiberacker, A. Baltuska, V. Yakovlev, F. Bammer, A. Scrinzi, Th. Westerwalbesloh, U. Kleineberg, U. Heinzmann, M. Drescher, and F. Krausz. Atomic transient recorder. *Nature*, 427:817–821, 2004.

[224] V. Véniard, R. Taïeb, and A. Maquet. Phase dependence of (n+1)-color (n>1) ir-uv photoionization of atoms with higher harmonics. *Phys. Rev. A*, 54:721–728, Jul 1996.

[225] H. G. Muller. Reconstruction of attosecond harmonic beating by interference of two-photon transitions. *Appl. Phys. B*, 74:S17–S21, 2002.

[226] Y. Mairesse, A. de Bohan, L. J. Frasinski, H. Merdji, L. C. Dinu, P. Monchicourt, P. Breger, M. Kovačev, R. Taïeb, B. Carré, H. G. Muller, P. Agostini, and P. Salières. Attosecond synchronization of high-harmonic soft x-rays. *Science*, 302(5650):1540–1543, 2003.

[227] R. López-Martens, K. Varjú, P. Johnsson, J. Mauritsson, Y. Mairesse, P. Salières, M. B. Gaarde, K. J. Schafer, A. Persson, S. Svanberg, C.-G. Wahlström, and A. L'Huillier. Amplitude and phase control of attosecond light pulses. *Phys. Rev. Lett.*, 94:033001, Jan 2005.

[228] Y. Mairesse and F. Quéré. Frequency-resolved optical gating for complete reconstruction of attosecond bursts. *Phys. Rev. A*, 71:011401, Jan 2005.

[229] E. M. Kosik, L. Corner, A. S. Wyatt, E. Cormier, I. A. Walmsley, and L. F. DiMauro. Complete characterization of attosecond pulses. *J. Mod. Opt.*, 52(2-3):361–378, 2005.

[230] F. Quéré, J. Itatani, G. L. Yudin, and P. B. Corkum. Attosecond spectral shearing interferometry. *Phys. Rev. Lett.*, 90:073902, Feb 2003.

[231] Eric Cormier, Ian A. Walmsley, Ellen M. Kosik, Adam S. Wyatt, Laura Corner, and Louis F. DiMauro. Self-referencing, spectrally, or spatially encoded spectral interferometry for the complete characterization of attosecond electromagnetic pulses. *Phys. Rev. Lett.*, 94:033905, Jan 2005.

[232] Y. Mairesse, O. Gobert, P. Breger, H. Merdji, P. Meynadier, P. Monchicourt, M. Perdrix, P. Salières, and B. Carré. High harmonic xuv spectral phase interferometry for direct electric-field reconstruction. *Phys. Rev. Lett.*, 94(17):173903, May 2005.

[233] K. T. Kim, C. Zhang, A. D. Shiner, S. E. Kirkwood, E. Frumker, G. Gariepy, A. Naumov, D. M. Villeneuve, and P. B. Corkum. Manipulation of quantum paths for space-time characterization of attosecond pulses. *Nat. Phys.*, 9:159–63, 2013.

[234] D. G. Lee, J. J. Park, J. H. Sung, and C. H. Nam. Wave-front phase measurements of high-order harmonic beams by use of point-diffraction interferometry. *Opt. Lett.*, 28(6):480–482, Mar 2003.

[235] C. Valentin, J. Gautier, J.-P. Goddet, C. Hauri, T. Marchenko, E. Papalazarou, G. Rey, S. Sebban, O. Scrick, P. Zeitoun, G. Dovillaire, X. Levecq, S. Bucourt, and M. Fajardo. High-order harmonic wave fronts generated with controlled astigmatic infrared laser. *J. Opt. Soc. Am. B*, 25(7):B161–B166, Jul 2008.

[236] J. Gautier, P. Zeitoun, C. Hauri, A.-S. Morlens, G. Rey, C. Valentin, E. Papalarazou, J.-P. Goddet, S. Sebban, F. Burgy, P. Mercère, M. Idir, G. Dovillaire, X. Levecq, S. Bucourt, M. Fajardo, H. Merdji, and J.-P. Caumes. Optimization of the wave front of high order harmonics. *Euro. Phys. J. D*, 48(3):459–463, 2008.

[237] E. Frumker, G. G. Paulus, H. Niikura, D. M. Villeneuve, and P. B. Corkum. Frequency-resolved high-harmonic wavefront characterization. *Opt. Lett.*, 34(19):3026–3028, Oct 2009.

[238] E. Frumker, G. G. Paulus, H. Niikura, A. Naumov, D. M. Villeneuve, and P. B. Corkum. Order-dependent structure of high harmonic wavefronts. *Opt. Express*, 20(13):13870–13877, Jun 2012.

[239] David T. Lloyd, Kevin O'Keeffe, and Simon M. Hooker. Complete spatial characterization of an optical wavefront using a variable-separation pinhole pair. *Opt. Lett.*, 38(7):1173–1175, Apr 2013.

[240] D. R. Austin, T. Witting, C. A. Arrell, F. Frank, A. S. Wyatt, J. P. Marangos, J. W.G. Tisch, and I. A. Walmsley. Lateral shearing interferometry of high-harmonic wavefronts. *Opt. Lett.*, 36(10):1746–1748, May 2011.

[241] T. Ruchon, C. P. Hauri, K. Varjú, E. Mansten, M. Swoboda, R. López-Martens, and A. L'Huillier. Macroscopic effects in attosecond pulse generation. *New J. Phys.*, 10(2):025027, 2008.

[242] J.-P. Brichta, M. C. H. Wong, J. B. Bertrand, H.-C. Bandulet, D. M. Rayner, and V. R. Bhardwaj. Comparison and real-time monitoring of high-order harmonic generation in different sources. *Phys. Rev. A*, 79:033404, Mar 2009.

[243] Toshiaki Kita, Tatsuo Harada, N. Nakano, and H. Kuroda. Mechanically ruled aberration-corrected concave gratings for a flat-field grazing-incidence spectrograph. *Appl. Opt.*, 22(4):512–513, Feb 1983.

[244] N. Nakano, H. Kuroda, T. Kita, and T. Harada. Development of a flat-field grazing-incidence XUV spectrometer and its applications in picosecond xuv spectroscopy. *Appl. Opt.*, 23:51–57, 1984.

[245] T. Harada, K. Takahashi, H. Sakuma, and A. Osyczka. Optimum design of a grazing-incidence flat-field spectrograph with a spherical varied-line-space grating. *Appl. Opt.*, 38:2743–2748, 1999.

[246] G. W. Fraser, M. A. Barstow, J. F. Pearson, M. J. Whiteley, and M. Lewis. The soft x-ray detection efficiency of coated microchannel plates. *Nucl. Instrum. Meth. Phys. Res.*, 224:272–286, 1984.

[247] O. H. W. Siegmund, E. Everman, J. V. Vallerga, and M. Lampton. Extreme ultraviolet quantum efficiency of opaque alkali halide photocathodes on microchannel plates. In C. S. Bowyer and J. S. Seeley, editors, *Optoelectronic Technologies for Remote Sensing from Space*, volume 0868, 1988.

[248] P. Salières, A. L'Huillier, and M. Lewenstein. Coherence control of high-order harmonics. *Phys. Rev. Lett.*, 74:3776–3779, May 1995.

[249] P. Salières, T. Ditmire, M. D. Perry, A. L'Huillier, and M. Lewenstein. Angular distributions of high-order harmonics generated by a femtosecond laser. *J. Phys. B*, 29(20):4771, 1996.

[250] M. B. Gaarde and K. J. Schafer. Quantum path distributions for high-order harmonics in rare gas atoms. *Phys. Rev. A*, 65:031406, Mar 2002.

[251] E. Benedetti, J.-P. Caumes, G. Sansone, S. Stagira, C. Vozzi, and M. Nisoli. Frequency chirp of long electron quantum paths in high-order harmonicgeneration. *Opt. Express*, 14(6):2242–2249, Mar 2006.

[252] G. Sansone, E. Benedetti, J.-P. Caumes, S. Stagira, C. Vozzi, M. Pascolini, L. Poletto, P. Villoresi, S. De Silvestri, and M. Nisoli. Measurement of harmonic phase differences by interference of attosecond light pulses. *Phys. Rev. Lett.*, 94:193903, May 2005.

[253] F. Schapper, M. Holler, T. Auguste, A. Zaïr, M. Weger, P. Salières, L. Gallmann, and U. Keller. Spatial fingerprint of quantum path interferences in high order harmonic generation. *Opt. Express*, 18(3):2987–2994, Feb 2010.

[254] A. Zaïr, M. Holler, A. Guandalini, F. Schapper, J. Biegert, L. Gallmann, U. Keller, A. S. Wyatt, A. Monmayrant, I. A. Walmsley, E. Cormier, T. Auguste, J. P. Caumes, and P. Salières. Quantum path interferences in high-order harmonic generation. *Phys. Rev. Lett.*, 100:143902, Apr 2008.

[255] M. Holler, A. Zaïr, F. Schapper, T. Auguste, E. Cormier, A. Wyatt, A. Monmayrant, I. A. Walmsley, L. Gallmann, P. Salières, and U. Keller. Ionization effects on spectral signatures of quantum-path interference in high-harmonic generation. *Opt. Express*, 17(7):5716–5722, Mar 2009.

[256] M. Bellini, C. Lyngå, A. Tozzi, M. B. Gaarde, T. W. Hänsch, A. L'Huillier, and C.-G. Wahlström. Temporal coherence of ultrashort high-order harmonic pulses. *Phys. Rev. Lett.*, 81:297–300, Jul 1998.

[257] C. Lyngå, M. B. Gaarde, C. Delfin, M. Bellini, T. W. Hänsch, A. L' Huillier, and C.-G. Wahlström. Temporal coherence of high-order harmonics. *Phys. Rev. A*, 60:4823–4830, Dec 1999.

[258] Z. Chang, A. Rundquist, H. Wang, I. Christov, H. C. Kapteyn, and M. M. Murnane. Temporal phase control of soft-x-ray harmonic emission. *Phys. Rev. A*, 58:R30–R33, Jul 1998.

[259] M. Kretschmar, C. Hernández-García, D. S. Steingrube, L. Plaja, U. Morgner, and M. Kovačev. Spatial contributions of electron trajectories to high-order-harmonic radiation originating from a semi-infinite gas cell. *Phys. Rev. A*, 88:013805, Jul 2013.

[260] T. Sekikawa, T. Ohno, T. Yamazaki, Y. Nabekawa, and S. Watanabe. Pulse compression of a high-order harmonic by compensating the atomic dipole phase. *Phys. Rev. Lett.*, 83:2564–2567, Sep 1999.

[261] J.-F. Hergott, M. Kovačev, H. Merdji, C. Hubert, Y. Mairesse, E. Jean, P. Breger, P. Agostini, B. Carré, and P. Salières. Extreme-ultraviolet high-order harmonic pulses in the microjoule range. *Phys. Rev. A*, 66:021801, Aug 2002.

[262] H. Merdji, M. Kovačev, W. Boutu, P. Salières, F. Vernay, and B. Carré. Macroscopic control of high-order harmonics quantum-path components for the generation of attosecond pulses. *Phys. Rev. A*, 74:043804, Oct 2006.

[263] F. Calegari, M. Lucchini, K. S. Kim, F. Ferrari, C. Vozzi, S. Stagira, G. Sansone, and M. Nisoli. Quantum path control in harmonic generation by temporal shaping of few-optical-cycle pulses in ionizing media. *Phys. Rev. A*, 84:041802, Oct 2011.

[264] M. Lucchini, F. Calegari, K. Kim, G. Sansone, and M. Nisoli. Nonadiabatic quantum path analysis of the high-order harmonic generation in a highly ionized medium. *New J. Phys.*, 14(3):033009, 2012.

[265] T. Sekikawa, T. Kanai, and S. Watanabe. Frequency-resolved optical gating of femtosecond pulses in the extreme ultraviolet. *Phys. Rev. Lett.*, 91:103902, Sep 2003.

[266] J. Mauritsson, P. Johnsson, R. López-Martens, K. Varjú, W. Kornelis, J. Biegert, U. Keller, M. B. Gaarde, K. J. Schafer, and A. L'Huillier. Measurement and control of the frequency chirp rate of high-order harmonic pulses. *Phys. Rev. A*, 70:021801, Aug 2004.

[267] C. Corsi, A. Pirri, E. Sali, A. Tortora, and M. Bellini. Direct interferometric measurement of the atomic dipole phase in high-order harmonic generation. *Phys. Rev. Lett.*, 97:023901, Jul 2006.

[268] A. Pirri, C. Corsi, E. Sali, A. Tortora, and M. Bellini. Interferometric measurement of the atomic dipole phase for the two electronic quantum paths generating high-order harmonics. *Laser Phys.*, 17(2):138–142, 2007.

[269] J.-H. Kim, D. G. Lee, H. J. Shin, and C. H. Nam. Wigner time-frequency distribution of high-order harmonics. *Phys. Rev. A*, 63:063403, May 2001.

[270] M. B. Gaarde, F. Salin, E. Constant, Ph. Balcou, K. J. Schafer, K. C. Kulander, and A. L'Huillier. Spatiotemporal separation of high harmonic radiation into two quantum path components. *Phys. Rev. A*, 59:1367–1373, Feb 1999.

[271] M. Gaarde. Time-frequency representations of high order harmonics. *Opt. Express*, 8(10):529–536, May 2001.

[272] W. Yang, X. Song, Z. Zeng, R. Li, and Z. Xu. Quantum path interferences of electron trajectories in two-center molecules. *Opt. Express*, 18(3):2558–2565, Feb 2010.

[273] A. Zaïr, T. Siegel, S. Sukiasyan, F. Risoud, L. Brugnera, C. Hutchison, Z. Diveki, T. Auguste, J. W.G. Tisch, P. Salières, M. Y. Ivanov, and J. P. Marangos. Molecular internal dynamics studied by quantum path interferences in high order harmonic generation. *Chem. Phys.*, 414(0):184 – 191, 2013. Attosecond spectroscopy.

[274] M. M. Mang, C. Bourassin-Bouchet, and I. A. Walmsley. Simultaneous spatial characterization of two independent sources of high harmonic radiation. *Opt. Lett.*, 39(21):6142–6145, Nov 2014.

[275] M. Kovačev, S. V. Fomichev, E. Priori, Y. Mairesse, H. Merdji, P. Monchicourt, P. Breger, J. Norin, A. Persson, A. L'Huillier, C.-G. Wahlström, B. Carré, and P. Salières. Extreme ultraviolet fourier-transform spectroscopy with high order harmonics. *Phys. Rev. Lett.*, 95:223903, Nov 2005.

[276] P. Tournois. Acousto-optic programmable dispersive filter for adaptive compensation of group delay time dispersion in laser systems. *Opt. Commun.*, 140:245–249, 1997.

[277] H. Stapelfeldt and T. Seideman. Colloquium: Aligning molecules with strong laser pulses. *Rev. Mod. Phys.*, 75:543–557, Apr 2003.

[278] J. Itatani, J. Levesque, D. Zeidler, H. Niikura, H. Pépin, J. C. Kieffer, P. B. Corkum, and D. M. Villeneuve. Tomographic imaging of molecular orbitals. *Nature*, 432:867–871, 2004.

[279] O. Smirnova, Y. Mairesse, S. Patchkovskii, N. Dudovich, D. Villeneuve, P. Corkum, and M. Y. Ivanov. High harmonic interferometry of multi-electron dynamics in molecules. *Nature*, 460(7258):972–977, 08 2009.

[280] Y. Mairesse, D. Zeidler, N. Dudovich, M. Spanner, J. Levesque, D. M. Villeneuve, and P. B. Corkum. High-order harmonic transient grating spectroscopy in a molecular jet. *Phys. Rev. Lett.*, 100:143903, Apr 2008.

[281] H. J. Wörner, J. B. Bertrand, D. V. Kartashov, P. B. Corkum, and D. M. Villeneuve. Following a chemical reaction using high-harmonic interferometry. *Nature*, 466:604–607, 2010.

[282] S. Watanabe, K. Kondo, Y. Nabekawa, A. Sagisaka, and Y. Kobayashi. Two-color phase control in tunneling ionization and harmonic generation by a strong laser field and its third harmonic. *Phys. Rev. Lett.*, 73:2692–2695, Nov 1994.

[283] H. Eichmann, A. Egbert, S. Nolte, C. Momma, B. Wellegehausen, W. Becker, S. Long, and J. K. McIver. Polarization-dependent high-order two-color mixing. *Phys. Rev. A*, 51:R3414–R3417, May 1995.

[284] U. Andiel, G. D. Tsakiris, E. Cormier, and K. Witte. High-order harmonic amplitude modulation in two-colour phase-controlled frequency mixing. *Europhys. Lett.*, 47(1):42–48, 1999.

[285] R. Bartels, S. Backus, E. Zeek, L. Misoguti, G. Vdovin, I. P. Christov, M. M. Murnane, and H. C. Kapteyn. Shaped-pulse optimization of coherent emission of high-harmonic soft x-rays. *Nature*, 406:164–166, 2000.

[286] I J. Kim, C. M. Kim, H. T. Kim, G. H. Lee, Y. S. Lee, J. Y. Park, D. J. Cho, and C. H. Nam. Highly efficient high-harmonic generation in an orthogonally polarized two-color laser field. *Phys. Rev. Lett.*, 94:243901, Jun 2005.

[287] N. Dudovich, O. Smirnova, J. Levesque, Y. Mairesse, M. Yu. Ivanov, D. M. Villeneuve, and P. B. Corkum. Measuring and controlling the birth of attosecond xuv pulses. *Nat. Phys.*, 2(11):781–786, 11 2006.

[288] D. Shafir, H. Soifer, B. D. Bruner, M. Dagan, Y. Mairesse, S. Patchkovskii, M. Y. Ivanov, and O. Smirnova N. Dudovich. Resolving the time when an electron exits a tunnelling barrier. *Nature*, 485:343–346, 2012.

[289] J. Ratner, G. Steinmeyer, T. C. Wong, R. Bartels, and R. Trebino. Coherent artifact in modern pulse measurements. *Opt. Lett.*, 37(14):2874–2876, Jul 2012.

[290] L. Le Déroff, P. Salières, B. Carré, D. Joyeux, and D. Phalippou. Measurement of the degree of spatial coherence of high-order harmonics using a fresnel-mirror interferometer. *Phys. Rev. A*, 61:043802, Mar 2000.

[291] T. Ditmire, E. T. Gumbrell, R. A. Smith, J. W. G. Tisch, D. D. Meyerhofer, and M. H. R. Hutchinson. Spatial coherence measurement of soft x-ray radiation produced by high order harmonic generation. *Phys. Rev. Lett.*, 77:4756–4759, Dec 1996.

[292] T. Ditmire, J.W.G. Tisch, E.T. Gumbrell, R.A. Smith, D.D. Meyerhofer, and M.H.R. Hutchinson. Spatial coherence of short wavelength high-order harmonics. *Appl. Phys. B*, 65(3):313–328, 1997.

[293] M.-C. Chen, M. R. Gerrity, S. Backus, T. Popmintchev, X. Zhou, P. Arpin, X. Zhang, H. C. Kapteyn, and M. M. Murnane. Spatially coherent, phase matched, high-order harmonic euv beams at 50 khz. *Opt. Express*, 17(20):17376–17383, Sep 2009.

[294] R. A. Ganeev, Z. Abdelrahman, F. Frank, T. Witting, W. A. Okell, D. Fabris, C. Hutchison, J. P. Marangos, and J. W. G. Tisch. Spatial coherence measurements

of non-resonant and resonant high harmonics generated in laser ablation plumes. *Appl. Phys. Lett.*, 104(2):021122, 2014.

[295] M. Born and E. Wolf. *Principles of Optics*. Cambridge University Press, 1999.

[296] E. Wolf. New theory of partial coherence in the space-frequency domain. part i: spectra and cross spectra of steady-state sources. *J. Opt. Soc. Am.*, 72(3):343–351, Mar 1982.

[297] E. Wolf. *Introduction to the Theory of Coherence and Polarization of Light*. Cambridge University Press, 2007.

[298] T. Young. The bakerian lecture: Experiments and calculations relative to physical optics. *Phil. Trans. R. Soc. Lon.*, 94:1–16, 1804.

[299] T. Young. A course of lectures on natural philosophy and the mechanical arts. 2, 1807.

[300] L. Mandel and E. Wolf. *Optical Coherence and Quantum Optics*. Cambridge University Press, 1995.

[301] Miguel A. Alonso. Wigner functions in optics: describing beams as ray bundles and pulses as particle ensembles. *Adv. Opt. Photon.*, 3(4):272–365, Dec 2011.

[302] D. T. Smithey, M. Beck, M. G. Raymer, and A. Faridani. Measurement of the wigner distribution and the density matrix of a light mode using optical homodyne tomography: Application to squeezed states and the vacuum. *Phys. Rev. Lett.*, 70:1244–1247, Mar 1993.

[303] A. I. Lvovsky, H. Hansen, T. Aichele, O. Benson, J. Mlynek, and S. Schiller. Quantum state reconstruction of the single-photon fock state. *Phys. Rev. Lett.*, 87:050402, Jul 2001.

[304] P. Thibault and A. Menzel. Reconstructing state mixtures from diffraction measurements. *Nature*, 494(7435):68–71, 02 2013.

[305] Jesse N. Clark, Xiaojing Huang, Ross J. Harder, and Ian K. Robinson. Dynamic imaging using ptychography. *Phys. Rev. Lett.*, 112:113901, Mar 2014.

[306] C. Dorrer and I. A. Walmsley. High-dynamic-range measurement of the two-point field correlation function by carrier-encoded spatial shearing interferometry. *Opt. Lett.*, 27(18):1613–1615, Sep 2002.

[307] M. A. Schofield and Y. Zhu. Fast phase unwrapping algorithm for interferometric applications. *Opt. Lett.*, 28(14):1194–1196, Jul 2003.

[308] F. Frank, C. Arrell, T. Witting, W. A. Okell, J. McKenna, J. S. Robinson, C. A. Haworth, D. Austin, H. Teng, I. A. Walmsley, J. P. Marangos, and J. W. G. Tisch. Invited review article: Technology for attosecond science. *Rev. Sci. Instrum.*, 83(7):071101, 2012.

[309] M. Schultze, A. Wirth, I. Grguras, M. Uiberacker, T. Uphues, A. J. Verhoef, J. Gagnon, M. Hofstetter, U. Kleineberg, E. Goulielmakis, and F. Krausz. State-of-the-art attosecond metrology. *J. El. Spectr. Rel. Phen.*, 184:68–77, 2011.

[310] M. D. Seaberg, D. E. Adams, E. L. Townsend, D. A. Raymondson, W. F. Schlotter, Y. Liu, C. S. Menoni, L. Rong, C.-C. Chen, J. Miao, H. C. Kapteyn, and M. M. Murnane. Ultrahigh 22 nm resolution coherent diffractive imaging using a desktop 13 nm high harmonic source. *Opt. Express*, 19(23):22470–22479, Nov 2011.

[311] G. Dai. *Wavefront Optics for Vision Correction.* SPIE, 2008.

[312] W. Wirtinger. Zur formalen Theorie der Funktionen von mehr komplexen Veränderlichen. *Math. Ann.*, 97:357–375, 1927.